Modelling the ultraviolet environment at the surface of Mars and design of the Beagle 2 UV sensor

Thesis

Modelling the Ultraviolet Environment at the Surface of Mars and Design of the Beagle 2 UV Sensor

Manish R. Patel

September 2003

A THESIS SUBMITTED TO THE OPEN UNIVERSITY IN THE SUBJECT OF PLANETARY SCIENCES FOR THE DEGREE OF DOCTOR OF PHILOSOPHY

Dedicated to the memory of my brother

Acknowledgements

Firstly I would like to express my gratitude to my supervisor Prof. John Zarnecki and the OU PSSRI group for giving me the opportunity to undertake this project and be part of the Beagle 2 endeavour. My eternal thanks also go to Dr. Elena Petrova at the Space Research Institute in Moscow, who (even though we have never actually met) has selflessly guided me through the realm of radiative transfer on Mars, and was always willing to offer the wisest advice over the past few years when I truly needed it. Also thanks to my examiners, Dr Charles Cockell and Dr Neil McBride, for some tough and gruelling (but fair!) questions.

I am also indebted to all those people in PSSRI whose advice and direction have been invaluable throughout this Ph.D. – Dr. Martin Towner and Mark Leese especially, thanks for enlightening me along the way, and taking the time to explain the mind-numbing intricacies of a space mission. Also to Mike Müller for the unenviable task of teaching me IDL, and putting up with me in sharing a house.

Thanks also go to my friends for keeping me busy out of work, be it playing football or sampling the local liquid delicacies – especially Baker, Taff, Daz and Sheridan – beyond the call of duty lads. To all the guys back at UKC – especially Lee and Andy – thank god we moved to the OU else I'd never have gotten round to finishing my Ph.D..... To Tim "Ringa" Ringrose, who has followed the same path as me through academia, and always kept me up to date with every episode of Neighbours throughout this Ph.D. Most importantly, to Louise, who has been by my side throughout the entirety of this thesis, and always been there for me when I needed her most.

My final thanks go to my family for their love and absolute support during my long voyage through academia – to my sister, mum and dad for their unquestioning support in giving me the chance to follow my own path, and for their faith in what I can achieve. Dad, thanks for showing to me the universe we live in, and for turning my head towards the stars.

Abstract

This thesis describes a multi-layer radiative transfer UV model which was used to aid in the design of the UV sensor on Beagle 2, which will soon provide the first ever *in situ* measurement of UV flux at the martian surface. The model uses the delta-Eddington approximation for diffuse flux and new low temperature gas absorption cross-sections and aerosol optical properties.

Dust, H_2O clouds and morning fogs are found to modify the martian surface UV spectrum. Dust storms have been shown to attenuate the surface UV flux by more than an order of magnitude, though some UV persists even at extremely high optical depths. The seasonal variation of surface UV irradiance was found to produce maximum exposure areas highly dependent upon dust activity over the martian year. Dust activity is also shown to distort the annual latitudinal dose, with high dust loading in the southern hemisphere resulting in a higher annual dose than in the north.

The introduction of O_3 abundances of 1.64×10^{17} cm^{-2} into the model resulted in only partial protection for micro-organisms, since wavelengths shorter than 230 nm still penetrate to the surface. DNA-weighting of a martian UV spectrum shows the surface UV environment to be 10^3 times more damaging than on Earth. UV detection signatures of atmospheric phenomena and anticipated events for the case of Beagle 2 are presented: a dust devil encounter creates a double minimum profile in the UV flux, and solar eclipses by Phobos produce a single minimum. Clouds increase the diffuse/direct UV ratio, and fogs create a distinct dip in the morning profile when normalised to clear days.

Publications

The following *refereed journal publications* were produced as a result of this Ph.D., covering a range of studies:

Patel, M.R., J.C. Zarnecki and D.C. Catling 2002. Ultraviolet radiation on the surface of Mars and the Beagle 2 UV sensor. *Planet. Space Sci.* **50** (9), 915-927.

Patel, M.R., A. Berces, C. Kolb, H. Lammer, P. Rettberg, J.C. Zarnecki and F. Selsis 2003. Seasonal and diurnal variations in martian surface ultraviolet irradiation: Biological and chemical implications for the martian regolith. *Int. J. Astrobiology* **2** (1), 21-34.

Patel, M.R., A. Berces, T. Kerekgyarto, G. Ronto, H. Lammer and J.C. Zarnecki 2003. Annual solar UV exposure and biologically effective dose rates on the martian surface. *Adv. Space Res.* (in press).

Patel, M.R., A.A. Christou, C.S. Cockell, T.J. Ringrose and J.C. Zarnecki 2003. The UV environment of the Beagle 2 landing site: Detailed investigations and detection of atmospheric state. *Icarus* (in press).

Ronto, G., A. Berces, H. Lammer, C.S. Cockell, G.J. Molina-Cuberos, **M.R. Patel** and F. Selsis 2003. Solar UV irradiation conditions on the surface of Mars. *Photochem. Photobiol.* **77** (1), 34-40.

Towner, M.C., **M.R. Patel**, T.J. Ringrose, J.C. Zarnecki, D. Pullan, M.R. Sims, S. Haapanala, A.M. Harri, J. Polkko and C.F. Wilson 2003. The Beagle 2 Environmental Sensors: Science goals and instrument description. *Planet. Space Sci.* (submitted).

Lammer, H., P. Wurz, **M.R. Patel**, R.M. Killen, C. Kolb, S. Massetti, S. Orsini and A. Milillo 2003. The variability of Mercury's exosphere by particle and radiation induced surface release processes. *Icarus* (in press).

Fulchignoni, M., A. Aboudan, F. Angrilli, M. Antonello, S. Bastianello, C. Bettanini, G. Bianchini, G. Colombatti, F. Ferri, E. Flamini, V. Gaborit, N. Ghafoor, B. Hathi, A.M.

Harri, A. Lehto, P.F. Lion Stoppato, **M.R. Patel** and J.C. Zarnecki 2003. A stratospheric balloon experiment to test the Huygens Atmospheric Structure Instrument (HASI). *Planet. Space Sci.* (submitted).

Ellery, A., C. Kolb, H. Lammer, J. Parnell, H. Edwards, L. Richter, **M.R. Patel**, J. Romstedt, D. Dickensheets, A. Steele and C.S. Cockell 2002. Astrobiological instrumentation for Mars – The only way is down. *Int. J. Astrobiology* **1** (4), 365-380.

Ellery, A., A.J. Ball, C.S. Cockell, H. Edwards, C. Kolb, H. Lammer, **M.R. Patel**, L. Richter and C. Welch 2003. Vanguard – A European robotic astrobiology-focussed Mars mission proposal. *Acta Astro.* (submitted).

The following are a selection of the *conference presentations* given over the course of this study:

Patel, M.R., M.C. Towner, T.J. Ringrose, J.C. Zarnecki, D. Pullan, S. Haapanala, A.-M. Harri, J. Polkko, C. Wilson, M.R. Sims. *The Beagle 2 Environmental Sensors: Science Goals and Instrument Description.* EGS XXVIII General Assembly, Nice, France, 6th-11th April, 2003.

Patel, M.R., J.C. Zarnecki, H. Lammer, C. Kolb, and F. Selsis. *Seasonal and Diurnal Variations of UV at the Martian Surface.* 2nd European Workshop on Exo/Astrobiology, Graz, Austria, 16th-19th September, 2002.

Patel, M.R. and J.C. Zarnecki. *Characterisation of the UV Environment of the Beagle 2 Landing Site.* 33rd LPSC, Houston, Texas USA, 11th-15th March, 2002.

Patel, M.R., A. Berces, T. Kerékgyártó, H. Lammer, C. Kolb, J.C. Zarnecki and F. Selsis. *Annual variation of the Biologically Effective UV Dose on the Martian surface.* EGS XXVII General Assembly, Nice, France, 21st-26th April, 2002.

Patel, M.R., R.D. Lorenz, M.C. Towner and J.C. Zarnecki. *Operational Verification of the Beagle 2 UV and Temperature Sensors through fieldwork in the Arizona region.* EGS XXVII General Assembly, Nice, France, 21st-26th April, 2002.

Patel, M.R., M.C. Towner and J.C. Zarnecki. *The Martian Surface UV Environment: Theoretical Modelling and In-Situ Measurements.* 2nd Granada Workshop "The Evolving Sun and its Influence on Planetary Environments", Granada, Spain, 18th-20th June, 2001.

TABLE OF CONTENTS

LIST OF FIGURES

LIST OF TABLES

LIST OF TERMS

A = Surface albedo
A_{avg} = Cross-sectional area
d = Mars mean orbital distance
DU = Dobson unit
e = eccentricity
F_0 = Top of atmosphere flux
$F_{1.52}$ = Flux at 1.52 AU
$F_{diffuse}$ = Diffuse Flux
F_{direct} = Direct Flux
FOV = Field of view
F_{total} = Total Flux
G = Local acceleration due to gravity
g = Particle asymmetry parameter
g' = Transformed asymmetry parameter
g_{bd} = Background dust asymmetry parameter
g_c = Cloud asymmetry parameter
g_{dd} = Dust devil asymmetry parameter
g_{eff} = Composite asymmetry parameter
g_{fog} = Fog asymmetry parameter
g_{gas} = Gas asymmetry parameter
h = Local hour angle
lat = Areocentric Latitude
L_s = Areocentric Solar Longitude
L_s^P = Solar longitude of perihelion
M_{mol} = Mean molecular mass
m_r = True airmass
n_0 = Atmospheric refractive index at the surface
n_{dd} = Particle density within a dust devil
n_x = Layer column abundance for species X
n_z = Atmospheric refractive index at altitude z
P = Pressure
P_{fn} = Phase function
Q = Scattering efficiency
Q_{ext} = Particle extinction efficiency
r = Sun-Mars Distance
$R(0)$ = Fog aerosol initial radius
$R(t_{fog})$ = Fog aerosol radius
r_d = Fog aerosol dust core radius
r_{dd} = Radial position within a dust devil
r_i = Fog aerosol ice mantle radius
R_m = Mean radius of Mars
SZA = Solar zenith angle
t = seconds from local noon
t_f = Time for complete sublimation
t_{fog} = Time from sunrise
T_{sol} = Martian solar day length in seconds
z = Altitude
z_0 = Atmospheric scale height
α_0 = Molecular polarisability
α_S = Ice mantle sublimation rate
∂ = Solar declination
ε = Obliquity
λ = Wavelength
μ_0 = cos (SZA)
μm-atm = micrometre-atmosphere
ρ = Atmospheric density at altitude z
ρ_0 = Atmospheric density at the surface
ρ_i = Ice density
ρ_n = Normal depolarisation ratio
ϕ = Azimuth angle
σ_{abs} = Gas absorption cross-section
$\sigma_{Rayleigh}$ = Rayleigh scattering cross-section
σ_{sca} = Scattering cross-section
τ' = Transformed optical depth
τ_{back} = Background dust optical depth
τ_{da} = Dust optical depth due to absorption
τ_{ddevil} = Dust devil optical depth
τ_{ds} = Dust optical depth due to scattering
τ_{eq} = Equatorial dust component
τ_{fog} = Fog optical depth
τ_{gaX} = Gaseous optical depth due to absorption
τ_{gsX} = Gaseous optical depth due to scattering
$\tau_{hicloud}$ = High altitude cloud optical depth
τ_{high} = High dust annual scenario
τ_{lcloud} = Low altitude cloud optical depth
τ_{low} = Low dust annual scenario
τ_N = Northern dust component
$\tau_{nominal}$ = Nominal dust annual scenario
τ_S = Southern dust component
τ_{sca} = Scattering optical depth
τ_{tot} = Total optical depth
ω' = Transformed single scattering albedo
ω_o = Single scattering albedo
ω_{bd} = Background dust single scattering albedo
ω_c = Cloud single scattering albedo
ω_{dd} = Dust devil single scattering albedo
ω_{eff} = Composite single scattering albedo
ω_{fog} = Fog single scattering albedo
ξ = Column abundance

Chapter One

Introduction

1.1 The Planet Mars

Since time immemorial the planet Mars has held the attention of astronomers, philosophers and poets alike. To the Babylonians, Mars was the 'Star of Death', and to the ancient Greeks it was known as the 'Fiery One'. Even the modern day name of Mars is a tribute to the Roman god of war, son to Jupiter, king of the gods. Since its discovery Mars has instilled in its observers a passionate emotion, one that still rings true to this day.

The recognition and study of the planets began many centuries ago, but the concept of a heliocentric world was not taken seriously until proposed by Nicolaus Copernicus in the 16th century. The question of Mars' apparent retrograde motion was not fully solved until 1604, by Johannes Kepler, as the full complexities of the orbital positions became apparent. With the advent of the telescope early in the 17th century, many lenses were turned towards the red planet, and numerous drawings were made. As technology advanced, so did mapping of the red planet. By the 1780s, astronomers such as Herschel had begun to focus upon the one martian issue that would dominate to this very day – the possibility of life. Herschel interpreted the light and dark patches he observed as areas of land and sea, and the varying surface features as the passage of clouds floating in the atmosphere. Herschel thus considered "...the inhabitants [of Mars] probably enjoy a situation similar to our own."

Indeed the red planet shares many attributes with Earth, making it one of the more probable places for the existence of extraterrestrial life in the Solar System. Both planets share terrestrial-like conditions. Mars possesses a significant gravity (~ ⅓ terrestrial) with a similar rotation period mimicking the terrestrial day-night cycle. Mars also has a comparable obliquity, inducing the same seasonal effects as experienced on Earth and creating similar large-scale atmospheric dynamics. Substantial differences exist though, which make the martian case unique. Though Mars possesses an atmosphere, it is far less dense, with a surface pressure less than 1% that of Earth, and of a different chemical composition. Surface pressure is observed to vary markedly over both seasonal and diurnal cycles, with a ~25% atmospheric mass change as the polar caps form and recede, exchanging CO_2 and H_2O with the atmosphere in a seasonal cycle (e.g. James *et al.* 1992).

The thin martian atmosphere allows greater penetration of high energy particles and electromagnetic radiation, both solar and galactic in origin, whereas the Earth's surface is screened by its thicker atmosphere. The typical thermal environment is also far colder on Mars due to its larger heliocentric distance, with a larger diurnal range due to the thin atmosphere. All these factors combine to create an environment that is in ways similar to the terrestrial case, yet distinct enough to require careful analysis and quantification of whether conditions are favourable for the persistence of organic material and biological activity.

1.2 Previous Mars Missions

Mars and Earth reach a minimum separation every 25 to 27 months at opposition, and consequently are at an ideal time for telescopic observation. At present the primary limitations in space exploration are energy requirements for orbital changes and transit times, and thus the schedule of recent Mars missions has also been based around this time period.

The first tentative steps to explore the red planet were taken by the former Soviet Union in 1960, initially resulting in several failures (a list of all martian missions to date and planned is shown in Table 1-1). The unnamed probes all failed to leave (or even reach) Earth orbit, and it was not until 1962 that a partially successful flight to the martian system was achieved. Although the probe failed before its flyby of Mars, it was the first spacecraft in the history of spaceflight to pass in close proximity to the red planet. These early setbacks were to mark the trend in the future of exploration to the red planet, with a significant proportion of missions resulting in failure.

The United States claimed the first full mission success with the flyby of Mariner 4 in 1964, returning the first scientific data from Mars. Subsequent Mariner missions 6, 7 and 9 continued to return valuable scientific data as the years went on, with the Soviets continuing their exploration attempts through the Zond 2, 3, Mars 69 and Mars 2 to 7 spacecraft. These missions continued into the early 1970s, when the turning point in Mars exploration occurred with the Viking 1 and 2 spacecraft. These orbiter-lander spacecraft marked a shift in focus of scientific experimentation towards the question of the possibility of life.

The landing element of each Viking spacecraft (VL1 and VL2) was equipped with complex biological instrumentation looking for the presence of chemical activity associated with the process of life. Though the results of these investigations appeared to return so called 'false positive' results, the findings of these experiments are still debated even today (e.g. Klein 1999). In spite of these ambiguous findings the Viking probes were deemed to be a resounding success, returning data from the surface for over six years (Zurek *et al.* 1992).

Mission Name	Launch Date	Comments
Unnamed (Mars 1M#1)	10/10/60	Launch failure
Unnamed (Mars 1M#2)	14/10/60	Launch failure
Sputnik 22	24/10/62	Failed in Earth Orbit (EO)
Mars 1	01/11/62	Lost contact, passed Mars
Sputnik 24	04/11/62	Failed in EO
Mariner 3	05/11/64	Failed
Mariner 4	28/11/64	Success – 22 pictures during flyby
Zond 2	30/11/64	Lost contact, passed close to Mars
Zond 3	18/07/65	Successful engineering test
Mariner 6	25/02/69	Success – 75 pictures during flyby
Mariner 7	27/03/69	Success – 126 pictures during flyby
Mars 1969A	27/03/69	Launch failure
Mars 1969A	02/04/69	Launch failure
Mariner 8	08/05/71	Launch failure
Cosmos 419	10/05/71	Failed in EO
Mars 2	19/05/71	Reached Mars orbit, lander crashed
Mars 3	28/05/71	Reached Mars orbit, 20s of lander signal
Mariner 9	30/05/71	Success – 7000 pictures from orbit
Mars 4	21/07/73	Failed to achieve Mars orbit
Mars 5	25/07/73	Achieved Mars orbit
Mars 6	05/08/73	Flyby, lander lost on landing
Mars 7	09/08/73	Flyby, lander missed Mars
Viking 1	20/08/75	Success – lander and orbiter
Viking 2	09/09/75	Success – lander and orbiter
Phobos 1	07/07/88	Lost communication in transit
Phobos 2	12/07/88	Partial success – 2 month operation in orbit
Mars Observer	25/09/92	Lost contact prior to Mars orbit insertion
Mars Global Surveyor	07/11/96	Success, in extended mission phase
Mars '96	16/11/96	Failed in EO
Mars Pathfinder	04/12/96	Success, deployed automated rover
Nozomi	04/07/98	Orbiter, arrival delayed to Dec. 2003
Mars Climate Orbiter	11/12/98	Failed at Mars arrival
Mars Polar Lander (DS-2)	03/01/99	Failed – contact lost prior to landing
Mars Odyssey	07/04/01	Success, entered Mars orbit Oct 2001
Mars Express	*02/06/03*	*En route, orbiter + Beagle 2 lander*
Spirit and Opportunity	*11/06 and 07/07/03*	*En route, twin rovers*
Mars Reconnaissance Orbiter	*2005*	*High resolution imager*
ExoMars	*2009*	*Proposed ESA exobiology rover mission*
NetLander	*?*	*Network of geophysical landers*

Table 1-1: Mars missions - past, present and future.

The next phase in exploration of the martian system took place in 1988, with the launch of the Phobos 1 and 2 spacecraft. Their objectives were to study the martian satellite Phobos, Mars, the Sun and interplanetary space. Phobos 1 was lost in transit, but Phobos 2 did return some scientific data on the atmosphere of Mars, orbiting the planet for nearly 2 months. After this saw the loss of yet two more spacecraft destined for the red planet, Mars Observer and Mars '96. The next successful venture to Mars did not occur until 1997 with the arrival of Mars Pathfinder (MPF). This surface probe contained a rover named Sojourner, which carried out geochemical studies of rocks in the local vicinity of the lander (Golombeck 1997). The mission was a complete success, revitalising public interest and desire to return to the martian world.

Following MPF in the same year, the Mars Global Surveyor (MGS) arrived at Mars. This long duration orbiter mapped the martian surface to an unprecedented resolution, offering images and topographic maps of great detail across the martian globe, giving insight into the various processes that shaped the terrain. Even today, after six years of operation, it is still returning highly valuable scientific data. Missions to Mars were now planned for each launch window available, adopting the philosophy to send regular, smaller scale missions as opposed to the Viking era. But the eagerness to build on the achievements of MPF and MGS were cut short by the subsequent loss of two more spacecraft in 1999, Mars Polar Lander (MPL) which carried the Deep Space 2 probes, and its sister craft Mars Climate Orbiter.

The loss of these spacecraft initiated a major re-think in how NASA would plan and execute such missions, delaying the Mars programme for a brief period. At present MGS has been joined in orbit by Mars Odyssey, a spacecraft with an instrumental focus towards the radiation environment around Mars and a detailed mineralogical analysis of the planetary surface from orbit. Initial investigations through analysis of slow neutron fluxes and gamma rays have revealed a hydrogen-rich sub-surface, giving the best indication to date of water trapped in the near surface regions of Mars (Boynton *et al.* 2002; Feldman *et al.* 2002;

Mitrofanov *et al.* 2002). Current missions *en route* to Mars are the NASA Mars Exploration Rovers (Spirit and Opportunity), the Japanese orbiter Nozomi and the ESA Mars Express mission which incorporates the Beagle 2 lander.

1.3 The Beagle 2 Mission

1.3.1 Mars Express

The main ESA focus on Mars is currently in the form of Mars Express (MEX), an orbiter designed for high resolution photogeology and mineralogical mapping, as well as spectroscopic atmospheric studies and the detection of sub-surface water. Following its successful launch by a Soyuz-Fregat rocket from Baikonour on 2nd June 2003, MEX is set to arrive at the martian system towards the end of December 2003, initially braking into an elliptical orbit before entering its final science orbit (Schmidt 2003). It will arrive at Mars just prior to the arrival of the ISAS spacecraft Nozomi and the NASA Mars Exploration Rovers, joining Mars Odyssey (and possibly MGS if still active). The Mars Express scientific payload is described in detail by Schmidt *et al.* (1999). An array of seven instruments will monitor the martian surface from orbit for a nominal mission time of two terrestrial years.

1.3.2 Beagle 2

MEX carries Beagle 2, a 29 kg surface element that will land on the surface of Mars in late 2003. The lander (shown in Figures 1-1 and 1-2) is planned to reach the martian surface in the Isidis Planitia region on 25th December 2003 at 02:54 (UTC), with nominal landing site coordinates of 11.6°N and 90.5°E, operating from mid-northern martian winter into mid spring. The primary instrument on the lander is focussed on astrobiology, with its main objective the detection of extinct life through biological markers left in the martian

surface/sub-surface material, or the detection of extant life through the identification of methane in the atmosphere, through the use of stepped combustion and a mass spectrometer.

Figure 1-1: The Beagle 2 model fully deployed.

The nominal mission duration is 180 sols, with the possibility of continuation dependent upon battery and solar panel performance. Though the lander is optimised for astrobiology, it will also investigate geochemical properties of the martian surface material, through the use of a Mössbauer spectrometer, a X-ray fluorescence spectrometer, an optical microscope, a rock corer-grinder, a stereo camera and a self-tapping Mole. These instruments are located on the end of a robot arm forming the Position Adjustable Workbench (PAW), allowing the investigation of the surrounding area (Wright *et al.* 2003). The Mole will extract samples from the martian surface and subsurface, delivering them to the lander for detailed chemical analysis of specific carbon isotopic ratios, with the aim of detecting the imprint of possible past life. The third area of research is monitoring of the local martian meteorological environment, through the Environmental Sensor Suite (ESS), which forms the context of this study.

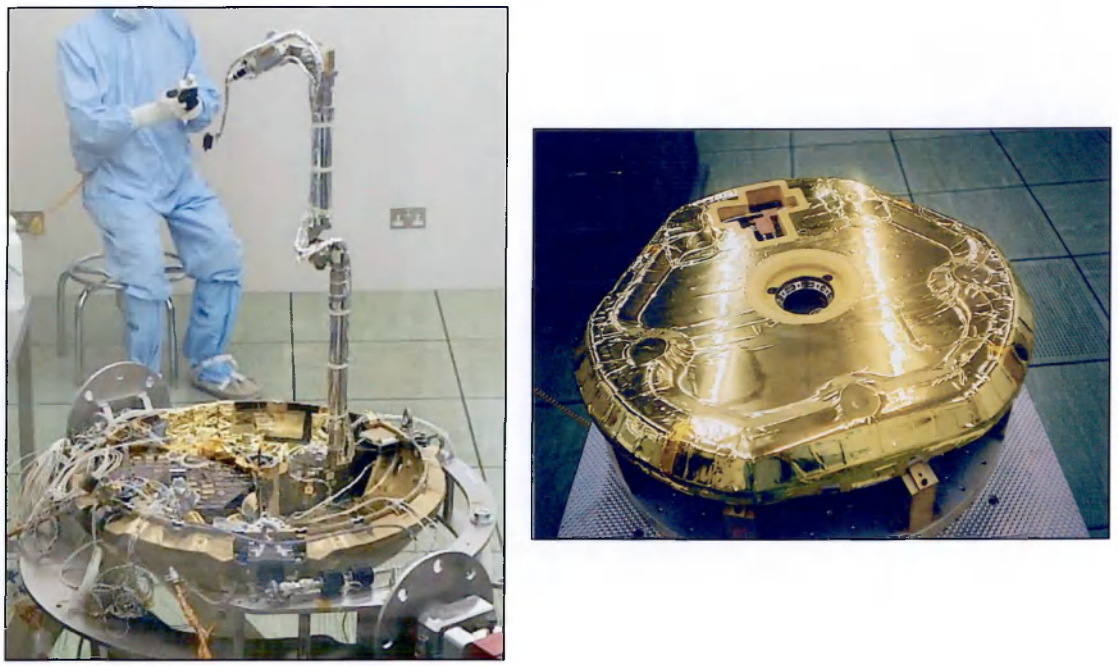

Figure 1-2: Beagle 2 with the arm deployed (left) and sealed for flight (right).

1.3.3 Environmental Sensor Suite (ESS)

The ESS package is a multi-functional miniaturised environmental package, designed to monitor the local meteorological and radiation environment of planetary surfaces. The package itself has a total mass of 153 g, and consists of 7 sensor sub-systems spread throughout the lander structure (Towner *et al.* 2003). ESS consumes a total of 450 mW when all sensor sub-systems are in operation.

The meteorological side of the package consists of instruments to measure air temperature and pressure, wind speed and direction, and dust impacts from saltation on the martian surface. Air temperature will be monitored by two identical sensors, one mounted on the edge of a solar panel and the other as part of the wind sensor. The sensor head consists of a 0.3 mm diameter platinum (Pt) bead, and is extremely fragile due to the necessity of a low thermal mass to surface area ratio, to couple effectively to the thin martian atmosphere. The

air temperature will be measured to an accuracy of ± 0.5 K and a resolution of 0.05 K. The total mass of the sensor including the front-end conditioning electronics is 6 g.

Pressure is measured using a silicon capacitive diaphragm, called Barocap, supplied by the Finnish Meteorological Institute (Harri *et al.* 1998). The capacitive diaphragm allows extreme sensitivity at low pressures, in this case measuring air pressure to an accuracy of ± 0.1 hPa (mbar) and a resolution of 0.01 hPa.

Wind speed and direction is measured using the thermal anemometry approach similar to that used by the wind sensor on MPF (Seiff *et al.* 1997). Three thin-film Pt heat transfer gauges are equally spaced around the circumference of a 1 cm diameter Rohacell vertical cylinder, and each film is resistively heated. The resistance of each film is measured, allowing the heat transfer coefficients to be calculated for each film. Ambient wind subsequently cools the films, and the difference in heat transfer coefficients allows the calculation of a 2-D horizontal wind vector perpendicular to the cylinder. Using this approach wind speed can be calculated to an accuracy of ± 0.1 ms^{-1} and wind direction to 10°.

The Dust sensor is designed to monitor dust impacts from the aeolian transportation of dust across the martian surface. The device consists of a 50 × 50 × 0.5 mm aluminium sheet, with a piezoelectric crystal on the reverse side. Dust impacts upon the sheet will be detected to a momentum sensitivity of 1×10^{-6} kg m s^{-1}.

Long term *in situ* measurements of these parameters serve as primary inputs to Global Circulation Models of the martian atmosphere, assisting in the understanding of the mechanics and evolution of the present-day martian atmosphere. The detection and investigation of transient events, such as dust-laden convective vortices will also be possible, allowing characterisation of these events in terms of their physical parameters, formation and occurrence.

The astrobiology-focussed side of the package consists of the Environmental Sensors Oxidation Sensor (ESOS), designed to measure the rate of oxidisation at the martian surface, and a UV sensor which has been designed specifically to monitor the martian UV environment, which provides the basis of this study. ESOS involves the first ever *in situ* vapour-deposition of a thin silver film on another planet, of which the resistive property over the mission lifetime is measured. A tungsten wire supports a silver bead within a hollow sapphire tube, and deposition is achieved through pulsing a high current to sublimate the bead and deposit a film of silver on the inside of the hollow cylinder. The silver film is expected to oxidise over the mission lifetime, and the corresponding rate of increase of resistive properties of the film will give an indication of the rate of oxidation of the film due to the oxidising species in the martian atmosphere. The remaining sensor, the UV sensor, forms the basis of this work and is described in detail later.

The final sub-system is the accelerometer, which forms part of the Entry and Descent Landing System (EDLS). During entry the accelerometers are used to trigger parachute deployment, but will also yield information on the density profile of the upper atmosphere through analysis of drag forces upon the probe. A summary of the ESS instruments is shown in Table 1-2.

Sensor	Description	Mass
UV sensor	Surface flux between 200 and 400 nm	19 g
ESOS	Determination of oxidation rate	20 g
Air Temp	Air temperature measurements to ± 0.5 K	6 g
Pressure	Pressure to ± 0.1 hPa	15 g
Wind sensor	Wind speed to ± 0.1 ms^{-1} and direction to ± 10°	17 g
Dust sensor	Momentum, rate of aeolian impacts	12 g
Accelerometer (×2)	Upper atmospheric density profile, orientation	48 g

Table 1-2: The ESS instrument breakdown.

The ESS package is designed to operate over the entire mission lifetime, recording both short (seconds, minutes, days) and long-term (seasonal) variations in the local environment. The relatively low data volume production from ESS sampling allows the suite to operate continuously in a low rate mode, switching to a high rate mode in the event of any transient or pre-determined events. The sampling software on the lander is fully flexible and can be changed throughout the mission, as sampling strategies will undoubtedly vary during operations as the mission evolves and data are received and interpreted. As a nominal baseline, the low rate mode was set at one sample every 30 minutes continuously throughout the day. In the event of any transient or pre-determined events (*i.e.* dust particle impacts or eclipses) the suite is switched into a high rate mode, sampling at 4 Hz. Alternatively, a circular buffer continuously stores high rate data, recording only the low rate sample rate if no event is observed. If however pre-specified thresholds (software variable) for any of the channels are exceeded, the suite is switched to the high rate recording mode, and the previous 5 minutes of high rate data stored in the circular buffer are recorded also. This process ensures that the pre-event conditions will always be known.

1.4 Scope of the Thesis

The focus of this thesis lies in the realm of the ultraviolet environment of Mars, and instrumentation designed to measure this property *in situ*. The origin of this work was centred around the unique opportunity to design and build a miniature UV instrument for flight on the Beagle 2 mission, all within the scope of a Ph.D. The work presented here thus follows two distinct tracks, namely the design and testing of the hardware built over the course of studying for the Ph.D., and the development of a radiative transfer model to simulate the UV flux at the martian surface. As a result of such a brief, the areas of work that have been involved became a dynamic process, venturing through a wide field of experimental and theoretical investigations. The modelling aspect was initially developed to aid in instrument design,

though after significant improvement now serves as a unique tool for exploration of the UV environment of Mars for a variety of situations.

The production of any spaceflight instrument requires an extensive design and testing phase, and the rationale and results relating to both these aspects respectively are presented here. The use of the model both as a tool for instrument development and as an aid for post-flight interpretation of data is shown, but the model is also shown to be of great importance in terms of research opportunities into UV irradiation conditions under previously unexplored or investigated scenarios.

Chapter Two provides an introduction to the two defining factors in the thesis, namely UV radiation, and the role of this on Mars in terms of scientific importance and the relevance to life. Chapter Three is devoted to the detailed description of the UV radiative transfer model of the martian atmosphere, developed specifically for this work. Chapter Four concerns the design philosophy for the UV instrument built, and also covers data on the spaceflight qualification, testing procedures, results and calibration. Chapter Five applies the theoretical model to a wide range of martian global scenarios. Chapter Six builds upon Chapter Five by providing an in-depth analysis of the Beagle 2 landing site in terms of the UV environment the sensor is expected to observe, and reveals characteristic UV signatures for a host of atmospheric phenomenon and events. The results of long-term fieldwork returned from a modified terrestrial version of the instrument are presented, in analogy to the conditions the sensor will experience on Mars. The thesis ends with a summary of conclusions and further work, and appendices containing the core of the IDL code used to construct the model and details of the circuit configuration of the UV sensor.

Chapter Two

UV Radiation and its Relevance to Mars

2.1 Ultraviolet Radiation

Ultraviolet radiation (UV) comprises a relatively small part of the solar spectrum (typically < 5% of the solar radiation output), with wavelengths (λ) between that of visible light (400 nm) and X-rays (10 nm) as shown in Figure 2-1. Though the relative contribution of UV to the total solar output is relatively small, the effects of UV radiation are extremely important in a range of photochemical, biological and geochemical reactions, due to the high photon energies in this region of the spectrum.

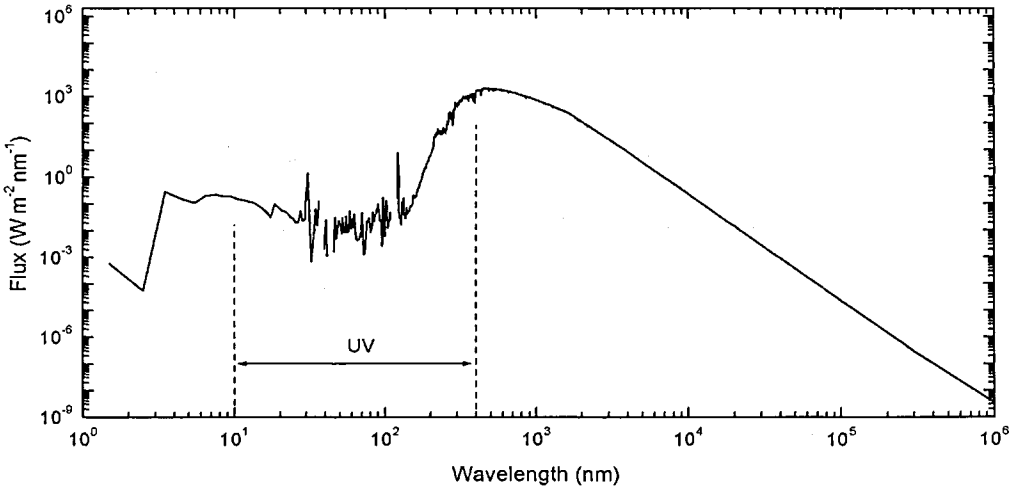

Figure 2-1: The solar spectrum over a wide range of wavelengths (Kent Tobiska *et al.* 2000).

The UV region is sub-divided into different wavelength regions shown in Figure 2-2. The regions of interest in this study that are expected at the martian surface are the UV-C, UV-B and UV-A regions, with wavelength ranges 100-280 nm, 280-315 nm and 315-400 nm respectively, as defined by the *Commission Internationale de l'Eclairage* (*CIE* 1987). These three distinct bands are a modern classification based on the biological effectiveness of the radiation in each region, generally becoming progressively more damaging through each band with decreasing wavelength.

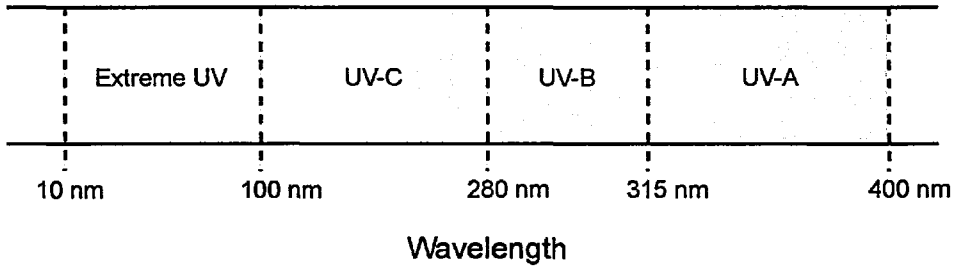

Figure 2-2: The sub-classification of UV wavelength regimes.

Solar UV radiation at these wavelengths originate from the upper photosphere of the Sun. The solar UV output has been observed to vary over an 11 year period (associated with the appearance and decay of active regions on the solar disc), with a smaller variation seen over the 27 day (apparent) rotational period of the Sun (Floyd *et al.* 2002). The variation in the output flux is wavelength-dependent, ranging from approximately 1% at 300 nm to 10% at 200 nm (Rottman *et al.* 2001). The variation at long wavelengths is inconsequential, but variations of around 10% at the shorter wavelengths must be considered. The last solar minimum occurred in late 1996, therefore the next expected minimum is expected to occur around 2007/8. The modelling described here is based around the Beagle 2 mission to Mars in 2003, which will occur during relatively high solar activity levels as the cycle begins to reduce in intensity. For this reason, an active solar UV spectrum (*i.e.* data taken from just after a time of peak cycle activity) is used to describe more accurately the UV output from the

Sun for this mission timeframe, resulting in slightly elevated short wavelength UV with respect to the minimum activity periods.

2.2 UV Damage to Biological Organisms

2.2.1 Damage and Repair Mechanisms

The primary risk associated with UV radiation concerns the damage that is caused during interaction with living organisms. For humans, the damaging effect of UV radiation is apparent in everyday life, such as the occurrence of sunburn following prolonged exposure to the Sun, which is a visible indicator of active damage to exposed tissues. UV photons are energetic enough to interact directly with biological structures, in some cases causing severe damage through temporary or permanent alterations that result from photochemical reactions with different target molecules susceptible to UV (chromophores).

Damaging effects of UV radiation to humans include erythema (sunburn), cataract formation and DNA damage. The main photochemical reactions within cellular DNA involve direct absorption of short wavelength (UV-B and UV-C) radiation by the base pairs resulting in dimerisation[1] of adjacent bases, disrupting the coding and replicative functions of the nucleic acid. Subsequent effects may result in the formation of cancerous cells, and in cases of extreme exposure, complete inactivation of the organism. Secondary effects can also result in significant damage, such as the effects of indirect damage through the production of free radicals within the biological system. The most common of these are excited oxygen species, such as superoxide radicals, singlet oxygen or hydroxyl radicals.

For the case of Mars, the most probable type of extinct/extant life will be in the form of micro-organisms, either at or near the surface region. The response of micro-organisms to

[1] Dimerisation is the chemical union of two free radicals.

UV is generally similar to that of DNA, since this is the primary chromophore for short wavelength UV in simple single-celled and complex multi-cellular organisms. The UV environments revealed in this study are therefore intended primarily towards biological interpretation from the viewpoint of possible micro-organisms, which may reside in the martian near-surface region.

In reality the true biological consequence of photochemical interaction depends upon whether the system is capable of quickly repairing the damaged components. Several different repair mechanisms exist, in the case of DNA usually following the process of either photoreactivation or excision repair[1]. Such repair mechanisms are essential for the persistence of complex multi-cellular organisms, since the damage of over-exposure to natural sunlight (especially now in ozone-depleted regions) can often be completely mitigated over time, allowing long-term survival of the organism. For the case of single-celled organisms, the efficiency of repair mechanisms directly determines whether or not the organism is killed – here, a single damaging event could be lethal.

Though it is fair to consider the effects of UV on biological systems to be mainly deleterious, it is inaccurate to portray the effect of UV as solely damaging. It is a modern notion that 'sun tanning' (either by natural sunlight exposure or by artificial lamp) resulting in darkening of the skin is a sign of good health. Those who do are well aware of the risk of sunburn, which in itself is a direct indication of genomic damage to the skin tissue. However, in the process of exposure to the Sun, solar UV does stimulate the beneficial production of vitamin D which is essential in the regulation of calcium and skeletal structure in humans. Other beneficial effects are also observed in many sections of the animal kingdom. For example, UV-A is involved in butterfly wing recognition during mating, and flower

[1] Photoreactivation involves the splitting of dimers by specific binding enzymes when illuminated by long wavelength UV. Excision occurs in the absence of any light, through the direct removal of damaged bases and whole strands of DNA.

recognition by pollinating insects such as bees (see Cockell and Knowland (1999) and references therein for a detailed discussion). Thus UV radiation can in some cases be beneficial to living organisms, and should not be regarded as exclusively destructive.

2.2.2 Biological Action Spectra

Not all UV wavelengths have the same ability to cause biological damage or initiate photochemical reactions. An increase in the degree of damage caused (covering orders of magnitude) is generally seen with decreasing wavelength, and is described by an action spectrum or weighting function which represents the changing response of a given process as a function of wavelength through the entire UV region. Such functions provide a relative weighting to UV spectra, increasing the contribution from short wavelength radiation which is in general more damaging. The most widely used reference action spectra are those for erythema (sunburn) in human skin (McKinley and Diffey 1987) and DNA damage (Setlow and Doyle 1954).

Many types of action spectra however provide only a *relative* weighting of the UV spectrum, and do not always specify the absolute damage sustained by the organisms as a whole, *i.e.* what type of damage actually occurs or whether complete inactivation takes place. Some forms of action spectra do provide this information (sometimes known as survival spectra), but are far less common. To calculate the action spectrum for inactivation, specific calibrated monochromatic intensities for separate biological samples are required over the full UV range, to determine the intensity required at each wavelength to cause inactivation[1]. The use of action spectra here gives a relative understanding of the UV environment only in terms of the harshness of the environment, and is usually compared to standard Earth conditions in extraterrestrial investigations. Through the use of action spectra the wavelength-dependent

[1] In this study, we are only concerned with the relative effects of martian UV, not the absolute inactivation levels.

nature of UV damage is compensated for, and integration of the spectrum gives an indication of the 'relative dose' experienced by the organism.

For examples of the biological interpretation of UV spectra calculated in this study, an action spectrum for DNA is used to weight the calculated flux as a function of wavelength. The use of this action spectrum is not a claim that any putative martian microbes will be based on DNA biochemistry, but rather a standard technique of gauging the UV stresses which will be experienced from a terrestrial microbial viewpoint. The DNA action spectrum is generally a good model for the response of complex carbon-based molecules, many of which absorb strongly in the UV-B and UV-C. DNA is a 'best guess' for the basis of extraterrestrial life since it forms the biochemical foundation of life on Earth, but is in no way guaranteed. Martian microbes may have evolved in a vastly different environment than on Earth, and as such may be based on a different biochemistry unknown on Earth.

The high resolution DNA-weighting spectrum of Setlow and Doyle (1954) is used between 255 and 365 nm, and interpolated between 365 and 400 nm. In order to weight accurately the flux across the entire martian UV spectrum, DNA-weighting is required for wavelengths as short as 180 nm. For this part of the action spectrum, the data of Munakata *et al.* (1991) were used. These data for 170, 190, 220, 235 and 254 nm were used, with spline interpolation used to define the full 180-254 nm action spectrum. For ease of comparison to terrestrial studies, the action spectrum was normalised to 300 nm, which is standard procedure in the analysis of terrestrial DNA-weighted UV spectra. The two sets of data are combined in Figure 2-3 to give an accurate representation of the DNA action spectrum between 180 and 400 nm at the martian surface.

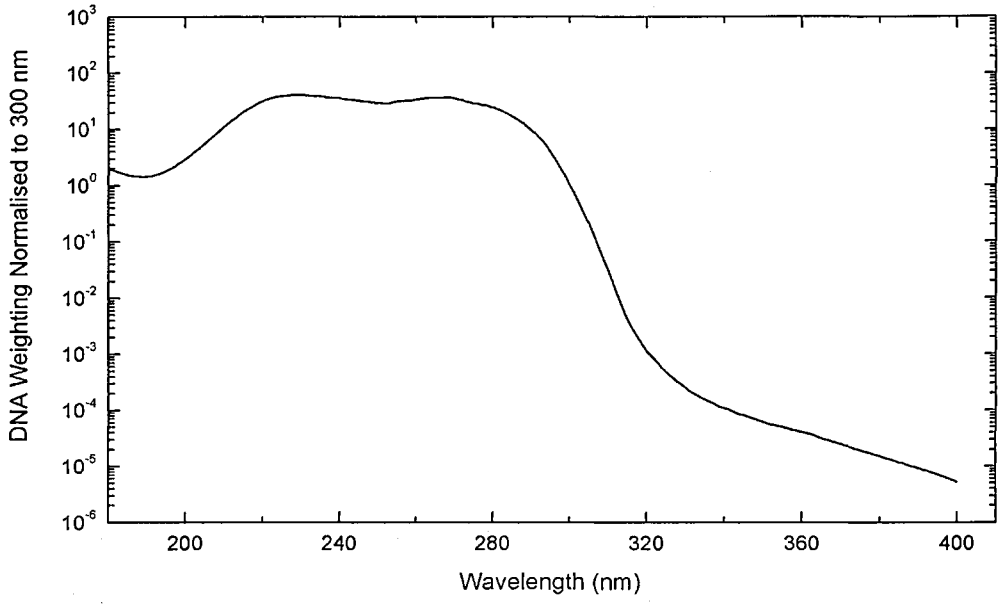

Figure 2-3: The DNA action spectrum (Setlow and Doyle 1954; Munakata *et al.* 1991).

2.3 Other Effects of UV

2.3.1 Photochemistry

Solar UV radiation is of paramount importance in regulating the chemistry of upper planetary atmospheres. UV photons are energetic enough to initiate photoionisation of molecular species, stimulating photochemical reactions between gaseous species in the atmosphere. The radiation provides energy during molecular interaction large enough to overcome the chemical bonds binding molecules together. The net result is a series of photochemical reactions which perpetuate to continually produce and destroy molecular species in upper planetary atmospheres.

An important photochemical process in the terrestrial atmosphere is the regulation of ozone (O_3). O_3 plays an important part in the chemistry of the Earth's atmosphere, even though it is a minor species in terms of abundance. Unlike most other atmospheric gases, O_3 is not found in constant fractional abundance, but instead concentrations vary sharply

dependent upon altitude. O_3 is both created and partially destroyed in the martian atmosphere, in the presence of solar ultraviolet radiation (e.g. Atreya and Gu 1995). Molecular oxygen (O_2) is photodissociated by UV absorption (denoted as $h\nu$, for $\lambda < 242$ nm), allowing the combination of atomic oxygen ($\dot{O}$) with molecular oxygen (in the presence of a third body M) to form O_3:

$$\begin{aligned} O_2 + h\nu &\rightarrow \dot{O} + \dot{O} \\ \dot{O} + O_2 + M &\rightarrow O_3 + M \end{aligned} \qquad (2\text{-}1)$$

Another major source of $\dot{O}$ in the martian atmosphere which significantly increases O_3 production as described above, is through the photodissociation of CO_2 ($\lambda < 204$ nm),:

$$CO_2 + h\nu \rightarrow CO + \dot{O} \qquad (2\text{-}2)$$

The corresponding decay of O_3 follows two distinct paths. The first is direct photolytic destruction by UV absorption ($\lambda < 325$ nm):

$$\begin{aligned} O_3 + h\nu &\rightarrow O(^1D) + O_2 \\ O_3 + h\nu &\rightarrow O(^3P) + O_2 \end{aligned} \qquad (2\text{-}3)$$

The second is the chemical destruction associated with the photolytic dissociation of water vapour ($\lambda < 246$ nm) and the generation of hydrogen radicals:

$$\begin{aligned} H_2O + h\nu &\rightarrow H\dot{O} + \dot{H} \\ O_3 + \dot{H} &\rightarrow H\dot{O} + O_2 \end{aligned} \qquad (2\text{-}4)$$

The formation of the $\dot{H}$ by-product from the breakdown of H_2O molecules in the atmosphere plays a major role in the catalytic destruction of O_3, and as such O_3 and H_2O are strongly anti-correlated in the atmosphere of Mars, where such trace species are so variable. The full range of photochemical reactions is too vast to cover here, but nevertheless the importance of solar UV in chemical regulation of planetary atmospheres can be emphasised here.

O_3 is an important species in planetary atmospheres not only from a photochemical point of view, but also from the perspective of biology. The most outstanding feature is the relationship between the absorption spectrum of O_3 and the DNA action spectrum. O_3 has an unusually strong absorption band located at the critical biological wavelengths (230-290 nm), and so acts as an effective filter to shortwave radiation despite its low relative abundance.

UV radiation is also responsible for the possible production of oxidising species in the martian atmosphere. The production of highly reactive oxygen species from intense UV irradiation of molecular O_2 has been well established (Che and Tench 1982; Che and Tench 1983; Lunsford 1973), and was recently proposed to explain the chemical reactivity of the martian soil. Strong oxidative properties in the martian surface-atmosphere interaction region were invoked to explain the Viking Gas Exchange (GEx) and Labelled Release (LR) experiments (Klein *et al.* 1992). The evolution of O_2 (GEx) and CO_2 (LR) were proposed to have occurred due to the presence of a strong oxidising species in the martian regolith. Recent laboratory studies of the exposure of martian-analogue surface materials to UV in the presence of atmospheric oxygen and low water vapour abundances revealed the formation of superoxide radical ions (O_2^-) (Yen *et al.* 2000). These superoxides could in part be responsible for the apparent absence of organic material at the martian surface. The true nature of the oxidative environment at the surface of Mars however still remains largely unknown, and in all investigations of this aspect of the martian environment the role of UV irradiation must always be considered.

2.3.2 Degradation of Materials

The effect of UV radiation upon materials is of importance not only in the case of Mars, but also in terrestrial applications where materials are exposed to solar illumination for long periods of time. Plastics are the most common industrial materials susceptible to UV-induced damage. Organic-based polymers undergo photolytic and photo-oxidative reactions during

exposure to UV radiation, reducing the integrity of the material over time. Such polymers contain groups such as carbon-carbon double bonds (C=C) and carbonyl (C=O) groups which are capable of directly absorbing radiation at UV wavelengths, and interact in the photoreactions that result in the overall degradation of the polymer. Examples of such polymers are polyethylene (commonly known as polythene) and polypropylene, which are particularly susceptible to UV damage.

Polymer degradation effects range from aesthetic discolouration of the polymer appearance, through to severe mechanical damage of the bulk material affecting performance ratings. Many of the more severe photodegradation reactions which occur in plastics cause either polymer chain scission or chain lengthening, resulting in loss of strength or increased brittleness. Surface effects of short wavelength UV include etching on the order of several μm.

In the context of Mars and current/planned missions to the red planet, the effects of UV on materials are extremely important. The two most important material implications revolve around the use of thermal control materials for spacecraft, and the long-term stability of any martian construction materials for future habitation. Thermal control materials form an integral part of any spacecraft, with the survival of the entire mission often dependent upon the stability of these components. Thermal control materials generally take the form of extremely thin (typically 100 μm) sheeting blanketed around temperature critical parts of the spacecraft. Examples of organic-based materials are aluminised Kapton® and silverised Teflon® thermal blanketing. These materials have been used in long-duration orbital satellites, and showed severe degradation effects attributable to UV exposure upon return (Stiegman and Liang 1993). The photochemical effects on these types of materials are similar to the aforementioned processes, but here a corresponding change in the absorptivity due to the degradation of the blanket/paint compromises the thermal control characteristics of the materials. The cumulative effect over time is a slow loss of thermal control, which can

ultimately result in failure of the entire spacecraft. A better understanding of the long term effects of UV (and other environmental effects) upon these types of material will lead to the development of more stable thermal control materials, designed to last over longer lifetimes at the required specification.

2.3.3 Future Exploration

The implications for future manned exploration of Mars are centred around the issue of protecting all parts of the human body from the damaging UV radiation. Any human explorers on the red planet would quickly suffer extreme biological damage if exposed, and similar methods of suit protection to that used on the manned Apollo missions to the Moon would be required for any extra-vehicular activity. Such protection involves bulky spacesuits with visor protection and lack of delicate motor control, and whilst this form of protection was suitable on the short duration visits to the lunar surface, this would not be feasible in the case of Mars. Optimum orbital alignment of Mars and Earth occurs every 25-27 months, so any manned mission to the martian surface would be required to stay for a relatively long time. Artificial habitats of some form may be required to sustain the explorers until the next launch window to return to Earth occurred. Such a habitat would ideally house a sustainable mini-ecosystem, for example an area of plant life for natural oxygen production from human waste material. The natural sunlight at the martian surface could in theory be used to recreate efficiently the terrestrial environment, as suggested by Cockell (2001) through the use of novel *in situ* material production. An efficient ecosystem would require a terrestrial-like UV and visible spectrum, supplying the necessary UV-A and photosynthetically active radiation (PAR, $\lambda = 400\text{-}700$ nm) required for optimum oxygen production. It was suggested in the same paper that ethylene could in theory be produced on Mars through the reaction of hydrogen with carbon monoxide, which in turn could be polymerised to produce polyethylene and plexiglass. Other novel material techniques were also suggested, which would provide the balance of required long wavelength UV with blocking of the harmful UV-C.

The UV conditions on the surface of Mars are thus of paramount importance for a number of reasons in the realm of human exploration of Mars, both directly through severe damage to human tissue and indirectly through the sustainability of a viable ecosystem and long term materials.

2.4 Previous Martian UV Spectra Investigations

2.4.1 Experimental Investigations

To date, no *in situ* measurements of martian surface UV have been attained, and the Beagle 2 UV sensor will provide the first ever direct measurement of UV flux at the martian surface. All experimental investigations to date have taken the form of either telescopic or orbital observations, concentrating primarily on the reflection properties of the atmospheric aerosols. The drawback of orbital and telescopic observations in the derivation of surface spectra is that the detected radiation is only that which has been reflected from the planet. The derivation of aerosol and surface UV properties is heavily dependent upon certain assumed properties. Surface spectra can be roughly estimated through comparison of the reflected UV with the solar UV spectrum, though this technique can be inaccurate, in some cases leading to large deviations from 'ground-truth' values of up to 20% (e.g. Martin *et al.* 2000; Peeters *et al.* 2000). Many assumptions must be made, such as which region is reflecting the light and what contribution scattering and absorption has upon reflection. A collation of all past and present experimental investigations of martian UV is shown in Table 2-1.

Spacecraft	Launch	Instrument Name	Detector Type	UV λ range (nm)	Notes
Rocket flight	1957	n/a	Photometer	255-285	*Crude measurement of reflectivity*
Rocket flight	1965	n/a	Spectrometer	240-350	*Upper limit for O_3 abundance of 1×10^{16} cm^{-2}*
OAO-2	1968	WEP	Spectrometer	100-400	*Whole disc spectra of the full UV region,*
Mariner 6 and 7	1969	UVS	Spectrometer	110-430	*Upper atmosphere emission detected, surface pressure and reflectance measurements*
Mars 2 and 3	1971	n/a	Photometer	105-134, 122.5-134, 105-118	*Upper atmosphere emission detected, surface pressure and reflectance measurements*
Mariner 9	1971	UVS	Spectrometer	210-350	*O_3 detection, surface pressure and reflectance measurements*
Mars 5	1973	n/a	Filtered photometer	255-265, 275-285	*Detection of O_3 layer and density, also detected aerosol layers at 20 and 60 km*
Phobos 2	1988	KRFM	Spectrometer	315, 328, 346 and 363	*Aerosol abundances and profiles*
HST	1990	WFPC 1 and 2	CCD imaging	225-285 and 306-366	*Reflectance measurement, O_3 detection, aerosol study*
HST	1990	FOS	Spectrometer	223.1-329.2	*High resolution O_3 and aerosol measurements*
Nozomi	1998	UVS	Spectrometer	115-310	*Main aim of upper atmospheric emission detection*
MEX	2003	SPICAM	Spectrometer	118-320	*O_3 detection, vertical profile of aerosols*
Beagle 2	2003	UV sensor	Filtered photodiode array	200-400	*First ever in situ surface UV measurement, 19 g mass. 5-point averaged spectra, seasonal/diurnal variations.*

Table 2-1: Past and present experimental martian UV investigations.

The first detection of reflected UV from Mars was in 1957, by means of an Aerobee rocket flight which reached an altitude of approximately 140 km (Boggess and Dunkelman 1959). The experiment consisted of a free spinning filtered photometer centred at 270 nm, with a bandpass of 30 nm. Observation of Mars was only achieved once, and was barely above the instrumental noise levels. A reflectivity of 0.24 was derived from this observation, far higher than values derived through later studies. Later studies were again conducted using a high altitude Aerobee rocket in 1965, which used a grating spectrometer to measure the reflectivity of Mars from 240 to 350 nm at approximately 5 nm resolution (Evans 1965). Their investigations revealed an increase in albedo towards shorter wavelengths (*i.e.* a Rayleigh scattering atmosphere) with a reflectivity between 0.04 and 0.08, and gave an upper limit for O_3 column abundance of 1×10^{16} cm^{-2} (Rea 1966).

The Wisconsin Experiment Package (WEP) onboard the Orbiting Astronomical Observatory (OAO-2) obtained the first orbital telescopic investigations of Mars. Its position outside the terrestrial atmosphere allowed detailed observations at wavelengths that would not be viewable from the Earth's surface due to atmospheric absorption. Low resolution spectral scanners were used (Wallace *et al.* 1972) to study the whole-disc reflected UV from the martian surface and atmosphere, giving albedo curves covering the range 200-370 nm. These data showed a spectrum that exhibited high albedo towards short wavelengths, consistent with reflection from a Rayleigh scattering atmosphere at extremely short wavelengths, and the presence of O_3.

The Mariner 6 and 7 spacecraft swept past Mars in 1969, obtaining data through the Ultraviolet Spectrometer Experiment (USE). The spectrometer comprised an Ebert-Fastie scanning monochromator with dual photomultiplier detectors (Pearce *et al.* 1971). Over 400 reflectance spectra of the martian disc were obtained between 190-430 nm (Hord 1972), with absorption observed in the 255 nm region that was attributed to the presence of O_3 in the atmosphere (Barth and Hord 1971). Two distinct spectral types were observed, associated

with snow/ice covered polar regions and non-polar regions. The polar regions were observed to be generally brighter in the reflectance profiles, owing to the larger surface albedo of the ice. Again however, these measurements were of the reflected martian UV spectrum, combining the effects of incoming atmospheric absorption and scattering, surface reflection and reflected outgoing absorption and scattering all together.

Mars 2 and 3 reached Mars in 1971, carrying identical versions of a three channel UV photometer. The detectors were NO and CH_3Br-filled Geiger photon counters, capable of measurements in the far UV in three spectral ranges, covering 105-134 nm, 122.5-134 nm and 105-118 nm respectively. The primary aim of the instruments was to measure UV emissions from the upper martian atmosphere, including solar Lyman-α radiation scattering and atomic oxygen emissions (Dementyeva *et al.* 1972; Kurt *et al.* 1974). A neutral oxygen density value of $2\text{-}8 \times 10^9$ cm^{-3} at 100 km was derived. Since the instrument was focussed towards the detection of UV emissions solely from the upper martian atmosphere, no investigations of surface spectra were made since the wavelength regime was too short.

Mariner 9 entered the martian system in November 1971, carrying a similar copy of USE as flown previously on Mariner 6 and 7. The mission was a Mars orbiter, with a total experimentation period spanning nearly a year. The UV spectrometer onboard Mariner 9 studied martian atmospheric UV reflectance spectra, scanning between 110 and 350 nm (Hord *et al.* 1970). At the time of arrival the planet was engulfed by a global-scale dust storm, preventing UV surface spectra measurements (Pang and Hord 1973). Later into the mission the atmosphere cleared, allowing surface reflectance spectra to be measured. The reflected UV flux spectra in a 10 nm band centred at 305 nm were used to compile a topographic map, using the relation between surface pressure and column abundance of CO_2 above the surface point. During the global storm period, work performed on data from this experiment primarily took the form of investigation into the scattering properties of the martian dust which was observed (Pang *et al.* 1976).

Mars 4 and 5 carried Lyman-α detectors similar to Mars 2 and 3, but in addition to this was a long wavelength UV photometer (Krasnopol'skii *et al.* 1975). A loss of propellant on Mars 4 resulted in a loss of data return from this instrument, but the photometer on Mars 5 did return data. The detector was a two-channel filtered photometer, using photomultiplier tubes for detection of UV photons. The two channels were centred at 260 nm and 280 nm with bandpasses of 10 nm, aimed at measurements of O_3 in the martian atmosphere through ratio comparisons of reflectance profiles across the martian limb and terminator. A maximum O_3 density of 1×10^{10} cm^{-3} was derived from observations, situated in an ozone layer approximately 7 ± 1.5 km thick at an altitude of 38 ± 2 km (Krasnopol'skii *et al.* 1977). Two other aerosol layers were discovered, situated at 60 km and 20 km, and were attributed to ice particles.

The Phobos 2 spacecraft obtained a set of limb-to-limb brightness distribution measurements in the equatorial region, using the Combined Radiometer-Spectrophotometer for Phobos and Mars (KRFM) spectrometer in the UV-A region at wavelengths of 315, 328, 346 and 363 nm. These data were analysed to extract the optical properties of the suspended dust at these wavelengths, through the use of approximate and doubling-adding methods (Moroz *et al.* 1993; Wuttke *et al.* 1997). Though these investigations revealed valuable data on the optical properties of the suspended aerosols, they did not investigate the resulting surface UV spectrum at high resolution due to the constrained observation wavelengths.

Recent telescopic investigations of Mars in the UV have been performed using the Wide Field Planetary Camera (WFPC 1 and 2) onboard the Hubble Space Telescope (HST). Multispectral imaging investigated aerosol and O_3 concentrations through the use of wide-band filtered imaging at wavelengths of 230 nm, 255 nm and 335 nm (James *et al.* 1994; Wolff *et al.* 1997). Equatorial limb-to-limb reflectance profiles were measured through the variation of pixel signal in each image, and the data were reduced to determine the single scattering albedo of the martian atmospheric species at wavelengths of 210, 300 and 400 nm.

More recent spectral scans using a diffraction grating over the wavelength region 223.1-329.2 nm at a resolution of 0.2 nm were taken by Clancy *et al.* (1999), revealing new optical depth values for clouds and dust loadings, along with the detection of small column abundances ($4.8\text{-}9.7 \times 10^{15}$ cm^{-2}) of O_3 in low-to-mid latitudes.

Present-day orbital instrumentation currently *en route* to Mars are the Ultraviolet Spectrometer (UVS) onboard Nozomi and SPICAM-light on Mars Express. UVS consists of a grating spectrometer combined with a D/H absorption cell photometer, measuring over the wavelength region 115 nm to 310 nm at 2-3 nm resolution (Fukunishi *et al.* 1999). The photometer will measure hydrogen (H) and deuterium (D) Lyman-α emissions, as performed by the Mars 3 and 5 spacecraft. The primary aims of this instrument are to investigate H and O coronas around Mars, the D/H ratio of the upper atmosphere, atmospheric phenomenon such as aurora, dayglow and nightglow, as well as investigation of aerosols and O_3 in the martian atmosphere.

SPICAM-light (Spectroscopy for the Investigation of the Characteristics of the Atmosphere of Mars) is a relatively small (9 kg) UV-IR spectrometer on Mars Express. The instrument consists of two grating spectrometers, covering the regions 118-320 nm at 0.8 nm resolution and 1.1-1.7 μm at 1 nm resolution (Bertaux *et al.* 2000; Muller *et al.* 2001). The instrument operates in a variety of modes, including nadir viewing, limb viewing and vertical profiling through stellar occultation. O_3 abundance will be measured in nadir mode, and detailed profiles of CO_2, O_3, aerosols and temperature will be measured through limb viewing and stellar occultation. The presence of SPICAM-light is fortunate, since it will make possible for the first time simultaneous observations of UV from orbit and the surface, through coordination with the Beagle 2 UV sensor. During surface measurements of UV flux, SPICAM-light will be capable of measuring the vertical profile of atmospheric aerosols, aiding in the understanding of data and modelling simulation.

2.4.2 Theoretical Modelling

Theoretical investigations into the martian UV environment have been performed previously, though never in any great detail. Kuhn and Atreya (1979) first investigated martian surface UV using a simple model calculating the attenuation of direct solar UV through a CO_2 atmosphere, revealing a distinct cut-off near 200 nm due to CO_2 absorption, seen in all martian surface UV spectra. The effects of O_3 absorption upon the surface spectrum were also shown, absorbing in the UV-C region. Their work however did not include the effects of scattering by both molecular and particulate species, which (in the case of Mars) can contribute significantly to the total UV flux.

Further work was progressed by Catling *et al.* (1999) and subsequently Cockell *et al.* (2000) both using the same UV model, considered a significant improvement upon that of Kuhn and Atreya (1979). Their model used the delta-Eddington approximation for radiative transfer, where the martian atmosphere was represented by a single homogenous layer (Haberle *et al.* 1993). The transmission of radiation through the single-layer atmosphere could then be given through the solution of a single equation, yielding the transmission value of the atmosphere. Dust optical properties were taken from a variety of sources (Zurek 1978; Pollack *et al.* 1979; Haberle *et al.* 1993), offering a preliminary view of the effect of dust on the transmission of UV through the atmosphere. The focus of their work was aimed at biological implications of the martian UV environment in the past, present and future. Theoretical spectra were calculated for a range of conditions, including high latitude regions and medium-scale dust storms (and thus optical depth).

No detailed investigation to date however has been made into the UV environment at the surface of Mars. A realistic representation of the atmosphere (*i.e.* representative layers) coupled with a detailed coverage of all atmospheric species is required, to model accurately the transfer of solar UV through the martian atmosphere. A host of new data concerning absorption cross-sections at low temperatures for molecular species is now available, and can

be used to refine previous models. Of particular importance is the role of aerosols in the interaction of UV with the atmosphere – no investigations to date have studied the effect of varying optical properties upon the surface spectrum. A detailed model of the martian atmosphere coupled to an accurate radiative transfer approximation is therefore required for in-depth investigation of the martian UV environment, and forms the subject of the next chapter.

Chapter Three

Martian Radiative Transfer UV Model

The work in this chapter has been published in Patel *et al.* (2002), and describes in detail the construction of the UV radiative transfer model of the martian atmosphere, which allows calculation of the surface UV flux on Mars between 180 and 400 nm at 1 nm resolution.

3.1 Model Description

For the case of planetary atmospheres, especially in the situation of the relatively dusty atmosphere of Mars, there are two distinct processes which govern the passage of radiation to the surface: direct attenuation and diffuse scattering/absorption. The model is separated into calculation of the two flux components, the direct flux (F_{direct}) and the diffuse flux ($F_{diffuse}$). The total surface flux ($F_{surface}$) is then given as the sum of F_{direct} and $F_{diffuse}$. Each component of the model is described, with an explanation of each component property and calculation of the surface irradiance. The model was created using the Research Systems Inc. Interactive Data Language (IDL), and details of the main code for transmittance of the martian atmosphere can be found in Appendix A.

3.1.1 Solar UV Flux

Specifically for the case of Mars, we require knowledge of the solar output between 180 and 400 nm only (CO_2 blocks all UV below around 190 nm, addressed later). This region of the UV covers the UV-A, UV-B and UV-C regions. Solar UV spectral data gathered by the SUSIM UARS instrument onboard ATLAS-1 were used to define the UV flux in 1 nm bins at 1 AU (Cebula *et al.* 1996; Floyd *et al.* 1999). This was then scaled through the inverse square law to the mean martian orbital distance of 1.52 AU for incorporation into the model (variation due to eccentricity is addressed shortly). The solar spectrum at this distance and wavelength range thus obtained is shown in Figure 3-1.

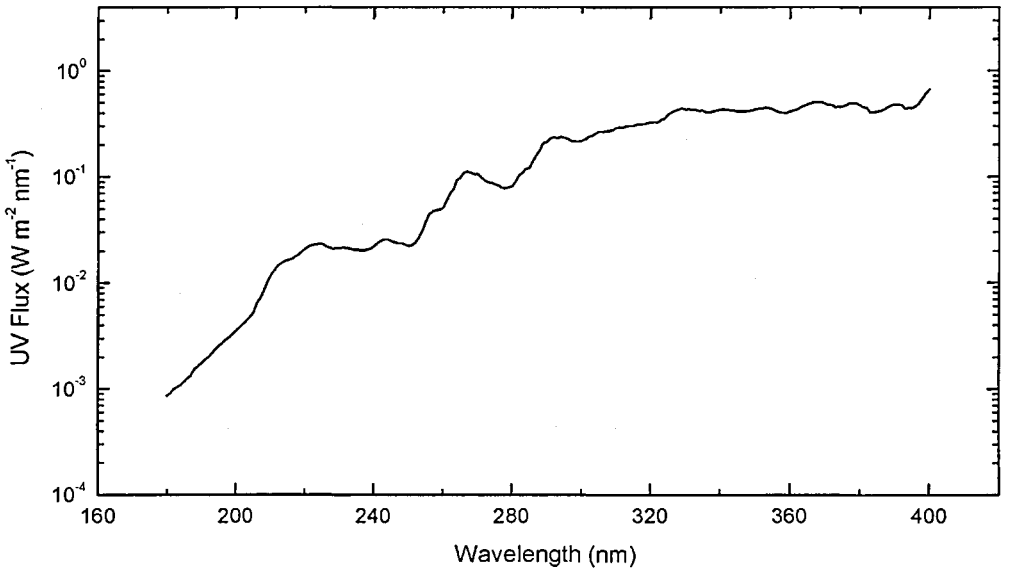

Figure 3-1: The solar UV spectrum at 1.52 AU.

3.1.2 The Layered Martian Atmosphere

Previous UV models of the martian atmosphere have all used a single homogeneous layer to represent the martian atmosphere (e.g. Kuhn and Atreya 1979; Cockell *et al.* 2000). In this model, the martian atmosphere is represented by 10 separate homogenous layers. Ten atmospheric layers were chosen to represent accurately the martian atmosphere – ideally a layered model at 1 km vertical resolution would be preferable, but since this model was

developed in parallel with many other areas of work throughout this Ph.D., this was not possible due to time constraints.

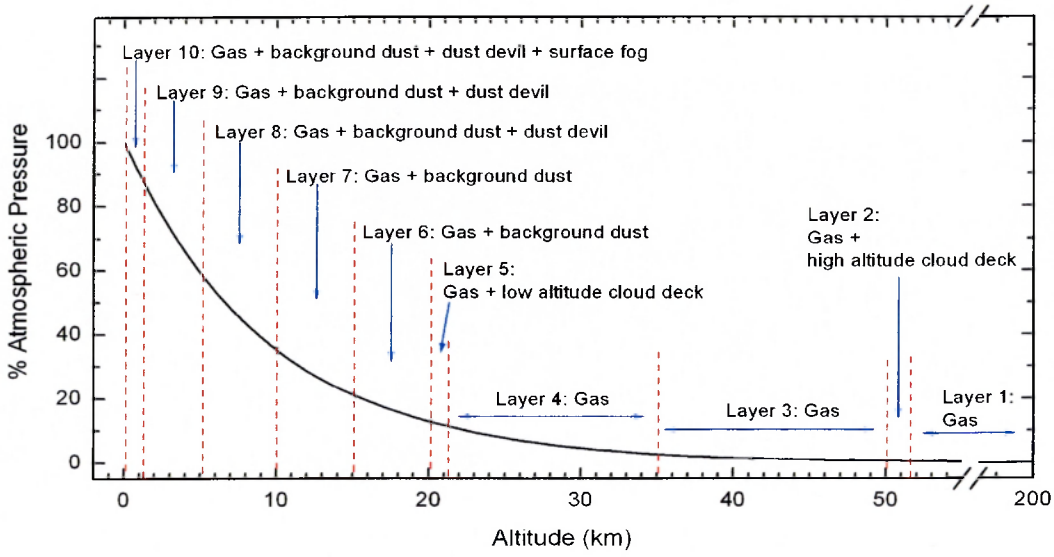

Figure 3-2: Multi-layer representation of the martian atmosphere.

Two classes of general species comprise the martian atmosphere, namely gases and aerosol particles. These are distributed amongst the atmospheric layers, from 0 km (surface) to 200 km (assumed top of atmosphere), shown in Figure 3-2. The layers are not of uniform thickness, but are more finely spaced close to the surface becoming wider with increasing altitude, due to the exponential decrease of pressure with altitude. The altitude distribution of the gaseous species follows the pressure decrease, except for the case of O_3, which is addressed later. Background dust aerosols are confined to the lower 20 km with the same scale height as the atmospheric gas (Korablev *et al.* 1993; Moroz *et al.* 1994). Two 1 km thick cloud decks are also included, to allow simulation of high (50 km) and low altitude (20 km) CO_2/H_2O cloud formation in the model, consistent with the observations of Rodin *et al.* (1997) and Clancy and Sandor (1998). Transient phenomena near to the surface such as the occurrence of near-surface morning fog or dust devil aerosols are confined to the lower 1

and 10 km layer respectively, resulting in separate layers between 0 and 200 km consisting of varying gas and aerosol abundances.

3.1.3 Model Input Parameters and Solar Zenith Angle

The primary input parameters to the model are: local surface pressure (P), areocentric latitude (lat), areocentric solar longitude (L_s), local time (t), O_3 abundance, and various aerosol optical depths (background dust (τ_{back}), high altitude cloud (τ_{hcloud}), low altitude cloud (τ_{lcloud}), surface fog (τ_{fog}) and dust devil (τ_{ddevil})). Mars possesses a similar planetary obliquity (25.19°) to that of Earth (23.45°), giving rise to the same range of seasonal variations. Due to the relatively high eccentricity of the martian orbit (0.0935, compared to 0.0167 for the Earth) the seasonal index L_s (areocentric solar longitude) is used to quantify the position of Mars within its orbit, shown schematically in Figure 3-3. The (martian) vernal equinox occurs at $L_s = 0°$, followed by (martian) autumnal equinox at $L_s = 180°$.

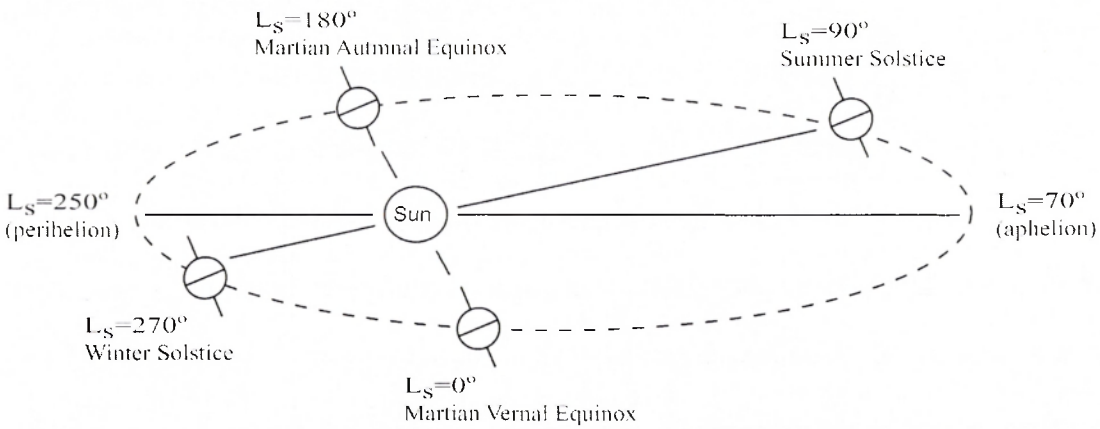

Figure 3-3: Variation of L_s through the martian orbit.

Due to the relatively high eccentricity and greater mean orbital distance (1.52 AU) of the martian orbit, the variation of input solar flux over L_s must be accounted for. Solar insolation is seen to vary markedly, ranging from 717 W m^{-2} at perihelion to 493 W m^{-2} at aphelion, due

to the varying Sun-Mars distance. The Sun-Mars distance r at any point in the martian orbit can be found as a function of L_s through the relation:

$$\frac{r}{d} = \frac{(1-e^2)}{1+e\cos(L_s - L_s^P)} \tag{3-1}$$

where d is the mean Mars orbital distance (1.52 AU), e is the martian eccentricity and L_s^P is the areocentric solar longitude of perihelion (250°) (e.g. Haberle *et al.* 1993). The flux at any point in the martian orbit can then be found through scaling of the flux at 1.52 AU ($F_{1.52}$) to the orbital point defined by L_s using Equation 3-1. The flux normal to the top of the atmosphere (F_0) above any point at the martian surface can be found through consideration of the solar zenith angle (*SZA*), which is calculated from the input parameters and defines the geometry of the Sun in the sky. F_0 is given by:

$$F_0 = \mu_0 F_{1.52}\left(\frac{d}{r}\right)^2 \tag{3-2}$$

where $F_{1.52}$ is the solar flux at 1.52 AU and $\mu_0 = \cos(SZA)$. The $(d/r)^2$ term scales $F_{1.52}$ to the orbital position, and μ_0 compensates for the change in effective atmospheric input area (and hence input flux) with viewing angle over increasing latitude[1] (all values of latitude are regarded as in the areocentric frame in the model). *SZA* is a function of a number of geometric components (e.g. Jacobson 1999), and is given by:

$$\cos SZA = \sin lat \sin \partial + \cos lat \cos \partial \cos h \tag{3-3}$$

where ∂ is the solar declination and h is the local hour angle. Solar declination is given as a function of L_s through:

$$\partial = \sin^{-1}(\sin \varepsilon \sin L_s) \tag{3-4}$$

[1] At high latitudes, the input solar flux is incident on the slant of the atmosphere. Thus the input flux is spread over a greater effective input area, increased by a factor equal to the cosine of *SZA*.

where ε is the planetary obliquity. The local hour angle is given by:

$$h = \frac{2\pi t}{T_{sol}} \tag{3-5}$$

where T_{sol} is the duration of the martian solar day (88775 s) and t is seconds from local noon. Substitution of the above terms into Equation 3-2 gives:

$$F_0 = \left[(\sin lat \sin \varepsilon \sin L_s) + \cos lat \cos\left(\frac{2\pi t}{T_{sol}}\right)(1 - \sin^2 \varepsilon \sin^2 L_s)^{1/2} \right] F_{1.52} \left[\frac{1 + e\cos(L_s - L_s^P)}{1 - e^2} \right]^2 \tag{3-6}$$

i.e. a term which describes the top of atmosphere flux at any time and any point above the martian surface, given the model input parameters *lat*, L_s and *t*.

3.1.4 Correction for Atmospheric Curvature

A limiting assumption so far is the use of a plane-parallel atmosphere, *i.e.* the curvature of the atmosphere is not accounted for in the calculation of the observed airmass from *SZA*. The general effect here is to overestimate the observed airmass, given as the secant of *SZA*. At small *SZA* the errors introduced by the plane-parallel assumption are negligible and need not be addressed, but at zenith angles which bring the solar disc near to the horizon, the effects should be corrected for accuracy. In order to compensate for this systematic error, the airmass correction term of Kasten (1966) was introduced into the model, where the true airmass m_r is given by:

$$m_r = \frac{1}{\rho_0 z_0} \int_0^\infty \left(1 - \left[\frac{R_m}{(R_m + z_0)^2} \right] \left(\frac{n_z}{n_0} \right)^2 \sin^2 SZA \right)^{1/2} \rho \, dz \tag{3-7}$$

where ρ_0 and ρ are the atmospheric density at the surface and altitude z respectively, R_m is the mean radius of Mars, z_0 is the atmospheric scale height (= 10.8 km, (Zurek *et al.* 1992)) and n_0 and n_z are the refractive indices of the atmosphere at the surface and altitude z respectively. The baseline density-altitude profile of the martian atmosphere was taken from Magalhaes *et*

al. (1999) which gives temperature and pressure profiles during the entry of MPF. Data are given from 140 km to 10 km, with the final 10 km calculated through extrapolation to the surface. Density as a function of altitude was then calculated using the Ideal Gas Law, where the air density is found from pressure divided by the product of the temperature with the gas constant. The martian atmosphere is primarily CO_2 gas at an extremely low pressure, where refractive effects become minimal – subsequently, the real part of the refractive index can be assumed not to change considerably, and thus the ratio of n_z/n_0 is taken as unity. This assumption is justifiable since a hypothetical increase of 10% in the ratio n_z/n_0 (which certainly will not occur) resulted in a variation of only 0.1% in the calculated airmass, which is acceptable here.

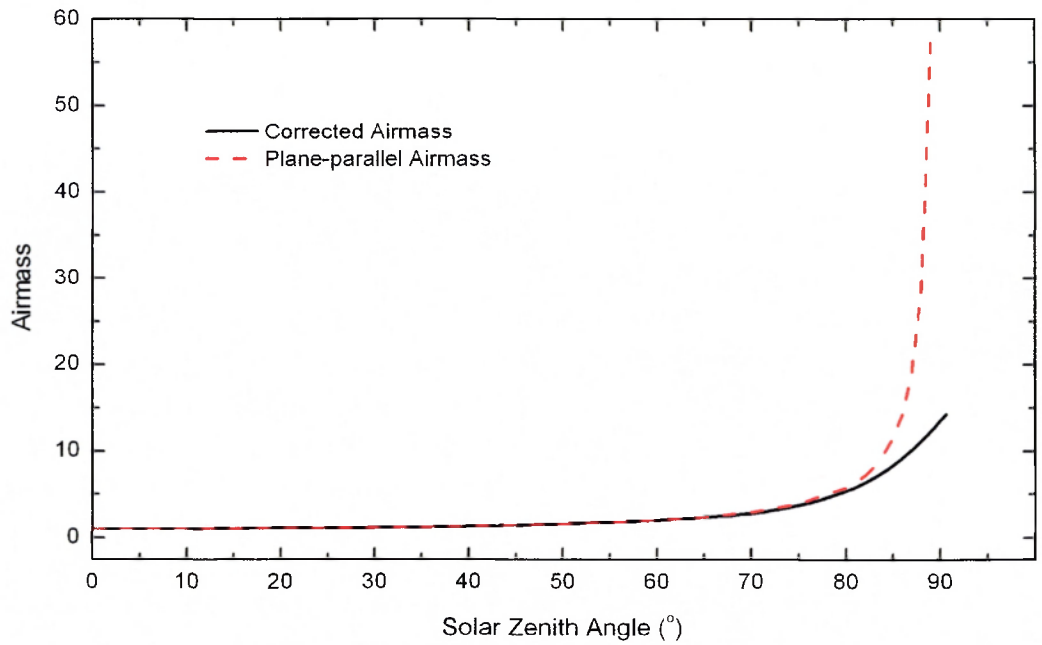

Figure 3-4: Plane-parallel vs. corrected airmass comparison.

Equation 3-7 was integrated over altitude for values of *SZA* between 0° and 90°, giving the real airmass values as a function of *SZA*. The variation of both the plane-parallel and corrected airmass can be seen in Figure 3-4. Negligible difference is observed between the two at small to medium zenith angles, and it is only when the Sun is low in the sky that the

effects of atmospheric curvature begin to manifest. A noticeable difference is only observed towards approximately 80°, where the plane-parallel case suddenly diverges, rapidly increasing towards 90°. At 89°, the uncorrected airmass overestimates the viewed airmass by nearly a factor of four.

A correction term for this overestimation was therefore included in the model, specifically for cases when *SZA* exceeds 60°. *SZA* is still calculated in the same manner, but the airmass calculation (airmass = secant(*SZA*)) used to define gaseous abundances has been modified to rectify the overestimation.

3.2 Gaseous Species

3.2.1 Gas Abundances

The martian atmosphere consists primarily of CO_2, with a balance of nitrogen, argon and trace species, shown in Table 3-1 (Owen 1992). Two of the trace species (H_2O and O_3) are variable in concentration dependent upon season. Both these species play important roles in photochemical reactions, which essentially govern their concentrations.

Gaseous Species	Abundance
CO_2	95.32%
N_2	2.7%
Ar	1.6%
O_2	0.13%
CO	0.07%
O_3	variable
H_2O	0.03% (variable)
Ne	2.5 ppm
Kr	0.3 ppm
Xe	0.08 ppm

Table 3-1: The martian atmospheric composition (Owen 1992).

The default model pressure value was set at 7.5 hPa due mainly to the heritage of the modelling work. The origin of this model lies in the design of the UV sensor on Beagle 2, with certain restrictions on landing site locations defining the areas available for exploration. One restriction required a landing site at least 1.1 km below the reference pressure geoid, to ensure sufficient atmospheric mass to decelerate the lander during entry and descent, minimising landing risks. The Beagle 2 landing site is at an altitude of -3.4 km, and the surface pressure at this altitude is approximately 7.5 hPa. For this reason this default pressure value was set in the model, unless otherwise specified.

To determine the amount of gaseous material the incident solar flux must traverse to reach the surface, the column abundance (ξ, particles cm^{-2}) of the total atmospheric column needed to be defined. This was achieved through use of the input surface pressure (P) and mean molecular mass (M_{mol} = 43.4 AMU), except for the case of O_3, which is specified manually. H_2O is also non-uniformly distributed with altitude (Rodin *et al.* 1997), but the effect of this species is not relevant to this study since H_2O does not absorb between 180 and 400 nm. M_{mol} and temperature are assumed constant with altitude, *i.e.* a constant mixing ratio throughout the atmosphere. This is acceptable since the majority of the atmosphere is CO_2, with all other species offering negligible effects except for O_3 which is defined separately. Small variations in mixing ratios will offer negligible effects on the spectrum due to the minor effects of the other species.

Column abundance (ξ) is defined as the number of particles in a column (conventionally with a cross-section of 1 cm^2) above a specified area (integrated from the surface to top of the atmosphere), and can be described as a function of surface pressure through use of the barometric law (see Chamberlain 1978), Equation 1.1.6). The resulting standard relation for ξ is given as:

$$\xi \approx \frac{P(z)}{G(z)M_{mol}} \tag{3-8}$$

where $P(z)$ and $G(z)$ are the pressure and local acceleration due to gravity at altitude z respectively. $G(z)$ decreases by approximately 10% from the surface to 200 km, but can be considered to be constant with altitude for simplicity, since the majority of the martian atmosphere (~95%) is within the first few scale heights (~50 km altitude) and this term will therefore have negligible effect. Thus we have an expression which describes ξ in terms of P directly, and can be defined at each atmospheric layer interface.

Once the integrated column abundance was known, the species specific column abundance was then determined using the mixing ratios given in Table 3-1. The next step was to distribute each species specific column abundance across the 10 layer martian atmosphere. This was achieved by consideration of the pressure (and thus density) profile used previously to define the layer heights. The relative 'layer pressure' of each individual layer with respect to the total surface pressure was calculated, and these percentage values were used to fractionate the column abundance of each species into layer column abundances. Thus, for each individual layer and each individual gas species, the total layer column abundance (no. of particles cm^{-2}) denoted by n_x (where x is the gas species) was defined.

O_3, however, is not distributed uniformly in the martian atmosphere and varies dramatically over L_s, and is therefore manually specified in the model. The relative distribution of O_3 with altitude to determine the fractional layer abundance in the model was taken from photochemical modelling studies (L. Lara, *personal communication*) based upon the photochemical model of Rodrigo *et al.* (1990). It should be noted that this method was used only to define the *relative* distribution of O_3 abundance with altitude, allowing an individual O_3-fraction to be assigned to each atmospheric layer. The manually specified total column abundance is thus distributed across the atmospheric layers in a photochemically accurate variation with altitude. O_3 abundance and its variation throughout the martian year is discussed further in Chapter Five.

3.2.2 Rayleigh Scattering

The transmission of UV through the atmosphere is dependent on two distinct processes, namely scattering and absorption. These two factors combine to define an overall attenuation of the radiation towards the surface. In the case of gaseous species, to quantify the atomic and molecular interaction with incoming solar UV, the scattering ($\sigma_{Rayleigh}$) and absorption (σ_{abs}) cross-sections need to be known. Knowing these cross-sections, the optical depths due to scattering and absorption can be found by the product of the cross-section with the column abundance.

This section details the scattering effects of the gaseous species. Though this effect influences the resultant spectrum to a lesser degree than absorption, it is still calculated for each species for completeness. The gaseous scattering process which occurs in the martian atmosphere at these wavelengths is Rayleigh scattering, which occurs when the scatterer radius is much smaller than the incident radiation wavelength. This process is highly wavelength dependent ($\propto \lambda^{-4}$), scattering more towards shorter wavelengths and responsible for creating the blue colour of the terrestrial sky. The Rayleigh scattering cross-section ($\sigma_{Rayleigh}$) for gases as derived by Heddle (1962) is defined by:

$$\sigma_{Rayleigh} = \frac{128\pi^5\alpha_0}{3\lambda^4}\left(\frac{6+3\rho_n}{6-7\rho_n}\right) \tag{3-9}$$

where α_0 is the polarisability of the molecule, and ρ_n is the normal depolarisation ratio[1] (see Heddle 1962). For symmetric gaseous molecules $\rho_n \rightarrow 0$, and for asymmetric gaseous molecules ρ_n is $<< 1$ (typically around 0.01 for the terrestrial atmosphere), and is assumed here also to be zero (the corresponding uncertainty of ~1% in $\sigma_{Rayleigh}$ created by this assumption is acceptable here). Thus the bracketed depolarisation term in Equation 3-9 tends

[1] Polarisability refers to the measure of charge distribution in a molecule, and the normal depolarisation ratio is the ratio of parallel to perpendicular polarised scattered light.

to unity, and the Rayleigh cross-section reduces to a function of only α_0 and λ. The α_0 values for CO_2, N_2, Ar, O_2, O_3 and CO were taken from Miller (1991) and references therein, and are 2.911, 1.740, 1.641, 1.581, 3.210 and 1.950 ($\times 10^{-30}$ m^2) respectively. $\sigma_{Rayleigh}$ was calculated for each gaseous species between 180 and 400 nm.

3.2.3 Absorption Cross-sections

In terms of UV absorption in the wavelength regions considered here, the only relevant gaseous absorbers present in the martian atmosphere are CO_2, O_3 and O_2. For all other gaseous species in the martian atmosphere, σ_{abs} is close to zero at these wavelengths. The absorption cross-sections of CO_2, O_3 and O_2 were also defined as a function of λ, since absorption by molecular species is highly dependent upon the energy (and thus λ) of the incoming photon. The CO_2 cross-section values were taken from Lewis and Carver (1983) for $\lambda < 197$ nm. This species cross-section value is critical as it defines the lower wavelength cut off in all martian UV spectra. The CO_2 absorption cross-section increases dramatically below this wavelength, and coupled with the large abundance of CO_2 in the atmosphere creates an absorption cut-off in the spectrum. Lewis and Carver (1983) published data on the CO_2 cross-section at low temperatures near 200 K which is appropriate for the cold martian atmosphere. The temperature dependence of the absorption cross-sections is non-negligible and cannot be ignored – in the case of CO_2 the cross-section at 300 K can be almost an order of magnitude greater than that at 200 K, leading to significant overestimation of the absorption effects. The data of Lewis and Carver (1983) for the CO_2 absorption cross-section can be seen in Figure 3-5 for temperatures of 200, 300 and 370 K. Above 197 nm the absorption cross-section becomes indistinguishable from the Rayleigh cross-section.

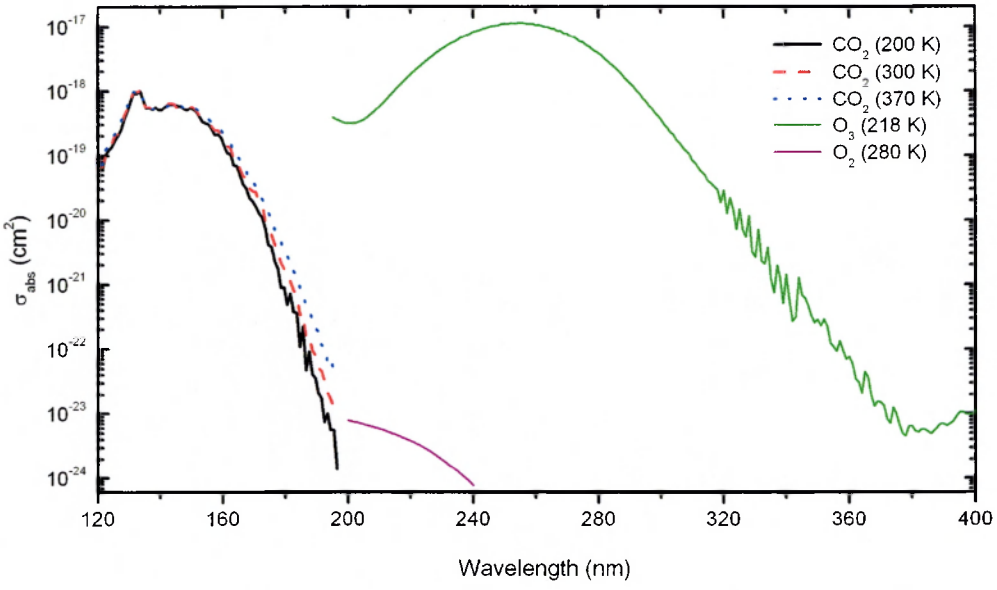

Figure 3-5: CO_2, O_3 and O_2 absorption cross-sections (Lewis and Carver 1983; Malicet *et al.* 1995; Amoruso *et al.* 1996).

The remaining two relevant species which require explicitly defined absorption cross-sections are O_3 and O_2. O_3 is only a trace species in the martian atmosphere and is highly variable in concentration, varying as a function of season and latitude. However, the extremely large cross-section of O_3 in the UV region means that even a small abundance of this molecular species results in significant absorption in the UV spectrum. O_3 possesses two distinct absorption bands in the 180-400 nm region; a strong absorption band centred around 250 nm in the Hartley continuum, and weaker absorption peaks in the Huggins band between 300 and 350 nm. The absorption cross-section data for O_3 of Malicet *et al.* (1995) at 218 K were used, shown in Figure 3-5 appropriate to the mean martian atmospheric temperature.

The final UV absorber in the martian atmosphere covered here is O_2. Due to its relatively small absorption cross-section in the UV range, coupled with its rarity in the martian atmosphere, this trace species plays a negligible role in the absorption of martian UV between 190 and 400 nm, but is nevertheless included here. The opposite case is observed on Earth, where though the cross-section is still small, the large relative abundance of the molecule amplifies its absorptive effects. The data of Amoruso *et al.* (1996) were utilised for the O_2

absorption cross-section, with data between 208 and 240 nm covering the weak Herzberg continuum. These data were taken at 280 K, which is warmer than the mean martian atmospheric temperature, but since the effect upon the spectrum is minimal these data will be sufficient. Variation of the absorption cross-section of O_2 with λ is shown in Figure 3-5.

3.3 Aerosol Species

The presence of aerosols in planetary atmospheres has many possible effects, resulting in both local and global environmental consequences. On Mars a range of aerosols is encountered, but the key major aerosol contributor takes the form of suspended dust. Other types of martian aerosols include cloud formations, forming from the condensation of either CO_2 or H_2O at high altitudes. Surface fogs are also encountered, observable in the early morning for short periods of time, and in some low altitude regions such as Nirgal Valley persisting throughout the entire day. In this chapter, only background dust aerosols are dealt with in detail, since they are the dominant aerosol species. The remaining types of aerosols and the derivation of their optical properties are dealt with in Chapter Six. The optical properties of the other aerosols are incorporated into the model in the same way as explained here for the background dust aerosols, when required.

3.3.1 Suspended Dust

The ubiquitous presence of dust in the martian atmosphere is clearly inferred from the present day view of an arid barren planet. Dust is formed via constant weathering of surface rock by martian winds, and lofted into the atmosphere. In addition to this, high speed localised vortical air columns known as 'dust devils' are believed to be a significant contributing factor to the injection of dust into the atmosphere.

The occurrence of suspended dust is an ever-present factor that needs to be properly addressed during any martian atmospheric modelling simulations. Dust suspended in the atmosphere interacts directly with incoming solar radiation, through the process of both absorption and scattering. An increase in the atmospheric absorption of solar radiation by dust results in a more isotropic altitude-temperature profile (over the range of altitude the dust is present) when compared to a non-aerosol laden atmosphere, since the dust acts as an effective atmospheric thermal stabiliser. As well as absorption of solar radiation, dust also plays an important role in the scattering of incoming solar UV. Scattering significantly affects the optical depth of the atmosphere, attenuating the amount of transmitted UV to the surface. Such scattering effects are evident on Mars, perpetuated by the continuous presence of a background 'haze'. The presence of high dust loading is significant in the context of the relative effects between direct and diffuse illumination at the martian surface – large amounts of dust will quickly reduce direct input, but the effect of diffuse scattering may lessen the overall extinction.

The temporal variation of dust activity has been observed to correlate approximately with season. Viking lander 1 and 2 (VL1 and VL2) optical depth measurements show distinct periods of high and low optical depths, attributable mainly to variation in atmospheric dust loading. Results have revealed quiet periods during the clearer northern spring/summer between L_s = 0 to 180°, with optical depth values of 0.4 to 0.7 at λ = 670 nm (Pollack *et al.* 1977). Following this is the more dusty southern summer (L_s = 180 to 360°) when optical depths increase in general, which also coincided with the two great dust storms of the Viking era resulting in optical depths exceeding 3. Thus dust activity has a marked seasonal effect, possibly tied to the relatively high eccentricity of the martian orbit and corresponding variation of solar insolation. This trend is presented in Figure 3-6, which shows optical depth data taken from the VL1 camera over the course of the martian year (Pollack *et al.* 1979).

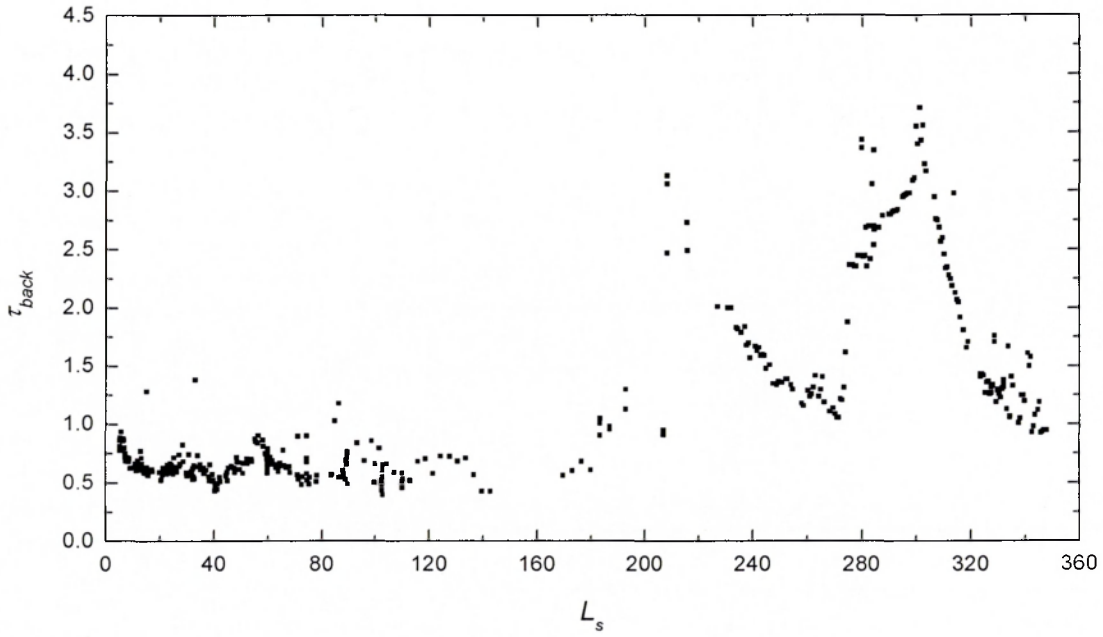

Figure 3-6: Seasonal optical depths from the VL1 camera at λ = 670 nm (Pollack *et al.* 1979).

In the next major missions to the martian surface some 20 years later, MPF and MGS recorded similar trends in the variation of optical depth, though to a lesser degree, suggesting this behaviour to be characteristic of the martian annual dust cycle (Smith and Lemmon 1999; Smith *et al.* 2001). The proximity of Mars to the Sun at perihelion is believed to be a possible trigger of hemispherical and global dust storms, beginning in the southern hemisphere and proceeding northwards to encompass most of the planet to latitudes of around 45° (Pollack *et al.* 1979). This process is still poorly understood however, and requires more long term observations and modelling of dust activity.

As τ_{back} is a primary input to the model and always present in the martian atmosphere, the spatial and temporal variation of dust in the martian atmosphere needs to be defined, if annual and global variations are to be investigated. Three different seasonal dust optical depth models are employed in this model, to recreate clear, nominal and dusty martian years. The dust scenarios used are those constructed by the Mars Climate Database (MCD) as fits to observational data (Lewis *et al.* 1999). These consist of the following scenarios:

1. Low dust scenario τ_{low}, where τ_{back} (and thus dust loading) is spatially constant over latitude and temporally constant over L_s, and taken as:

$$\tau_{low} = 0.1 \tag{3-10}$$

2. High dust scenario τ_{high}, where the optical depth is spatially constant over latitude but temporally dependent upon L_s, and given by:

$$\tau_{high} = 0.7 + \cos(L_s + 80^o) \tag{3-11}$$

This variation is a fit to the peak removed (*i.e.* global dust storms) variations as observed during the Viking era.

3. Nominal dust scenario $\tau_{nominal}$, where τ_{back} is spatially dependent upon latitude and temporally dependent upon L_s. This scenario is a mathematical fit to recent MGS Thermal Emission Spectrometer (TES) mapping results, consisting of data for all martian seasons from multi-annual experiments (Smith *et al.* 2001). This experimentally derived scenario is believed to be the best representation of the current nominal Mars dust environment, and is given by:

$$\tau_{nominal} = \begin{cases} \tau_N + \frac{1}{2}(\tau_{eq} - \tau_N)(1 + \tanh((45^o - lat) \times 10)) & for\ lat \geq 0^o \\ \tau_S + \frac{1}{2}(\tau_{eq} - \tau_S)(1 + \tanh((45^o - lat) \times 10)) & for\ lat < 0^o \end{cases} \tag{3-12}$$

where

$$\tau_{eq} = 0.2 + 0.3 \times (\cos(0.5 \times (L_s - 250^o)))^{14} \tag{3-13}$$

$$\tau_S = 0.1 + 0.4 \times (\cos(0.5 \times (L_s - 250^o)))^{14} \tag{3-14}$$

$$\tau_N = 0.1 \tag{3-15}$$

The default annual dust scenario for the model is the nominal model, which specifies $\tau_{back} = \tau_{nominal}$. However, any one of the three scenarios can be selected to define the background dust content at any point in the martian orbit.

Figure 3-7 shows the variation of the nominal dust optical depth over latitude and L_s. The sharp increase in dust activity can be seen towards perihelion. During the rest of the year the dust loading in the atmosphere is relatively stable, consistent with observations cited previously.

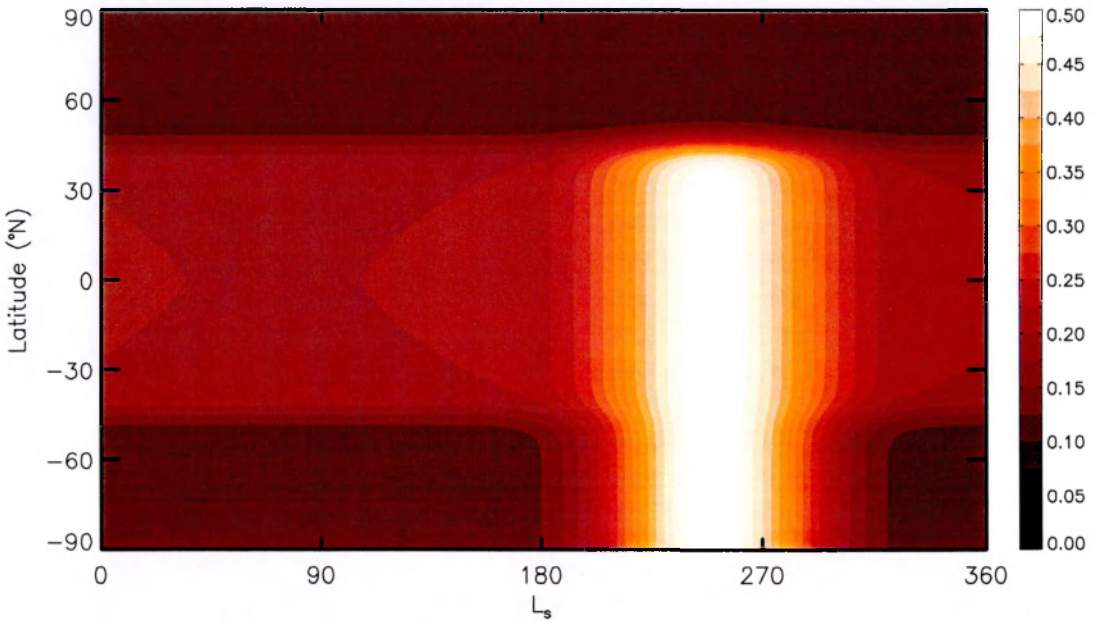

Figure 3-7: Nominal variation of τ_{back} over latitude and L_s.

In order to represent accurately the wavelength dependence of optical depth, τ_{back} was scaled linearly with the extinction efficiency (Q_{ext}) of the background dust over λ. Q_{ext} is a measure of the ratio of the extinction cross-section to the geometric cross-section of the particle. Input background dust optical depth is referenced to $\lambda = 670$ nm. It is common practice to use this wavelength reference, since the value of the extinction efficiency is close to the value averaged over the solar spectrum (Pollack *et al.* 1979). The optical depth was then scaled from 670 nm across the UV region linearly with Q_{ext}, to account for the variation of optical depth as a function of wavelength. Since the extinction efficiency is a measure of the extinction cross-section as a function of wavelength (*i.e.* directly related to the optical depth), this term can be used to scale τ_{back} appropriately in the UV region.

As part of the radiative transfer calculation, certain optical properties need to be defined for each aerosol species in question, namely the single scattering albedo (ω_o) and the asymmetry parameter of the phase function of the particle (g). ω_o is defined as the ratio of scattered light to that both scattered and absorbed, and is thus a measure of the degree of scattering (or conversely absorption) that occurs per particle-light interaction. A particle which is completely absorbing has a single scattering albedo of 0, and a particle which is completely scattering with no absorbing properties has a single scattering albedo of 1. ω_o can be quantified as the ratio of the scattering cross-section (σ_{sca}) to that of the total extinction cross-section of the aerosol (σ_{ext}), and is related to the scattering and extinction optical depth (τ_{sca} and τ_{tot} respectively) through the relation:

$$\omega_o = \frac{\sigma_{sca}}{\sigma_{ext}} \equiv \frac{\tau_{sca}}{\tau_{tot}} \tag{3-16}$$

The asymmetry parameter (g) is directly related to the phase function, $P_{fn}(\Theta)$, of the aerosol concerned, where Θ is the angle of scatter with respect to the incident beam. The phase function (also known as the scattering diagram) gives the angular distribution of scattered energy as a function of direction. For isotropic scattering, the angular distribution of scattered energy is equal in all directions, and $P_{fn}(\Theta) = 1$. For Rayleigh scattering, $P_{fn}(\Theta)$ is:

$$P_{fn}(\Theta) = \frac{3}{4}\left(1+\cos^2\Theta\right) \tag{3-17}$$

Figure 3-8 shows the phase functions for both Rayleigh scattering (typical of gaseous molecules) and 'forward-stretched' scattering species (typical of particulate scattering, where the phase function is equal to $1 + 3g\cos[\Theta]$ and stretched into the forward hemisphere) versus scattering angle. For isotropic phase functions, scattering intensity is equal in all directions, and would be circular in Figure 3-8. Rayleigh scattering does not project equally in all directions, with an enhanced projection in the backwards and forwards directions. The case

for particulate scattering deviates strongly from that for Rayleigh scattering, with the majority of the scattered light projected into the forward hemisphere.

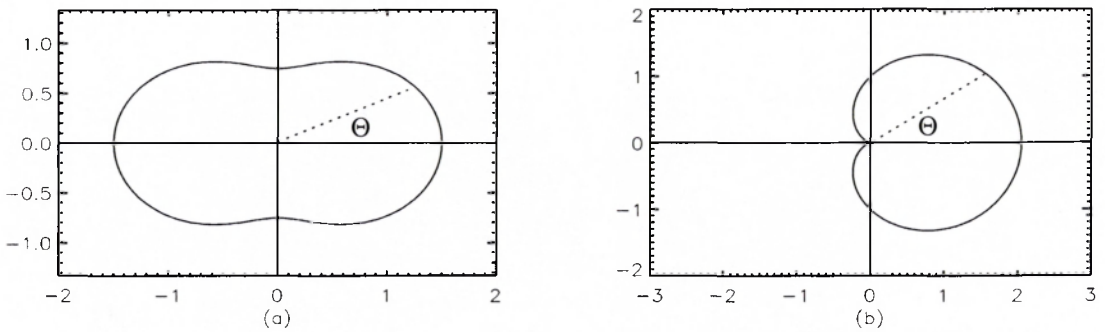

Figure 3-8: Phase function distribution in polar coordinates for (a) Rayleigh and (b) forward-stretched scattering.

g is defined as the first moment of the phase function, and describes the average cosine angle of emergent scattered light from the particle. This parameter yields the *relative* direction of scattering by particles or gases. For particles which scatter predominantly in the forward direction (scattering angle 0°), g tends towards 1. Correspondingly, particles which mainly backscatter have particle asymmetry values tending towards -1 (scattering angle 180°). Isotropically scattering particles have g equal to zero, since all the energy is scattered in equal amounts in all directions. Rayleigh scattering is not isotropic, since more radiation is scattered into the forward and backward directions. The distribution of energy is, however, evenly spread between the forward and backward hemispheres as shown in Figure 3-8, which also results in a zero asymmetry parameter. Each of these two parameters always need to be explicitly defined as a function of wavelength for radiative transfer calculations.

The choice of optical parameters in the UV is a contentious subject and is explored in the next section. For this model, the data of Ockert-Bell *et al.* (1997) are used to describe quantitatively the optical properties of martian background dust between 180 and 400 nm, namely ω_{bd} and g_{bd}. Their data is taken from a variety of observations, combining data from

VL1 and VL2 (Pollack *et al.* 1995), Phobos 2 (Moroz *et al.* 1993) and orbital telescopic observations (Wallace *et al.* 1972) to give a model of the optical properties of martian dust over the spectral range 0.21-4.3 μm. Data in the UV region is sparse, so spline interpolation between data points was used here to characterise fully the required parameters between 180 and 400 nm, shown in Figure 3-9.

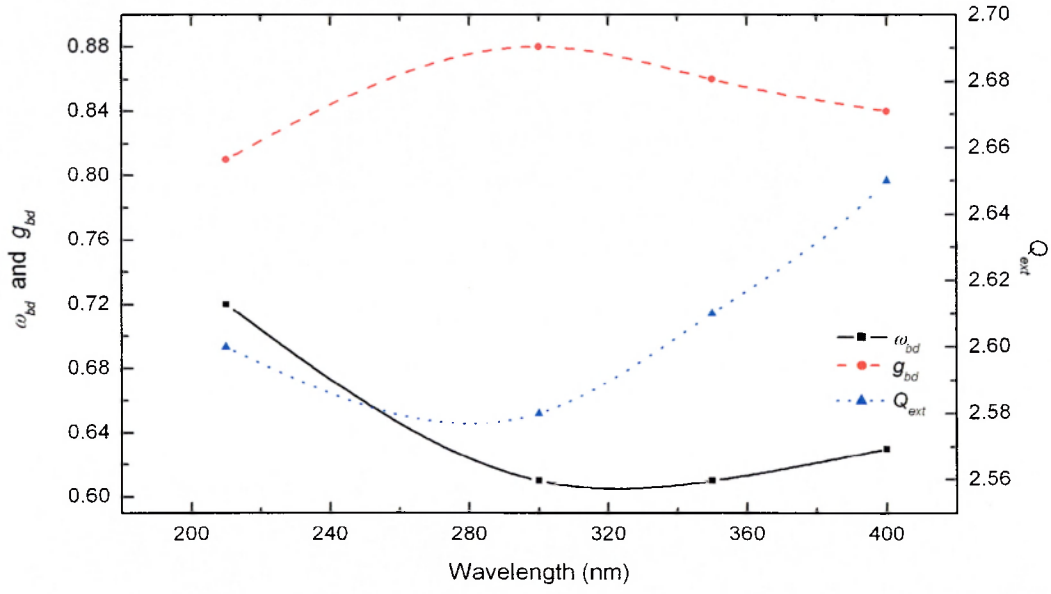

Figure 3-9: ω_{bd} and g_{bd} values used for suspended martian dust (Ockert-Bell *et al.* 1997).

3.3.2 Comparison of Background Dust Properties

The optical properties of martian dust in the UV region remain uncertain, with relatively little work performed to date. Significant variations of the optical properties in the UV have been reported, with little agreement between different sources as shown in Figures 3-10 and 3-11. Pang *et al.* (1976) analysed results from Mariner 9 UVS data to derive complex indices of refraction at 268 nm and 305 nm using Mie theory for spherical particles, with Chylek and Grams (1978) repeating the analysis using non-spherical particle theory. These studies found the dust at these wavelengths to be less absorbing than the results of Ockert-Bell *et al.* (1997).

The opposite result is seen in HST data from Wolff *et al.* (1997) who used the Wide Field Planetary Camera for observations of dust storms in the Hellas and polar regions, deriving a more absorbing dust in the UV region (*i.e.* smaller ω_{bd} values – no values of g_{bd} were published in their paper). Zurek (1978) used further complex indices of refraction from the data of Pang and Ajello (1977) to derive the optical properties ω_{bd} and g_{bd} at wavelengths of 201, 308 and 388 nm in the spherical approximation. These results show an agreement with Wolff *et al.* (1997) for ω_{bd} at 201 nm, but differ towards 300 nm tending more to the value of Ockert-Bell *et al.* (1997), only to diverge again at 388 nm. Much more investigation from orbiting or surface instrumentation is required (contrasting the visible-IR range, which is far better defined and consistent between studies) to gain a more complete and accurate dataset.

Other factors need to be considered when addressing the UV properties of dust. The published work has been carried out at different periods of dust activity and in differing regions, and as a result variations in optical properties would be expected. Small variations in particle size distribution and complex refractive index across the martian terrain could occur, affecting the optical properties of the dust. Size distributions may for example vary as a result of differing weathering processes or rates in different regions. Also, for example, a small variation in a UV absorbing component which is commonly present in small quantities (such as TiO_2 as proposed by Pang and Ajello (1977), and verified by Bell III *et al.* (2000) through MPF results) could account for a slight variation in imaginary index of refraction and thus optical properties of dust between different areas.

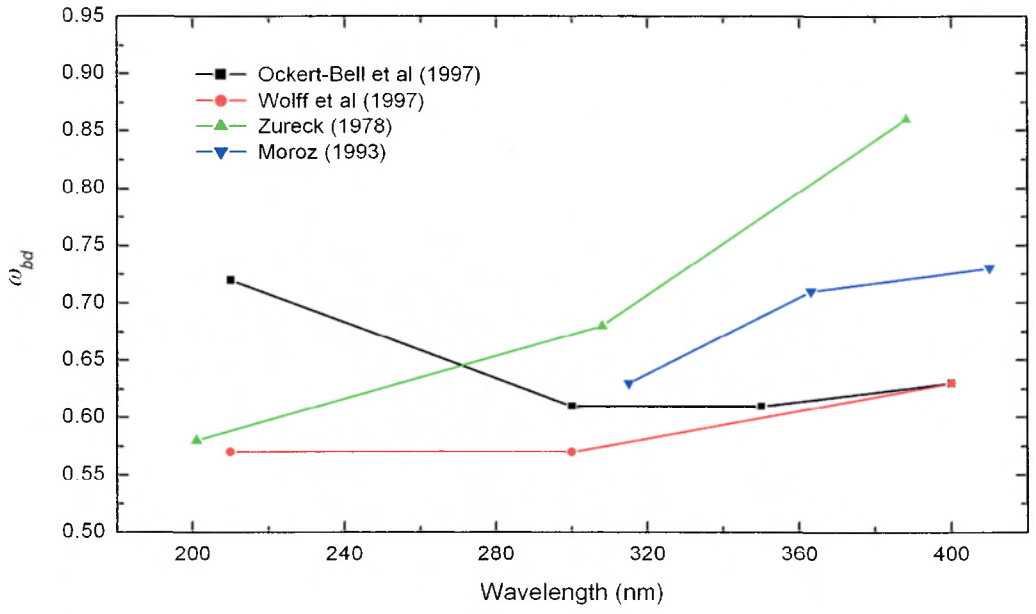

Figure 3-10: Comparison of published values of ω_{bd}.

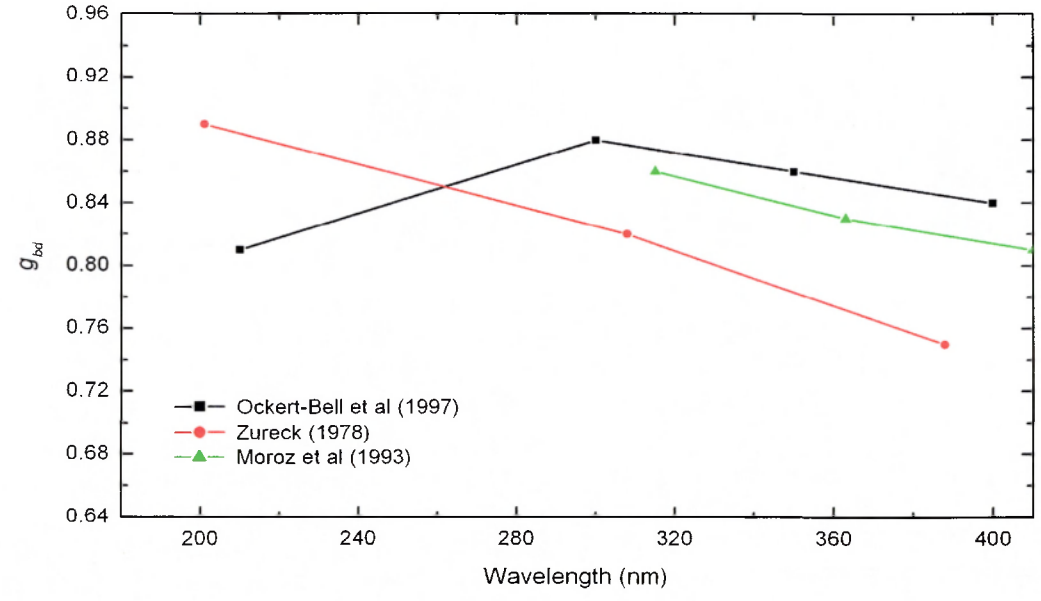

Figure 3-11: Comparison of published values of g_{bd}.

Quantifying the effect that these possible variations will have upon the optical properties is beyond the scope of this work, and is an area which needs to be investigated. More consistent optical properties are seen in the visible range, where many *in situ* observations

have helped constrain the particle scattering properties. This has yet to occur for the case of the UV region, which requires further investigation for more accurate constraint upon the dust optical properties. The fact that the diffuse spectrum may change slightly with differing optical properties should therefore always be considered with the results presented here.

The values derived by Ockert-Bell *et al.* (1997) however rely on whole disk spectra taken from telescopic observations covering a range of planetary environments including limb hazes and polar cap regions (Owen and Sagan 1972). Dust optical properties derived from these observations and applied to specific regions are not always completely reliable and can be a source of error. Due to the limitations of available data the approach used here for martian dust optical properties is the best that can be achieved at present, and caution should always be considered with the results. Further detailed observational work coupled with rigorous modelling is required in future to constrain these optical parameters more accurately.

3.3.3 Composite Optical Properties

To gauge the individual effect upon interaction with incoming UV radiation, the optical properties for each (major) species have been described. The degree and nature of the interaction of each individual species is now known, but for the purposes of atmospheric transmission, the effective 'composite' optical properties of the total gas and aerosol mixture are now required. This involves combining the individual optical properties of each type of aerosol and gas into a single composite property, representative of the relative contribution from each species.

The optical depth due to both scattering and absorption needed to be explicitly defined for each species. For gaseous molecules (species X), each optical depth due to scattering (τ_{gsX}) and absorption (τ_{gaX}) is defined as the sum of n_X with σ_{scaX} and σ_{absX} respectively. The total gaseous optical depth due to scattering and absorption are then found through summation of the individual values.

The contribution to optical depth due to aerosol scattering (τ_{ds} – for the moment, only background dust is regarded here) was found through the product of ω_{bd} and τ_{back} (Equation 3-16). The component of dust optical depth due to absorption (τ_{da}) was then found from the difference of τ_{back} and τ_{ds}. With these parameters defined for all gaseous and aerosol species in the atmosphere, the effective scattering properties of the composite atmosphere was calculated. The effective single scattering albedo ω_{eff} was found through the combination of the above derived parameters by:

$$\omega_{eff} = \frac{\tau_{gs} + \tau_{ds}}{\tau_{gs} + \tau_{ga} + \tau_{ds} + \tau_{da}} \tag{3-18}$$

The effective asymmetry factor g_{eff} was calculated as the weighted sum of the individual species asymmetry parameters (*i.e.* the gaseous asymmetry parameter g_{gas} etc), giving:

$$g_{eff} = \frac{(\tau_{gs} + \tau_{ga}) g_{gas} + \tau_{back} g_{bd}}{\tau_{gs} + \tau_{ga} + \tau_{back}} \equiv \frac{\tau_{back}\, g_{bd}}{\tau_{gs} + \tau_{ga} + \tau_{back}} \tag{3-19}$$

since the asymmetry parameter for gaseous molecules (g_{gas}) is equal to zero. In both the above equations, additional aerosols can be added through inclusion of their respective properties in the same manner as for the background dust. The total composite atmospheric optical depth (τ_{tot}) is the final parameter required for the radiative transfer calculations, given as the sum of each species' individual scattering and absorption optical depths. The composite optical properties were then explicitly defined for each individual layer using Equations 3-18 and 3-19.

3.4 The Delta-Eddington Approximation

3.4.1 Radiative Transfer Process

The view from an evening walk on a summer's day of the reddish setting Sun with blue sky all around is a direct observation of the effects of radiative transfer (RT). The essence of RT is the quantitative description of how radiant energy is transferred from one location to another, and its importance is not confined solely to the realm of atmospheric modelling, but also applications ranging from the modelling of stellar interiors to medical imaging. The radiative transfer equation gives the change in irradiance along a beam of electromagnetic (EM) energy through the atmosphere, governed by absorption and scattering processes. There are a number of factors which affect the intensity of EM energy through a given path through an atmosphere shown schematically in Figure 3-12a: scattering of radiation out of the path; absorption along the path; single scattering back into the path, and multiple scattering back into the path.

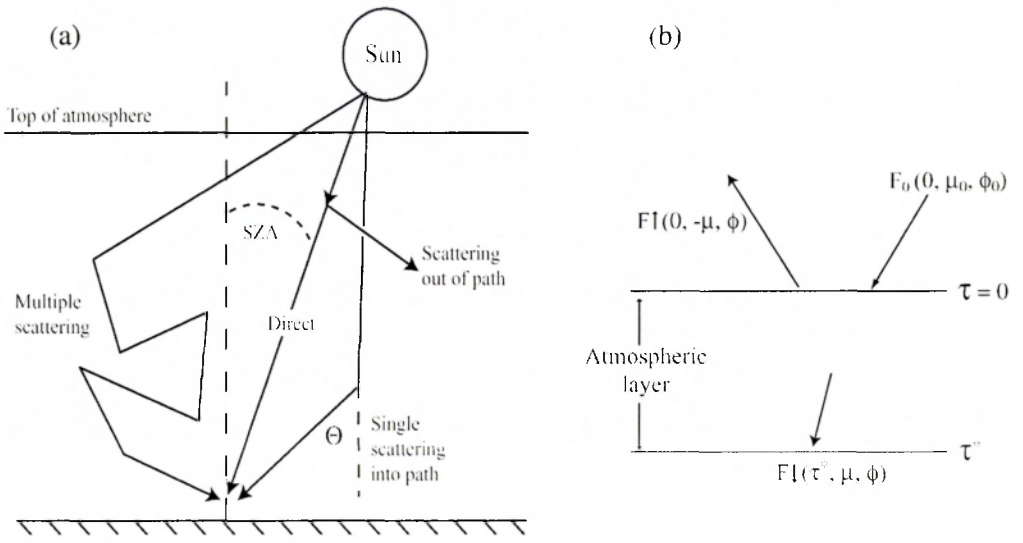

Figure 3-12: Scattering processes in the atmosphere. (a) shows the various processes which affect the path of energy arriving at the surface. (b) shows the two-stream diffuse representation for an atmospheric layer (layer 1 in this case), where F↑ is the reflected component and F↓ is the transmitted component.

The process of scattering can therefore both attenuate and intensify the magnitude of energy which is received at the surface, and the purpose of RT modelling is to quantify this effect. In the context of RT, any energy which has not been scattered through its path through the atmosphere is termed the direct component. Conversely, radiation which has undergone either single or multiple scattering events is designated as the diffuse component. In this study, RT principles are applied to determine the nature of the diffuse UV component at the surface of Mars.

The equation of transfer describing the diffuse radiance $I(\tau, \mu, \phi)$ is:

$$\mu \frac{dI}{d\tau}(\tau,\mu,\phi) = -I(\tau,\mu,\phi) + \frac{\omega_{eff}}{4\pi} \int_0^{2\pi} \int_{-1}^{+1} P_{fn}(\mu,\phi;\mu',\phi') I(\tau,\mu',\phi')\, d\mu'\, d\phi' + \frac{\omega_{eff} F_0}{4} P_{fn}(\mu,\phi;\mu_0,\phi_0) e^{-\frac{\tau}{\mu_0}} \tag{3-20}$$

where ϕ is the azimuth angle, and $P_{fn}(\mu, \phi ; \mu', \phi')$ is the phase function defining the light incident at μ', ϕ' which is scattered in the direction μ, ϕ. The first term in Equation 3-20 describes the decrease of radiance through absorption and scattering *out* of the path. The second term accounts for the increase formed through scattering of diffuse radiance *into* the path, and the third term quantifies the increase in radiance due to scattering of the direct component *along* the path.

The Eddington approximation provides a relatively simple representation of the equation of transfer of diffuse irradiance originating from the two-stream method based on analytic representation of the downward (transmitted) stream of diffuse flux (F↓) and upward (reflected) stream of diffuse flux (F↑), both at and between layer boundaries in a homogenous medium, shown in Figure 3-12b. The process of approximation of the diffuse radiance for the delta-Eddington approximation is equivalent to that for the Eddington approximation, except with transformed optical parameters (addressed later), and the following derivation of solutions (Equations 3-20 to 3-39) is taken from Shettle and Weinman (1970).

The diffuse radiance, $I(\tau, \mu)$, can be expanded as a series of Legendre polynomials, and the Eddington approximation assumes that this series can be truncated after the second term, *i.e.* to first order in μ:

$$I(\tau,\mu) = I_0(\tau) + \mu I_1(\tau) \tag{3-21}$$

giving a diffuse term independent of SZA (I_0) and a term dependent on SZA (I_1). Under conditions of extreme multiple scattering (such as within a cloud), it would be expected that I_0 should be much larger than I_1. Conversely, under conditions of single scattering, I_1 should be larger than I_0. The phase function can also be expanded in terms of Legendre polynomials, and as a result of the orthogonality properties of these polynomials, all terms of order greater than one tend to zero when the integrals over μ' and ϕ' are evaluated in Equation 3-20 when Equation 3-21 is used for the diffuse irradiance. The phase function for each scattering species then becomes

$$P_{fn}(\cos\Theta) = 1 + \psi(\tau)\cos\Theta \tag{3-22}$$

where $\psi(\tau)$ is a constant. Using these terms for the phase function and irradiance, Equation 3-20 can be reduced to a simpler form, and integration of the resulting expression gives a pair of equations for I_0 and I_1:

$$\frac{dI_1}{d\tau} = -3\left[1-\omega_{eff}(\tau)\right]I_0 + \tfrac{3}{4}\omega_{eff}(\tau)F_0 e^{-\frac{\tau}{\mu_0}} \tag{3-23}$$

$$\frac{dI_0}{d\tau} = -\left[1-\omega_{eff}(\tau)\,g_{eff}(\tau)\right]I_1 + \tfrac{3}{4}\omega_{eff}(\tau)g_{eff}(\tau)\mu_0 F_0 e^{-\frac{\tau}{\mu_0}} \tag{3-24}$$

Analytical solutions are not possible for Equations 3-23 and 3-24, however they can be solved for the special case of an atmosphere constructed from separate homogeneous layers,

where ω_{eff} and g_{eff} are constant in each layer. In such a case, the solutions to Equations 3-23 and 3-24 are given in Equations 3-29 and 3-30.

The Eddington approximation, however, is inaccurate when dealing with highly asymmetric phase functions, typical of particulate scattering. This deficiency was overcome by the introduction of delta-function scaling, in which a fraction (f) of the scattered energy (equal to the square of g_{eff}) is considered to be in the forward peak approximated by a Dirac delta function, providing an accurate and computationally fast method of calculating the diffuse flux through homogenous layered atmospheres (Joseph *et al.* 1976). This modification allows the accurate handling of scattering by aerosols with highly asymmetric phase functions, and forms the modified delta-Eddington approximation for diffuse flux. The delta-Eddington approximation uses standard scattering parameters (g′, ω′ and τ′), transformed for the modified phase function, which is given by:

$$P_{\delta-Edd}(\cos\Theta) = 2f\delta(1-\cos\Theta)+(1-f)(1+3g'\cos\Theta) \tag{3-25}$$

where f is the fractional scattering into the forward peak and g' is the truncated composite asymmetry factor.

The delta-function adjustment incorporates the forward peak truncation through adjustment of the optical properties, such that the fraction of scattered energy in the forward direction (f) is removed from the scattering parameters through transformation. These transformations, which permit the use of the solutions from the Eddington approximation, are:

$$g' = \frac{g_{eff}}{1+g_{eff}} \tag{3-26}$$

$$\omega' = \frac{\left(1-{g_{eff}}^2\right)\omega_{eff}}{1-\omega_{eff}\,g_{eff}^2} \tag{3-27}$$

$$\tau' = \left(1 - \omega_{eff}\, g_{eff}^2\right)\tau_{tot} \tag{3-28}$$

The introduction of the Dirac delta function into the delta-Eddington approximation makes this algorithm particularly useful when addressing dust and ice particulates in the martian atmosphere. These aerosols are mainly scattering in nature, with ω_o values generally above 0.5 and thus scattering predominantly in the forward direction, where the Eddington approximation began to break down.

3.4.2 Calculation of Layer Solutions

Given the transformations detailed in Equations 3-26 to 3-28, the solutions to the transfer of radiation through the layered atmosphere can be used to calculate the diffuse flux at the surface. Qualitatively, the transfer of light is determined as a function of optical depth. The layer notation is such that layer 1 is situated at the top of the atmosphere, with layer 10 at the surface. For non-conservative ($\omega' \neq 1$) homogeneous layers, solutions for I_0 and I_1 in the ith atmospheric layer (i=1, 2, 3, ...N, where N is the no. of atmospheric layers) as defined in Shettle and Weinman (1970) are:

$$I_0(\tau') = I_0^i(\tau') = C_1^i e^{-k_i\tau_i'} + C_2^i e^{k_i\tau_i'} - \alpha_i e^{-\tau_i'/\mu} \qquad \tau_{i-1}' < \tau' < \tau_i' \tag{3-29}$$

$$I_1(\tau') = I_1^i(\tau') = P_i\left(C_1^i e^{-k_i\tau_i'} - C_2^i e^{k_i\tau_i'}\right) - \beta_i e^{-\tau_i'/\mu} \qquad \tau_{i-1}' < \tau' < \tau_i' \tag{3-30}$$

where

$$k_i = \left[3\left(1-\omega_i'\right)\left(1-\omega_i' g_i'\right)\right]^{\frac{1}{2}} \tag{3-31}$$

$$P_i = \left[\frac{3\left(1-\omega_i'\right)}{\left(1-\omega_i' g_i'\right)}\right]^{\frac{1}{2}} \tag{3-32}$$

$$\alpha_i = \frac{3\omega_i' F_0 \mu^2\left[1 + g_i'\left(1-\omega_i'\right)\right]}{4\left(1-k_i^2\mu^2\right)} \tag{3-33}$$

$$\beta_i = \frac{3\omega_i' F_0 \mu\left[1+3g_i'(1-\omega_i')\mu^2\right]}{4\left(1-k_i^2\mu^2\right)} \tag{3-34}$$

In order to determine the 2N number of C_1^i and C_2^i constants in Equations 3-29 and 3-30, 2N equations are required. The boundary conditions at the top of atmosphere and surface provide two equations. At the top of atmosphere, the downward diffuse component is equal to zero. At the surface, the upward diffuse component is equal to the product of the downward diffuse component with the albedo of the surface. Using Equation 3-39 which gives the diffuse flux in terms of the above relations, these boundary conditions respectively give:

$$\left(1+\tfrac{2P_1}{3}\right)C_1^1 + \left(1-\tfrac{2P_1}{3}\right)C_2^1 = \alpha_1 + \tfrac{2\beta}{3} \tag{3-35}$$

$$C_1^{10}e^{-k_{10}\tau'}\left[1-A-\tfrac{2P_{10}(1+A)}{3}\right]+C_2^{10}e^{k_{10}\tau'}\left[1-A+\tfrac{2P_{10}(1+A)}{3}\right]=\left[(1-A)\alpha_{10}-\tfrac{2\beta_{10}(1+A)}{3}+A\mu F_0\right]e^{-\tau/\mu} \tag{3-36}$$

where A is the surface albedo taken as 0.03, consistent with observations from OAO-2 (Caldwell 1971) and Mariner 6 and 7 (Hord 1972). A wavelength invariant surface albedo was used since negligible variation was encountered with changing values of A. An order of magnitude increase in surface albedo value resulted in only a 1% variation in UV flux.

The remaining 2N-2 equations are derived from the requirement that I_0 and I_1 are continuous across each layer boundary, *i.e.* at each layer interface, I_0 and I_1 calculated in neighbouring layers should be equivalent:

$$I_0^i(\tau_i') = I_0^{i+1}(\tau_i') \qquad i=1,2,\ldots(N-1) \tag{3-37}$$

$$I_1^i(\tau_i') = I_1^{i+1}(\tau_i') \qquad i=1,2,\ldots(N-1) \tag{3-38}$$

Given these requirements, a set of 20 equations (since N=10 in this model) were derived. Matrix representation of the equations was used to determine the 10 C_1^i and C_2^i coefficients,

achieved through inversion of the 20×20 matrix to reveal the coefficients. Once C_1^i and C_2^i were known, $F_{diffuse}$ at each layer interface was calculated using Equations 3-29 and 3-30 through the relation:

$$F_{diffuse}(\tau) = 2\pi \int_0^1 (I_0 + \mu I_1)\mu \, d\mu \equiv \pi\left[I_0(\tau) + \tfrac{2}{3} I_1(\tau)\right] \tag{3-39}$$

This process was performed at 1 nm resolution between 180 and 400 nm, giving the diffuse flux at the surface. The delta-Eddington approximation is particularly useful in climate modelling studies due to its applicability to a wide range of situations (in terms of atmospheric scatterers) along with its relative simplicity and computational speed. However, its applicability must be justified before the process can be implemented in any form of investigation.

The validity of the delta-Eddington approximation was investigated by Joseph *et al.* (1976), and the ranges of applicability of this approximation are shown in Table 3-2. These values are well within parameters encountered on Mars, for all atmospheric species. The only exception to this situation is the case at extreme solar zenith angles when the Sun is grazing the horizon, *i.e.* cos *SZA* < 0.1. In these cases, any results should be treated with care since the forward truncation reduces the observed intensity. More recently the radiative transfer code has been validated against a standard reference doubling-adding multiple scattering code (Stephens *et al.* 2001). The delta-Eddington radiative transfer code is commonly used to model accurately the transfer of UV through the terrestrial atmosphere, in both standard climate models (e.g. Briegleb 1992) and independent investigations (e.g. Carlson and Caverly 1977; Scourfield and Bodeker 2000) and is used here as a valid radiative transfer code for the martian atmosphere.

Parameter	Tested Valid Range
g'	0 – 0.95
τ'	0.01 – 100
ω'	0.1 – 0.99
cos *SZA*	0.1 – 1.0

Table 3-2: Tested range of validity of the delta-Eddington approximation (Joseph *et al.* 1976).

3.4.3 Calculation of Direct Flux

In addition to the diffuse flux created by the scattering effect of the atmospheric aerosols, the direct solar UV must also be accounted for. In optically thin atmospheres, this component forms the majority of the surface irradiance. The Beer-Lambert law was used to calculate the attenuation of the direct field, which increases as an exponential function of the observed optical depth of the total atmosphere. The direct flux (F_{direct}) is given by:

$$F_{direct}(\lambda) = F_0 e^{-\frac{\tau_{tot}(\lambda)}{\mu_0}} \equiv F_0 e^{-\frac{(\tau_{gs}(\lambda)+\tau_{ga}(\lambda)+\tau_{back}(\lambda))}{\mu_0}} \tag{3-40}$$

As before, the optical depth of the complete composite atmosphere is required, which in turn is equal to the sum of each individual gaseous species' scattering and absorption optical depth and the total aerosol optical depth. This process was also performed at 1 nm resolution and calculated at each layer interval. F_{direct} was then summed with $F_{diffuse}$ to give the total UV flux at the surface between 180 and 400 nm from the entire sky (2π steradians).

A typical output from the model is shown in Figure 3-13 showing direct, diffuse and total surface fluxes for the case of local noon at the equator at $L_s = 0°$, using the nominal dust scenario. An important point in this spectrum which is always observed in all modelled martian surface UV spectra is the distinct cut off seen around 190 nm. This effect is caused

by the sudden increase in the absorption cross-section of CO_2 at this wavelength, which coupled with its large abundance in the martian atmosphere creates the characteristic cut off in all observed martian surface UV spectra. Above 200 nm the CO_2 absorption cross-section becomes indistinguishable from the Rayleigh scattering cross-section, and only molecular scattering is observed. The contribution of the direct and diffuse components to the total UV flux is also shown in Figure 3-13.

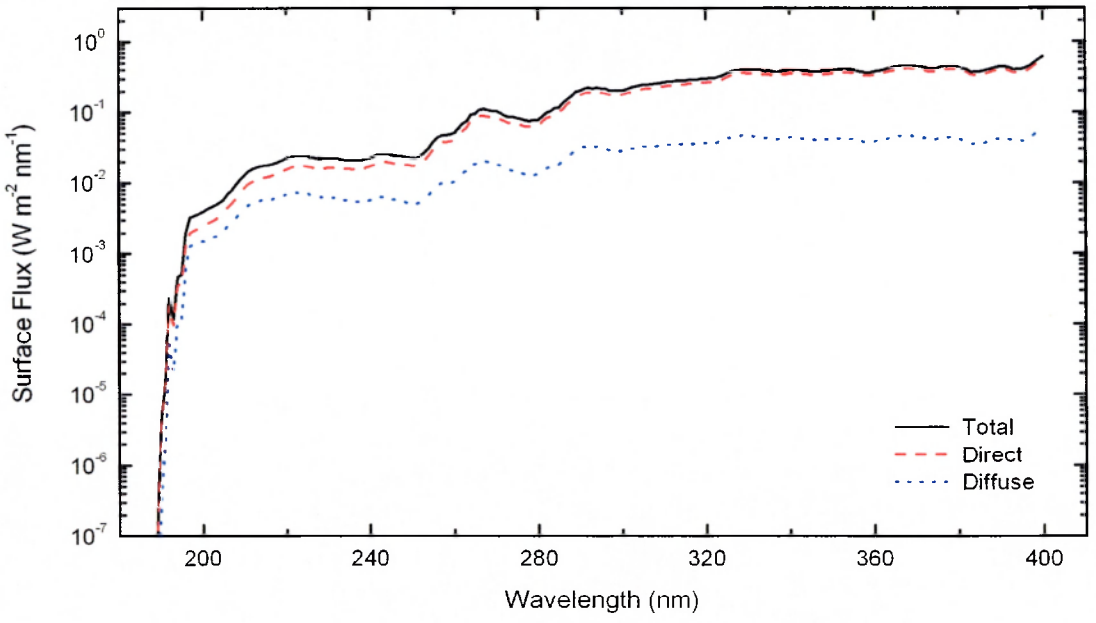

Figure 3-13: Nominal martian surface UV spectrum.

The majority of the flux takes the form of direct non-scattered UV, with the diffuse component contributing to a lesser degree. This is consistent with a relatively clear atmosphere, but in the case of Mars the persistence of dust in the atmosphere amplifies the diffuse flux. Towards shorter wavelengths near 240 nm, the diffuse component increases in relative proportion to the direct flux, as scattering effects become more predominant and the direct flux diminishes.

3.5 Model Dependence on Dust Optical Properties

The uncertainty in the optical properties of martian aerosols in the UV cannot be stressed enough. Here the variation in the model output is investigated as a function of the optical properties used, in an attempt to understand better the dependence of surface spectra on assumed aerosol properties. As shown previously, ω_{bd} and g_{bd} show variation in the published values, in some cases being more/less absorbing, and more/less forward scattering.

In order to assess the dependence of the derived spectra upon the single scattering properties, both ω_{bd} and g_{bd} are varied both independently and in combination, and the effects upon the surface diffuse spectrum are discussed. All cases are taken for local noon at $L_s = 0°$ at the equator ($lat = 0°$N), using the nominal dust scenario. The only alternative complete set of optical parameters in the UV is that calculated by Zurek (1978). Again these published parameters were incorporated into the model using spline interpolation between data points. The diffuse surface spectra derived using the values of Zurek (1978) are shown in comparison to the nominal diffuse irradiance (*i.e.* data from Ockert-Bell *et al.* 1997), in Figure 3-14.

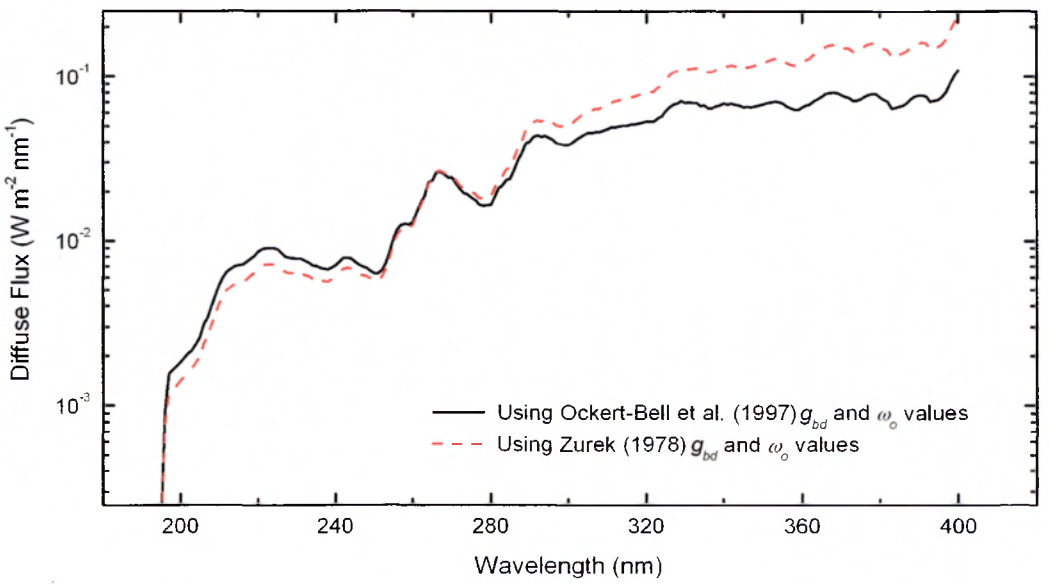

Figure 3-14: Comparison of diffuse flux using alternative optical properties.

The distinct difference in the optical properties of Zurek (1978) to the nominal optical properties manifests in the diffuse surface spectrum. At short wavelengths ω_{bd} is far lower in the data of Zurek (1978), and at long wavelengths it is greater, implying a more absorbing dust particle at short wavelengths and a less absorbing particle at longer wavelengths. This implication is evident in Figure 3-14, where the alternative optical properties underestimate the flux between 200 and 250 nm, and overestimate between 270 and 400 nm. Using the two sets of data, the effect of choice of parameters is evidently important on both the shape and magnitude of the resulting diffuse spectrum.

The individual and combined effects of variations in ω_{bd} and g_{bd} were also investigated in terms of relative effect. Both parameters were varied by up to -30% and +20% from the values of Ockert-Bell *et al.* (1997), and the effects upon the diffuse spectra were calculated. The variation of the diffuse spectrum while ω_{bd} is varied and g_{bd} is kept constant is shown in Figure 3-15.

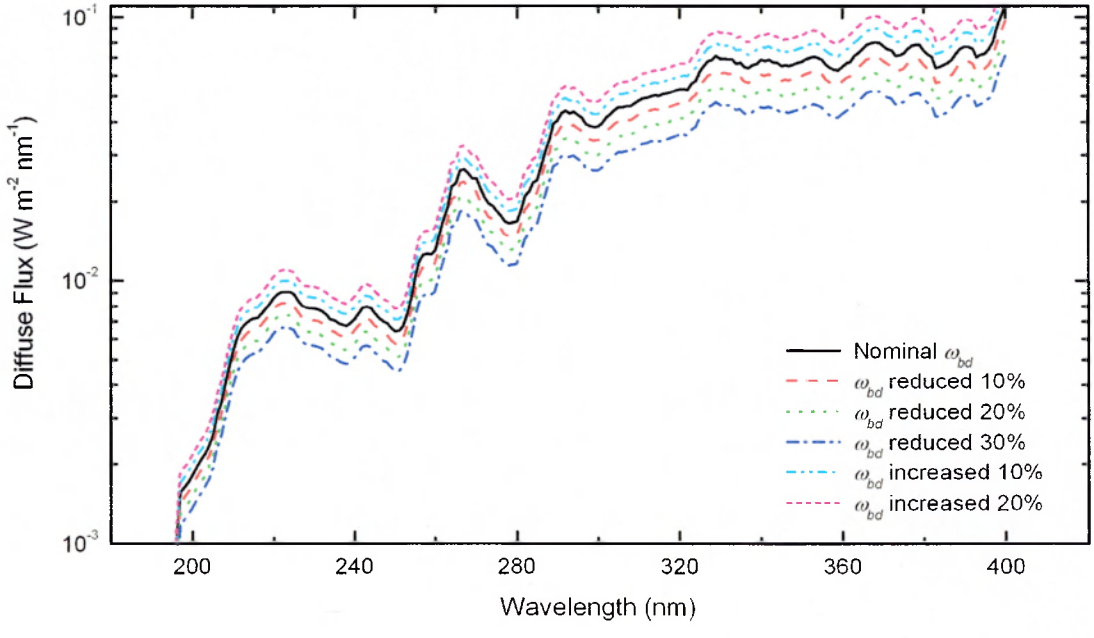

Figure 3-15: Effect of the variation of ω_{bd} on diffuse spectrum.

As ω_{bd} reduces, the diffuse flux experienced at the surface is also found to reduce. As stated previously, this effect is due to the increased absorption properties associated with lower ω_{bd} values, as more UV is absorbed by the dust particles. An increase in the value of ω_{bd} has the opposite effect, with a corresponding increase in diffuse UV flux experienced at the surface. As expected, this effect is due to the reduced absorptive properties implied by a ω_{bd} value closer to 1, so less UV flux is absorbed and more is scattered in the form of diffuse flux.

The corresponding variation of g_{bd} whilst ω_{bd} is kept constant is shown in Figure 3-16. The opposite effect is observed here, with the surface diffuse irradiance increasing (decreasing) as the value of g_{bd} is reduced (increased). This arises due to the nature of the creation of the diffuse spectra. Since g_{bd} is a measure of the 'forward scattering' nature of the aerosol in question, as g_{bd} increases the irradiance at each scattering event is directed in a more forward direction. Thus the irradiance per scattering event contributes less to the diffuse irradiance, as it becomes relatively less and less re-directed, remaining on its original path direction.

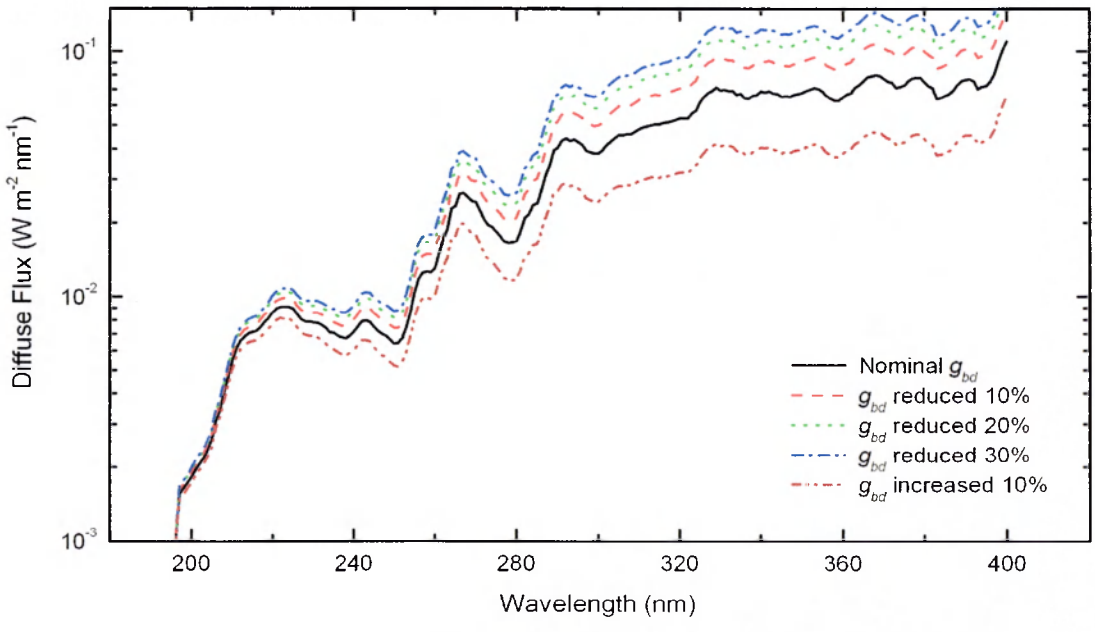

Figure 3-16: Effect of the variation of g_{bd} on the diffuse spectrum.

Conversely, as g_{bd} is reduced, the degree of forward scattering is reduced and the scatter direction per scattering event becomes more isotropic in direction. This in turn creates a greater contribution to the diffuse irradiance, as more radiation is effectively being scattered in a wider average spread of directions.

The effect of the variation of both ω_{bd} and g_{bd} is shown in Figure 3-17. An interesting point revealed here is the insensitivity to the *degree* of combined decrease of ω_{bd} and g_{bd}. A deviation is observed for a 10% decrease, above 290 nm. The effect of further decreases to 20% and 30% however are indistinguishable from the 10% decrease. The reported values from Wolff *et al.* (1997) for ω_{bd} are a maximum of 20% lower than those of Ockert-Bell *et al.* (1997). Assuming that their value for g_{bd} is also 20% lower, the resultant effect is an increase of 20% in the diffuse irradiance above 290 nm.

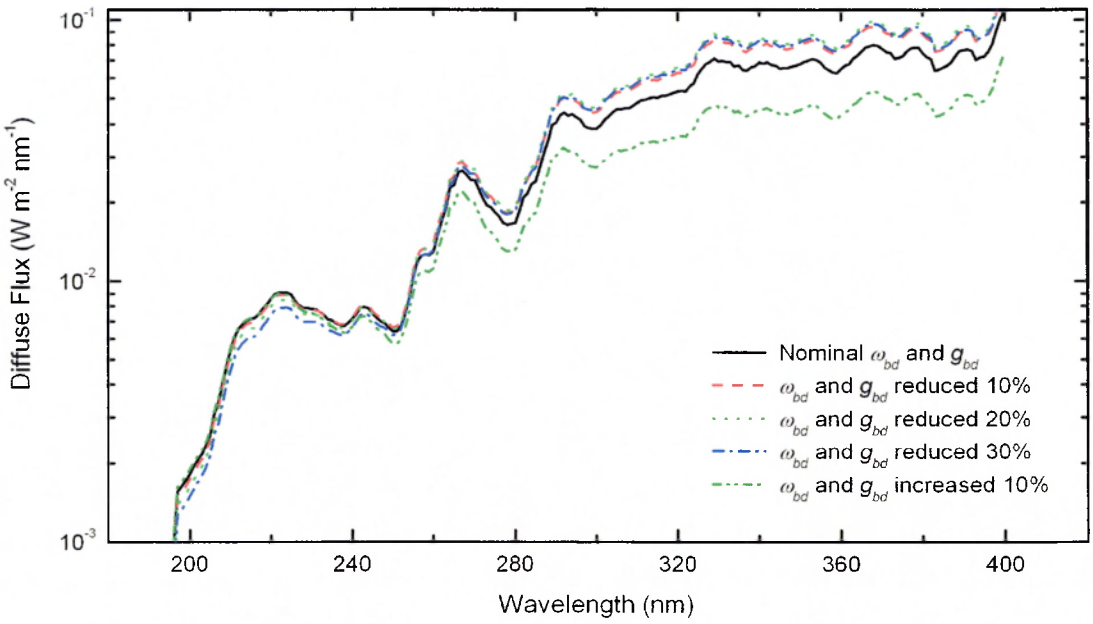

Figure 3-17: Effect of the variation of both ω_{bd} and g_{bd} on the diffuse spectrum.

Analysis of Figures 3-15 to 3-17 highlights the importance that when considering any data presented here regarding diffuse spectra, it should always be noted that the true nature of the UV optical parameters of martian dust remains highly debated, and results should always

be treated with care. Future investigations by *in situ* instrumentation will help constrain values of ω_{bd} and g_{bd}, through the iterative fitting of optical parameters to match observed diffuse spectra. The Beagle 2 UV sensor will provide the first ever measurement of this kind to aid in the problem of the UV optical properties of martian dust, and the details of this instrument are described in the following chapter.

Chapter Four

The Beagle 2 UV Sensor

The chance to both design and build a spaceflight instrument for use on Mars offered a unique opportunity to combine theoretical and instrumentation expertise into a single piece of work. At the time of issue, the opportunity to build the ESS instrument package was open to a wide range of possibilities. After careful review and examination the package was optimised, offering the maximum science return in the range of the appropriate fields of interest (Towner *et al.* 2003). The UV sensor offered delivery of a hitherto unmeasured value from the martian surface of astrobiological and chemical relevance, and formed the context of this study over the Ph.D.

The brief for such an instrument was to measure the UV flux *in situ* at the martian surface, at wavelengths between 200 and 400 nm. A range of methods for the detection of UV were available, but a number of factors needed to be considered during the design phase to provide the optimum scientific return within the available parameters. As with the general ESS philosophy, the focus was towards the utilisation of miniaturised commercially available products, which could be utilised for planetary exploration. In this chapter, the methods and philosophy of design and testing/calibration of the UV sensor are covered.

4.1 Methods of UV Detection

Methods for the detection of UV light can be broadly classed into three areas – chemical detectors, biological detectors and physical detectors. Chemical detectors work on the quantitative detection of reaction products from photochemical reactions, or the measurement of change in optical density or colour due to a photolytic reaction. Biological detectors function through the measurement of the inactivation of bacterial spores, which give an indication of the UV dose. In this study however we are only concerned with physical detectors.

A range of physical detectors exist for the measurement of UV light. Physical detectors may be divided in to two further sub-classes, namely non-wavelength and wavelength dependent detectors. Examples of non-wavelength dependent detectors[1] are bolometers and thermopiles (which both function on the process of the heating effect of the radiation) and radiometers (which depend on the deflection of a very light vane suspended by a thin fibre). For planetary exploration, wavelength-dependent devices are preferred, for detailed spectroscopic studies. The leading methods for this type of detector include spectrometers, photomultiplier tubes (PMT) and photodiodes.

Spectrometers can offer extremely high resolution data regarding the UV spectrum through the use of high precision optics. The standard minimum setup involves collimating mirrors, a diffraction grating and a charge coupled device (CCD), all precisely arranged in an optical bench. Incident UV enters the bench, and is focussed into a collimated beam. The beam then encounters a diffraction grating, which spreads the light as a function of wavelength onto a CCD via another collimating mirror. Each element of the CCD is then read, and the intensity of incident photons as a function of wavelength (related to the CCD

[1] Non wavelength-dependent detectors are generally used for applications involving extremely low fluxes.

element) is measured. This technique allows complete spectra to be recorded at high resolution, depending on the choice of grating and CCD.

PMT devices use the photoemissive effect where the absorption of a photon by a sample of material results in the ejection of an electron. The electron is then accelerated by electric or magnetic fields into an amplifier where the electron is detected. Such devices are extremely sensitive, capable of single photon detection under the right circumstances. The principle of operation is based upon the cascade effect of electron generation. The input photon is absorbed at the input cathode, which is typically held at a potential of around 1 kV lower than the anode. The electron liberated is then accelerated and focussed by electric fields until they strike a dynode. The surface of this dynode is made of material which liberates a number of electrons when struck by a single high-energy electron. These secondary electrons are then accelerated into the surface of another dynode, where the process is repeated along a chain of dynodes until the electrons are collected at the anode.

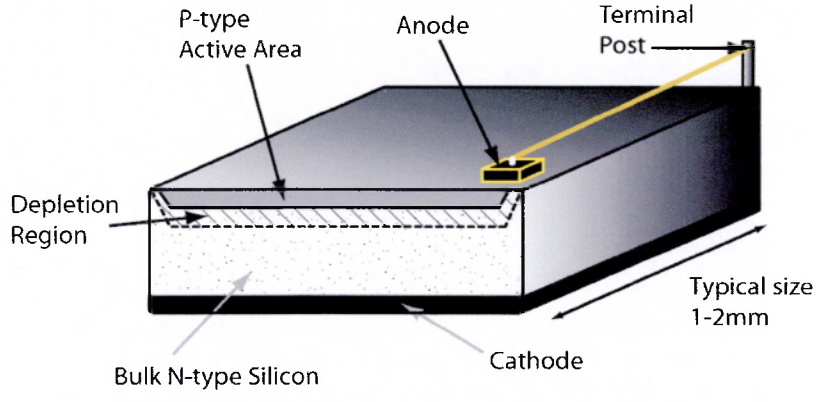

Figure 4-1: A typical photodiode chip cross-section.

Photodiodes are based on semiconductor technology, the most common of which are silicon photodiodes. The photodiode construction shown in Figure 4-1 consists of a small (mm scale) square silicon based element, based on a standard p-n junction design. Silicon forms the base ("n" material) of the box shaped element which acts as the cathode (typically 1

to 4 mm^2 and 1 to 2 mm high) with a thin ("p" material) layer on the top surface which acts as the anode. The interface between these two material is the p-n junction. The region at this interface is called the depletion region, as the silicon becomes depleted of electrical charge. Light which is absorbed in the active area creates an electron-hole pair. The electron and hole become separated, with the electron moving towards the 'n' region and the hole towards the 'p' region. This separation of electrons and holes is known as the photovoltaic effect, and creates a current as a direct consequence of the absorption of light in the active area.

4.2 Design Constraints

4.2.1 Mass, Power and Wavelength Requirements

All space missions impose strict constraints on the component hardware, but for the case of the Beagle 2 mission, extreme constraints were required. Beagle 2 has the highest scientific payload mass to overall mass ratio of any planetary mission in history, achieved by strict mass constraints. The implication for ESS was extreme miniaturisation of instrumentation, with strict limits which were imposed from the onset of the design phase. The total mass budget for all the ESS sensors combined was 180 g, and being one of seven sub-systems the mass of the UV sensor was confined to a maximum of 25 g. This mass was used as part of the selection process, to evaluate at an early stage what would be feasible and what could be disregarded.

In addition to the mass constraint, the power and energy requirements of the sensor in question were constrained. Power hungry devices could not be considered, since the available power budget for ESS was initially set as approximately 200 mW for the entire suite. Thus the UV sensor was restricted to a small part of this budget, ideally to be kept below 30 mW to allow a fair division of power to the other instruments.

Investigations into martian UV at the time of design indicated a surface UV spectrum extending down to wavelengths as short as 200 nm (Kuhn and Atreya 1979; Catling *et al.* 1999). Thus the aim of the sensor was to monitor UV wavelengths from the edge of the UV at 400 nm to at least near 200 nm, either as a complete spectrum or focussing on specific areas of interests dependent upon technical feasibility. The footprint area designated for the UV sensor at the mission design phase is shown in Figure 4-2.

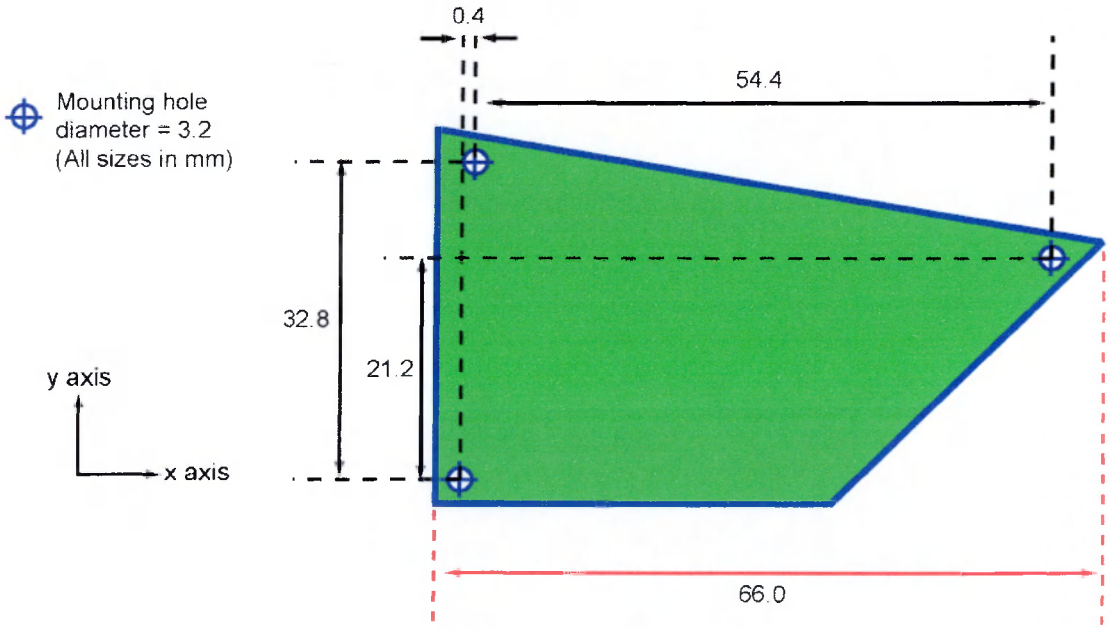

Figure 4-2: Footprint of the UV sensor.

The maximum length of the sensor is only 66 mm, and the total surface area is 20.1 cm^2. The footprint defines the printed circuit board (PCB) size, on which the sensor heads and front-end electronics must be accommodated. The area given was irregularly shaped since the UV sensor had to fit on a small plate mounted on one of the three struts in Beagle 2 next to where the PAW is stowed. The general location within the lander base is indicated in Figure 4-3.

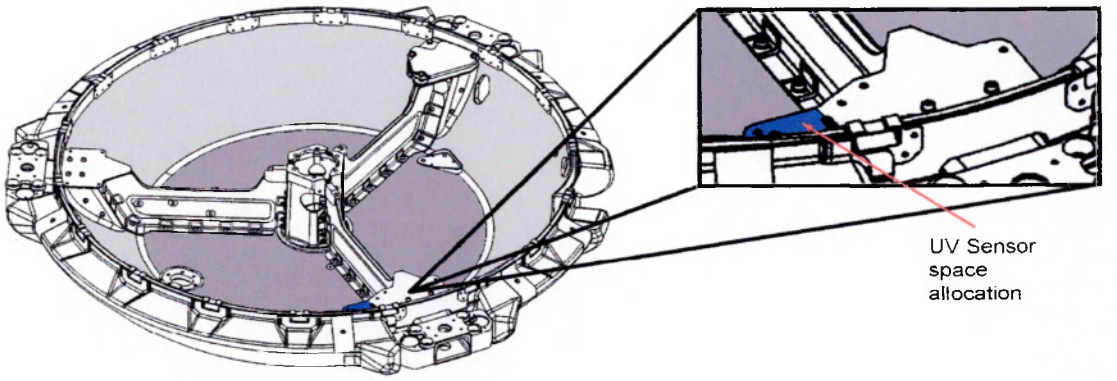

Figure 4-3: Sensor area allocation within Beagle 2.

4.2.2 Environmental Survivability

The environment of Mars, though the most similar to that of Earth in the solar system, presents a host of challenging environmental dangers which need to be considered when designing an instrument for long term operation. In addition, throughout the cruise phase *en route* to Mars long term exposure to vacuum, low temperatures and high radiation doses will have to be endured. The surface temperatures on Mars exhibit a wide range of variations. VL2 measurements revealed a 75 K diurnal variation in surface temperature, ranging from 180 K during the night to 240 K just after midday (Hess *et al.* 1977). Such large temperature variations are typical of the martian environment, and any instrumentation must have the capability to function after and sometimes during such temperature variations. In the case of Beagle 2, thermal modelling of the worst case diurnal temperature extremes for the location of the UV sensor *within* the lander structure are given in Table 4-1 (Peskett 2001).

L_s	UV sensor location temperature (K)	
	Minimum	Maximum
322°	207	290
53°	200	267

Table 4-1: Min. and max. temperature values for the location of the UV sensor on Beagle 2 from thermal modelling – L_s = 322° and 53° correspond to beginning and end of mission respectively.

These values vary between beginning and end of mission not only as a result of the change in season (and thus insolation), but also due to the anticipated degradation of thermal control systems on Beagle 2 over the mission. Any instrumentation for ESS would thus need to survive this temperature cycling over the 180 sol nominal mission. In terms of powered operation, the UV sensor will gather data throughout the entire day, and as such design requirements necessitate the ability to operate at temperatures as low as 200 K.

An important environmental constraint will also be in the form of radiation exposure. Though no *in situ* measurements have yet been taken of the ionising particle radiation environment at the martian surface, the ionising radiation dose encountered will be far higher than on Earth due to the thin martian atmosphere, which provides minimal shielding from high energy particles (e.g. Simonsen *et al.* 1990). The lander will however experience a substantial part of the total mission radiation dose *en route* to Mars, since the spacecraft must spend an extended period of time (~6 months) in interplanetary cruise, where no protection from galactic and solar radiation is available. Optical instruments are extremely susceptible to ionising radiation, since high energy protons and alpha particles can often interact with the charge-sensitive elements of the detectors, and also cause darkening of optical filters with significant doses. For the Beagle 2 mission, a total ionising radiation dose of 50 Gy over the mission duration was set as the nominal dose to which each instrument would be exposed.

The low pressure of the martian environment is also an important issue. The pressure at the landing site is expected to be around 7.5 hPa, and any instrumentation must be robust enough to function for an extended period at this pressure. In addition to this, Beagle 2 will endure a 6 month period during cruise exposed to space-vacuum conditions. During this time the ESS sensors will be inactive, but must nevertheless be resilient to vacuum conditions.

Dust in the atmosphere of Mars also presents a risk to instrumentation. Fine grain (sub-μm) particles are ubiquitous in the martian atmosphere, with a constant settling out of dust upon surfaces. This settling layer of dust is one of the limiting factors of lander lifetimes,

since the obscuring build up of dust inhibits the collection of solar energy from the solar panel arrays, effectively killing the lander in terms of power. Such particles can also penetrate into mechanical joints, and act as an abrasive during high wind conditions.

4.2.3 Selection Of Detector Type

All of the above considerations were taken into account during the selection process. In terms of priority, mass and size took precedence. From this standpoint, the use of spectrometers was dismissed. At present, the smallest miniaturised spectrometers available have a total mass of around 200 g, which far exceeds the mass budget for the UV sensor. Spectrometers also utilise an optical bench setup, where the incident light is dispersed by a diffraction grating. This type of setup requires a physical area for the optical bench alone greater than the entire footprint allocation for the UV sensor, and thus could not be accommodated.

Photomultipliers and photodiodes are far smaller in both mass and size, since they do not require a complex optical setup. Photodiodes provide the smallest detectors, with active areas smaller than 1 mm^2. Photomultipliers are slightly larger, currently with typical sizes of around 10 mm diameter for the miniature units, and also have a larger mass. PMT devices also require extra mass for a high voltage supply (typically around 1 kV generated from the 24 V bus voltage), and consequently the power demands are higher than with the case of photodiodes.

The choice of photodiodes was inevitable given such stringent mass, power and size constraints. Photodiodes offered the greatest coverage of the UV region, since more channels could be accommodated in the small footprint available whilst keeping mass and power budgets to a minimum level, and were chosen as the preferred sensor head for the instrument.

4.3 Sensor Refinement

4.3.1 Wavelength Regions of Interest

After selecting photodiodes as the sensing element, the spectral regions of interest to be measured at the martian surface were investigated using the radiative transfer model described in Chapter Three. A typical martian UV spectrum, for the case of $L_s = 0°$ at the equator (0°N) at local noon, is shown in Figure 4-4.

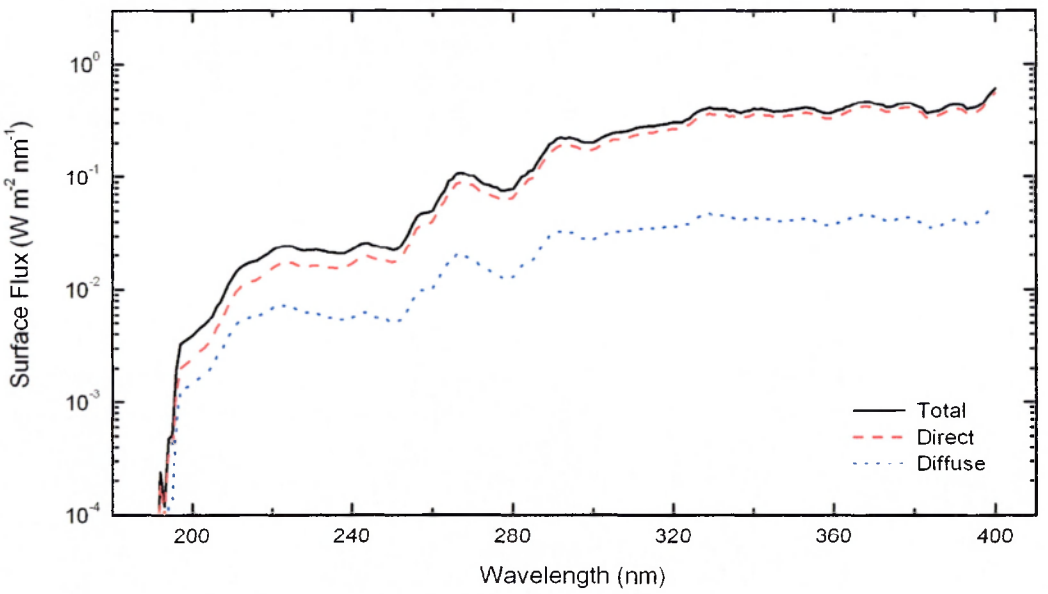

Figure 4-4: Typical martian UV surface spectrum.

The spectral characteristics of martian surface spectra can be split into two regimes: 280-400 nm, and < 280 nm. Between 280 and 400 nm (the UV-A and UV-B regions) the spectrum is relatively invariant, with a plateau-like shape. Below 280 nm the spectrum fluctuates to a greater degree, until near 200 nm the CO_2 cut-off is encountered. Six sensor output channels were available for the UV sensor unit (due to limitations of the PCB area accommodating all sensor heads and front-end electronics). With this configuration, concentrating more narrow wavelength channels in the more varying UV-C region gave the

optimum spectral coverage within the constraints. Three narrowband channels were chosen below 280 nm, centred at 250, 235 and 210 nm. 250 nm was chosen since this wavelength is near the centre of the O_3 absorption band, which is covered in Chapter Five and shown in Figure 5-8. 210 nm is close to the edge of the CO_2 cut-off, and chosen due to the possible presence of the TiO_2 absorption band in martian atmospheric dust, as proposed by Pang and Ajello (1977), and 235 nm was used as an intermediate value. For the plateau region, two broadband channels were chosen to monitor the region, centred at 350 nm and 300 nm. A sixth unfiltered 'open' channel covering the full UV range was chosen as the final channel.

4.3.2 Electronics

All the ESS sub-systems incorporate unique front-end electronics to amplify and condition the output from the sensor heads, which are then read by the lander common electronics processor (CEP). Since photodiode units were used for the UV sensor, two stages in the front-end electronics from the sensor head output signal were required. Photodiodes are current-output devices, and consequently the first stage of signal conditioning required the use of a charge-sensitive amplifier to convert and amplify the current output of the photodiode to a voltage signal. The circuit diagram for a single channel is shown in Figure 4-5.

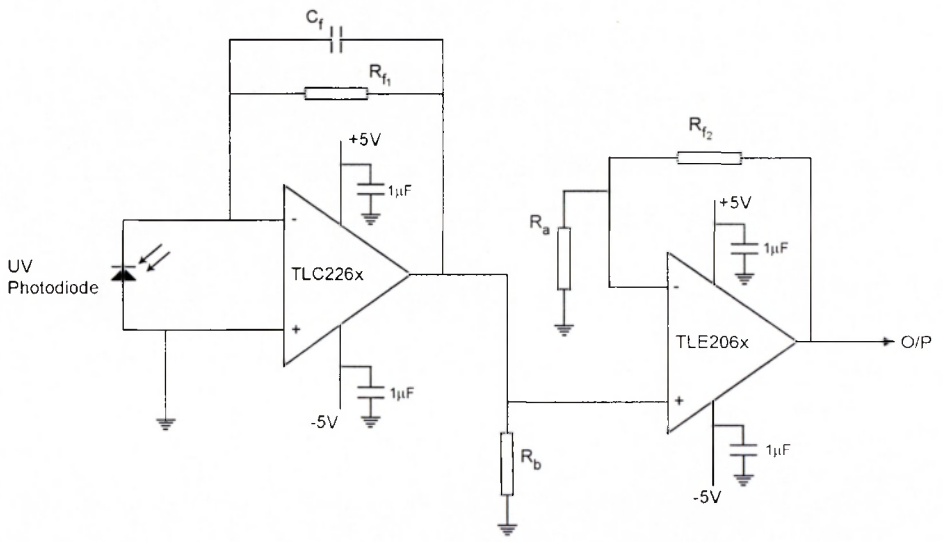

Figure 4-5: Single channel UV circuit diagram.

Careful design of this stage was required, since in two-stage amplification processes, the signal-to-noise ratio (S/N) is dictated by the first stage. The second stage consisted of a standard non-inverting amplifier, amplifying the voltage signal from the first stage to a level compatible with the dynamic range of the CEP (0-3.5 V). This philosophy was implemented for each of the six channels available for the UV sensor.

Various operational amplifiers (op-amps) were available for use for each stage of the front-end electronics. Mass saving was achieved by the use of quadruple (quad) and dual op-amps, where a dual (quad) op-amp consists of a single integrated circuit (IC) chip capable of processing two (four) channels simultaneously, removing the requirement of separate op-amps for each channel.

The conversion of input current to output voltage in the first stage of the circuit in Figure 4-5 is dictated by the feedback capacitor C_f. The voltage output (V_{out}) from a charge sensitive amplifier is directly proportional to the charge (q) flowing into the input (and thus the current (I_{in}) for a period of time (t_{in})), and inversely proportional to C_f:

$$V_{out} = \frac{q}{C_f} \equiv \frac{I_{in}}{C_f} \quad for \ t_{in} = 1 \tag{4-1}$$

The time constant (T_c) of the circuit (*i.e.* the rate at which the charge is discharged from the op-amp) is given by the product of the feedback resistor (R_{f1}) with the feedback capacitor (C_f). T_c was set through choice of R_{f1} for each channel at 0.25 s since the maximum sampling rate for ESS is 4 Hz.

The second stage consists of a standard non-inverting amplifier to boost the signal to levels readable by the CEP. The gain of such an op-amp (G_{op}) is varied by the choice of feedback resistor R_{f2}, and given by:

$$G_{op} = \frac{R_a + R_{f2}}{R_a} \tag{4-2}$$

For the first stage charge sensitive amplifier, a quad TLC2264 and a dual TLC2262 advanced LinCMOS™ op-amp were used, and for the second voltage amplification stage a quad TLE2064 and a dual TLE2062 micro-power op-amp were used. The choice of op-amps was driven largely by noise level and power consumption, but also by availability in MIL-SPEC ceramic dual in-line packaging (DIP) which is rated to operate safely to temperatures as low as -55°C and be vacuum compatible. The TLC226x series requires very little operating current rated at a maximum of 250 μA per channel, and for the TLE206x series the maximum supply current is 320 μA per channel.

Due to the space limitations of the footprint for the sensor, the electronic components were distributed to both sides of the PCB and grouped extremely close together. This resulted in great difficultly during the process of soldering components onto the PCB, but could not be avoided. A 50 μm thick conformal coating of Parylene-C[1] was then applied to the sensor after completion, to protect the PCB and sensor heads (excluding the diode viewing window) within a polymer coating. This process provides a physical, thermal and electrical barrier around all the sensor heads and electronic components, providing extra integrity beneath surface mount devices and more resistance to solder joint breakdown after extended thermal cycling.

4.4 Component Specifications

4.4.1 SiC Photodiodes

Silicon Carbide (SiC) photodiodes are a relatively new technology supplied by Laser Components UK[2], resulting in a significant improvement in UV detection capabilities. This

[1] Parylene-C belongs to the polymer group of poly-para-xylene.

[2] Laser Components UK, Goldlay House, 114 Parkway, Chelmsford, Essex, CM2 7PR, U.K.

type of detector was deemed the most suitable for use on a planetary mission for a number of reasons. An important advantage of SiC photodiodes is that they are effectively blind to solar radiation at wavelengths longer than 400 nm due to the wide band gap of 3 eV. Solid-state UV detectors are typically made of silicon, which has a narrow band gap of 1.1 eV, narrow enough to allow electron stimulation by both visible and ultraviolet light. Visible light is not energetic enough to traverse the band gap in SiC and is therefore not detected, removing the need for long wavelength cut-off filters to isolate the detection of UV. The detection regime of SiC detectors also matches exactly the UV environment of Mars, with a detection range from 200 to 400 nm. The penetration depth of UV into SiC is also larger by two orders of magnitude when compared to silicon, making the absorption of light in the detection region more uniform, minimising surface processes and resulting in a superior long term stability.

The noise levels of SiC detectors are also extremely low. Photodiode 'noise' is expressed in terms of dark current, *i.e.* the output current measured from the photodiode under zero illumination conditions. Typical values of silicon photodiode dark currents are on the order of 10 pA, whereas for SiC diodes the dark current is rated at approximately 2 fA, almost three orders of magnitude lower than that of other standard detectors. Dark current also decreases with decreasing temperature, and is therefore expected to be lower than this value when operated in the martian thermal environment. SiC detectors are also insensitive to ionising radiation, with no effects observed over long duration exposure to radiation. This insensitivity to radiation makes SiC ideal for cruise phase to Mars and also long term deployment on the martian surface (Neudeck 2001).

4.4.2 Filter Specifications

The SiC diodes monitor the UV region over the entire 200-400 nm region, and the main aim of the design phase was to adapt these sensor heads to monitor selectively specific regions within this regime. This was achieved through the use of bandpass filters, to allow

only specified parts of the UV spectrum into the sensing area. As mentioned, two wide band filters above 280 nm were used, along with three narrow band filters at shorter wavelength. The wide band filters were commercially available devices, with centre wavelengths (CWL) at 300 nm and 350 nm. The filter characteristics for each channel are shown in Table 4-2.

CWL (nm)	FWHM (nm)
210	16
233.7	11
250.5	18
300	30
350	72

Table 4-2: UV filter characteristics.

FWHM is the Full Width Half Maximum of the filter transmission profile, defining the width of the bandpass. The filters used for the < 280 nm channels were custom-built by Barr Associates Inc.[1]. Narrow band filters were used since more variation is seen in this part of the martian UV spectrum, with the initial aim of keeping the maximum bandwidth of these filters below 20 nm. The end product filter bandwidth was determined by the manufacturing process which set limits on the final filter characteristics shown in Table 4-2. The substrate material used for all the filters was fused silica (silicon dioxide), which is a standard synthetic UV transmitting material produced from $SiCl_4$, commonly used in optics due to its efficient transmittive properties over broad wavelength regions (170 nm to 2.5 μm). For the 235 nm and 250 nm filters, non-metallic filter depositions were used on the substrate, namely hafnium dioxide (HfO_2) and silicon dioxide (SiO_2) which offered good transmission and blocking properties in the spectral regions of interest for these filters.

[1] Barr Associates Inc., 2 Lyberty Way, Westford, MA 01886 U.S.A.

The only difficulty encountered during manufacture of the filters occurred with the 210 nm filter. Substantial problems occurred trying to construct a bandpass filter with good transmission properties near 200 nm with sufficient blocking properties near 400 nm. For this filter, aluminium oxide (Al_2O_3), silicon dioxide (SiO_2) and aluminium (Al) depositions were used to construct the 210 nm bandpass filter. The use of metal-dielectrics as part of the filter was a significant compromise. Non-metallic-dielectric filters are more stable after prolonged UV exposure. Metal-dielectric filters however degrade significantly after prolonged UV dose, with 'darkening' occurring in the filter. This effect is a loss of transmission in the filters, resulting in significant opaqueness after extended UV dose. This problem however could not be avoided since the required filter spectral characteristics could not be achieved using non-metallic-dielectric depositions.

For this reason a sixth, unfiltered channel was incorporated into the sensor, which will also give the total UV flux across the 190-400 nm region. Over time, the individual filter performances are expected to degrade by varying degrees, and the unfiltered channel (which will be relatively insensitive to prolonged UV dose) will give an indication of how severe the darkening effect is.

Figure 4-6 shows the transmission properties of the filters used in each of the filtered channels. The 300 nm and 350 nm filters are commercial products, offering extremely high transmission properties and a well defined shape. The 350 nm filter is a simple long pass filter – long wavelength blocking is not required, since the diode response falls to zero above 400 nm. The spread of the transmission profiles can be seen, adequately covering the region below 260 nm.

The high spectral quality of the 235 and 250 nm filters is evident, with high peak transmission and steep bandpass gradients. The difficulties encountered during manufacture of the 210 nm filter are apparent – the peak transmission of around 10% was the best achieved, and the bandpass is not as well defined as in the 235 and 250 nm cases.

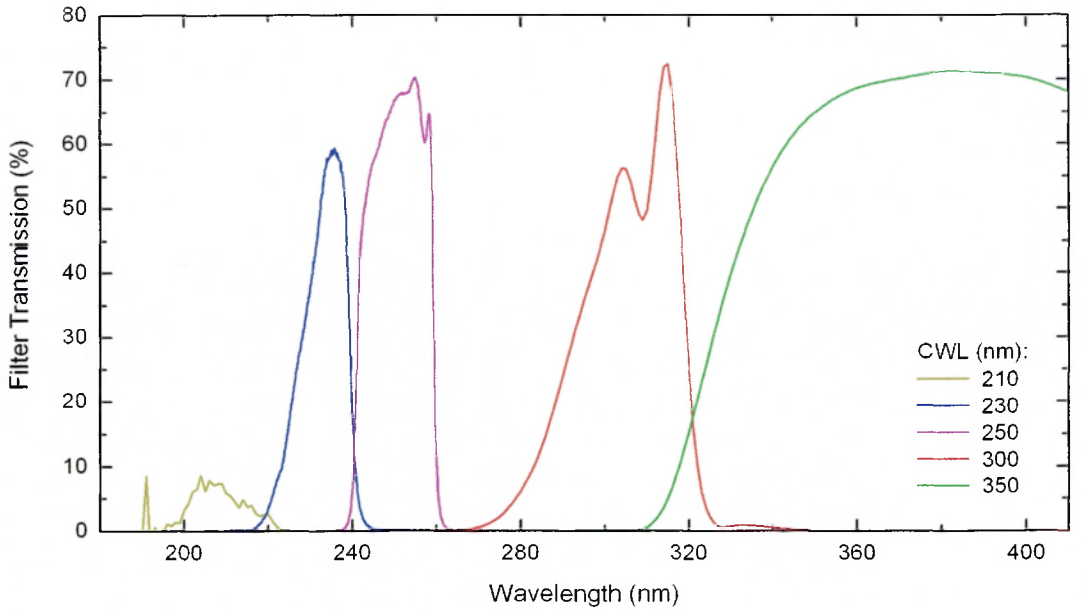

Figure 4-6: Filter transmission curves.

In addition to the transmission properties of the filters, the out-of-band blocking characteristics of the filters was also of paramount importance. At short wavelengths especially, the UV flux at longer wavelengths can be as much as an order of magnitude higher, so even a small leakage at long wavelengths could distort the signal. To gauge the out-of-band blocking characteristics of the filters, optical density is used. Optical density is related to the transmittance T_r by:

$$Optical\ Density = \log_{10}\left(\frac{1}{T_r}\right) \tag{4-3}$$

The optical density as a function of wavelength between 200 and 400 nm for each custom built filter is shown in Figure 4-7. The out-of-band blocking for the 250 and 235 nm filters is extremely good, with optical densities of at least 5 ($T_r < 0.006\%$) outside of the bandpass. The 210 nm filter optical density is less smooth in the bandpass region, but still offers adequate out-of-band optical densities of at least 3.5 ($T_r < 0.03\%$).

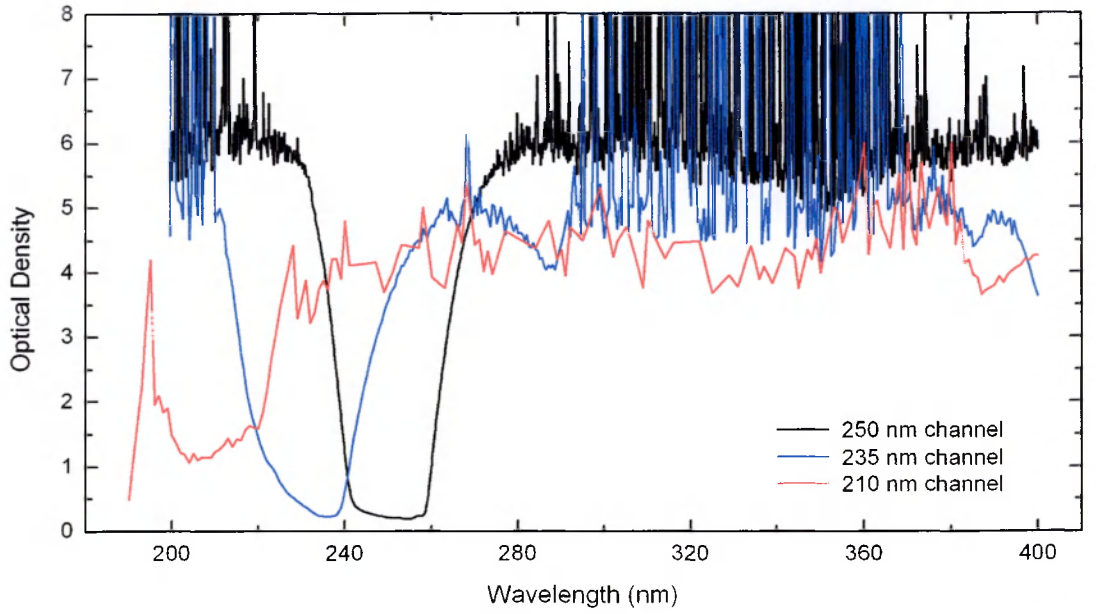

Figure 4-7: Out-of-band blocking for the 210, 235 and 250 nm filters.

4.4.3 Diode Assembly and Field of View

Six photodiode sensor heads were used on the PCB footprint. The SiC diodes were hermetically sealed within industry standard transistor cans. TO-5 cans were used for the filtered channels, with space limitations forcing the use of a smaller TO-18 can for the open channel. The dimensions of the two types of can housing are shown in Figure 4-8.

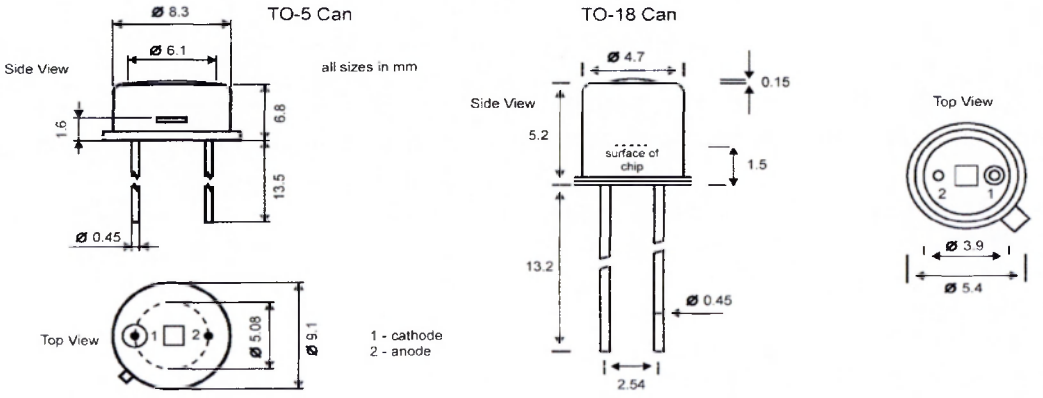

Figure 4-8: Schematic of the photodiode housing.

The photodiode chip resides at the base of the can, which is hermetically sealed with dry N_2 at 1000 hPa, and vacuum tested to ensure survivability. In this arrangement the TO-5 cans have a half angle field of view (FOV) of 30°, and the TO-18 can (open channel only) has a half angle FOV of 27°. The restricted field of view was unavoidable – ideally a sensor would measure the flux from the whole sky, but the mass limitations would not permit this. This constraint presents a possible problem for the UV sensor, since Beagle 2 is not guaranteed a horizontal resting position. If the lander comes to rest in a rocky area, there is a possibility that the base of the lander (and thus the FOV of the UV sensor) will be pointing away from zenith.

This FOV problem may affect the chances of observing some of the phenomena described in this thesis which depend on direct flux observation, such as diurnal variations, total dose (Chapter Five) and cloud observations (Chapter Six). Without measurements of the direct component, the peak dose levels cannot be measured, and the diffuse/direct ratio cannot be found. Other more specific events, such as dust devil encounters, near-surface morning fog presence and partial eclipses by Phobos (Chapter Six) however will still be detectable, if only the diffuse flux is within the FOV. This issue is wholly dependent upon the final resting position of the lander, and cannot be anticipated. Thus for all modelling aspects concerned here, the position of Beagle 2 is assumed to be simply horizontal.

In the case of the filtered channels, the custom built filters were incorporated into the TO-5 can itself, suspended between the entrance window and the photodiode. A cage-type structure was used to hold the filter in place above the diode, and is shown schematically in Figure 4-9. The filter slots through the parallel aperture, and the ends of the metal cage are bent down upon the filter, securing it firmly within the structure. This method allows selective screening of light by the filter before it is detected by the diode.

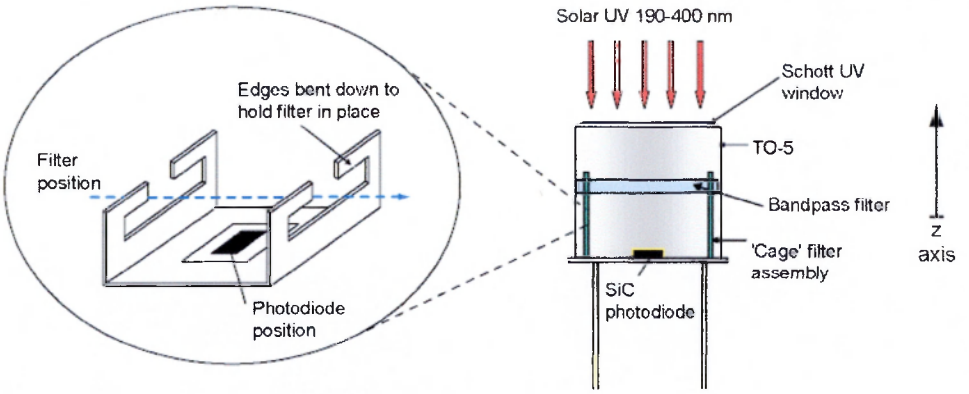

Figure 4-9: Filter-diode assembly.

The photodiode cans were positioned on the PCB on top of tubular supports. These tubes act as stand-offs for the sensing heads from the PCB, so that the observing aperture of each diode is above the surrounding solar absorber material (part of the lander thermal control system), and also provide electrical shielding for the sensor head outputs. Each was electrically grounded, since the initial pre-amplification current output from the photodiode itself is very small and susceptible to noise pick-up. The tubular supports were constructed from 304 grade aluminium. For the TO-5 cans, tubular supports with an inner diameter (ID) of 7.00 mm, outer diameter (OD) of 8.00 mm and length of 5.90 mm were used, whilst for the TO-18 can, a tubular support with an ID of 4.07 mm, OD of 4.98 mm and length of 7.50 mm was used. This configuration brought all the sensor heads to an equal level, standing 12.7 mm in height from the PCB. This placed the top of the sensor head flush with the top surface of the lander, allowing an unobscured view once the lander is deployed.

The tubular supports were bonded to the diode base and the PCB using Epotek H20E[1]. This epoxy offers an extremely strong bond between surfaces, and is also space-qualified for outgassing and stability over thermal-vacuum cycling. The use of Epotek H20E allowed electrical conduction between the diode, tubular support and PCB, ensuring electrical

[1] Supplied by Epoxy Technology, 14 Fortune Drive, Billerica, MA 01821, U.S.A.

grounding (and thus shielding) of the entire structure. The completed UV sensor with all photodiodes, epoxied support tubes and electronics is shown in Figure 4-10. Top and bottom views are shown (right), as well as an isometric view with a ruler scale for size comparison (left).

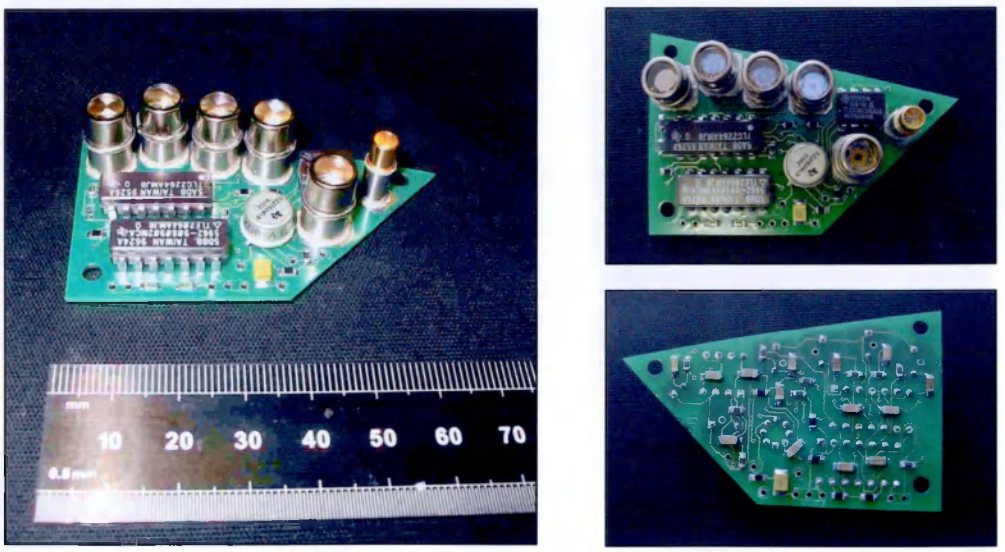

Figure 4-10: The Beagle 2 UV sensor.

4.4.4 Theoretical Response

The manufacturer supplied data on the current output per watt of the bare SiC diode are given in Figure 4-11 between 200 and 400 nm, equivalent to the open channel response. Also shown are the manufacturer supplied output response of the 350 nm and 300 nm channels, all shown as current output per watt over wavelength.

The response of the remaining channels (210, 235 and 250 nm) was determined through simple convolution of the bare SiC diode response (open channel in Figure 4-11) with the transmission profile specific to each custom made filter (corresponding spectral curve in Figure 4-6). The current output per watt as a function of wavelength for all channels (except 210 nm) in Figure 4-11 are referenced to the right axis, whilst the 210 nm channel is

referenced to the left axis, since the response of this channel is far lower than the other channels.

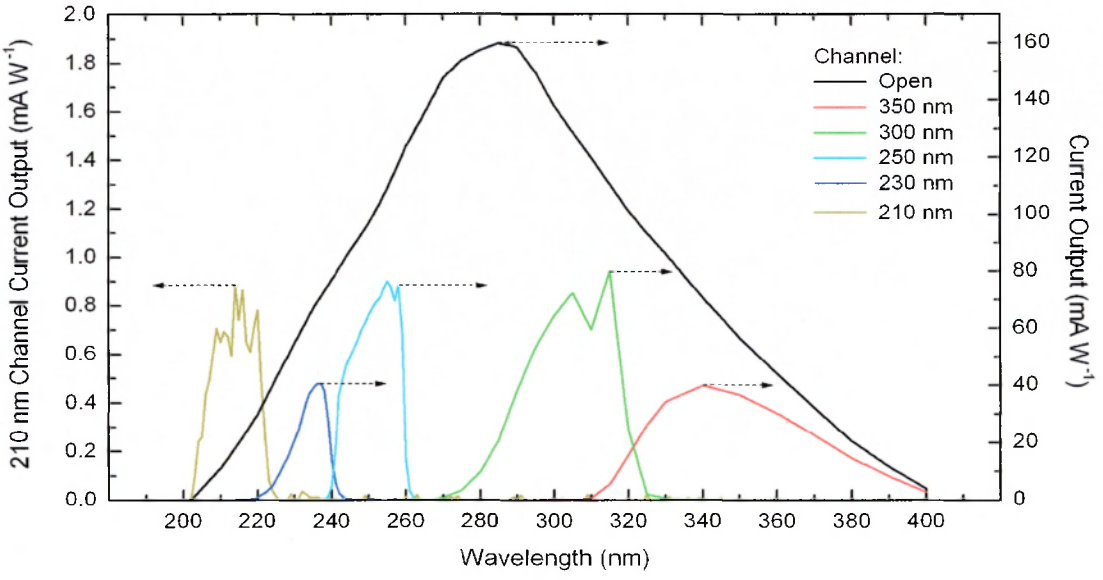

Figure 4-11: Wavelength dependent current response of each UV channel.

The choice of charge conversion and gain settings for the electronic configuration of each channel (C_f and R_{f2} in Figure 4-5) were determined through convolution of the channel response in Figure 4-11 with a predicted martian UV spectrum. The amplification of the circuit is linear over increasing flux levels, allowing the use of a 'maximum flux scenario' to set the maximum voltage output of the sensor under extreme conditions at 3.5 V. For Beagle 2, the maximum case spectrum was taken for local noon at $L_s = 0°$. A margin of 25% was then added to the spectrum for added safety – a saturated signal would result in a greater loss of science than a lower than expected signal, and it was for this reason the margin was incorporated.

The 190-400 nm spectrum was convolved with the current output per watt response for each channel and integrated over λ to yield the output current under maximum irradiation. C_f and R_{f2} were then chosen using Equations 4-1 and 4-2 to produce an output voltage of 3.5 V

under this condition for each channel. Complete circuit details of the UV sensor including all passive component values are given in Appendix B.

The output generated by the UV sensor is a five point spectrum covering the range 200 to 400 nm (the sixth channel is a 200-400 nm total). Each data point is an average value over the waveband for each specific channel. To verify whether this type of data would accurately represent the original spectrum, the maximum output voltages from each channel were processed into a five point average spectrum and compared with the original spectrum, shown in Figure 4-12.

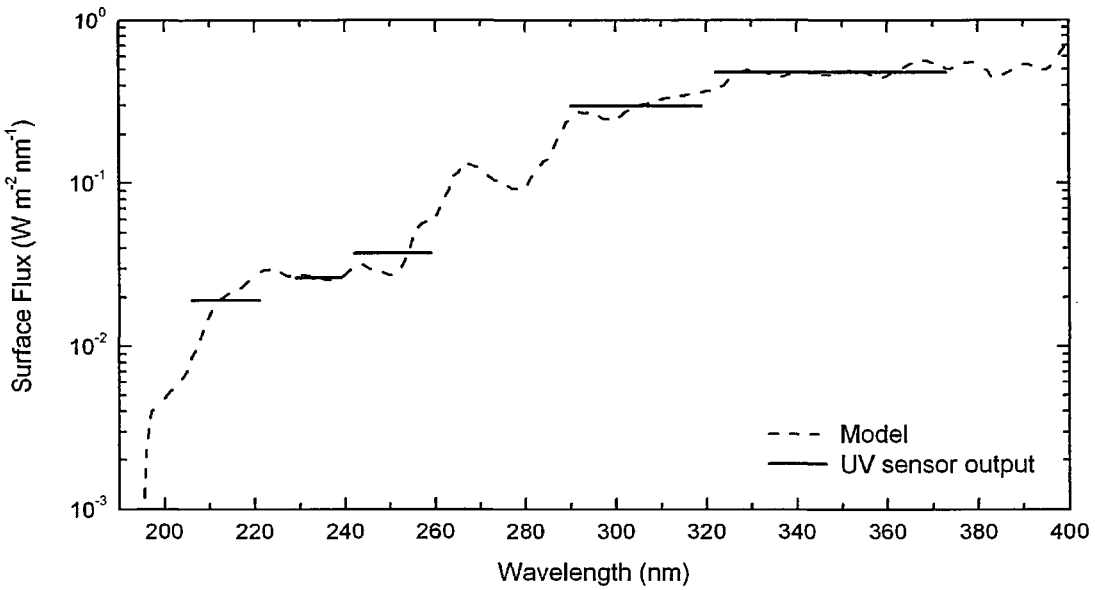

Figure 4-12: Simulated UV sensor spectral output.

The simulated output shows good agreement with the original spectrum, validating the concept of the sensor. Though the fine detail of the spectrum is lost in the photodiode output, the average flux levels in each regime are represented well by the sensor output levels. Using this type of output, it will be possible to extract low resolution optical properties using the diffuse UV data that will be returned from the martian surface. Using optical depth values

derived from the Beagle 2 camera data, the values of ω_{bd} and g_{bd} can be iteratively fitted in the model to match the 5 point average spectrum measured by the UV sensor.

4.5 Calibration and Environmental Testing

A vital stage in the production of spaceflight hardware is the calibration and environmental testing phase. Environmental testing concerns the extreme conditions that are endured during the lift-off, cruise, landing and operations stages of the mission. The most important factors during these times in terms of instrument survival are vibration levels and thermal cycling in near-vacuum, which form the main part of the environmental tests performed for the UV sensor. Detailed calibration of the sensors is also a prerequisite, allowing accurate interpretation of data returned from the mission. The environmental testing and calibration phase was contracted to the *Centro de Astrobiología* (*CAB*, based in Madrid, Spain) as part of a cooperation agreement between *CAB* and the Beagle 2 project. The environmental testing was performed at the space division of the *European Aeronautic Defence and Space Company* (*EADS-CASA*), and calibration at the Institute of Applied Physics, part of the *Consejo Superior de Investigaciones Cientificas* (*CSIC*) affiliated to the Ministry of Science and Technology, both based in Madrid. The experiments were performed here since the complex calibrated optical set-up and space qualification environmental test facilities were available for use through *CAB*.

4.5.1 Out of Band Blocking and Absolute Calibration

The voltage output as a function of wavelength for each individual channel of the unit needed to be accurately known, to interpret the expected output of the sensor. The voltage output per watt irradiance at discrete wavelengths for each channel was measured at 2 nm intervals across the response band of each channel.

Two light sources were used, to provide adequate UV flux output over the 200-400 nm region. A Xe OSRAM 150 W lamp was used to provide illumination at short wavelengths ($\lambda < 260$ nm), with illumination at longer wavelengths provided by a deuterium Hamamatsu LA-4505 50 W lamp. The flux output from the lamp was directed through a Jobin Ivon Mod. Spex 500 monochromator to provide accurate wavelength selection. The grating had a groove density of 2400 lines mm^{-1} with a slit width of 2 mm, allowing wavelength selection at a FWHM of 3.2 nm. The monochromator was then computer controlled to provide a 2 nm scanning step. This monochromatic output flux was focussed onto the sensor and the voltage outputs were recorded. The true irradiance at each wavelength at the sensing point was measured precisely using a standard TG1 detector, consisting of a pre-calibrated three photodiode light trap (Shaw *et al.* 1999). The full set-up of the optical bench and controlling electronics is shown schematically in Figure 4-13.

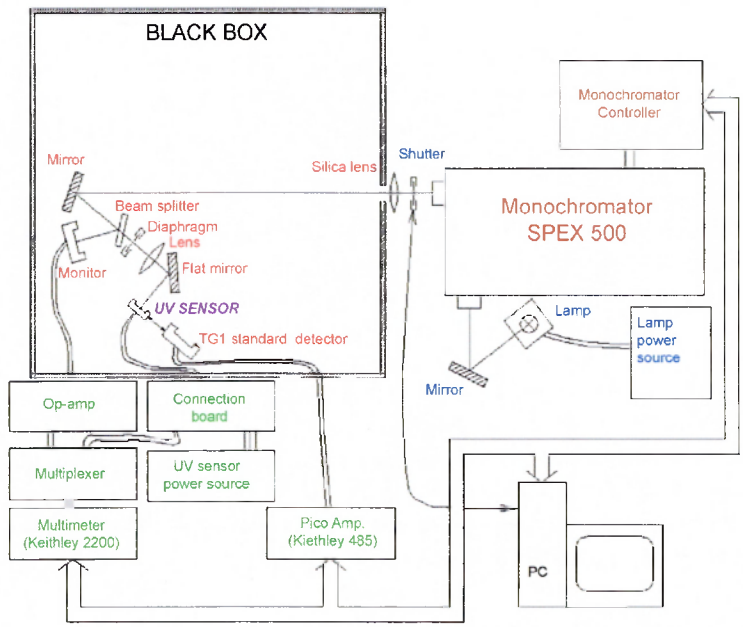

Figure 4-13: Schematic of the optical setup for responsivity tests.

The filter-diode method allows discrete parts of the overall photodiode response region to be selected. Before calibration, the out of band blocking of each channel (except the open

channel) needed verification, which would also aid in optimisation of calibration regions for each specific channel. To achieve this, each channel was scanned through the entire UV region from 200 to 400 nm, and the (uncalibrated) output was measured to gauge the response region of each channel. These measurements provided confirmation of the integrity of the filter-diode assembly, and no discrepancies were found in the blocking characteristics of the filters. The voltage response of each channel was expressed in terms of V W^{-1}, *i.e.* the output voltage produced when 1 watt of energy at a specific wavelength is focussed on the active sensor area. The values are extremely high (10^5 V W^{-1} or higher) since the actual solar UV flux levels in 1 nm wavelength bands are typically of the order of μW. The conversion to flux measurement is easily achieved by consideration of the active area (mm^2) of each channel sensor head. The voltage response at an accuracy of 10% for each channel as a function of wavelength is shown in Figure 4-14.

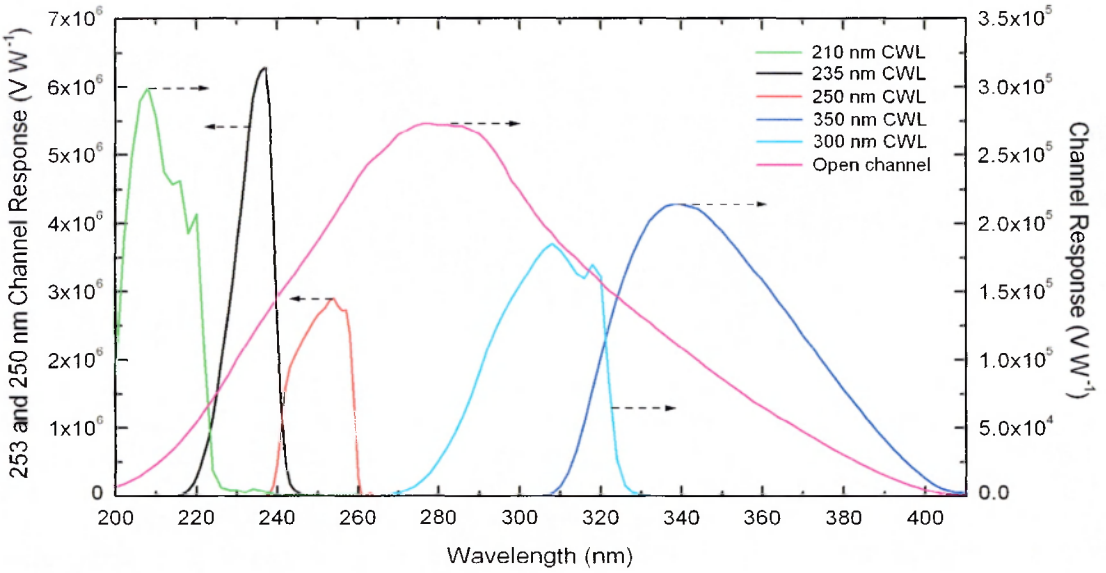

Figure 4-14: Absolute voltage response of each UV sensor channel.

The short wavelength channels (235 nm and 250 nm) required a greater 2nd stage signal amplification, since in this wavelength region the UV flux reduces significantly with respect to the longer wavelength channels. For the short wavelength channels the voltage response is

of the order of 10^6 V W^{-1}, with the corresponding longer wavelength responses around 10^5 V W^{-1}. The 210 nm channel required substantial amplification since the flux at these wavelengths is extremely low. Unfortunately amplification of signal also increased the offset voltage levels, so an upper limit was reached in terms of second stage amplification.

After the calibration of absolute responsivity was completed, the sensor was exposed to the UV source at a distance of 50 cm with no collimation, resulting in a beam footprint much larger than the diode sensing area, such as is experienced during exposure to the Sun. It was found that a small leakage was present in the short wavelength channels, where some of the incident UV was internally reflected within the can, bypassing the filter around the edge. This problem does not manifest in the long wavelength channels, since smaller (1 mm^2) diodes were used. The use of 4 mm^2 diodes on the shorter wavelengths (due to lower flux levels) resulted in less effective coverage by the filter, and consequently a small amount of UV was able to reach the diode through reflection on the inside of the can without traversing the filter. This leakage was noted for the 210, 230 and 250 nm channels, with preliminary results indicating that the excess flux can be removed from the detected signal. The measurement of the extent of the excess flux is however currently delayed due to financial negotiation with *CAB*, and therefore cannot be presented here.

4.5.2 Low Temperature Calibration

The behaviour of the sensor as a function of temperature was also investigated, since the sensor would undergo a wide range of temperatures as mentioned previously. The temperature dependence of each individual component of the sensor heads is minimal, so no significant variation was expected in the performance of the unit as a whole. The responsivity of the SiC diode drops by only 7% between temperatures of 300 K and 223 K, so no major degradation of responsivity is expected at low temperatures (Brown *et al.* 1993). In the case

of SiC photodiodes, the dark current decreases towards lower temperatures, which will result in an improved S/N ratio when operating in the martian environment.

The filter characteristics are not expected to vary significantly with reduced temperatures, with only a negligible shift in CWL and FWHM. Planned absolute calibration activities were to occur at temperatures of 293 K, 273 K and 243 K to understand the behaviour of the sensor as a function of temperature. Unfortunately due to time constraints of hardware delivery to the lander and ongoing contract negotiations, the calibration was only performed at 293 K and 273 K. A reduction of only 3% in responsivity of the sensor was observed, indicating that the temperature dependence of the unit will not be severe over the martian temperature range (Cabeza 2003). As with many spaceflight instruments, further low temperature tests are planned with a ground reference copy of the sensor to complete this aspect of testing, once appropriate resources become available.

4.5.3 Thermal-Vacuum Cycling and Vibration

Calibration activities were performed both prior to and after environmental testing of the units, to ensure functional integrity of the sensor after exposure to environmental loads. The tests consisted of thermal-vacuum cycling and vibration exposure. These tests are designed to simulate the temperature conditions encountered during cruise and operations, and the vibration loads expected during launch and landing.

Vacuum baking of hardware is an effective method of minimising contaminant transfer through outgassing at low pressures, by accelerating the diffusion processes of molecular outgassing of volatile materials and chemicals which are not liberated at standard temperature and pressure. Thermal-vacuum testing also provides the necessary assurance that sub-systems, components and assemblies will survive the conditions of interplanetary cruise, and operate successfully in the thermal extremes and low pressure of the martian environment. Thermal-vacuum cycles and vibration tests were conducted at two levels:

qualification and acceptance. Qualification is an extreme test designed to over-test non-flight hardware to ensure the reliability of the design, and was performed on the Flight Spare unit (FS). Acceptance levels are designed to represent better the true mission environment and are less extreme than qualification levels, designed for the Flight Model (FM) hardware which will be integrated onto the lander.

For the case of the Beagle 2, the thermal-vacuum minimum temperature limits for the UV sensor were calculated as the values in Table 4-1 with an additional 15 K margin, to account for any uncertainties in the thermal model. An additional 5 K on minimum temperature was then added for the qualification test. The qualification tests were carried out by cycling the sensor 5 times between 180 K and 298 K, and acceptance levels were conducted as 2 cycles between 185 K and 298 K. The filters incorporated inside the diode assemblies impose a maximum temperature ramp rate of 2 K min^{-1} to allow the substrates to expand and contract uniformly, and for this reason the ramp rate was kept to 1 K min^{-1} to ensure no damage was incurred. The sensors passed thermal-vacuum cycling tests, with no alteration in performance after cycling.

Vibration testing is generally required to expose the instrument to the accelerations encountered during launch, due to both the operation of the launch vehicle main engines and aerodynamic buffeting as the launcher rises through the Earth's lower atmosphere. For the case of Beagle 2, the vibration level regimes also cover the landing phase, where the lander will be delivered to the martian surface via the use of airbags, similar as to that successfully used on MPF. Once the airbags are at rest on the surface, Beagle 2 will be dropped to the ground from a height of around 1.5 m (*i.e.* the centre of the airbag configuration), when the airbags are jettisoned to a safe distance.

The shock encountered during airbag jettison and surface impact was initially simulated on a flight representative version of the diode-filter assembly, to verify its suitability for use at the design stage. The sensor head was mounted on duplicate tubing and PCB base,

representative of the final configuration. Testing was performed at the Space Research Centre, Leicester University, to re-create the extreme vibration shock when the lander impacts the surface. Vibrations were generated through the flexure of a thick nylon beam, clamped 40 cm from one end. The sensor was placed near the end and the flexed beam was released, creating the intense vibration shock. An acceleration of 360 g_{earth} at 60 Hz was applied in the z axis, and 300 g_{earth} at 60 Hz in the x and y axes. Visual and electrical inspection of the sensor before and after testing showed no damage to the sensor due to the extreme shock encountered during this phase of the landing sequence.

The vibration tests are designed to cover all these accelerations and are therefore higher than usual for space-qualification. Vibration tests were carried out in the same qualification and acceptance groups as before. Two sub-sets of vibration testing were incorporated to represent different forms of vibration: sine and random vibration. The sinusoidal vibration is employed to verify the instrument's resonant structural capability, but is not fully representative of launch vibrations. The random vibration test is used to subject the instrument to a representative spectrum of random vibrations such as will be encountered during launch and landing. This process has the advantage of simultaneously subjecting the structure to a range of frequencies such that no resonance in the instrument is allowed to build up. As a consequence, the vibration loads in general are far more severe than in the sinusoidal test.

Both sinusoidal and random tests were performed at qualification and acceptance levels, on all three axes of the sensor (x, y and z axes as indicated in Figures 4-2 and 4-9). The acceleration levels over various frequencies are shown in Tables 4-3, 4-4 and 4-5 as defined for the UV sensor by Sykes (2002), with acceleration expressed in terms of terrestrial surface gravity g_{earth} (9.81 m s^{-2}).

Frequency Range (Hz)	X and Y axis (g_{earth})		Z axis (g_{earth})	
	Acceptance	Qualification	Acceptance	Qualification
0.1-100	10	15	25	30
Sweep rate	4 octaves min^{-1}	2 octaves min^{-1}	4 octaves min^{-1}	2 octaves min^{-1}

Table 4-3: Sine vibration test levels.

Frequency Range (Hz)	X and Y axes	
	Acceptance	Qualification
20-30	+9 dB $octave^{-1}$	+9 dB $octave^{-1}$
30-80	1.00 $g_{earth}^2 Hz^{-1}$	2.25 $g_{earth}^2 Hz^{-1}$
80-200	-6.7 dB $octave^{-1}$	-6.6 dB $octave^{-1}$
200-500	0.13 $g_{earth}^2 Hz^{-1}$	0.3 $g_{earth}^2 Hz^{-1}$
500-2000	-3 dB $octave^{-1}$	-3 dB $octave^{-1}$
Overall (r.m.s.)	15.28 g_{earth}	22.92 g_{earth}
Duration	1 min	2 min

Table 4-4: Random vibration test levels (x and y axes).

Frequency Range (Hz)	Z axis	
	Acceptance	Qualification
20-30	+6 dB $octave^{-1}$	+6 dB $octave^{-1}$
30-80	1.11 $g_{earth}^2 Hz^{-1}$	2.50 $g_{earth}^2 Hz^{-1}$
80-200	-21.9 dB $octave^{-1}$	-23.1 dB $octave^{-1}$
200-500	0.16 $g_{earth}^2 Hz^{-1}$	0.35 $g_{earth}^2 Hz^{-1}$
500-2000	-3 dB $octave^{-1}$	-3 dB $octave^{-1}$
Overall (r.m.s.)	20.03 g_{earth}	30.04 g_{earth}
Duration	1 min	2 min

Table 4-5: Random vibration test levels (z axis).

The sensors were calibrated for absolute responsivity before and after the vibration tests, and showed no significant variation in the responsivity of each channel, proving that the filter-diode assembly had safely been qualified for the environment to which Beagle 2 would be subjected. A very small variation in dark current after thermal-vacuum cycling was observed (~ few mV) on some channels, but of no significant concern. This minor variation is easily compensated for by ensuring that at least one reading per martian sol of the dark current is taken, *i.e.* a standard data sample during the martian night.

4.5.4 Ageing Simulation

An important factor which will only manifest during the course of the mission will be the effect of long term exposure to both ionising and non-ionising radiation. Towards the end of the 180 sol mission the total accumulated UV and ionising radiation doses will become significant, inevitably affecting instrument components to varying degrees. The SiC diodes are insensitive to long term UV and ionising radiation exposure, however the optical components (*i.e.* filter and can window) are not. High energy radiation (UV-C, protons and alpha particles) can cause 'darkening' of optical components, which can (given sufficient time) cause the filters to become opaque. This will be inevitable for the 210 nm filter which is composed of metal-dielectric substrates prone to such darkening effects. The remaining filters do not contain materials susceptible to high energy radiation, and will be more stable over the mission lifetime. The open channel will also present a relative comparison of the effects of filter darkening on 'observed' flux levels – a long term analysis will reveal an apparent decrease in flux levels throughout the course of the mission, which will in part be attributable to the increasing opacity of the optical components. This effect will be far lower in the non-filtered channel, and can be used as a relative comparison of this effect.

One factor which will affect all sensor channels simultaneously towards the end of the nominal mission will be the settling of atmospheric dust on the diode windows. This effect

was unavoidable, since mass constraints prevented the inclusion of any mechanism which could remove the dust. Over the mission lifetime, a layer of fine particles is expected to build up on the diode windows, which will result in a gradual drop in 'observed flux' due to attenuation by the dust particles. This effect will also manifest in the long term performance of the solar cells, which will gradually decrease in efficiency with continued dust build up. A dust layer thickness on the order of 5-10 μm was derived for the MPF site at the end of the 83 sol mission, through observations of radiometric calibration targets (Johnson *et al.* 2003). Assuming similar dust deposition conditions, Beagle 2 can expect to possess a dust layer coating of around 11-22 μm at the end of the nominal mission. The effect of this build up will be apparent in the long term variation of the measured signals – over time as the layer builds up, there will be a corresponding drop in signal, which can be verified by comparison to the long term variation in the solar panel performance.

In order to prepare for compensation of such effects in the data returned towards the end of the nominal mission, long term simulation of the aforementioned factors was included in the test schedule in an effective 'ageing test'. This process would simulate the end of mission state of the sensor by incorporating the cumulative effects described above, to ascertain the rate of degradation of the sensor response over the entire Beagle 2 mission lifetime. Such a test is required to determine whether the sensor will function adequately through to the end of the nominal mission, and whether extended operation will be feasible. Data from this test will not affect the results presented in this thesis, since the scenarios presented in the proceeding chapters can be achieved at the beginning of the mission, and do not rely on extended operations.

Unfortunately however, again due to the current lack of funds and various contractual complications, this aspect of testing has been severely delayed and cannot be presented at this time. The ageing test is expected to be conducted in the near future, once the relevant resources become available.

4.5.5 Instrument Delivery

The FM and FS units were successfully delivered in November 2002 ready for integration into the Beagle 2 lander. The unit was sterilised in accordance with Category IVa+ planetary protection requirements, and also stringent requirements for the Aseptic Assembly Facility (AAF) where the lander was constructed (Pillinger *et al.* 2002). Efficient sterilisation was achieved using a H_2O_2 plasma wash performed at Leeds General Infirmary (Spry 2001). Figure 4-15 shows the UV sensor during electrical integration onto the lander (right) and just prior to probe closure, indicated by the red dashed circle (left).

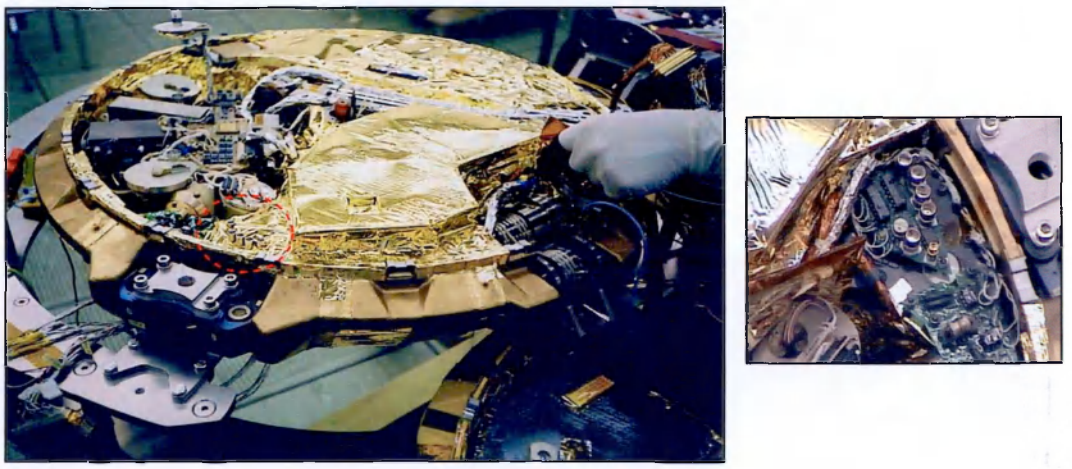

Figure 4-15: Electrical integration and final shroud covering of the UV sensor on Beagle 2.

The sensor is covered with layers of Kapton sheeting (100 μm thick) offering efficient thermal protection of the electronics on the PCB. The diode window apertures penetrate the Kapton sheeting, with an unobscured upward view. The UV sensor was tested after integration into Beagle 2 and operated within nominal parameters. Thus an *in situ* UV instrument was designed, developed and built over the course of this study and coupled to a radiative transfer model, offering the chance to gather hitherto unmeasured data on the martian surface UV environment.

Chapter Five

Investigation of Martian UV Conditions

As well as aiding in the design of the Beagle 2 UV sensor, the development of the radiative transfer model allows investigation of a range of martian UV environments. This chapter covers a variety of situations encountered over the martian surface at different times, and is based upon the work published in Patel *et al.* (2003a).

5.1 Comparison of Martian and Terrestrial Flux

Before specific investigations of the martian UV environment are conducted, it is useful to place the range of the magnitudes of the martian flux levels in context. A typical terrestrial UV spectrum is used for comparison, to highlight the relative levels of martian flux (Engelsen and Kylling 2001). A comparison of spectra for two 'equivalent' situations on each planet is shown in Figure 5-1. The martian data are calculated for vernal equinox ($L_s = 0°$) at the equator ($lat = 0°$N) at local noon, with a nominal dust loading of $\tau_{back} = 0.20$. The terrestrial case is given also for vernal equinox at the equator, at local noon under cloudless sky with an ozone abundance of 300 DU (these units are addressed in section 5.4). The terrestrial spectrum penetrates only partly into the UV-B, with a cut-off at around 290 nm. The martian

UV spectrum however extends far deeper into the UV, penetrating as far as the UV-C towards 190 nm.

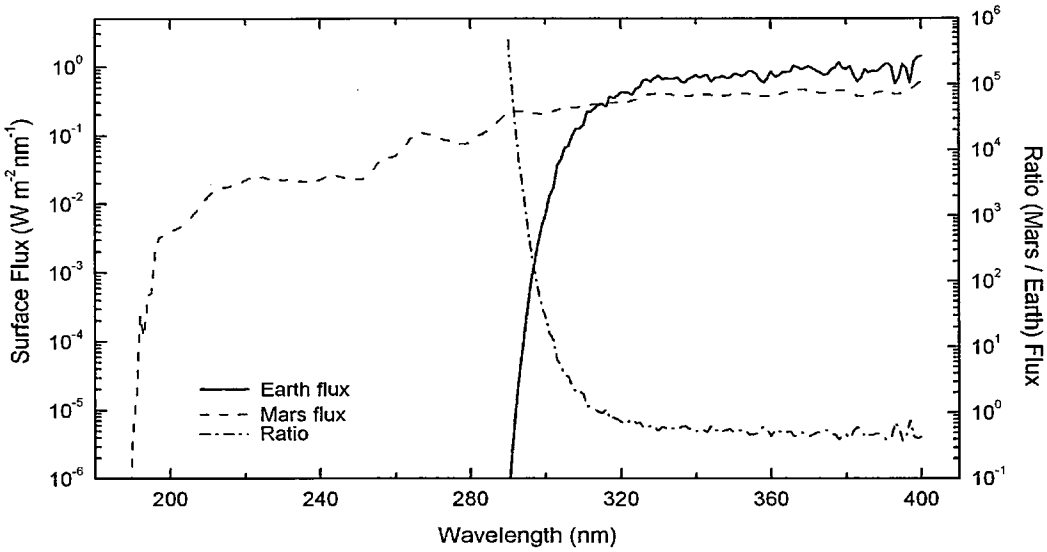

Figure 5-1: Comparison of martian and terrestrial UV flux spectra.

The ratio of the martian and terrestrial flux is also shown in Figure 5-1. The trend in the data shows the martian/terrestrial flux ratio between 400 and 340 nm to be approximately 0.5. On both planets, negligible absorption occurs in this regime, and the results are consistent with a $1/r^2$ flux decrease due to the greater average distance of Mars from the Sun. Between 340 and 315 nm the ratio increases to around 1, as weak absorption by O_3 and atomic oxygen in the upper terrestrial atmosphere begins to take effect. Between 315 and 304 nm, the ratio begins to rise rapidly, increasing to approximately 10. Below this wavelength the ratio increases exponentially, increasing by almost 5 orders of magnitude at 290 nm when compared to 400 nm.

Below 290 nm negligible UV penetrates to the terrestrial surface, whereas on the martian surface, UV penetrates to wavelengths as short as 190 nm. Thus above approximately 315 nm the martian and terrestrial fluxes are not too dissimilar, with only a small difference between the two due to the smaller flux at the more distant martian orbit. Below this wavelength, in

the UV-B region, irradiance levels at the martian surface steadily rise with respect to the terrestrial case, and towards the UV-C region the levels are orders of magnitude greater.

5.2 Biological Weighting

5.2.1 DNA Weighting

The DNA action spectrum was applied to the output model irradiance, and can be defined for either F_{direct}, $F_{diffuse}$ or F_{total}. The resultant spectrum shown in Figure 5-2 is a convolution of the martian surface irradiance spectrum in Figure 5-1 with the DNA action spectrum in Figure 2-3. The effect of the convolution is apparent at longer wavelengths where the DNA response to UV is minimal and thus the weighted flux is diminished. The peak sensitivity of DNA occurs around 260 nm, causing the UV-B and UV-C region of the spectrum to be amplified, reflecting the damaging effect upon the DNA structure.

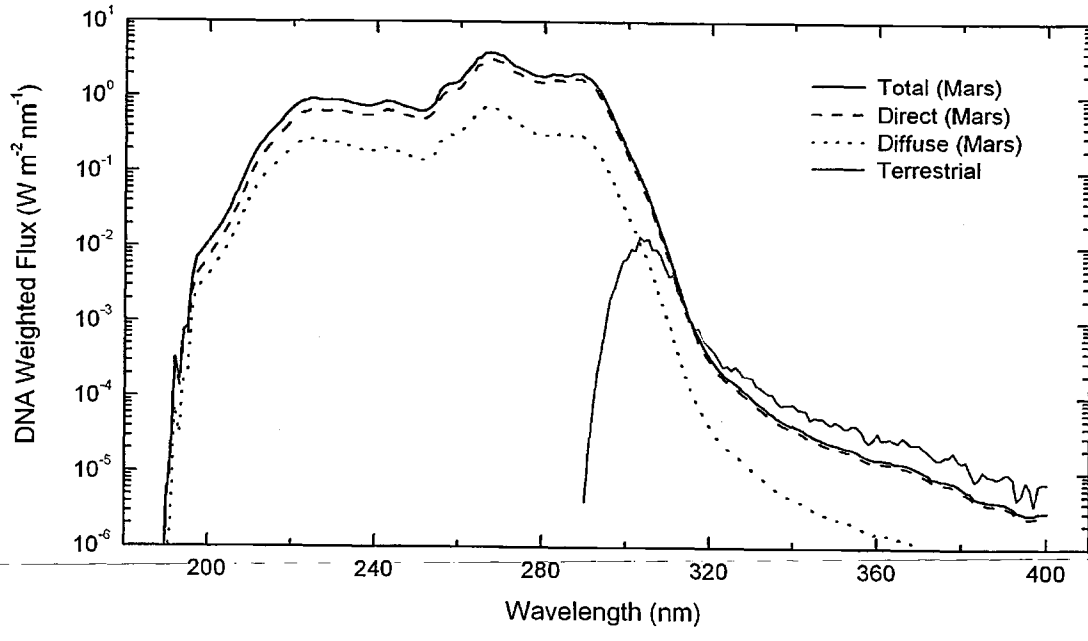

Figure 5-2: Comparison of martian and terrestrial DNA-weighted surface UV flux.

The typical terrestrial DNA-weighted spectrum shown in Figure 5-2 emphasises the harsh environment at the martian surface. In the UV-A region the terrestrial weighted flux is higher due to the proximity of the Earth to the Sun. However, this region of the UV is relatively benign, and the crossover point in the spectra is observed to occur around the onset of the UV-B region. Here severe biological damage begins to occur, and the martian weighted spectrum increases rapidly. The integrated martian weighted spectrum[1] is approximately 120 W m^{-2}. The relevance of this number is understood when compared to the terrestrial integrated spectrum. On Earth, the corresponding value is only 0.13 W m^{-2}, nearly three orders of magnitude lower than on Mars.

Horneck (1993) showed through exposure experiments on Apollo 16, Spacelab-1 and the Long Duration Exposure Facility (LDEF) that the DNA action spectrum roughly correlates with the action spectrum for loss of viability of *Bacillus subtilis* spores, indicating that DNA is the critical chromophore for lethality for this micro-organism. Using the above effective integrated flux, any similar organisms present at the martian surface would therefore experience a UV environment approximately 10^3 times more intense than on the Earth, from a biological viewpoint.

Other factors will also contribute to the loss of viability, such as increased ionising radiation doses and reduced pressure at the martian surface. Exposure of *Bacillus subtilis* spores to low temperatures showed little variation in photosensitivity, except at extremely low temperatures of 80 K when the photosensitivity decreased (Dose and Klein 1996). Dehydration of micro-organisms due to low atmospheric pressure is however an important effect which increases loss of viability (Horneck 1993). Any such (terrestrial-like) organisms would therefore not be expected to survive for long when fully exposed to the martian environment.

[1] The units here are not strictly power, but rather an effective power, since the absolute power has been normalised by an effective weighting function.

5.2.2 Erythemal Weighting

The martian UV environment can also be interpreted in biological terms in the context of skin response. Erythema (sunburn) is a commonplace terrestrial reaction to elevated UV levels experienced mainly by caucasians, especially those with little pigmentation in the skin, and thus serves as a useful 'relative indicator' to a physiological effect most people are aware of. The response of the skin to UV-A is to cause pigmentation in the skin (tanning) which acts as a repair and protection mechanism, whereas the occurrence of erythema is a direct indication of genomic damage to the skin tissue by UV-B. On Mars the action of UV-B will be far more severe, as indicated in Figure 5-2.

As in the case of DNA weighting, an action spectrum specific to relative erythemal damage is used to gauge the severity of Sun exposure to human skin. Unfortunately there is little understanding of the erythemal response below 290 nm (it is arbitrarily given a relative value of 1) since humans do not experience these wavelengths at the Earth's surface and as a result there is a distinct lack of published data on this subject. Though an action spectrum cannot be applied to the full martian spectrum, a first order assumption can be made to gauge the relative effect. The assumption is to presume that erythema follows roughly the same damage spectrum as DNA below 290 nm, thus accounting for the major contribution from the UV-C region. This is only a rough approximation however, and should only be treated as a first approximation to the true skin damage levels.

The standard method of conveying to the general public the severity of solar exposure in terms of UV danger to skin is through the use of the Sun Index (globally recognised as the UV Index), regularly announced on TV weather reports and in newspapers during the summer. This public awareness measure was introduced in 1994 by the World Meteorological Organisation and the World Health Organisation, describing qualitatively the risk to human skin. The definition of the Sun Index is the spectral UV irradiance (W m^{-2}) weighted by the standard *CIE* erythemal action spectrum (McKinley and Diffey 1987) and

multiplied by 40. Maximum values reach around 15 on Earth in equatorial regions at the subsolar point, indicating periods when minimal exposure times (~20 mins) and suitable protection (screening compounds etc) are required. If one follows the assumption that erythemal damage basically follows the DNA damage spectrum, it can be inferred that the levels of erythemal damage will also be roughly three orders of magnitude higher as is the case in DNA-weighted doses. If television weather reports were to include daily martian weather forecasts, they would report Sun Index values of approximately 10,000 for a sunny martian day. This value provides an easy conception of just how dangerous the martian UV environment is to human skin tissue.

5.3 Large-scale Dust Storms

5.3.1 Optical Properties

One of the most striking and dynamic events in the martian atmosphere is the occurrence of dust storms. Such storms are akin to sand storms on Earth, where high wind speeds loft large quantities of dust into the atmosphere. These events occur on both a local and global scale, in some cases encircling the entire planet such as observed by Mariner 9, VL1, VL2 and MGS (Martin 1974; Ryan and Sharman 1981; Smith *et al.* 2002). Small-scale dust storms can occur throughout most of the year, though generally activity is seen to peak towards perihelion in the southern hemisphere as mentioned previously. Global-scale dust storms occur less frequently, with no discernable pattern to their frequency of occurrence. As a consequence of such high atmospheric dust loading, surface irradiances will be significantly affected, and here the effect upon the UV spectrum is investigated.

The case of the dust storm introduces a high degree of uncertainty into the issue of the dust optical properties in the atmosphere. At the onset of the storm, atmospheric disturbances loft a wide range of particle sizes into the atmosphere. At this time, the size distribution of

atmospheric dust particles can be highly variable, dependent upon a variety of parameters such as soil size distribution (particular to the region of interest), composition and adhesion properties as a few examples. Determining these parameters and the resulting size distributions produced is however far beyond the scope of this work. A relevant observation by both Mariner 9 (Toon *et al.* 1977) and MGS (Bandfield *et al.* 2000; Smith *et al.* 2000) was the behaviour of global dust storms as a function of time. It was observed that as expected, during the onset of the storms, the particle size distribution (and thus optical properties) changed due to the injection of fresh dust into the atmosphere. However, only a short period after the initial onset while optical depths were still relatively high, it was observed that the dust absorption spectra were relatively invariant throughout the decay and disappearance of the storm, providing a good indication that the particle size distribution does not vary significantly at this time from the background haze. Therefore, though we cannot model with confidence the conditions immediately during the onset of these dust events, we can approximate the transmission a short time after the beginning, while optical depths (and therefore dust loadings) are still high, using the same optical parameters as for the background haze.

5.3.2 Effect upon the UV Spectrum

The surface UV spectrum was modelled for the case of a major dust storm, in the southern hemisphere at a latitude of 20°S at perihelion ($L_s = 250°$) at local noon. The dust optical depth for such a storm was taken as $\tau_{back} = 4.0$, consistent with observations by VL1 and VL2 which endured such major dust storms (Pollack *et al.* 1979). The resultant surface spectrum for this case is shown in Figure 5-3. The overall shape of the spectrum appears similar to the nominal case, but important differences exist in the spectrum. Though the shape remains similar, the total 190-400 nm irradiance is reduced by 75% when compared to a nominal dust case for the same situation, as indicated in Figure 5-3. High dust loading thus has a significant effect on the magnitude of the total surface UV spectrum.

A major difference is also seen in the *relative* magnitude of the component UV fluxes. In the nominal case, the majority of the total UV originates from the direct component. Though a significant diffuse component is characteristic of the nominal martian UV environment, it is still relatively small with respect to the direct component. For the case of a dust storm given in Figure 5-3, a distinct change occurs in the relative magnitudes of the components. The direct flux is attenuated rapidly, as expected with an optically thick atmospheric layer. The diffuse flux is now the dominant component, with the total surface irradiance primarily due to scattered UV. Irradiance will not only change in absolute level, but will also be seen to originate from a different 'source', *i.e.* a ubiquitous diffuse irradiance.

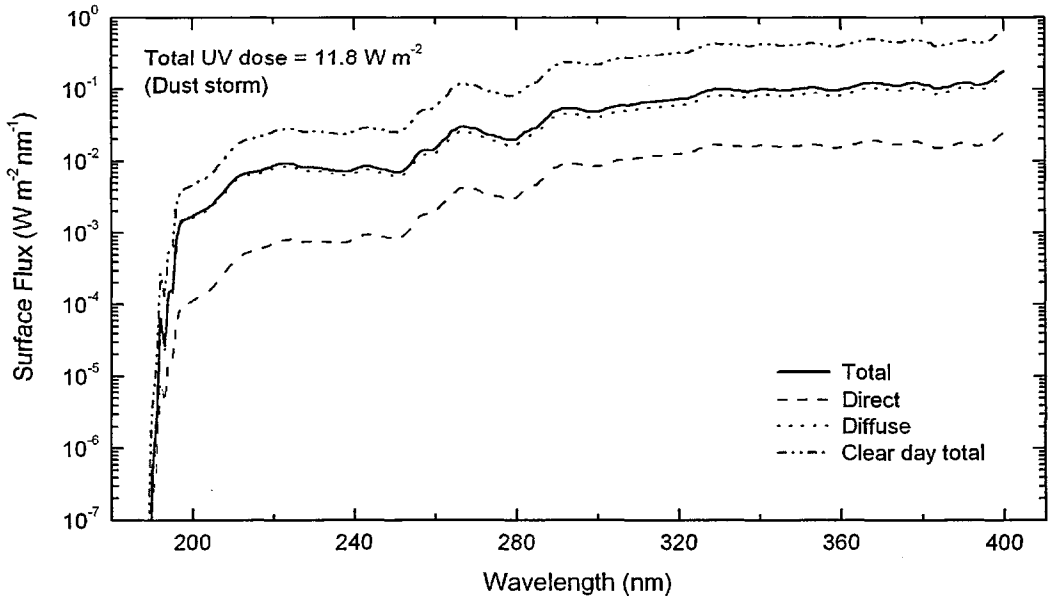

Figure 5-3: UV spectrum during a major dust storm at $L_s = 250°$, *lat* = 20°S at local noon.

Since the UV spectrum depends so heavily upon dust loading in the atmosphere, the variation of the full 190-400 nm flux with dust loading was investigated. The variation of total, direct and diffuse irradiances with dust optical depth is shown in Figure 5-4, covering optical depths ranging from 0.1 to 9.0. The case investigated here is for vernal equinox ($L_s = 0°$) at the equator at local noon.

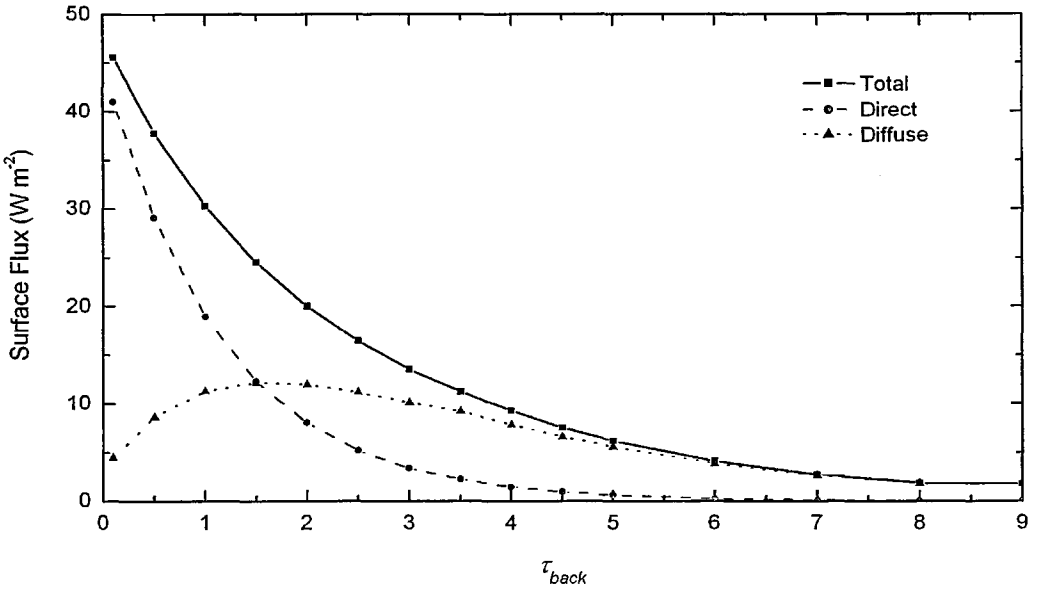

Figure 5-4: Variation of 190-400 nm UV flux with background dust optical depth.

As demonstrated in Figure 5-3, increased dust loading results in a decrease in the 190-400 nm total surface UV flux. The direct flux is attenuated rapidly, approaching zero towards an optical depth of 6. The total flux however still persists, due to the presence of the diffuse component created through aerosol scattering. At optical depths below 2, the direct and diffuse fluxes are anti-correlated in magnitude. At low optical depth ($\tau_{back} < 0.5$) the direct flux is the dominant component, with little contribution from the diffuse flux. At an optical depth of 1.5 the two components are equal in magnitude, and above this value the diffuse component starts to dominate.

The rate of attenuation of the diffuse component is far shallower than for the direct component, which results in an important conclusion. Even at extremely high optical depths beyond any previously observed martian conditions (> 5) UV radiation still persists at the ground (albeit a only a small amount ~5 W m^{-2}), formed solely from the diffuse component as a consequence of multiple scattering by the aerosols.

5.4 High Latitude Conditions

The situations resulting from the polar day/night, increased airmass and O_3 formation indicative of martian high latitude conditions were investigated. Before proceeding, certain commonly used non-standard units need to be defined relating to the abundance of atmospheric gases, namely the micrometre-atmosphere (μm-atm) and the Dobson unit (DU). 1 μm-atm is defined as the thickness of the O_3 column in μm when at standard temperature and pressure (STP) on Earth, and corresponds to 2.69×10^{15} molecules cm^{-2}. 1 DU is the total O_3 column thickness at STP in units of hundredths of a millimetre, equivalent to 10 μm-atm. DU is the most commonly used unit when addressing terrestrial O_3 column abundance, and is included here to provide easy comparison between martian and terrestrial O_3 abundances.

5.4.1 Polar Day/Night

As on Earth, the daylight period encountered at the martian surface is highly dependent upon both latitude and season. As latitude increases, the minimum *SZA* varies from minimum to maximum dependent upon the season. Summer time decreases the minimum *SZA*, and conversely winter time increases the minimum *SZA*, and this variation consequently alters the daylight period. At extremely high latitudes however, the minimum *SZA* can be altered enough to ensure that the Sun is always above or below the horizon throughout the day (*i.e.* *SZA* is always less than or greater than 90° respectively). These situations arise only towards the polar regions, where the effects of obliquity become severe. The regions where these situations occur can be seen by comparison of Figures 5-14 and 5-17 in the high latitude regions (addressed later). At latitudes where the noon flux values are low but the daily dose values are high, the effect of extended daylight periods can be inferred. This situation occurs also on Earth, due to the similar obliquity. On Earth, regions which are in continual daylight throughout the day are known as 'polar day' regions, and conversely regions in continual

darkness through the day are called 'polar night' regions. These same terms are applied to the martian case.

An example of the martian polar day is shown in Figure 5-5, at a latitude of 75°N at $L_s = 90°$ where $\tau_{back} = 0.10$. Though the peak flux only reaches 24 W m^{-2}, the continual daylight provides a total day dose of 1267 kJ m^{-2}. This value exceeds that of the maximum case in Figure 5-13 (addressed later), even though here the latitude is nearly 3 times greater.

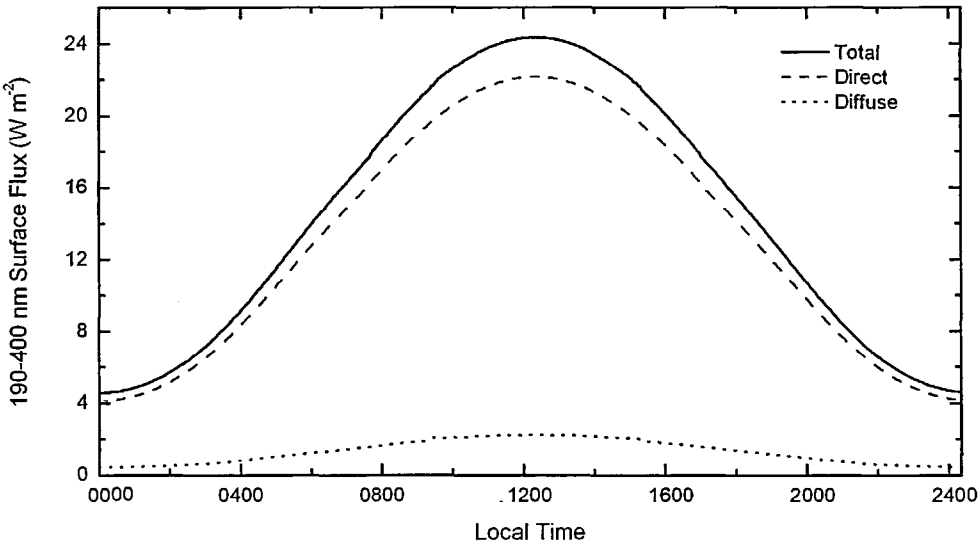

Figure 5-5: Polar day diurnal UV profile.

A more extreme case is shown in Figure 5-6, at the same time of year but at a higher latitude at 84°N. At such extreme latitudes, the variation of *SZA* throughout the day is minimal, since the rotational axis of Mars is at its closest orientation towards the Sun. Thus the higher the latitude the point of observation is, the smaller the apparent altitude variation of the Sun (and thus UV flux) appears throughout the day. Though the peak noon flux is even lower than in Figure 5-5, the total day dose of 1300 kJ m^{-2} is still slightly larger. Again the importance of increased daylight period is demonstrated, with continual daylight producing a higher total daily dose despite the lower maximum flux. Polar night regions by definition have zero irradiance throughout the entire day. Each area which experiences the polar day

effect will subsequently experience the polar night each martian year, in the relevant winter period. These regions, extending from north and south pole to latitudes of roughly 60°N and 60°S respectively therefore undergo regular annual extremes in terms of sustained UV exposure.

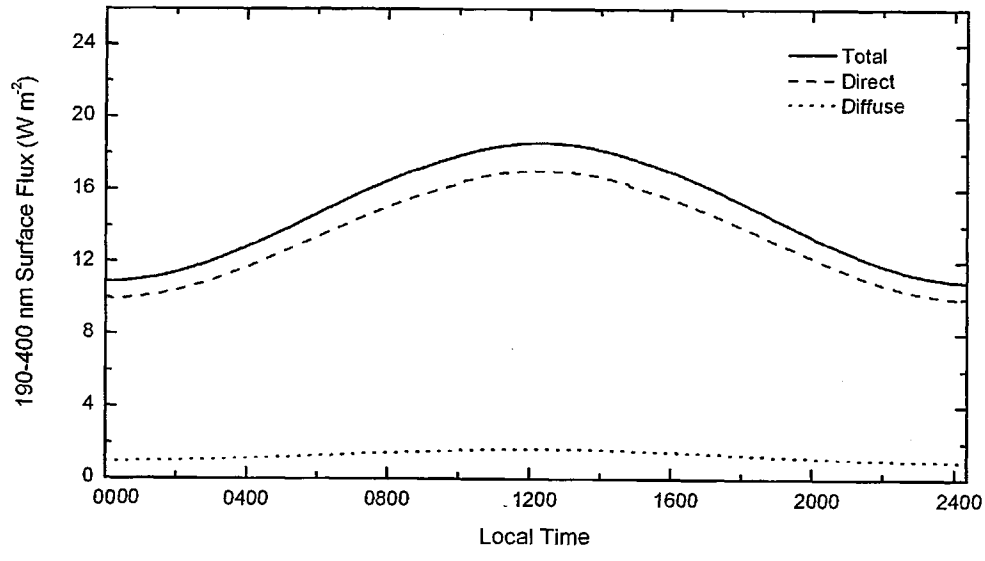

Figure 5-6: Extreme polar day diurnal profile.

5.4.2 High O_3 Cases

O_3 is a minor constituent in the martian atmosphere, but its large absorption cross-section in the UV region makes its role in surface UV spectra extremely important. O_3 absorbs strongly in the Hartley band, centred around 250 nm. Terrestrial O_3 is vital for the persistence of most forms of life on Earth, offering screening (in combination with molecular and atomic oxygen) from wavelengths shorter than approximately 290 nm at the Earth's surface. In the terrestrial atmosphere O_3 is present over all altitudes, though the majority of O_3 is concentrated in a region named the "ozone layer" situated in the stratosphere at an altitude ranging roughly between 20 and 40 km. The terrestrial ozone layer at mid-latitudes corresponds typically to between 260 and 380 DU. Above this altitude, short wavelength UV-C is present as in the case at the martian surface. A typical terrestrial UV spectrum is

shown in Figure 5-7, which highlights the cut-off formed primarily by O_3 in the terrestrial atmosphere (Engelsen and Kylling 2001). This case shows the surface spectrum in northern spring at a latitude of 10°N, under cloudless sky with moderate O_3 levels (350 DU).

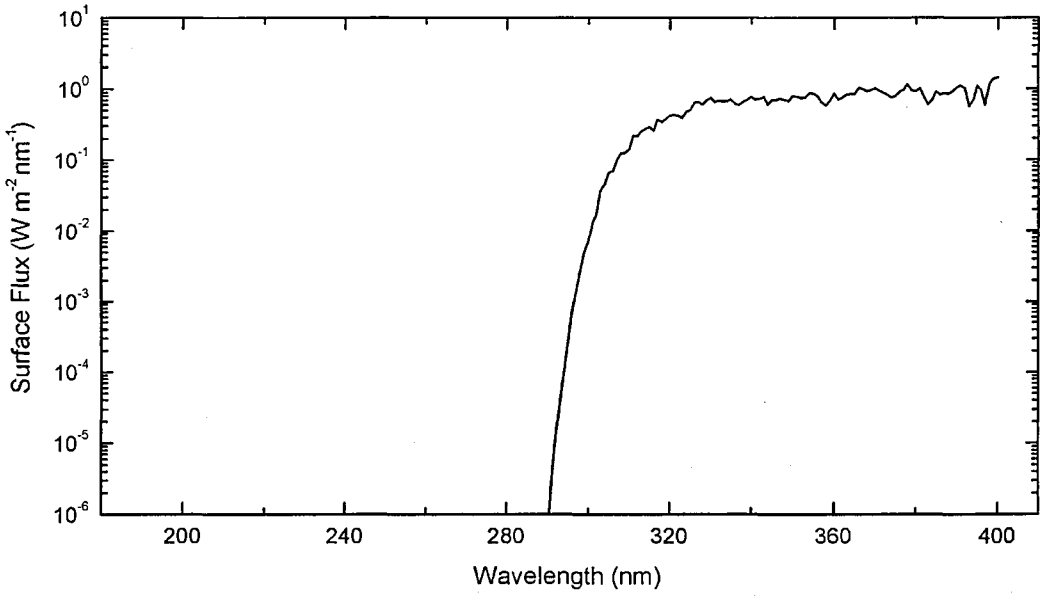

Figure 5-7: Terrestrial surface UV spectrum (Engelsen and Kylling 2001).

The presence of O_3 in the martian atmosphere was first detected in the southern polar region of the martian atmosphere through measurements using the UVS experiment onboard Mariner 7 (Barth and Hord 1971). O_3 is a temporally and spatially varying constituent of the martian atmosphere, as indicated by data from the Mariner 9 UVS experiment which found that significant O_3 column abundances of up to 1.64×10^{17} cm^{-2} (6.0 DU) only occur at high latitudes towards northern winter, declining sharply towards spring (Barth and Dick 1974). Further work using the HST Faint Object Spectrograph showed results in agreement with these data, also improving on the lower detection limit of the Mariner 9 instrument to measure the presence of small amounts of O_3 (8.3×10^{15} cm^{-2} or 0.3 DU) at low latitudes towards aphelion (Clancy *et al.* 1996).

O_3 abundance reaches a maximum towards northern winter, and begins to decrease during spring as the northern polar cap begins to recede, releasing trapped water vapour which in turn begins the photolytic destruction of O_3 (Equation 2-4). In general, the presence of O_3 in the atmosphere is correlated with the presence of the polar hood, which condenses atmospheric H_2O in the form of clouds. However, the presence of the polar hood is only an indirect indication of the presence of O_3, and as such is a necessary but not a sufficient condition. Significant O_3 column abundances have been observed in regions void of the polar hood, where the atmosphere is cold and dry (Barth and Dick 1974).

The surface irradiance is modelled here for such a case of O_3 presence in a region void of polar hood cloud. The reason for this choice is the complete lack of knowledge concerning the optical properties of the polar hood. The physical properties, apart from the major composition being H_2O, are not at all understood, so the efforts which would be needed to model transmission through such a cloud would inevitably be in vain. Detailed observations of the physical and optical properties of the polar hood phenomenon are required before any attempts at understanding the scattering properties can be achieved. Thus the case is modelled here to highlight the effects of O_3 alone upon the UV spectrum, and quantify the implication of the presence of this chemical species in the atmosphere.

The region of interest here is that where Mariner 9 detected maximum O_3 abundances over the north polar region in late winter, at $L_s = 352°$ and a latitude of 58°N (Barth and Dick 1974). UVS measured a maximum column abundance of 1.64×10^{17} cm^{-2} (60 μm-atm or 6 DU). The resulting surface UV spectrum for this case at local noon is shown in Figure 5-8. The effect of O_3 is to create an absorption feature with respect to the nominal spectrum in the UV-C region, centred around 250 nm. The reduction due to O_3 is almost two orders of magnitude near 250 nm. This region is the biologically damaging regime which is screened in the terrestrial case by the relatively thick ozone layer.

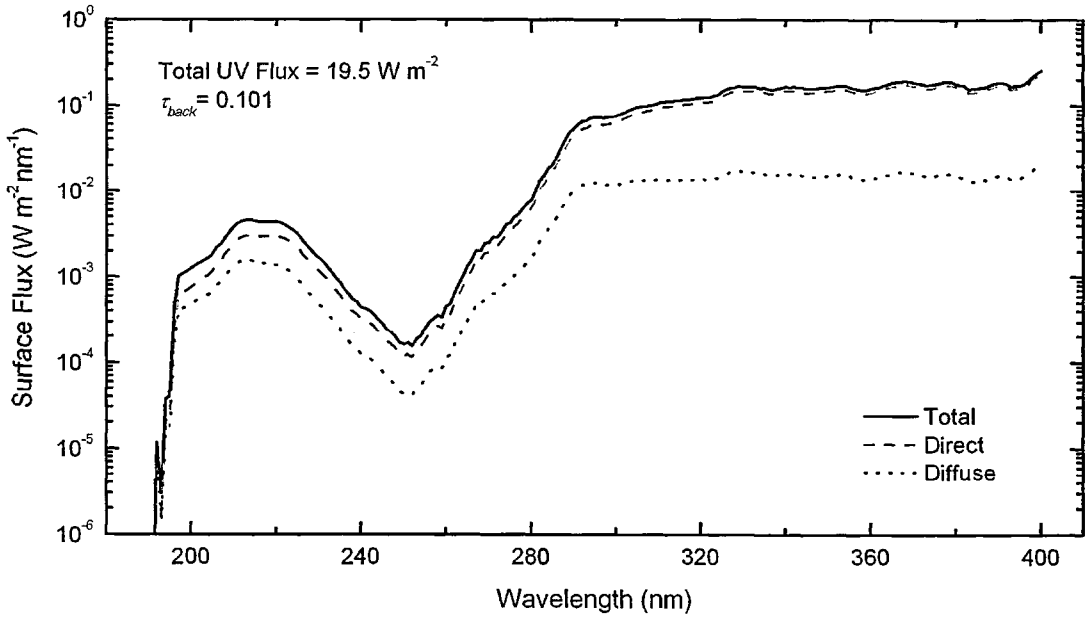

Figure 5-8: Absorption in the martian atmosphere due to an O_3 abundance of 1.64×10^{17} cm^{-2}.

O_3 presence on Mars, though lower in general by almost two orders of magnitude when compared to Earth, could still offer partial protection for micro-organisms on the surface of Mars. However, the presence of a second DNA absorption peak at 220 nm near the edge of the Hartley band means damage would still be incurred to exposed organisms – the relatively low O_3 concentrations result in significant absorption only towards the centre of the absorption band. Also, the variation of significant O_3 abundance limits this possible partial biological protection towards northern winter at high latitudes only. Thus geographical constraints and the presence of the secondary DNA absorption band effectively limit the degree of potential O_3 protection available.

Though low O_3 abundance in the martian atmosphere offers only partial protection against UV-C, higher levels should intuitively offer terrestrial-like UV protection. As O_3 abundance was increased, a broadening of the absorption band shown in Figure 5-8 was observed, as O_3 absorption effects become more prominent. Previously in the evolution of the martian atmosphere, O_3 may have been in sufficient abundance through the biotic generation

of O_2 to provide substantial protection from incoming solar UV. This concept of increased O_3 levels has also been suggested as a possible approach for limiting the degree of global UV damage on Mars, in the context of terraforming (Hiscox and Lindner 1997). By using the present-day martian atmosphere, and increasing the O_3 abundance to 2×10^{19} cm^{-2} (an increase of two orders of magnitude), a terrestrial-like UV spectrum is attained shown in Figure 5-9 for northern summer at the equator.

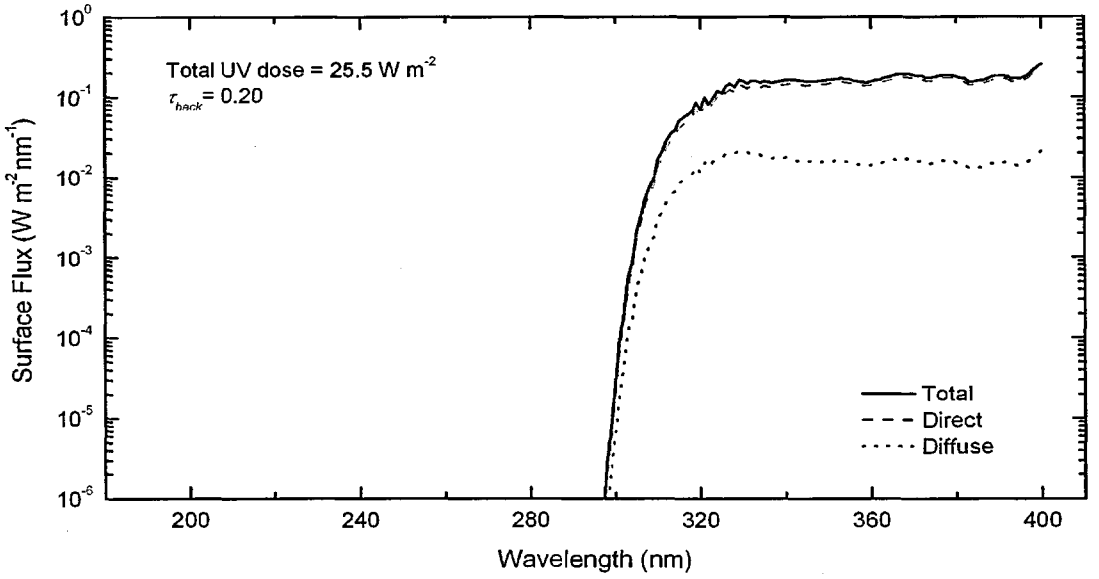

Figure 5-9: Hypothetical martian UV spectrum with highly elevated O_3 abundance.

At this O_3 abundance, the DNA-weighted dose is comparable to that encountered on present-day Earth. The early martian atmosphere however would be substantially different to the present atmosphere, possibly with higher CO_2 partial pressures on the order of 500 to 3000 hPa, and decreasing throughout time (Haberle *et al.* 1994). The effect of increased CO_2 abundance in the atmosphere is to increase the effects of scattering, increasing the component of diffuse flux whilst reducing the direct flux. Early atmospheric compositions remain highly debated, with uncertainties in the photochemical environment leaving the atmospheric composition largely unknown. Figure 5-9 thus serves only as an indication that elevated O_3 abundances *could* have offered a terrestrial-like UV environment, given the conditions present

today, and places a lower limit upon the required O_3 abundances in the context of terraforming Mars.

Assuming however a pure CO_2 atmosphere decreasing over large periods of time towards the present-day CO_2 partial pressure value, the O_3 abundance required to achieve terrestrial DNA-weighted doses was investigated. The CO_2 partial pressure was varied in the model between 7.5 and 1000 hPa, and the O_3 column abundance was manipulated to provide an Earth-like DNA-weighted dose, shown in Figure 5-10.

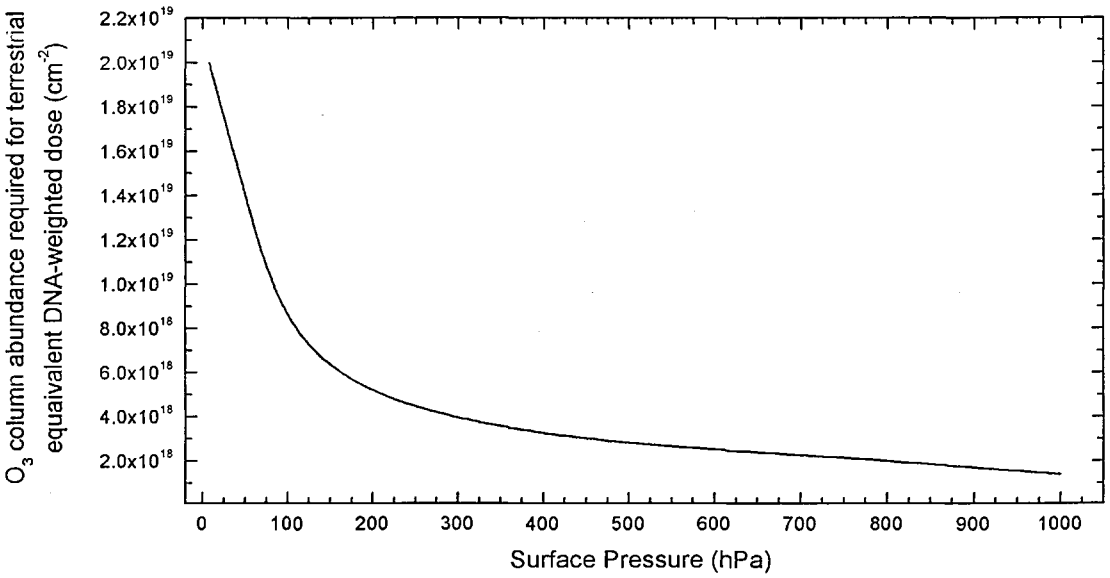

Figure 5-10: Required O_3 column abundance for terrestrial equivalent DNA-weighted doses at the martian surface, over varying CO_2 partial pressures.

The calculated O_3 column abundances are consistent with the work of Cockell *et al.* (2000), who calculated required O_3 abundances in the same context for CO_2 partial pressures of 100 and 500 hPa. Though the CO_2 partial pressures throughout the martian history still remain uncertain, given any partial pressure up to 1000 hPa, the required O_3 column abundance for present-day equivalent terrestrial DNA-weighted doses can be derived from Figure 5-10.

5.5 Seasonal Variations

5.5.1 Pressure Variation

Atmospheric pressure on Mars is seen to vary as a function of season, time of day and geographical location. Seasonal variations in pressure are regulated by the eccentricity of the martian orbit, and caused by the seasonal mass exchange of CO_2 between the polar caps and atmosphere. As temperatures decrease towards winter, CO_2 vapour condenses onto the polar regions, lowering the atmospheric pressure. As summer approaches, temperatures rise and the CO_2 is released back into the atmosphere, increasing the atmospheric pressure. This cycle continues as a function of season in both hemispheres, controlling the atmospheric pressure in a regular cycle (James *et al.* 1992). The amounts of CO_2 condensed at each polar cap are not equal, due in part to the eccentricity of the martian orbit. Since the condensation periods at southern winter are longer than at northern winter coupled with the reduced input solar flux, more CO_2 is condensed at this time due to the longer condensation duration, resulting in a greater reduction of pressure.

The Viking landers returned data on pressure variations for over 3 years, giving valuable *in situ* measurements of the long term variation of surface pressure at two separate locations. The greatest pressure increase occurs during southern summer, when the larger southern polar cap begins to sublimate. This is followed by a smaller increase towards northern summer, due to the release of CO_2 from the smaller northern polar cap. At times the situation is complicated as northern cap sublimation can occur simultaneously with southern cap condensation, but there are periods where only one process is active, such as near $L_s = 150°$ (just prior to autumnal equinox) where the minimum global pressure is encountered. At the VL1 landing site the maximum atmospheric pressure observed was approximately 10 hPa, with a minimum of around 6.5 hPa at the VL2 site, *i.e.* a seasonal pressure variation of roughly 35% (Hess *et al.* 1980).

Smaller diurnal variations caused primarily by thermal tides are also observed, with maximum variations of approximately 3% (Hess *et al.* 1980). Pressure variations over the martian surface are also observed, with variations greater than the seasonal changes due to the variations in topographic relief. Topographic (and thus pressure) variations are extreme on Mars, such as low altitude regions at high atmospheric pressure (~12 hPa) in Hellas Basin, and high altitude regions at low atmospheric pressure (~1 hPa) on Olympus Mons, over an order of magnitude variation in pressure (Zurek 1992). Pressure at local noon as a function of latitude and longitude (5° resolution) across the entire martian surface towards perihelion (L_s = 300-330°) is shown in Figure 5-11, obtained from the Mars Climate Database (Lewis *et al.* 1999).

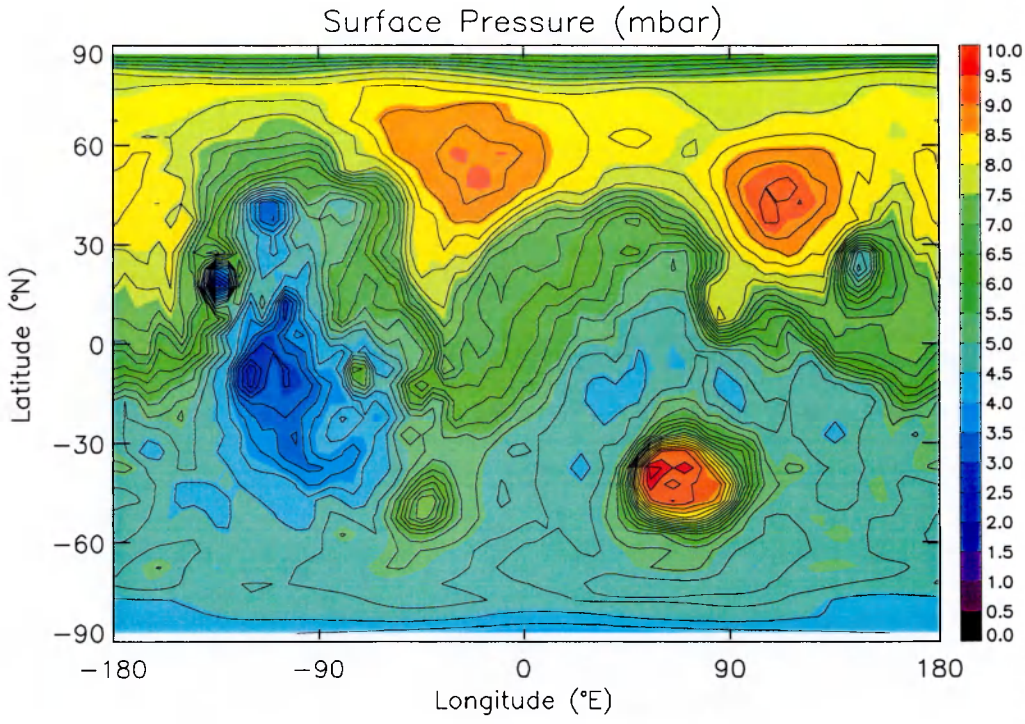

Figure 5-11: Variation of pressure over the martian surface (Lewis et al. 1999).

Considering the substantial variation of pressure encountered over the martian surface, the dependence of surface UV flux upon atmospheric pressure (and thus total atmospheric species column abundance) was investigated. The surface UV flux was calculated for values

of pressure ranging from 2 to 10 hPa at 1 hPa intervals. The dust component was removed to isolate the effect of pressure changes alone, since extreme high altitude regions (*i.e.* > 20 km) are above the majority of the dust. The dependence of UV flux upon pressure is shown in Figure 5-12.

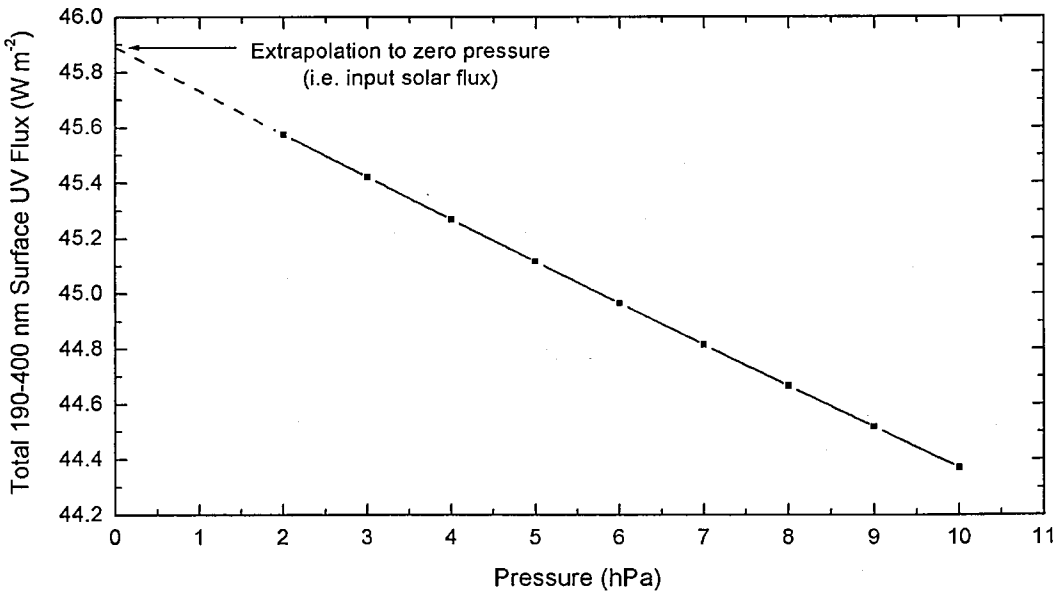

Figure 5-12: Pressure dependence of surface UV flux.

The variation of the surface UV flux with pressure is extremely small – a 50% reduction in pressure results in only a 1.5% increase in total UV flux. Even a reduction of an order of magnitude in the pressure (such as that experienced between Hellas Basin and Olympus Mons) results only in an increase of total UV flux of 3%. Extrapolation of the plot back to zero pressure yields a surface irradiance of 45.9 W m^{-2}, exactly equal to the value at the top of atmosphere, verifying the validity of the modelling. The differences encountered in UV flux over the martian surface due to pressure are thus found to be minimal.

The importance of realistic variations of atmospheric constituents on surface UV flux is highlighted in Figure 5-12 when compared with the relation revealed in Figure 5-4. Very little change is observed even with large deviations in pressure, whereas a corresponding

change in dust loading has a severe effect upon the spectrum. This highlights the minimal effect of gases in the martian atmosphere upon the resultant UV spectrum, except for O_3 and the CO_2 cut-off near 200 nm – the major influence on UV flux on Mars takes the form of atmospheric aerosols.

5.5.2 Daily dose

Mars shares similar characteristics with Earth, such as sidereal rotation period (88775 s) and obliquity (25.19°), and it is these properties which creates the terrestrial-like day-night variation and seasonal environments on Mars. On Earth, the seasonal effect is primarily due to variation in the minimum *SZA* throughout the day, which in turn varies the airmass through which the radiation must travel, changing surface fluxes. Earth's orbital eccentricity (0.0167) has little effect on the seasonal change in irradiances with a change in input solar radiation of only approximately 6% (Floyd *et al.* 2002), but on Mars the case is distinctly different. Mars' orbital eccentricity (0.0933) is over a factor of 5 times greater than that of Earth, resulting in a major change of input solar radiation of up to 40% (James *et al.* 1992).

As on Earth, the seasonal effect of varying daylight period is experienced on Mars due to the relatively large planetary obliquity. In terms of UV dose, this property is significant. As the daylight period increases, the total dose throughout the day also increases, and the resultant effect is a variation in total daily UV dose throughout the martian orbit. Since the daylight period is related directly to the length of the path the Sun traverses throughout the day, the maximum daylight period occurs when *SZA* reaches its minimum value at the specific latitude concerned.

An example of this is at summer and winter solstice at the tropical boundaries (equivalent to the terrestrial tropics of Cancer and Capricorn). Here, the case of zero minimum *SZA* during northern summer is calculated for $\tau_{back} = 0.20$, with a corresponding diurnal profile with similar peak flux but shorter day length during northern winter ($L_s = 270°$) for

$\tau_{back} = 0.01$, shown in Figure 5-13. This plot is not truly representative, since τ_{back} would not be as low as 0.01, but is shown to highlight the effect of change in daylight period on the total UV dose.

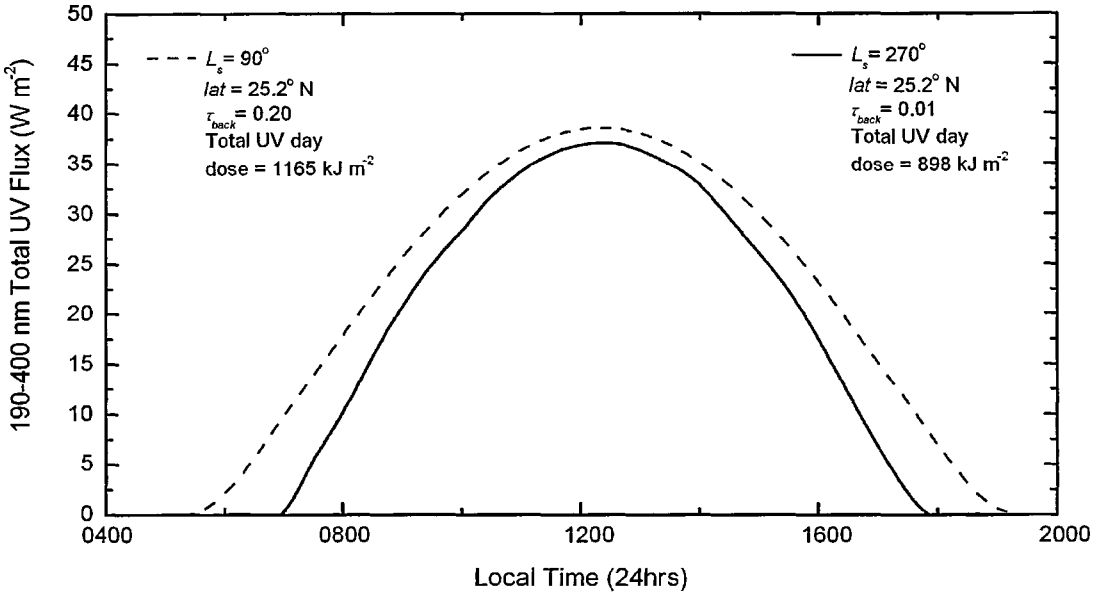

Figure 5-13: Effect of change in daylight duration on UV dose.

The difference in daylight periods is easily noticeable, with sunrise (sunset) occurring approximately 1.5 hrs before (after) in the $L_s = 90°$ case. The extended daylight period increases the total daily dose from 898 kJ m^{-2} at $L_s = 270°$ (daylight period = 11 hrs), to 1165 kJ m^{-2} at $L_s = 90°$ (daylight period = 14 hrs), a variation of nearly 30%. At even higher latitudes the variation in daylight duration is even greater.

5.5.3 Latitude – L_s variation

Since the surface UV flux is heavily dependent upon latitude and season, modelling these variations over time reveal important facts about the annual distribution of solar UV at the martian surface. The latitude and L_s model inputs were varied at 2° resolution to calculate the surface flux across a latitude strip of constant pressure from north to south pole, over the

entire martian orbit. It should be noted here that this type of plot is not a *geographical* representation, but rather a representation of a latitude strip over time. The strip itself is an arbitrary strip stretching from north to south pole along a line of constant pressure, and the plot is geographically representative of latitude only. Care must be taken when analysing these types of plots not to interpret them as latitude-longitude plots. The latitude-L_s variation was calculated using each of the annual dust scenarios, to highlight any dependence upon annual dust loading patterns on the resultant surface distribution of UV flux.

The latitude-L_s variation of instantaneous flux at local noon is shown in Figure 5-14 using the nominal annual dust scenario. The distribution of noon flux is non-uniform across the martian orbit. The distinct asymmetry in the plot is due to two combined effects, namely the relatively high eccentricity of the martian orbit and the obliquity of Mars. Eccentricity creates an asymmetry in L_s, where perihelion forms a concentrated maximum dose region, and obliquity creates an asymmetry in latitude, shifting the maximum into the southern hemisphere. The centre of this maximum is attenuated due to the increased dust loading encountered at $L_s = 250°$, splitting the maximum into two components. In the nominal scenario, the maximum instantaneous flux reaches a value of 50 W m^{-2} in the southern equatorial region towards perihelion. Also evident are the zero dose regions at high latitudes, where the polar night effect is experienced in both hemispheres.

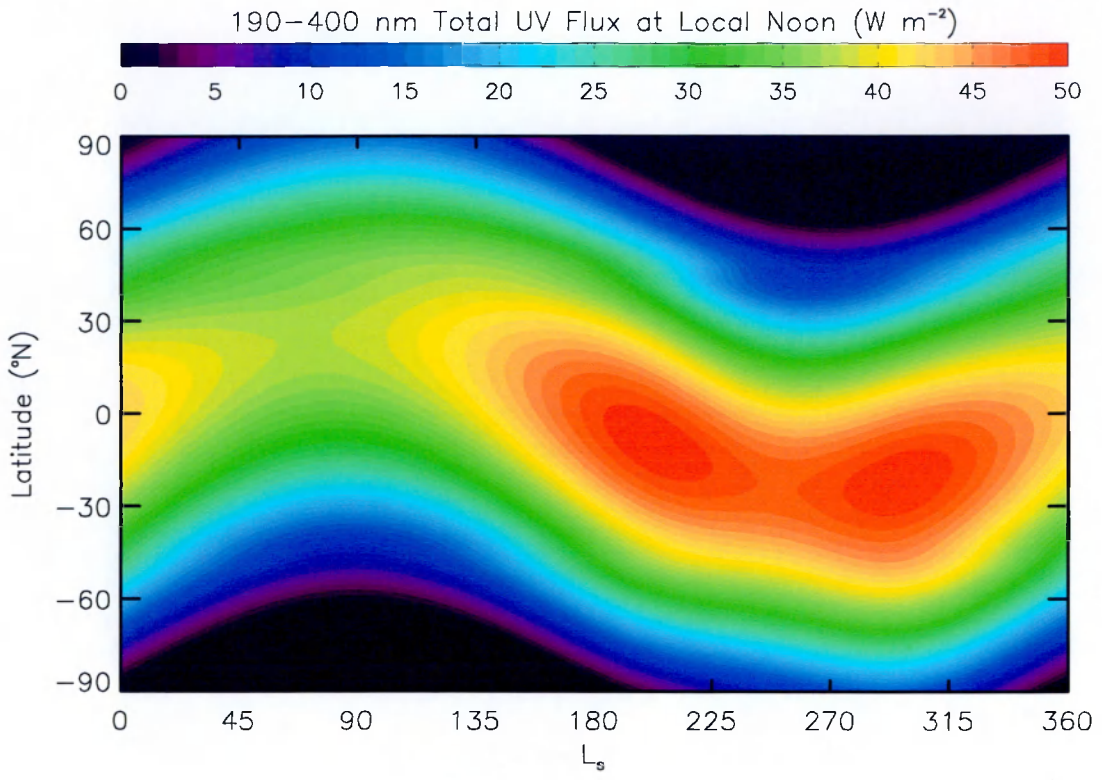

Figure 5-14: Latitude-L_s variation of local noon UV flux (nominal dust scenario).

An understanding of the effect of dust in the martian atmosphere over the martian year becomes apparent when alternative annual dust scenarios are used. Figure 5-15 shows the same annual variation of surface UV flux, except this time for the case of high dust loading throughout the martian year. The distribution of surface UV flux is significantly different to that in the nominal case. The corresponding maximum is now spread to a greater extent in both latitude and L_s. In this scenario, the maximum is spread throughout most of the equatorial region both north and south, for a much greater part of the martian year. Due to the higher dust loadings throughout the year, the levels of instantaneous UV flux are lower as expected, due to increased attenuation by the suspended dust. Maximum flux levels are around 40 W m^{-2}, 20% lower than in the nominal case.

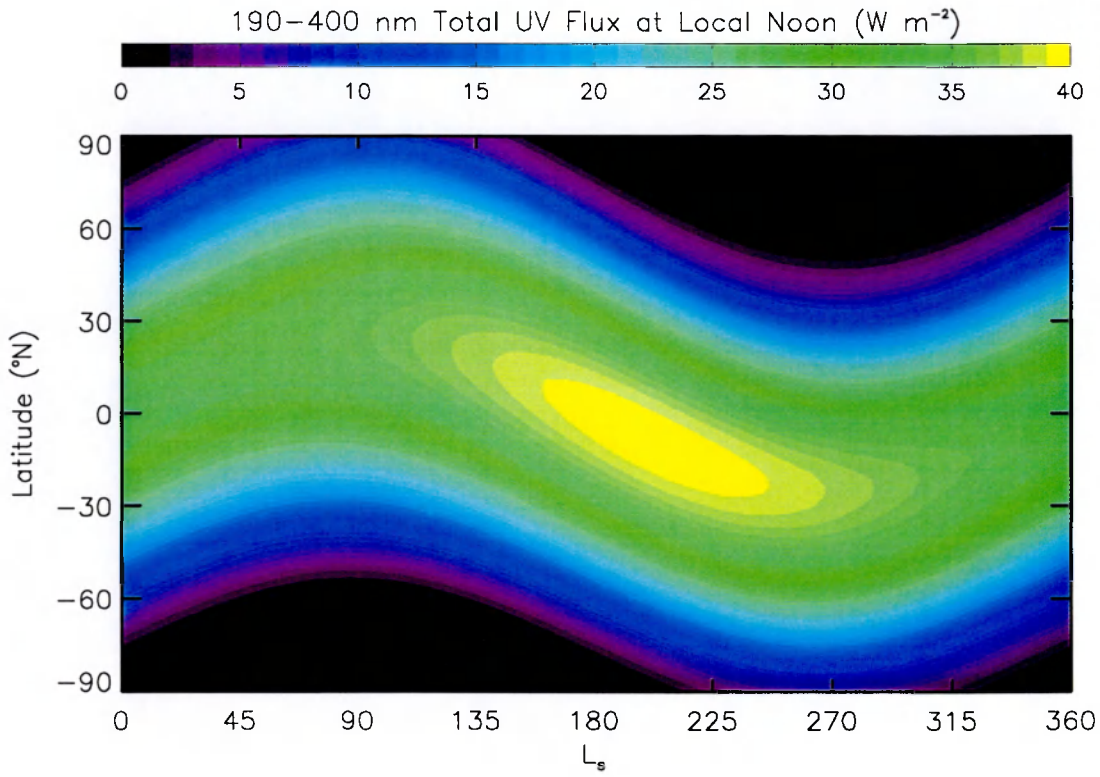

Figure 5-15: Latitude-L_s variation of local noon UV flux (high dust scenario).

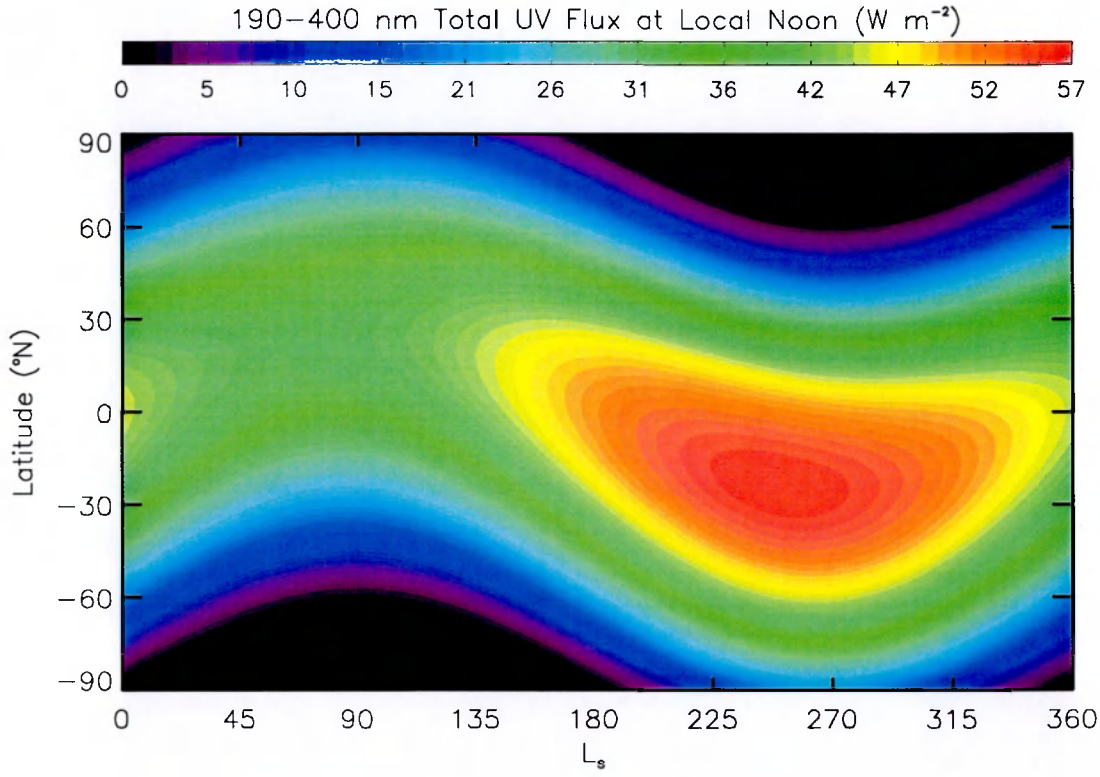

Figure 5-16: Latitude-L_s variation of local noon UV flux (low dust case).

Figure 5-16 shows the same variation except for the case of the low annual dust scenario. This scenario has a fixed low optical depth of 0.1 and thus yields the highest overall UV fluxes. Since the optical depth is invariant over latitude and L_s, the distribution of UV in Figure 5-16 is equivalent to the distribution of input top of atmosphere solar flux. Here the maximum occurs at perihelion towards the southern hemisphere, and is not distorted but smooth and confined. The peak flux level occurs at L_s = 250° and a latitude of 25°S, correlating extremely well with perihelion L_s (250°) and also the obliquity (25.19°) which causes the shift into the southern hemisphere. The maximum flux encountered is around 57 W m^{-2}, 12% higher than in the nominal case.

In all cases the rate of change of UV flux over latitude is high over the lower levels of UV, which tend to occur towards higher latitudes. This high gradient is due to the non-linear variation of airmass with *SZA*, as shown in Figure 3-4. The observed airmass at local noon is proportional to latitude, with less effect seen at lower latitudes where the zenith angle is small, increasing towards higher latitudes as the airmass increases. As the airmass increases, the input solar flux is reduced due to the greater path lengths traversed and angular dispersion at the top of the atmosphere.

Figures 5-14 to 5-16 all show the instantaneous surface fluxes throughout the martian orbit at local noon, but for a complete understanding of the long term implications of the irradiation pattern on the martian surface, flux values need to be evaluated in terms of total dose. Figure 5-13 highlights the fact that though instantaneous noon fluxes may be equivalent, daily doses due to varying daylight periods can be substantially different, and will ultimately distort the latitude-L_s distributions. The same process was therefore performed for the above scenarios, except the 190-400 nm total UV flux was integrated over time throughout the entire martian day. Figures 5-17 to 5-19 show the variation of the 190-400 nm *integrated total daily dose* (MJ m^{-2}) for each scenario as a function of latitude and L_s throughout the martian orbit.

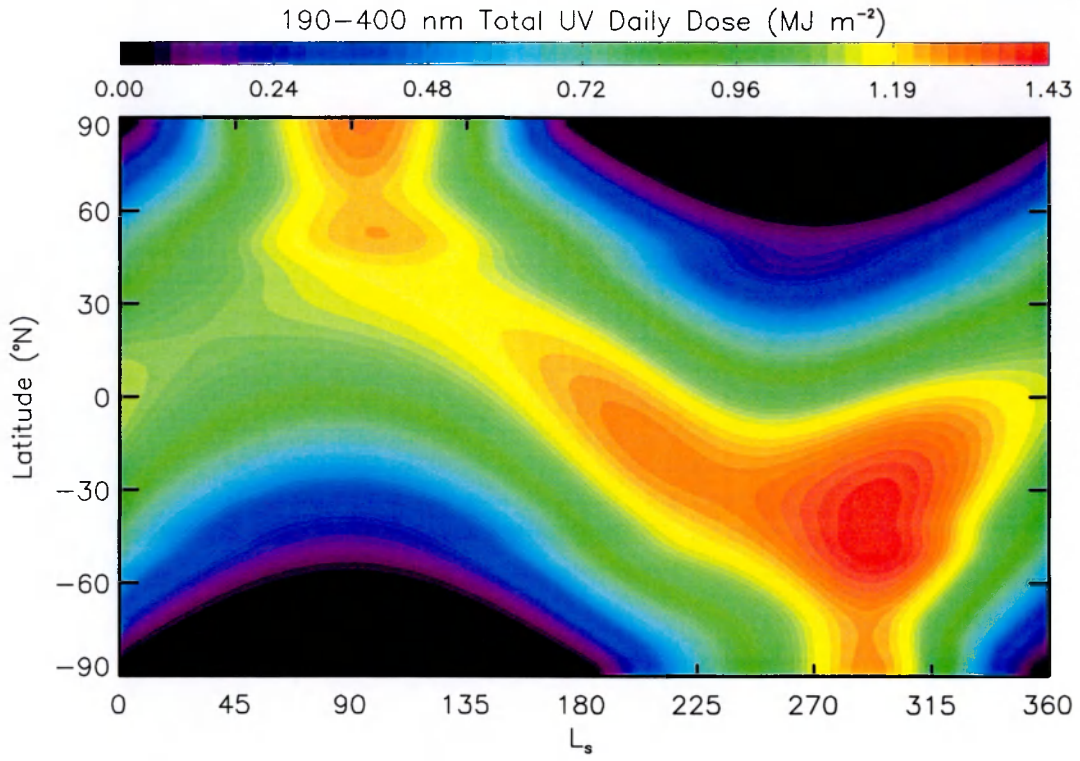

Figure 5-17: Latitude-*Ls* variation of daily UV dose (nominal dust scenario).

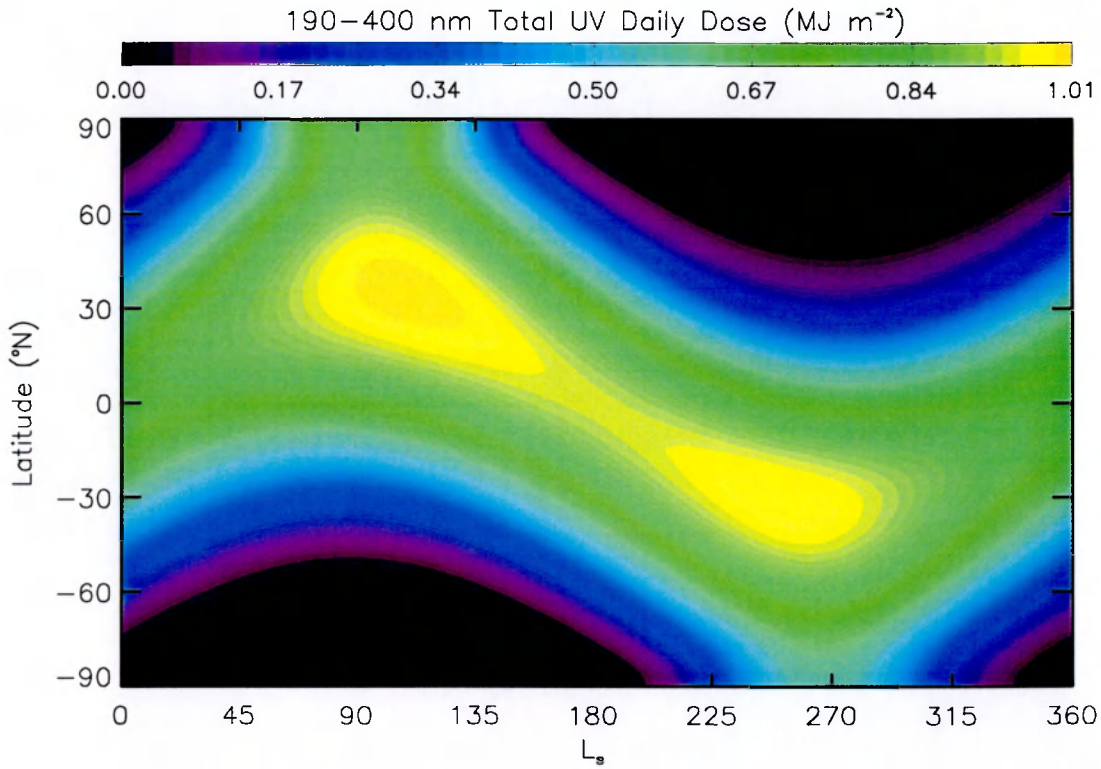

Figure 5-18: Latitude-*Ls* variation of daily UV dose (high dust scenario).

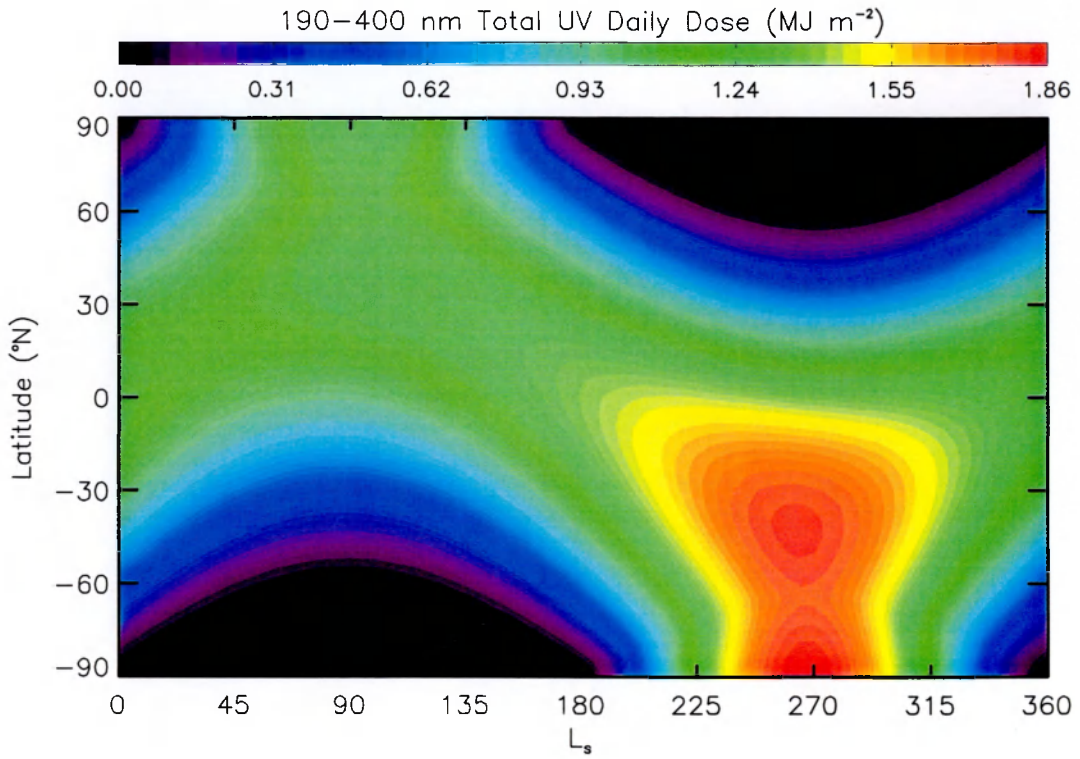

Figure 5-19: Latitude-L_s variation of daily UV dose (low dust scenario).

The distortion in UV exposure distribution between the instantaneous flux plots and the daily dose plots is strong, and the effect of the increased daylight period discussed previously is responsible. At high latitudes (around ± 75°N, near the polar regions) the daylight duration increases until the continuous polar day regime is reached. This continual irradiance throughout the day distorts the pattern seen in Figures 5-14 to 5-16, extending the relatively high dose levels into the polar regions. The low dust plot in Figure 5-19 shows the highest doses of UV concentrated in the southern near-equatorial and mid-latitude regions towards perihelion at $L_s = 270°$. This plot is also identical in distribution to the daily top of atmosphere input solar flux, analogous to Figure 5-16.

The maximum is slightly offset from the equator in the nominal scenario shown in Figure 5-17, occurring also in the southern mid-latitude region but slightly later at $L_s = 300°$. The maximum is also more dispersed throughout the year, extending towards the equator at earlier values of L_s. A secondary maximum also occurs in the northern polar region at

aphelion, with slightly lower dose values with respect to perihelion. Here, the polar day effect results in daily doses comparable to those encountered at the equator, though the instantaneous fluxes are far lower. In the nominal dust scenario, the peak dust activity occurs at perihelion at $L_s = 250°$ in the southern hemisphere, causing a maximum attenuation of the UV surface irradiance at this time, and thus shifting the maximum to a later value of L_s. The high dust scenario (Figure 5-18) has the lowest daily doses, with two discernable peak spots centred in the northern and southern mid-latitudes at aphelion and perihelion respectively. As mentioned previously, the high dust scenario distributes high dust loadings towards perihelion, reducing the surface UV due to increased attenuation during this period. Thus the aphelion and perihelion maxima are still observed, except a higher dust loading concentrated towards perihelion separates the region joining the two maxima which are present in Figure 5-17.

The peak flux calculated for nominal annual dust conditions can be seen in Figure 5-17, and occurs centred near $L_s = 300°$ and a latitude of 30°S. This area can be considered to be the most intense area on the martian surface in terms of total daily UV dose. It should be noted here that O_3 and cloud phenomena are not included in these simulations, and the calculated values should therefore be considered as an upper limit to the actual surface UV flux in certain regions. Cloud and polar hood aerosols can be present in the martian atmosphere, albeit to a far lesser degree and varying in occurrence over the martian year. The effects of clouds are discussed in Chapter Six, but are not included in the seasonal modelling due to their inherently variable nature of occurrence. The affected areas will occur generally at high latitudes towards winter, where both the production of O_3 and the formation of the polar hood will have differing effects upon the resulting UV spectrum at the surface.

The polar hood is a one of the most dynamic and least investigated atmospheric processes on Mars, highly variable both temporally and spatially. It consists primarily of condensed H_2O suspended in the martian atmosphere, creating a cloud formation covering the polar

regions. The spatial extent of the hood varies as a function of time, forming at high latitudes towards winter in both hemispheres. Ground-based telescopic observations have shown that the boundary of the polar hood is diffuse and irregular, generally concentrated in the 40-50° latitude region but varying in latitudinal extent and fluctuating daily and even hourly (Martin and McKinney 1974; Akabane *et al.* 1993). The periods of growth and recession of the hood throughout the year generally follows that of the polar caps. In the case of the northern polar hood, initial formation has been observed as early as early autumn at L_s = 159° in mid-latitude areas, reaching the pole at L_s = 171° covering the entire polar region (Akabane *et al.* 1995). The polar hood then persists through winter until early spring when the formation dissipates. The optical depth of the H_2O-ice crystals forming the polar hood is also seen to vary greatly, with observations yielding values in the range 0.5-0.8 (Akabane *et al.* 1995). Since this formation is one of the least investigated optical phenomena on Mars with no published data on the aerosol optical properties, the study of this phenomenon is omitted here. The general effects are likely to be similar to those of H_2O cloud formations, covered in Chapter Six, though possibly with greater optical depths.

5.5.4 Latitudinal Yearly Dose

The figures in section 5.5.3 reveal the variation of noon fluxes and daily doses as a function of latitude and L_s. Latitudinal areas which experience both high instantaneous and cumulative UV fluxes can be extracted from these plots for different seasons in the martian year. However, to define the long term UV dose (*i.e.* over many years) that a single latitude experiences throughout the year, another calculation is required. The same calculation was performed as for the latitude-L_s daily dose calculations, except here the daily dose was integrated over each martian sol and summed for the full martian year. The radiative transfer model was used to integrate total daily dose values over L_s = 0-359° at a latitude resolution of 2° from north to south pole, and the resultant annually integrated latitudinal doses are shown in Figure 5-20.

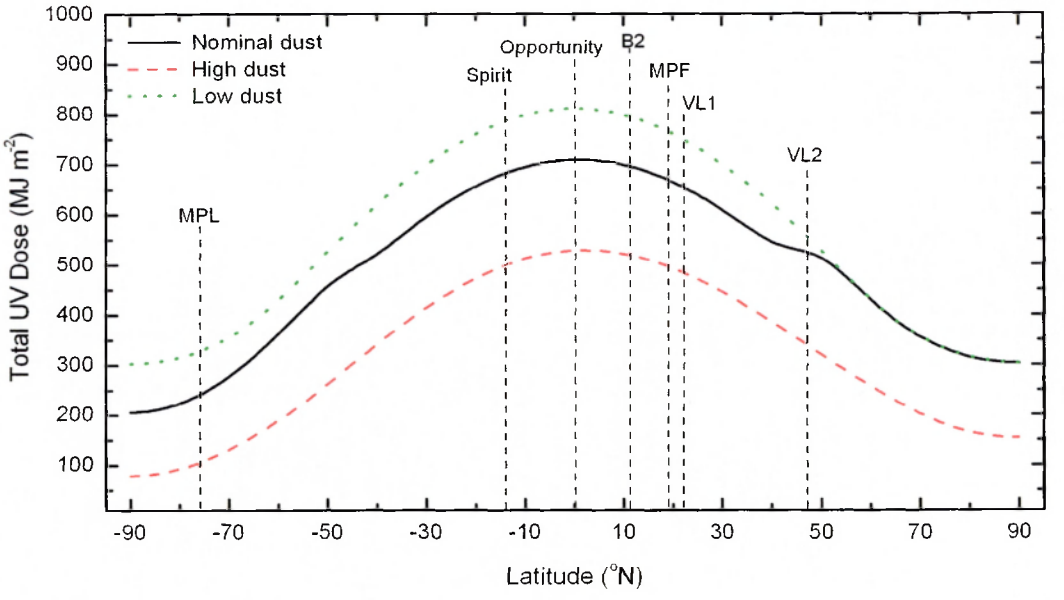

Figure 5-20: Annual 190-400 nm total UV dose as a function of latitude - locations of past and future landers are also shown.

All three variations in Figure 5-20 exhibit similar trends, with low doses at the southern polar region, increasing to a maximum towards the equator and decreasing again towards the northern polar region. The low dust scenario, as previously mentioned, yields the highest integrated annual dose. The distribution of annual dose in the low dust scenario shows a symmetric variation of total UV dose about the equator, declining by equal amounts towards each pole. Here the annual UV doses at the north and south polar regions are equal, with the annual dose at the equator 170% greater. This symmetry is lost however when varying dust loadings are taken into account throughout the martian year. In both the nominal and high dust scenarios, the northern hemisphere experiences significantly higher annual doses than the southern hemisphere. In the case of the nominal scenario, the north polar region is seen to experience a 50% greater annual dose than the corresponding southern region, and UV annual doses at the equator are 135% and 250% greater than at the north and south polar regions respectively. The same general pattern is seen in the high dust scenario except to a greater degree, with annual UV doses at the north polar region 95% greater than that at the southern

polar region. Annual fluxes at the equator are calculated to be 245% and 570% greater than in the north and south polar regions respectively.

The inflection in the nominal case variation in Figure 5-20 at latitudes of ± 45°N occurs due to the separate components required for the calculation of τ_{back} (Equations 3-13, 3-14 and 3-15). For $\tau_{nominal}$, the dust loading components as a function of L_s for the northern, equatorial and southern regions are individually described, then combined as a function of latitude. Towards high latitudes, the optical depth shows less variation (as was shown in Figure 3-7), and this effect is more extreme in the northern hemisphere. At high northern latitudes (> 50°N) the annual UV dose is equivalent to the low dust scenario dose, where the optical depth is invariant and equal to 0.1.

The general trend of the relation of annual doses between hemispheres is surprising when previous plots are considered. In the daily plots shown in Figures 5-17 to 5-19 significant maxima occur, generally displaced into the southern hemisphere. Intuitively, the latitudes at which these maxima occur would be expected to experience the highest UV doses, but this is not the case. In all scenarios in Figure 5-20, the maximum annual dose is encountered at the equator, offset from the maximum daily dose region. These regions consistently experience medium to high UV dose levels throughout the entire year. The regions of maximum daily dose are offset in latitude, and as such experience a greater degree of variation of UV daily dose throughout the year. Though the highest short-term levels do occur in concentrated regions, it is the lower daily dose values in the same latitude regions at other times in the year which counteract this effect.

The asymmetry observed between the two hemispheres when varying dust loading is considered is due to the distribution of dust across the martian surface and with L_s. In the constant dust case (low scenario) the latitudinal distribution of UV follows the same pattern as the input flux, and is correctly symmetric between hemispheres. The high dust scenario however distributes dust loading as a function of L_s, concentrating the dust loading towards

perihelion. Each polar region acquires the majority of UV dose during the polar day, either at perihelion or aphelion. Thus for the northern case at aphelion, dust loadings are relatively low, and the total UV dose is high. For the southern case at perihelion, dust loadings are higher offering greater surface attenuation of transmitted UV, reducing the level of annual UV dose at this latitude relative to the northern region. For the nominal case, the same reasoning applies, except here the dust loading distribution is a function of both L_s and latitude. Here, the peak dust loading also occurs at perihelion, but the decrease in dust loading with latitude is accounted for, increasing the southern hemisphere surface dose at mid-to-high latitudes, and decreasing for the corresponding northern regions. Thus the same general offset is seen between hemispheres, except to a lesser degree since the latitudinal effect is accounted for.

The interaction of dust in the martian atmosphere is shown here to have an extremely important effect upon the surface UV environment. Depending upon the annual dust loading distribution, UV surface fluxes can experience a wide range of values. Consistently active atmospheric conditions which continually raise particulate matter (*i.e.* large-scale dust storms) over many years would result in a significantly reduced annual surface UV dose. Correspondingly, quiet periods with little dust in the atmosphere will have the opposite effect, increasing the annual UV.

5.6 Implications for Past, Present and Future Landers

The latitude regions that planetary landers explore can be investigated in terms of the UV environment that the surface has experienced. The primary focus of present-day missions generally rests in analysis of surface materials for the detection of the presence of extinct or extant life. Using Figure 5-20, the degree of UV exposure between landing sites can be studied. Although UV radiation alone is not the only influence on the possibility of life, it is an important factor which must be considered. Different areas of the martian surface have been shown to experience both substantially different irradiation levels and annual patterns.

This 'history' of annual irradiation will inevitably make certain areas more inhospitable and chemically reactive, through enhanced oxidation formation at the surface due to UV photochemical reactions.

Areas of sustained UV irradiation may have higher levels of oxidation and chemical activity, which is dependent upon the input of solar UV. The lowest, and thus most benign, UV environment is encountered in the southern hemisphere, towards the polar regions at high latitudes. These regions would be expected to provide the least levels of oxidation, from the viewpoint of UV irradiation alone to a first approximation. In terms of exploration aimed at the detection of organics, the lowest UV dose regions would be expected to yield the most probable places to find organic remnants of extinct organisms, since UV induced breakdown will be at its lowest.

Other factors also play important roles in the probability of finding life markers in the martian regolith, such as humidity and temperature levels, but cases here are regarded purely from the viewpoint of UV. The latitude regions explored for past and future landers are overlaid on Figure 5-20 to show the UV doses experienced by specific region over long periods of time. The majority of martian missions have been located in the northern low-latitude regions, which from the viewpoint of UV offers the most unlikely place of finding organics in the martian regolith. The reasoning for landing sites on Mars in these regions originates from the most economical regions for fuel required for landing – generally, more fuel is required for high latitude landing sites, increasing the constraints on the mission. The only high latitude landing site in the southern hemisphere was MPL (though this mission was unsuccessful, it is included here to highlight the choice of landing site). In the context of long term regolith irradiation, the MPL landing site would have offered the least irradiated region and the most likely site so far for the detection of organic remnants of past life. More planned missions to these high latitude regions are required for the likely detection of past life.

The next martian spacecraft to land on the surface of Mars will be Beagle 2, Spirit and Opportunity. Spirit and Opportunity will land at 15°S and the equator respectively, placing them within the peak annual dose region. Beagle 2 will land nominally at 11.6°N, also in the peak annual UV dose region. Though this mission is an astrobiological mission, the UV environment is the close to the most severe possible encountered at the martian surface. This effect unfortunately lessens the probability of the detection of organic material at the martian surface. A number of other interesting atmospheric processes however will occur in this low-latitude region, forming the subject of the next chapter.

Chapter Six

The UV Environment of the Beagle 2 Landing Site

The radiative transfer model was utilised to analyse in detail the UV environment of the Beagle 2 landing site. This process allowed pre-landing determination of the possible UV fluxes that Beagle 2 will encounter, to aid in the post-flight interpretation of data returned through the identification of specific signatures of atmospheric phenomena, such as dust devils, clouds and fogs, and also for cases of partial solar eclipses by the martian moon Phobos. This chapter is based upon the work published in Patel *et al.* (2003b).

6.1 Seasonal/Diurnal Variation

6.1.1 Mission Dose

The UV surface flux at the Beagle 2 landing site was initially investigated to study the variation over the mission lifetime. Beagle 2 is a relatively short duration mission when compared to the Viking missions, with a nominal mission lasting for nearly a quarter of the martian year. The nominal mission fluxes are shown in Figures 6-1 and 6-2. Figure 6-1

shows the spectra expected at both beginning (BOM) and end of mission (EOM) at local noon. Little variation is seen between the two situations, corresponding to $L_s = 322°$ and 53° respectively. However, this representation does not accurately reflect the period throughout the entire mission, as the daily UV dose (190-400 nm) is found to both increase and decrease.

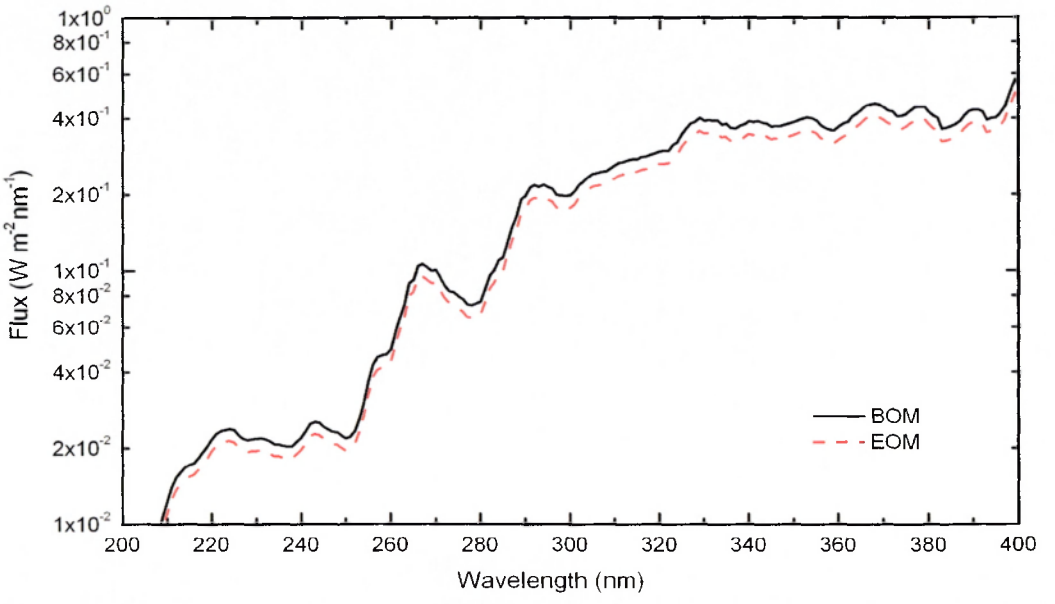

Figure 6-1: Beginning and end of mission fluxes.

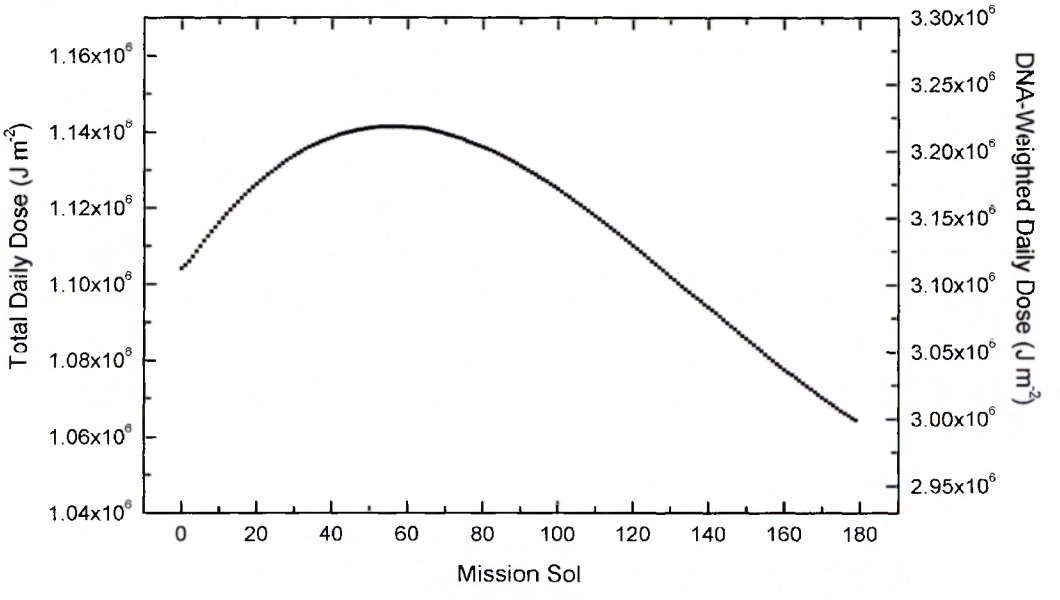

Figure 6-2: Daily UV doses throughout the mission.

Figure 6-2 shows the variation of total daily dose throughout the mission. The EOM daily dose is slightly lower than the BOM value, but an increase in daily dose is found before the mid-point of the mission. The initial increase in total daily dose is attributable to the progression of Mars towards northern summer, with longer daylight lengths and higher noon fluxes. The subsequent decrease of total dose is due to the general reduction in solar input flux as Mars moves towards aphelion. The combination of these two factors creates the peaked variation, increasing initially in the mission then declining towards the end as the effect of decreasing solar input begins to dominate over the smaller maximum solar zenith angles.

6.1.2 Diurnal Variations

The diurnal variation of UV at the landing site was also investigated, as throughout each sol the sensor will experience a wide range of flux. The diurnal plots here are modelled with a nominal background dust loading, with no other aerosols present. The sensor consists of six wavelength channels, covering 190-220 nm, 228-240 nm, 240-260 nm, 285-320 nm and 320-385 nm, as well as the full 190-400 nm flux. The diurnal variations expected in all six of the bandpasses are shown in Figure 6-3, for a latitude of 11.6°N at $L_s = 0°$, with a background optical depth of 0.20. The direct and diffuse components are also shown as a function of time of day. The effect of Rayleigh scattering due to gas in the atmosphere is noticeable as a function of λ. In Figure 6-3a (the shortest wavelength band at a centre wavelength (CWL) of 210 nm) the direct and diffuse components are of comparable magnitude, since the effects of Rayleigh scattering ($\propto \lambda^{-4}$) are more pronounced. As the centre wavelength increases through to 350 nm (Figure 6-3e) the diffuse component formed through the scattering process gradually decreases with respect to the direct component, as Rayleigh scattering effects decrease. In the open channel (Figure 6-3f) the total UV flux is primarily due to direct flux. Over two orders of magnitude difference in flux levels is experienced between the 210 nm

channel and the open channel. These diurnal curves should be typical of the conditions the sensor will experience on the martian surface.

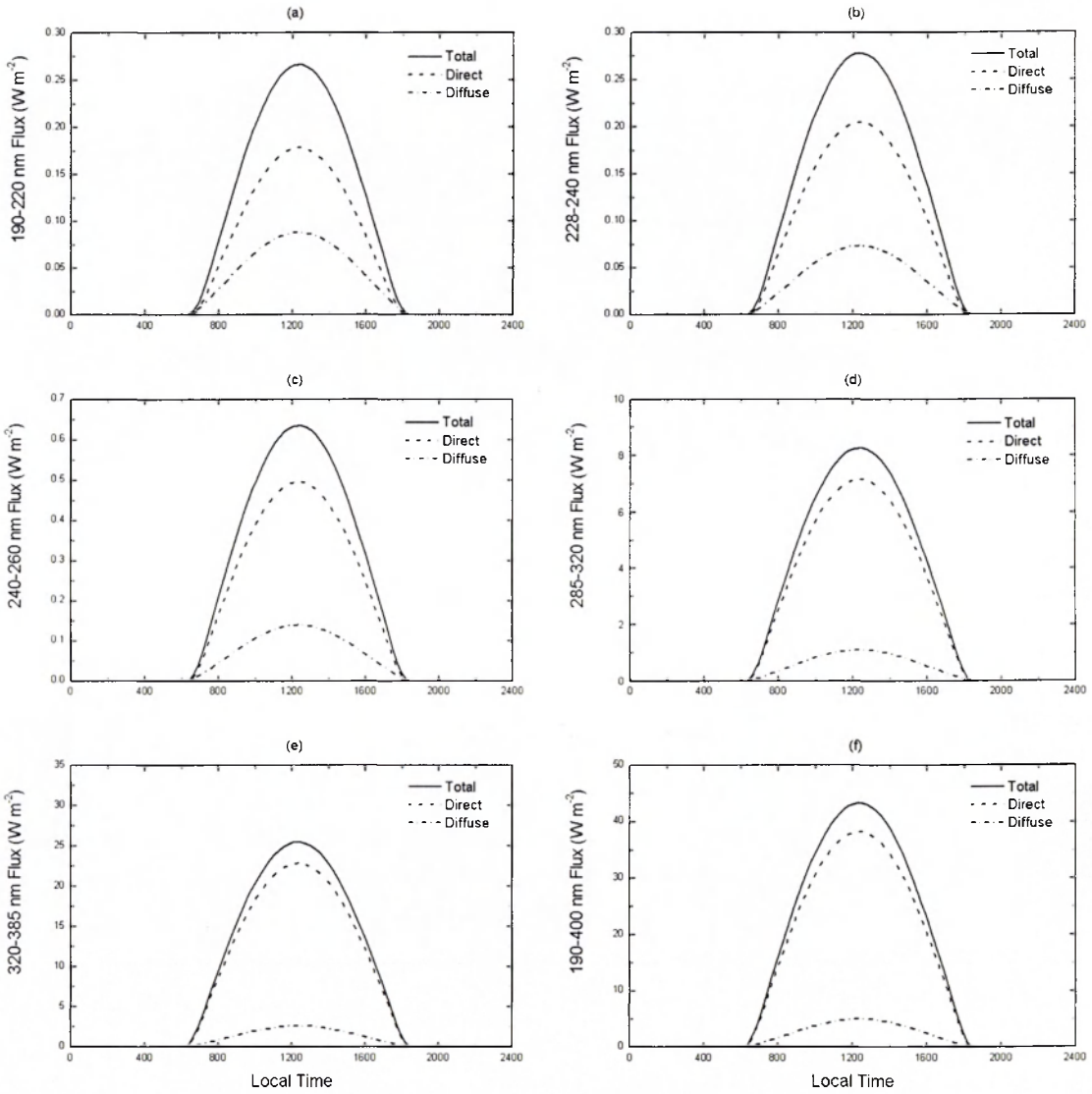

Figure 6-3: Diurnal flux variations in the UV sensor channels.

6.2 Dust Devil Encounter

6.2.1 Dust Devil Phenomena

Dust devils are dust laden convective vortices which form both on Earth and Mars through intense heating of the ground by the Sun. This surface heating creates convective

atmospheric plumes, rotated by surface eddies and obstacle deflected ambient wind shear. Dust devils tend to form in the early afternoon, when solar heating of the ground has reached its maximum and the surface layer is at its warmest. Intense heating of the atmosphere by the ground creates a turbulent near-surface layer, and the resultant convective vortex becomes visible when particulate material is lofted into the vortex core. Terrestrial and martian dust devils form in the same manner and have similar meteorological signatures, but terrestrial vortices tend to be approximately an order of magnitude smaller in size, as observed from a number of terrestrial field studies which have characterised their general structure (Sinclair 1966; Ryan and Carroll 1970; Metzger 1999). These vortices are of particular importance on Mars due to their contribution to the global martian dust cycle, and may play a major role in the triggering of local and global dust storms (Kahn *et al.* 1992; Cantor *et al.* 2001). The presence of dust devils also has important implications for surface landers, since the significant dust loading of these phenomena can inhibit solar array performance and cause severe problems with moveable joints and motors.

Dust devils raise significant quantities of dust, and consequently will be observable by imaging/light detection instrumentation. For the case of modelling the dust devil, the passage of the dust laden vortex was simulated by variation of τ_{ddevil} in the 0-1 km layer as a function of time, simulating passage of the vortex over a fixed point on the surface.

6.2.2 Calculation of Optical Properties

The process of calculating the optical parameters for dust devils is even more complex than in the dust storm case. The processes triggering these events and the general conditions which sustain such phenomena are still poorly understood, with no detailed *in situ* measurements previously taken on Mars. The formation of a convective vortex is qualitatively understood in terms of convection dynamics, created through heating of the martian surface at periods of high solar insolation. The process governing the actual lofting

of dust however is still not well understood, but work is currently being carried out in an attempt to quantify this process (Greeley *et al.* 2003). According to laboratory simulations of dust devil lofting (Hsu and Fattahi 1976) a free stream threshold wind speed in excess of 30 m s^{-1} is required to overcome the cohesive forces binding surface particulates (Greeley and Iverson 1985). Such surface wind speeds have never been directly observed on Mars and the exact nature of the lofting process remains in doubt, though various other processes such as the saltation of large particles impacting the surface may produce the desired threshold conditions.

Dust devils are characterised by sudden changes in wind velocity, rise in air temperature and a reduction in pressure. In general these events last a few minutes during which time they can loft significant amounts of particulate matter into the atmosphere (Metzger 1999). On Mars, dust devils range in size from tens of metres to a km in diameter and can be up to 10 km in height, although the visible dust core is approximately 10% of the total 'area of influence', and of that 50% is the dust free 'eye' of the vortex (Sinclair 1966; Metzger 1999).

A range of values was used to define physical parameters for the dust devil, taken only as a general representation of this highly dynamic event. The optical properties for this case needed to be explicitly defined, as a unique set of dust particles is introduced to the lower atmosphere over a short period of time. The following range of particle sizes was provided by T. Ringrose (*personal communication*), and is shown here to justify the choice of particle size required for the calculation of optical properties.

Dust devils loft a range of particles which is dependent upon a variety of parameters, such as the available regolith particle size distribution, dust abundance and internal wind speed within the dust devil as a few examples. In this case, to simulate to first order the most common dust aerosol sizes within a dust devil, the lofting of dust particle sizes as a function of wind speed was investigated. The frictional wind speed required to initiate lofting of a

particle is dependent upon the radius of the particle, and the most easily lofted particle radius[1] assuming nominal conditions is ~75 μm, at a wind speed of around 35 m s^{-1} (Greeley and Iverson 1985; Shao and Lu 2000). Given that each event will undoubtedly yield a unique set of mean particle sizes dependent upon a number of factors such as rotational wind speeds and particle distribution of the local terrain etc, 75 μm was used for the dust devil mean particle radius as a baseline to simulate the dust devil event.

Values of 50 μm and 100 μm were also used to demonstrate the effects of varying particle size, and indicate any trend in the dependence upon this parameter. An assumption here is that these particles originate from the same material as the background haze (Toon *et al.* 1977), thus allowing the use of the same refractive index values as the suspended dust. Given these mean particle sizes and refractive indices, the optical parameters (single scattering albedo (ω_{dd}) and asymmetry parameter (g_{dd})) for the dust devil aerosols were calculated, using the Mie scattering routine *bhmie.pro* (Bohren and Huffman 1983) in the spherical approximation. This method is justifiable since the particles are so large with respect to the incident radiation – at these very large sizes (> 50 μm in the UV) the effect of the shape of non-transparent particles on the parameters relevant to intensity becomes negligible. Mie calculations can therefore be used so long as only the parameters related to intensity are to be calculated. The extreme size of the particles results in a phase function which is effectively flat, with a very strong narrow peak in the forward direction, the width of which is dependent only upon the size of the particle – the larger the particle, the narrower the peak (Hansen and Travis 1974). The single scattering properties at these sizes and wavelengths become effectively insensitive to shape (Mishchenko *et al.* 2000).

The calculated values of ω_{dd} and g_{dd} are shown in Figure 6-4. Both optical properties are relatively invariant across the wavelength range, except close to 200 nm where ω_{dd} (g_{dd})

[1] This radius corresponds to the particle radius which requires the lowest frictional wind speed to initiate lofting.

sharply increases (decreases). It can be seen from the values of g_{dd} that scattering is strongly peaked in the forward direction consistent with scattering by particles which are extremely large with respect to wavelength, having values close to unity. Very little variation was seen in the calculated optical properties between 50, 75 and 100 μm sized particles, due mainly to the extreme size.

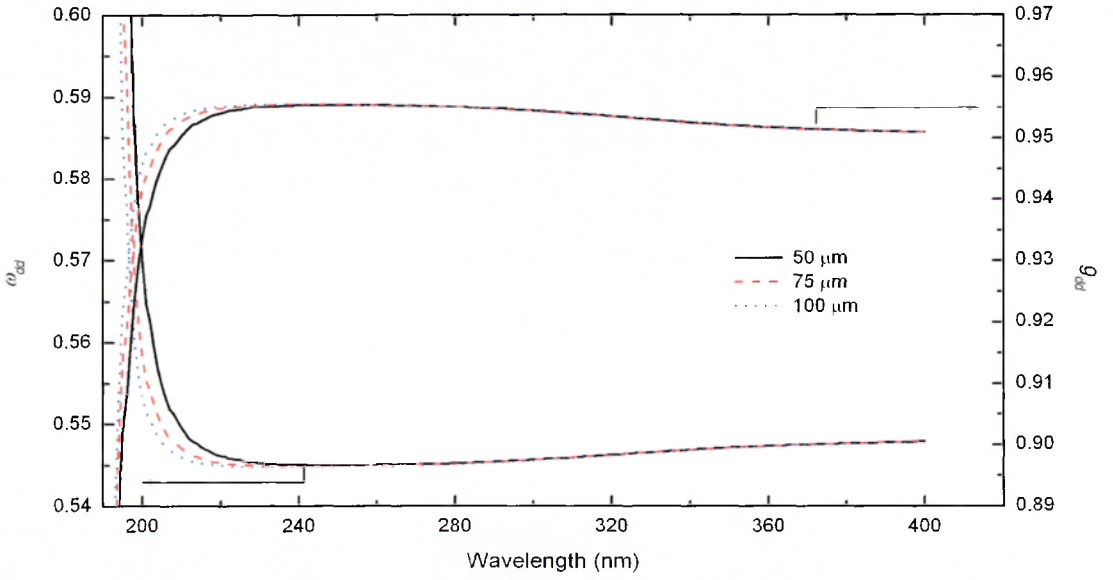

Figure 6-4: Dust devil aerosol ω_{dd} and g_{dd} values between 180 and 400 nm.

The dust loading as a function of radius was found by using the value of particle number density for martian dust devils as observed and analysed at the MPF landing site. A value of 7×10^{-6} kg m^{-3} was used for the total horizontal column particle density through the centre of the dust devil core, as derived through spectral differencing techniques applied to MPF camera images (Metzger *et al.* 1999). This density was integrated vertically over the height of the dust devil to provide a total vertical particle number density. To give a realistic radial density variation throughout the dust laden section of the core, and due to the large particle number population within this part of the dust devil, a Gaussian particle distribution was used, centred around the equilibrium position of the particle size, given by:

$$n_{dd}(r_{dd}) = \frac{1}{\sigma\sqrt{2\pi}} \exp\left[\frac{-r_{dd}^2}{2\sigma^2}\right] \tag{6-1}$$

where σ is the standard deviation and r_{dd} is the radial position within the dust laden core. This distribution can be used according to the central limit theorem, where for a large number population the probability distribution is approximated by a Gaussian distribution regardless of the parent function. The particle equilibrium position is determined through the balance of centrifugal and aerodynamic radial drag forces experienced by each individual particle (Sinclair 1966; Kish *et al.* 2001).

An approximation to the vertical optical depth is then readily obtained throughout the dust devil as a function of radial distance through the standard relation:

$$\tau_{ddevil}(r) = n_{dd}(r_{dd}) Q A_{avg} \tag{6-2}$$

where τ_{ddevil} is the optical depth of the dust devil, n_{dd} is the particle density, Q is the extinction efficiency of the particles (2.60) and A_{avg} is the cross-sectional area. Optical depth as a function of passage time was then derived by assuming an ambient wind speed of 2 m s^{-1} which carries the dust devil along the surface.

The structure of the dust devil is modelled here as a vertical dust column, with a clear inner core where no dust is present. In reality, the structure will be driven by ambient boundary layer wind which carries the vortex across the martian surface. This has the effect of shearing the structure to a non-vertical position in some cases, blocking the 'clear upward view' from the centre of the dust free core. However, for the case studied here only the effects of a uniform vertical column passing over the lander are considered, and the shearing effect is not included.

6.2.3 Passage simulation

The UV time profiles of the dust devil traversing the centre of the lander are shown in Figures 6-5 and 6-6. Figure 6-5a shows the profile for the total and direct UV flux for the case of a 1 km high dust devil. The resulting minima observed are due to the sudden obscuration caused by the introduction of a large amount of dust into the line of sight, resulting in the same effect as in the case of a dust storm, but differing by the far shorter duration of the event.

The transmission of total and direct UV reduces to a first minimum in Figure 6-5a where the leading edge is directly above the lander. As the leading edge passes over the lander, the core of the dust devil is encountered. This low pressure area of the vortex is dust-free, and thus offers a clear view of the sky. In this region, the transmission returns to full pre-event levels throughout the passage of the core. As the dust-free core passes beyond the lander, the trailing edge of the dust devil begins to pass over the lander. This portion of the vortex is again loaded with dust, and the characteristic dip is seen again in the flux profile.

The dependence upon particle size shows that the double minimum experienced intensifies for smaller effective particle sizes. Initially this effect seems counter-intuitive since the cross-sectional areas are smaller, but can be understood in terms of particle number densities. Larger particles occupy more volume than smaller particles, and thus for an equivalent mass load, the number density (n_{dd}) in a small particle vortex will be greater than that in a large particle vortex. Since n_{dd} is larger for smaller particles and the optical properties are relatively invariant over the sizes considered here, the subsequent optical depth as calculated in Equation 6-2 is larger for smaller particles.

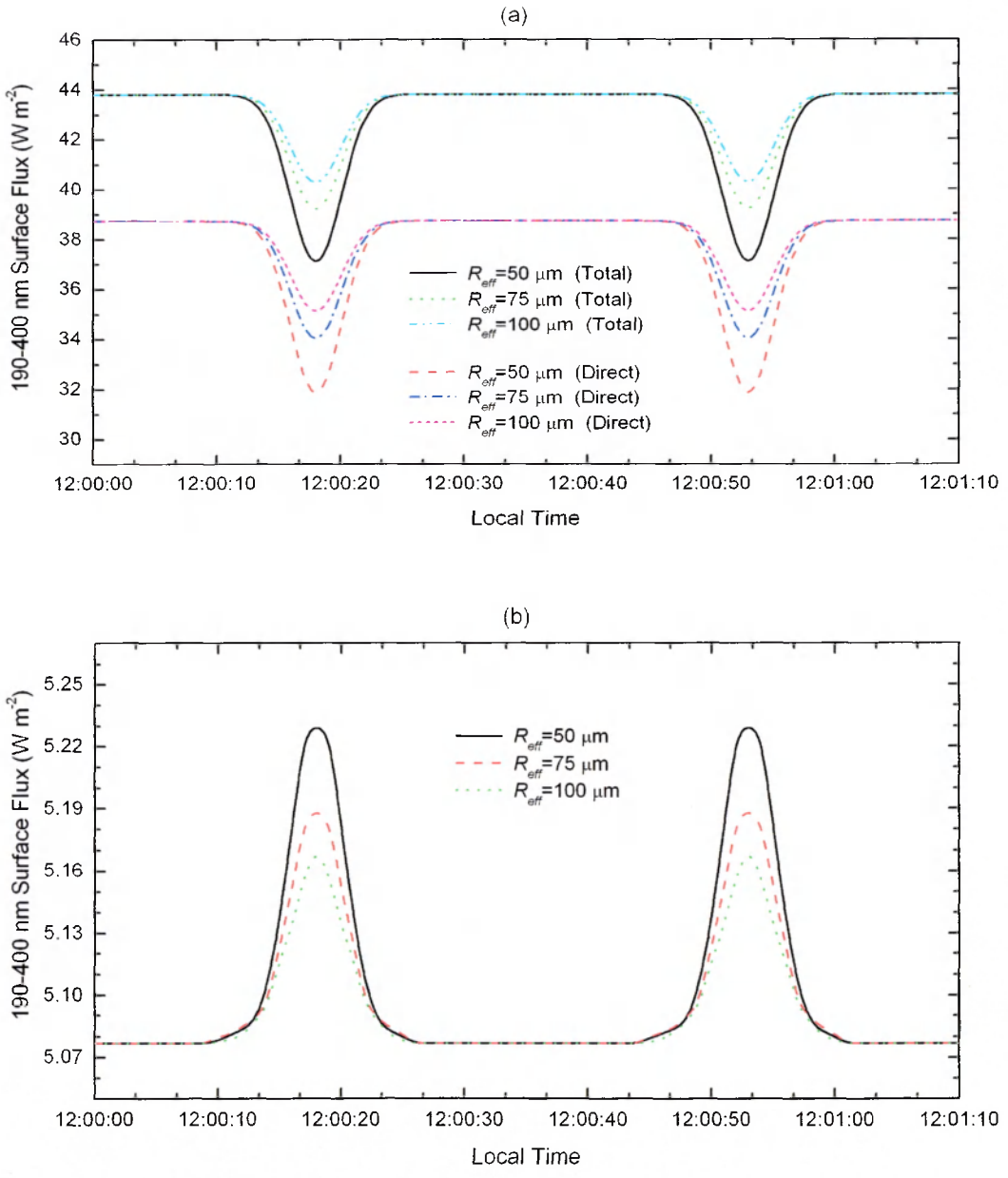

Figure 6-5: Dust devil UV profile for (a) direct and total fluxes and (b) diffuse fluxes.

Figure 6-5b shows the effect of a 1 km high dust devil passage upon the diffuse spectrum. In this case a double maximum is produced coincident with the minima of the total and direct flux, since the extra dust in the vicinity increases the component of UV formed through the scattering process. This phenomenon only however occurs for relatively low total optical depths – between total optical depths (τ_{back} + τ_{ddevil}) of approximately 0-1.5, the diffuse component increases as the dust loading increases, as demonstrated in Figure 5-4. Above

approximately 1.5 however, the diffuse component begins to decrease with increasing dust loading, as attenuation begins to dominate.

The effect of increased dust obscuration between dust devils upon the UV profile is shown in Figure 6-6, for cases of dust devils which are 1, 5 and 10 km in height. Here the consequence of greater amounts of dust with increasing height is to deepen the double minima. As expected, the greatest decrease in total UV is seen in the tallest (10 km) dust devil, with a drop in total UV flux of 65% at the centre of each minimum. The depth of the minima are thus shown to be related directly to the amount of dust contained within the dust devil.

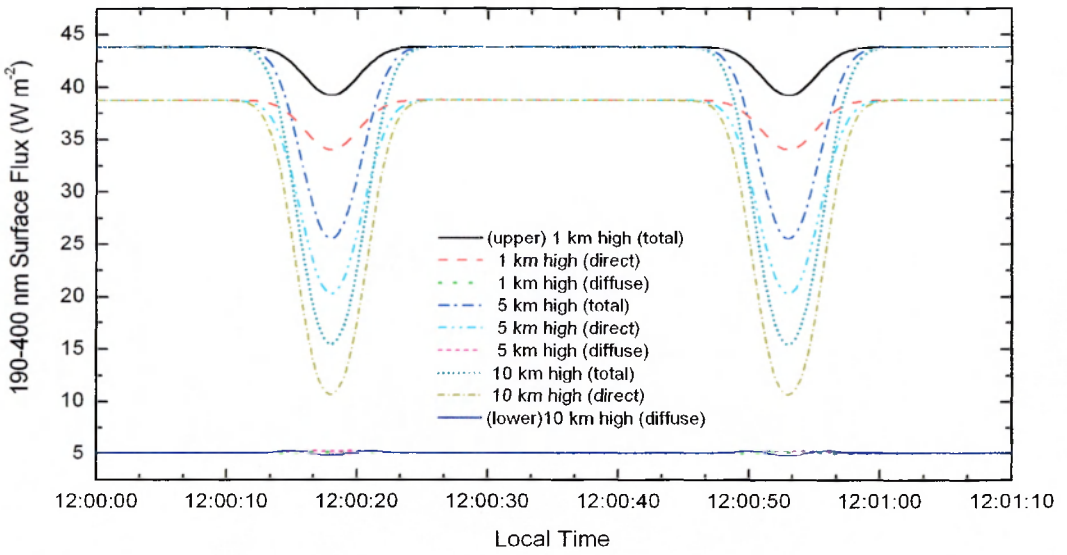

Figure 6-6: UV profiles for increasing dust devil sizes.

These events will change in profile as each vortex will be unique, with wind speeds and core sizes varying between each dust devil. An increase in the width of the dust devil was found to broaden the profile widths of the double minima and the central plateau, increasing the total passage time. Conversely, an increase in ambient speed resulted in the contraction of the two minima, since the duration of the passage is reduced by the higher wind speeds. Also, if the vortex is non-vertical the centre plateau between the two minima may not be observed

dependent upon the angle of the shear, and this peak may be slightly attenuated or non-existent if the shear angle is large enough.

Such a characteristic dip in the sensor profile as shown in Figures 6-5 and 6-6 (at times of non-eclipse events or shadowing) will give positive identification that a dust laden vortex has traversed the lander, especially when correlated with other environmental sensors such as pressure, wind velocity and air temperature.

6.3 Cloud Formation

6.3.1 H_2O/CO_2 Cloud Occurrence

The presence of discrete clouds in the martian atmosphere has been observed regularly, and has been monitored during most of documented telescopic history (Martin *et al.* 1992). Cloud formation on Mars can take many forms, as near-surface fogs (Pollack *et al.* 1977), tenuous clouds (Curran *et al.* 1973), equatorial belts (Clancy *et al.* 1996), and polar hoods (James *et al.* 1987) as examples. Orbital spacecraft have investigated the presence of condensate clouds, with Mariner 6 and 7 providing the first orbital observational evidence for CO_2 clouds (Herr and Pimental 1970). Condensate clouds on Mars form from either H_2O or CO_2 vapour in the atmosphere, when atmospheric conditions reach low enough temperatures for either species to condense. This condensation occurs at varying altitudes, attributable to the extreme seasonal and diurnal changes in temperature profiles experienced on Mars. One process of formation is believed to be nucleation around suspended dust particles (Pollack *et al.* 1977), where suspended dust in the lower atmosphere provides a basis onto which water vapour can condense, given adequate abundance and cold enough temperatures. The suspended aerosol thus becomes a dust-ice composite, with an inner core composed of dust, surrounded by an outer ice shell of thickness varying with time. This process varies diurnally, with water vapour condensing onto suspended dust particles during the night and evaporating

away towards midday (Colburn *et al.* 1989). At higher altitudes however, water vapour (and under colder conditions, CO_2) can condense as ice crystals, forming discrete observable cloud groups. High altitude regions, such as that surrounding the large shield volcano Olympus Mons, give frequent rise to significant cloud cover through the orographic uplift of relatively moist air, and have been observed regularly (Akabane *et al.* 2002).

6.3.2 Calculation of Optical Properties

The area of interest here is the Isidis region which falls within the area of the aphelion cloud belt, an annual equatorial cloud belt of varying opacity covering the region 10°S to 30°N (Clancy *et al.* 1996). This equatorial cloud feature usually becomes prominent towards late northern spring, and will become relevant late in the nominal Beagle 2 mission. It is formed primarily of H_2O aerosols at altitudes where temperatures falls low enough for water vapour to condense as crystals in the martian atmosphere. HST observations of the aphelion cloud belt revealed maximum optical depths of around 0.25, in low latitude regions towards L_s = 60°-100° (Wolff *et al.* 1999). Ground-based observations of the cloud belt by Nakakushi *et al.* (2001) indicated that the optical depth due to water ice aerosols alone can reach as high as 0.7 in the Isidis region close to midday, a value regarded here as an extreme upper limit. The opacities derived in such calculations depend heavily upon the phase function used for the water ice crystals, and it was noted by the authors that the use of an alternate viable phase function reduced the derived opacity by ~ ⅔ .

A cautious approach is therefore adopted here for the expected H_2O cloud opacities, and a value of 0.3 for τ_{lcloud} is considered nominal in this case. This value is justified because the conditions Beagle 2 will experience will be just prior to the maximum formation of the aphelion cloud belt, when cloud opacities reach their highest values. However to cover all reasonable situations of possible cloud formation and indicate trends, a range of optical depths was investigated. Cloud optical depths (τ_{lcloud}) of 0, 0.15, 0.3 and 0.45 were used in the

calculations – though 0.3 is considered a reasonable value, a slightly higher value was included to cover all possibilities and aid in the interpretation of any trend.

Observations by Phobos 2 indicated an effective ice particle radius for low-latitude clouds in northern spring of 2.3 ± 0.4 μm (Rodin *et al.* 1997), in agreement with the 2 μm value derived through TES onboard MGS (Pearl *et al.* 2001). These observations most closely match the expected conditions that Beagle 2 will experience, and this effective radius is taken as nominal for this case. Different observations however have yielded smaller particle sizes, such as Petrova *et al.* (1996) indicating radii < 1 μm, and a range of particle sizes are therefore used to cover all possibilities. Particle sizes of 0.5, 1.0 and 2.3 μm were used, covering the observations of Petrova *et al.* (1996), Rodin *et al.* (1997) and Pearl *et al.* (2001) – the 1.0 μm value provides an intermediate value between the observed sizes, to aid in the interpretation of trends.

The refractive indices for water ice of Warren (1984) were used, and the Mie code *bhmie.pro* (Bohren and Huffman 1983) was used for the case of spherical pure ice particles to determine the cloud single scattering albedo (ω_c) and asymmetry parameter (g_c). ω_c has unity value throughout the UV since the water ice has negligible absorption in the UV and scattering dominates completely. Calculated values of g_c are shown in Figure 6-7 for the range of aerosol sizes. Little net variation is seen in g_c for the 0.5 μm aerosol, with a value oscillating around ~0.83. The magnitude of the oscillation increases in the case of the 1 μm aerosol. For the 2.3 μm aerosol the oscillations decrease in frequency, though a reduction in g_c is present between 230 and 360 nm with respect to the smaller sizes.

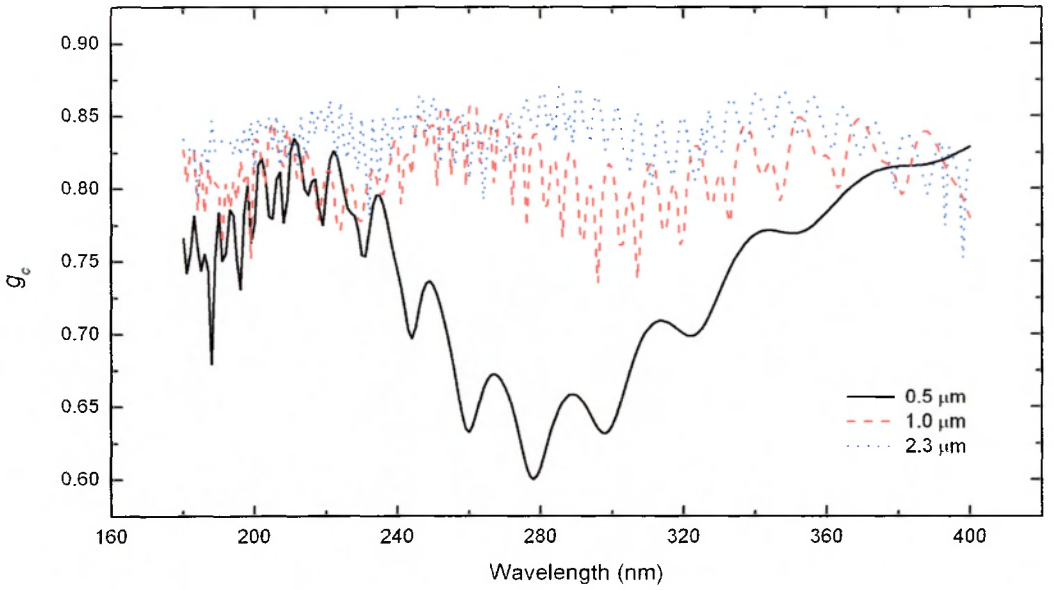

Figure 6-7: g_c values for 0.5, 1 and 2.3 μm H_2O aerosols.

Thus a water ice cloud formation at an altitude between 20 and 21 km was simulated, over optical depths of 0, 0.15, 0.3 and 0.45 at $L_s = 60°$ for local noon, with a range of effective particle radii of 0.5, 1.0 and 2.3 μm.

6.3.3 Event Occurrence

The effect of a cloud formation above the landing site is shown in Figure 6-8, which shows the ratio of diffuse to direct UV flux on a day with no cloud present compared to that with cloud present in varying abundance. Little variation in the total spectrum is observed between cloudy and clear days due to the low cloud optical depths involved (compared to Earth), so the data are displayed in terms of diffuse/direct ratio. The ratio shows the same general pattern between the four scenarios, but each one is found to be offset. For the clear day the diffuse flux is relatively weak, increasing gradually towards 200 nm. In all cases scattering increases with decreasing wavelength. On a day with cloud formation present, the same increase in diffuse contribution is observed, but the general contribution from all wavelengths is far higher.

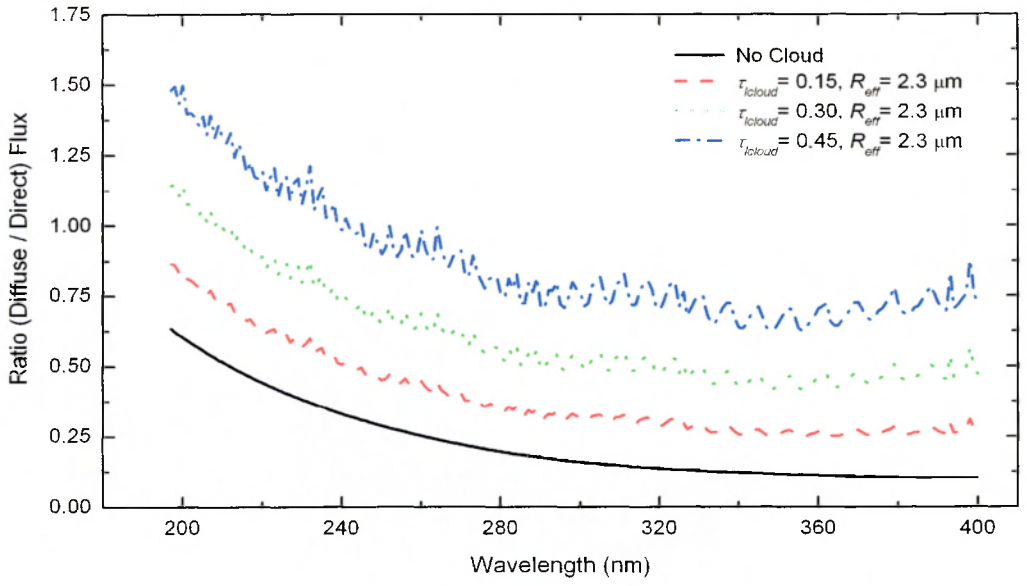

Figure 6-8: Diffuse/direct spectra ratio for 2.3 μm cloud particles over varying opacity.

The ratio reaches unity at around 210 nm in the case of a τ_{lcloud} = 0.3, and the diffuse component exceeds that of the direct UV flux in the case of τ_{lcloud} = 0.45 below 240 nm. A small oscillation is observed in the high optical depth cases, most notably in the case with τ_{lcloud} = 0.45. This effect arises due to the oscillation of the phase function at these wavelengths, manifesting in these calculations through g_c. Since the particles are non-absorbing, variations in g_c result in an oscillating variation of light scattered into the forward and backward directions, resulting in a oscillating spectrum at the surface.

Figure 6-9 shows the same ratio variation over optical depth, except for the case of smaller particle sizes. The same general effects are observed as in Figure 6-8, except here a particle size dependent effect is revealed. As R_{eff} decreases, a departure is seen in the diffuse/direct ratio over λ, occurring between 240 and 360 nm, and increasing in magnitude with increasing optical depth. Again, this feature is attributable to g_c – as R_{eff} decreases, the particles become less forward scattering, and g_c decreases correspondingly as shown in Figure 6-7. This results in a net increase in the amount of isotropically scattered light, increasing the diffuse flux and consequently increasing the diffuse/direct ratio. If elevated

diffuse flux levels are detected (using the above ratio comparisons) when there is no easily observable increase in dust loading through imaging data, it will be feasible to indirectly deduce the presence of condensate clouds.

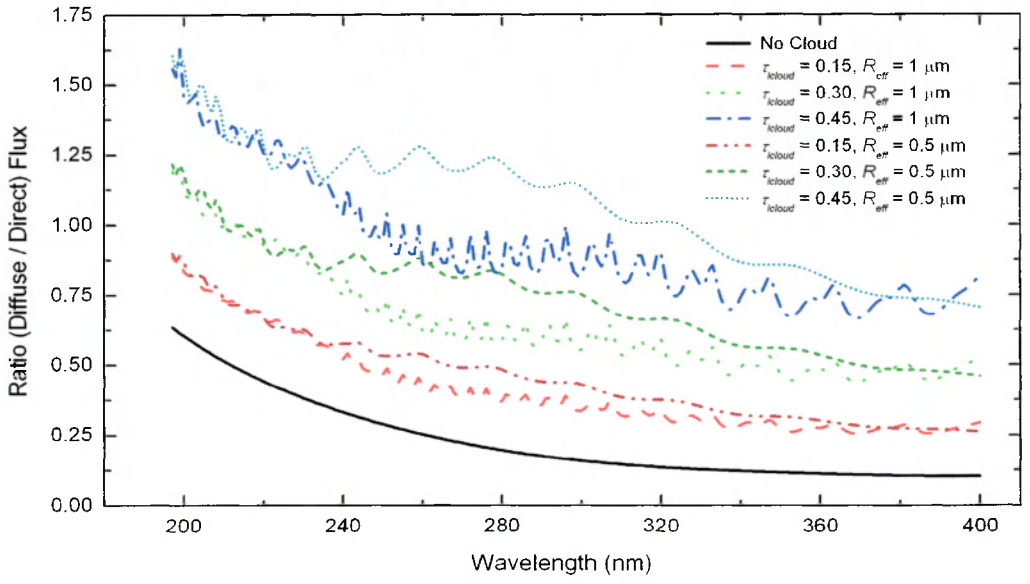

Figure 6-9: Diffuse/direct spectra ratio for 0.5 and 1 μm cloud particles over varying opacity.

6.4 Near-surface Morning Fogs

6.4.1 Occurrence

Cloud formation is characteristic of high altitude H_2O condensation, but a similar mechanism also governs the occurrence of near-surface fog phenomenon. The presence of near-surface fogs was observed by the Viking landers, manifesting as peculiarities in the diurnal optical depth profiles (Pollack *et al.* 1977). They noted that the morning optical depth values were consistently slightly higher than the afternoon optical depth values, and attributed this to the formation of a near-surface morning fog in the vicinity of the landing site. MPF and Phobos 2 optical depth observations also lead to the same conclusions for the enhanced morning optical depths (Smith and Lemmon 1999; Petrova *et al.* 1996). Formation is

believed to occur exclusively through nucleation around suspended dust particles in the atmosphere (as opposed to self-nucleation).

The behaviour of these fogs has been investigated previously (Petrova and Markiewicz 1998; Inada *et al.* 2002), and their appearance is believed to be a regular morning phenomenon. During the coldest periods of the martian night, temperatures drop low enough to allow water vapour in the near-surface region to condense onto the low-level dust particles, forming dust-ice composite aerosols. As sunrise occurs, the process of evaporation is initiated as input solar flux begins to provide thermal energy to the martian atmosphere, sublimating the ice shells. This continues towards midday, when the ice shell is completely sublimated. This coating of suspended dust particles with ice shells will have an impact upon the morning UV profiles that the sensor will measure, if this process occurs.

6.4.2 Optical Properties

Composite fog aerosols are defined here as standard background dust cores of radius r_d surrounded by a water-ice mantle of radius r_i. The single scattering albedo (ω_{fog}) and asymmetry parameter (g_{fog}) of these composite particles were calculated using the scattering code *bhcoat.f* (Bohren and Huffman 1983) for dust cores coated with an outer mantle. The radius and refractive indices of the dust cores were taken as for the background haze from Ockert-Bell *et al.* (1997), while the refractive indices of Warren (1984) were used for the water-ice mantle. The mantle radius is time-dependent, sublimating from the dust core after sunrise due to absorption of solar radiation. The time-dependent expression for the radius $R(t_{fog})$ of the composite particle is taken from Equation 4 of Petrova *et al.* (1996), who derived a fit to the observations of morning fogs from Phobos KRFM reflectance data given by:

$$R(t_{fog}) = r_d + \frac{\alpha_s}{\rho_i}(t_f - t_{fog}) \qquad for\ t_{fog} < t_f \tag{6-3}$$

where α_s is the sublimation rate of the ice mantle, ρ_i is the density of ice and t_f is given by:

$$t_f = \frac{\rho_i}{\alpha_s}[\,R(0) - r_d\,] \tag{6-4}$$

where $R(0)$ is the initial size of the fog aerosol before sunrise. ρ_i is taken to be 931 kg m^{-3} and α_s is taken as 1×10^{-6} kg m^{-2} s^{-1} as calculated in Petrova *et al.* (1996). It is assumed that a water ice mantle with an initial r_i 1.5 times greater than r_d exists coated around each particle, again roughly consistent in size with the model studies of Petrova and Markiewicz (1998) and Inada *et al.* (2002) for this part of the morning profile.

This expression was used to derive the variation in mantle radius at 5 minute resolution from sunrise, and at each point the optical properties were calculated. Calculated values of ω_{fog} and g_{fog} for the case of $t_{fog} = 0$ are shown in Figure 6-10. g_{fog} oscillates around 0.83, with ω_{fog} oscillating around 0.70 and increasing sharply below 220 nm. The mantle was found to sublimate completely after around 20 minutes, consistent with previous studies (Petrova and Markiewicz 1998; Inada *et al.* 2002). For this case, the profiles are investigated towards the middle of the nominal mission ($L_s = 0°$), between 0600 and 0700 Local Mars Time (LMT), consistent with previous observations (Petrova and Markiewicz 1998; Inada *et al.* 2002).

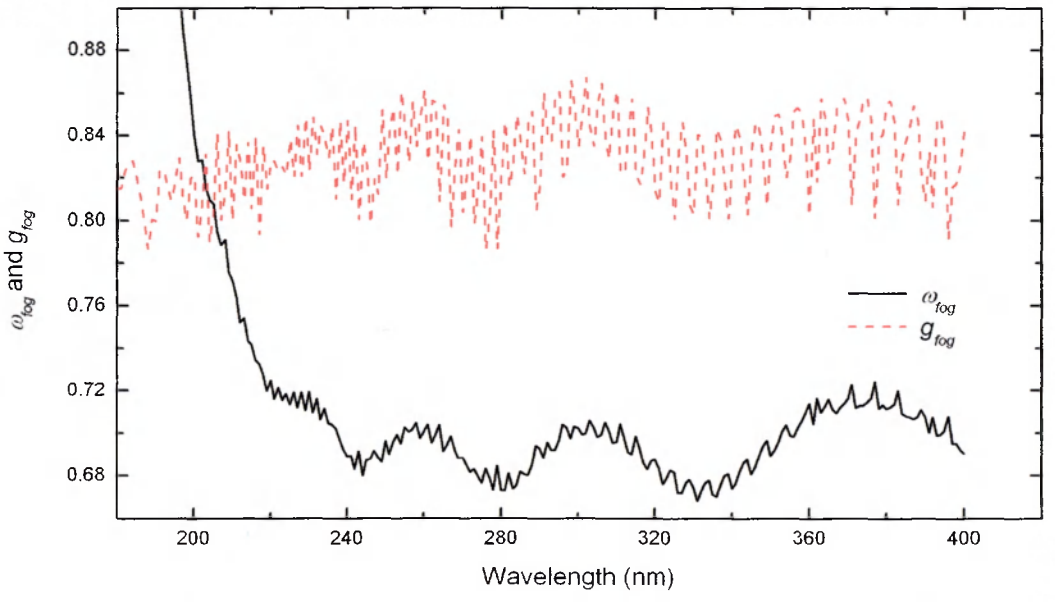

Figure 6-10: ω_{fog} and g_{fog} values for the case of $t_{fog} = 0$.

6.4.1 Resultant Spectra

Since the opacity of such fogs is typically small, the absolute difference between spectra is not easily observable since there is relatively little change in flux. Figure 6-11 thus shows the ratio of the total UV flux between a 'foggy' morning to that of a 'clear' morning (where no surface fog is present) as a function of time. Three different scenarios are modelled for varying levels of fog condensation, using optical thicknesses (τ_{fog}) of 0.01, 0.05 and 0.1 representing low, nominal and high fog levels respectively.

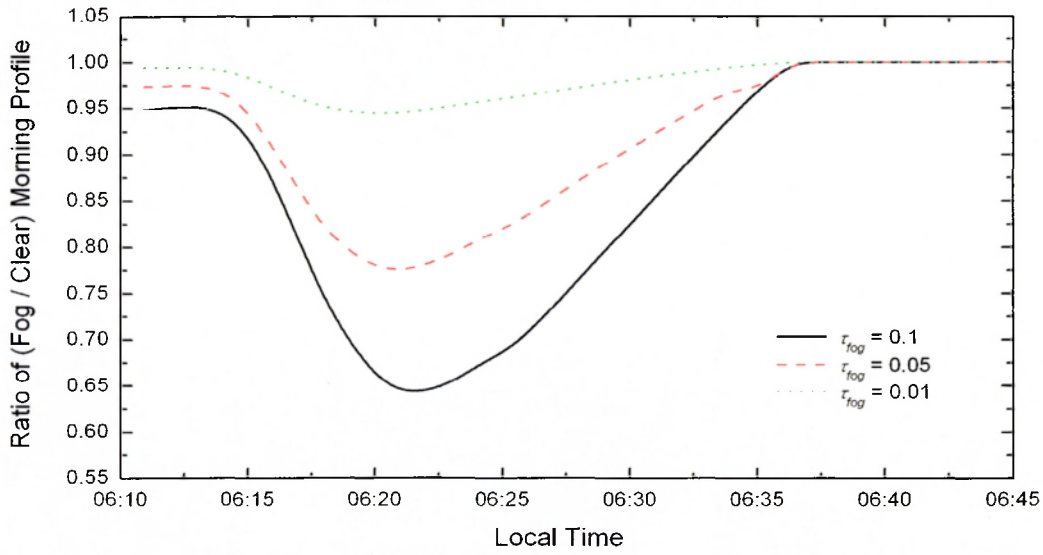

Figure 6-11: Fog/clear day UV ratio over varying opacity. Sunrise occurs for this case at 06:12 local time.

With the presence of a near-surface fog layer and associated (slight) increase in optical depth, a distinct pattern emerges in the morning part of the ratio profile. Immediately at the onset of sunrise, there is a 'dip' in the observed UV flux ratio. The fog/clear flux ratio falls immediately after sunrise, reaching a minimum then increasing gradually to unity. The shape of the resulting ratio curve is highly dependent on τ_{fog}. An optically thicker fog results in a much deeper curve, and though fog optical depths of 0.1 are less likely, the observed value of 0.05 (Petrova *et al.* 1996) is more likely to occur, and should result in a maximum 25%

reduction. A fog optical depth of 0.01 shows only a 5% deviation from a 'clear' morning profile, far lower than the other cases as expected. The validity of the modelling is verified for this situation, as the ratio returns to unity after the water-ice mantle has completely sublimated.

The shape of the curve can be understood by analysis of the separate UV components in the surface flux. Prior to sunrise, a diffuse illumination appears first as refracted and scattered light begins to emerge over the horizon from the Sun. There is a small time lag for the appearance of direct illumination, which only appears when the solar disc itself emerges over the horizon. Under low dust conditions, direct flux usually dominates the surface irradiance, but at this early time when the observed airmass is large, the diffuse flux dominates. During this time the coated fog aerosols exert their influence on the diffuse irradiance, reducing the surface irradiance mainly through scattering and creating the dip seen in the ratio profile. However, as the direct flux begins to increase, this effect is seen to reduce since the direct flux is relatively unaffected by the optically thin fog layer. This process also provides the majority of the input solar energy which in turn sublimates the water-ice coating, removing the fog. The cross-over point of direct and diffuse component UV fluxes is shown in Figure 6-12.

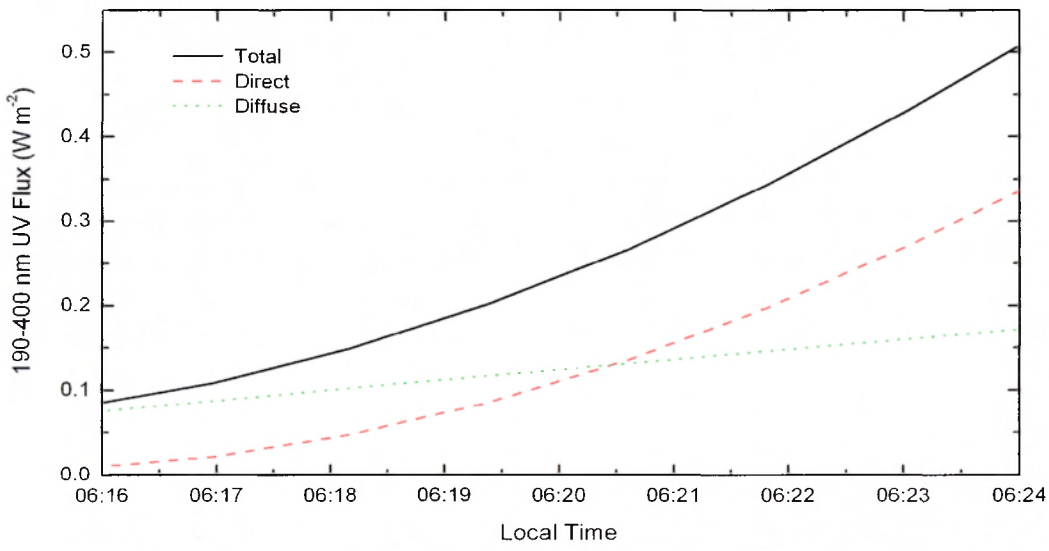

Figure 6-12: Component UV fluxes at sunrise.

A correlation is seen between the time at which direct flux begins to dominate and the change in gradient of the ratio minimum in Figure 6-11, implying that the emergence of direct flux is responsible for the change in ratio. Through analysis of UV fluxes at sunrise, it will therefore be possible to discern mornings with surface fogs present, through systematic day-to-day comparison of morning flux profiles. Mornings with high fog levels will manifest in the ratio profile data, and depending on the extent of the curve minimum, direct measurements of the degree the surface fog affecting the UV flux will be obtained. This, combined with total optical depth observations by the stereo camera on Beagle 2, will aid in placing limits on the optical thickness of the surface fog.

6.5 Partial Solar Eclipses by Phobos

An interesting phenomenon that will be observed during the landed operations phase will be partial eclipses of the solar disc by the moon Phobos. The latitude of the shadow of Phobos on the martian surface is a strong function of the season. During the nominal lifetime of the mission, the shadow path progresses through the equatorial region of the planet from north to south. The area of the selected landing site offers a view of such partial eclipses in late January and early February 2004, with a number of events observable within the landing ellipse (110 km by 60 km in size). Phobos, though small and irregular in shape, still offers a noticeable solar obscuration due to the proximity of its orbit to Mars. Phobos is too small to achieve total solar obscuration, but can reach up to ~40% obscuration at the sub-solar point when the apparent solar diameter is at its minimum near aphelion. Accurate observations of the partial eclipse beginning, mid-point and end times can help constrain the position of the landing site, given a high enough sampling rate and accurate enough time stamping. This will be the case for Beagle 2, which will use an ephemeris model developed to constrain the position of the lander within the ellipse to an accuracy of at least 10 km in longitude and 5 km in latitude (Christou 2002). Determination of the lander position is considered a priority from

the point of view of operations coordination with MEX – the only opportunity for a direct flyover of the landing ellipse with the present orbital plan occurs early in the Beagle 2 mission – after that, another opportunity will not be possible until after the nominal mission. Thus the position of Beagle 2 needs to be known at an early stage, to allow imaging of the lander and other important investigations to be made by the orbiter. Partial eclipse events will be observed by the UV sensor at a continuous high rate, to monitor accurately the change in flux as a function of time. A collection of partial eclipse events is given in Table 6-6, showing the *SZA* for each event, as well as ESS high rate sampling periods to cover fully each event with adequate contingency[1].

Date	Start Time (UTC)	End Time (UTC)	*SZA* (°)
31/01/2004	01:58:19	02:03:19	24
01/02/2004	00:44:12	00:49:12	23
01/02/2004	23:31:27	23:36:27	44
04/02/2004	05:37:08	05:42:08	35
08/02/2004	09:15:01	09:20:01	48
08/02/2004	00:51:25	00:56:25	80

Table 6-6: Partial eclipse observation windows for Beagle 2 (A. Christou, *personal communication*).

The effect of a 'high' probability event was modelled here, in this case assuming that Beagle 2 lands within the very centre of the landing ellipse at exactly 90.5°E and 11.6°N (the degree of probability of observation is dependent on exactly where Beagle 2 lands within the landing ellipse). The timing, duration and degree of obscuration will differ slightly for different areas within the ellipse, but the centre is used here as a baseline. The event analysed

[1] These times define 5 minute high rate sampling windows when the UV sensor will sample at 4 Hz – the start and end times of the partial eclipse itself lies within these windows.

here is predicted to occur on 1st February 2004 ($L_s = 343°$), beginning at 00:46:12 (UTC) or 11:06:05 AM (local Mars time) at the Beagle 2 site (A. Christou, *personal communication*). This event is particularly interesting as it occurs at a small *SZA* (23°) near local noon, within the field of view (FOV) of the UV sensor (assuming a horizontal landing). Figure 6-13 shows the modelled response of each sensor channel, normalised to immediate pre-eclipse flux levels.

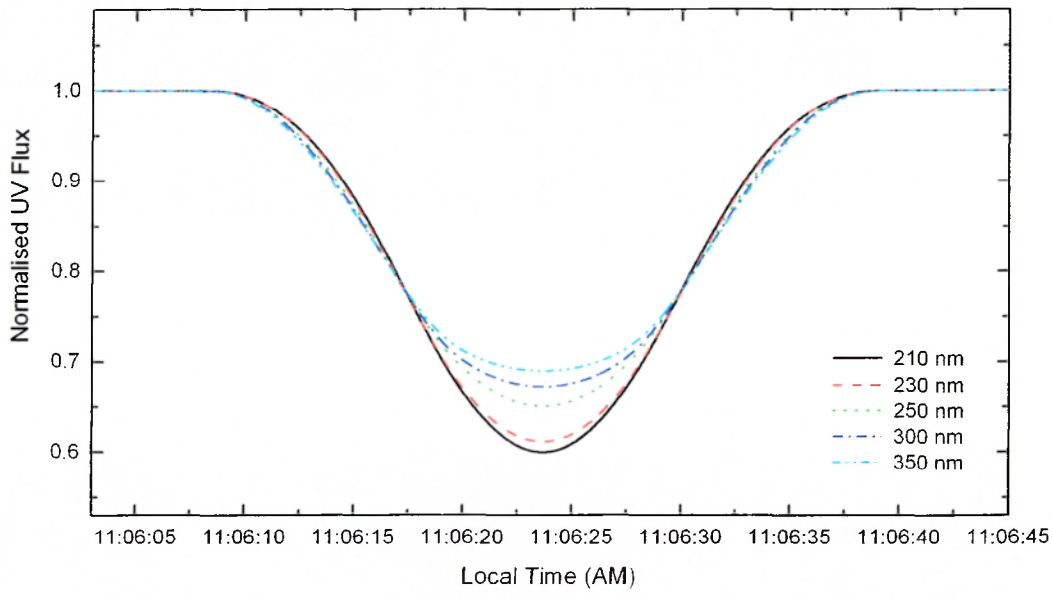

Figure 6-13: Normalised UV flux profile during a solar eclipse by Phobos.

A typical eclipse lightcurve lasts approximately 30 seconds, and flux levels are reduced by nearly 40%. The normalised curves allow the comparison of individual channel responses to the event. In this case it is evident that the largest relative reduction in light levels will be observed in the 210 nm channel band, which reduces to nearly 60% of the pre-eclipse flux levels. In contrast, the longer wavelength channel centred at 350 nm only reduces to ~70%. This effect arises because the limb darkening profile of the Sun is wavelength dependent, with profiles darkening to greater extent as wavelength decreases. Thus steeper limb darkening profiles are observed in the 210 nm band at maximum obscuration since the contribution from

the unobscured limb area (which provides illumination at this time as Phobos does not fully eclipse the solar disc) is less at shorter wavelengths, resulting in an overall smaller flux.

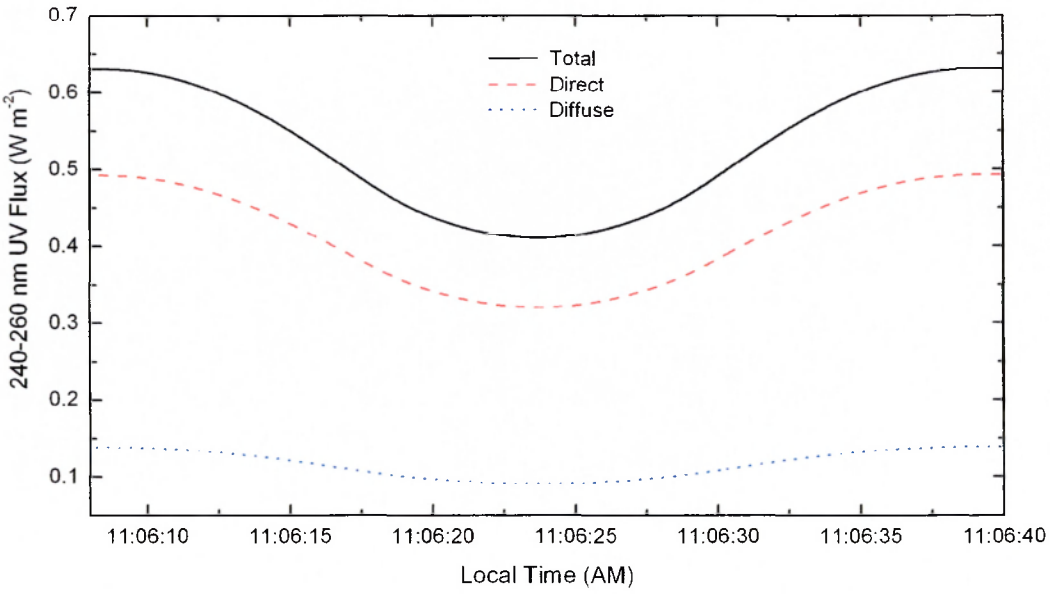

Figure 6-14: Reduction in 250 nm channel during a solar eclipse by Phobos.

An example of the effect of the eclipse on absolute light levels is shown in Figure 6-14. Here, the total, direct and diffuse flux levels are shown in the sensor channel centred at 250 nm (240-260 nm). The effect on the flux levels is much as would occur on Earth (at longer wavelengths) in terms of the total and direct flux. What is of curiosity in the case of Mars however is the effect of the eclipse upon the diffuse flux levels. The same characteristic lightcurve is observed, albeit to a lesser degree. This effect is important, as the diffuse flux is a ubiquitous illumination. The implication here is that even if the event itself is not observable, it may be possible to detect a Phobos near-eclipse through variation of the diffuse flux. The timing of each eclipse event is highly dependent upon the exact location of the landing site within the landing ellipse. There will be some instances when Phobos will pass in close apparent proximity to the Sun when viewed from the position of the lander, but will not actually traverse the solar disc. An eclipse event will then be viewable from a relatively close location to the lander, given the different geometry of the Sun-Phobos-observation alignment.

Near-eclipse events would manifest as a constant direct flux accompanied by a reduction in the diffuse illumination lasting approximately 30 s, resulting in a small total flux decrease (*i.e.* around 10% for the 250 nm channel) with a shape characteristic of the eclipse profile. Such a variation will be similar to the drop in diffuse flux shown in Figure 6-14, and well within the range of detection of the UV sensor. This observation will also apply to eclipse events which occur at the Beagle 2 site, but outside the FOV of the sensor – at these times the sensor will be monitoring the diffuse illumination alone.

6.6 Combination of Events

The events outlined in the preceding sections all indicate the existence of distinct UV signatures for the detection of atmospheric phenomenon. However, in reality it is unlikely that these events will occur under such tightly constrained conditions. Certain events may occur simultaneously, and an investigation of the combined effects under certain situations must be performed to see if such conditions prohibit the detection of these signatures. Clearly to cover every possible situation is beyond the scope of this work, but a discussion and analysis of some likely situations is given here.

Fortunately some of the combinations of events are mutually exclusive, and thus need not be considered. For example, the formation of condensate aerosols is generally inhibited by high dust activity. Elevated atmospheric dust levels result in an increase in the degree of absorption of solar radiation in the atmosphere, resulting in a more isothermal troposphere and inhibiting the formation of condensate aerosols (Gierasch and Goody 1972). Other combinations of conditions however may occur, such as elevated dust loadings during an eclipse or dust devil encounter, and high altitude condensate formation concurrent with morning fogs. These situations are investigated, and the detectability of such combined events is evaluated.

The detection of clouds will be possible, since no other modifiers of the spectrum are expected to occur under cloud formation conditions. Dust activity is generally low, and spectra can be measured at local noon to avoid the interference from morning fogs. Ratio level differences between the long and short wavelength regimes are almost a factor of 2 for cloud formation, a value which will be easily detectable by the UV sensor.

The issue of the morning fog however is somewhat different. Here the data must be taken at a specific time of day when unfortunately, cloud formation may be possible at higher altitudes. The presence of significant condensate clouds has the effect of skewing the morning ratio, placing the ratio well below unity for most of the morning. Thus the structure of the 'dip' is lost, and though the ratio levels will indicate that a condensate is present, no information about the specific nature of the condensate can be extracted from these data. Mornings with cloud formations will be identifiable, but the presence of fog aerosols will remain ambiguous and only detectable on days when there is no high altitude cloud present.

Observations of Phobos offer the most certain opportunity for atmospheric distortion, since this event is not a process of the atmosphere but rather orbital geometry. The issue of a dust devil encounter during an eclipse event is however extremely unlikely. An encounter rate at the Beagle 2 landing site of approximately 0.3 encounters per sol is anticipated, based on MPF meteorological data (Ryan and Lucich 1983; Ringrose *et al.* 2003). This coupled with the short event time durations (~30 s for eclipses and ~60 s for dust devils) results in an extremely low probability of simultaneous occurrence.

The effects of cloud formations during eclipse events are also inconsequential. Though the chance of occurrence is relatively high, the impact of cloud presence on the UV spectrum is minimal. Little overall attenuation occurs, and the only notable effect is a slight increase in diffuse flux. The formation of a water-ice cloud with $\tau_{Icloud} = 0.3$ has no significant effect on either the normalised or absolute eclipse lightcurves, and the event will remain detectable if this situation arises.

Elevated background dust conditions are also a possibility, such as if a local or regional dust storm was to occur. The partial eclipse event detailed in section 6.5 was re-calculated for a case of high atmospheric dust loading, with $\tau_{back} = 3$. No change is seen in the normalised profile with the variation remaining identical to Figure 6-13 as expected. Since the Phobos eclipse events result in a variation of top of atmosphere input flux, the normalised ratios are expected to remain the same.

The absolute flux levels however are far lower due to attenuation by the dust. Figure 6-15 shows the absolute flux variation during a 'dusty' eclipse. Even for the short wavelength channels (right axis) where the flux levels are lowest, a distinct lightcurve is still present in the profile. The smallest variation here is approximately 40 mW m^{-2}, calculated for the 210 nm channel. Such a small variation will still be detectable by the UV sensor, which has a minimum resolution capability of 1 mWm^{-2} for this channel. Thus even at times of high dust loading, partial eclipses by Phobos will still be detectable.

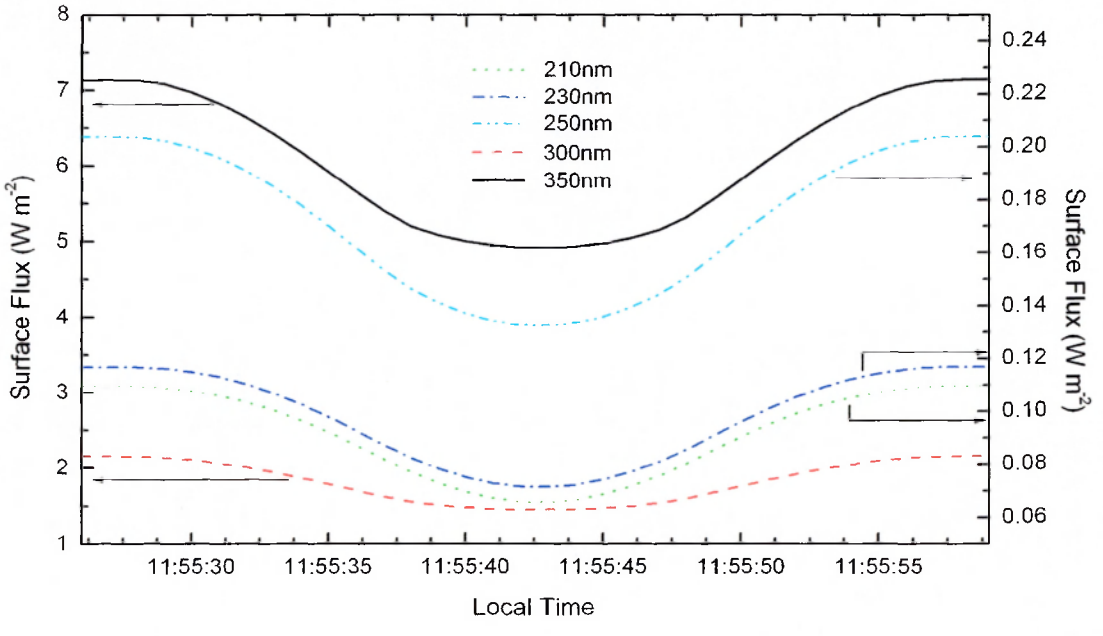

Figure 6-15: Partial solar eclipse profile at a time of high atmospheric dust loading.

Another possible scenario may be the encounter of dust devils during periods of relatively high dust loading. In order to determine whether the double minimum signature of a dust devil would still be observable given a high background dust opacity, the case outlined in section 6.2 for a 10 km vortex containing 75 μm sized particles was re-calculated with a background dust optical depth value of 2, and the resulting profile is shown in Figure 6-16.

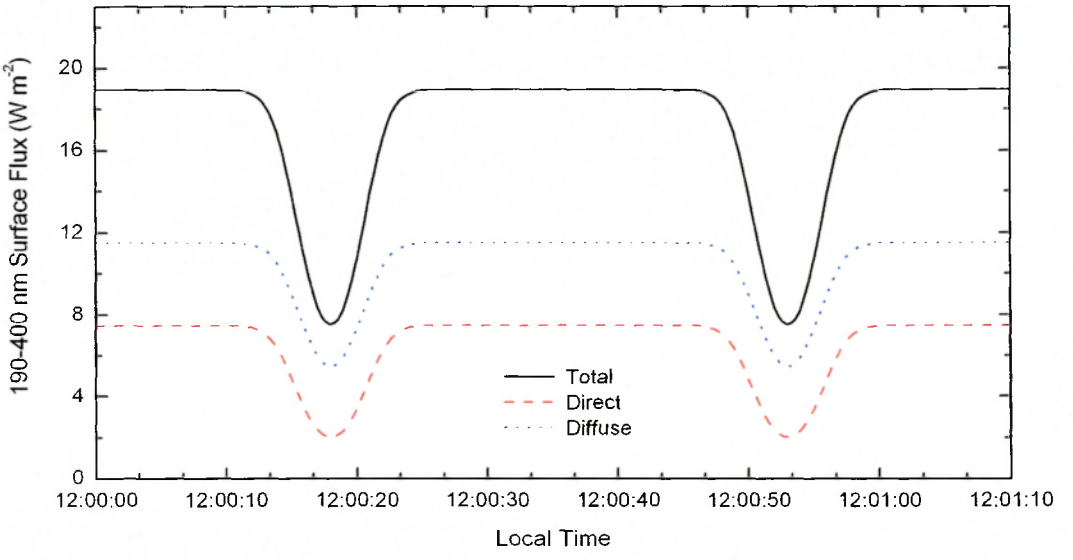

Figure 6-16: Dust devil signature during a time of high background dust loading.

Even at times of high dust loading the characteristic double minima are still present, but the relative contribution from component UV fluxes have changed. Previously in Figures 6-5 and 6-6 the minima were primarily a direct flux effect with only a small diffuse contribution, but an increase in τ_{back} results in a reversal of component fluxes. The same minima are observed, only to a slightly lesser extent than the case in Figure 6-6. Here a drop of around 50% is observed, compared to that of 65% in Figure 6-6. Thus even at high dust loadings the passage of a dust devil will still be detectable.

6.7 Comparison with Fieldwork

6.7.1 Arizona Field Unit

A terrestrial version of the UV sensor was also developed, allowing long term verification of the operation of the sensor under terrestrial conditions. The sensor was deployed in Tucson, Arizona at a longitude of 110° 56′ W and latitude of 32° 7′ N and an altitude of 750 m above sea level, operating from 23rd December 2001 to 30th December 2002, covering an entire terrestrial year. The sensor was a modified version of the Beagle 2 UV sensor, adapted to respond to the terrestrial UV spectrum. The shorter wavelength channels were omitted, since radiation below ~290 nm does not penetrate the atmosphere to the ground. Only the 300 nm, 350 nm and open channels were used, with modified electronics to respond to the elevated terrestrial UV-A levels. Each channel was sampled continuously throughout the day at 10-bit resolution over 0-2.5 V, recording measurements at 10 s intervals. Also present was a version of the Beagle 2 temperature sensor, but this instrument is not covered in this study.

6.7.2 Diurnal Variations

The variation of UV flux in the 350 nm channel is shown in Figure 6-17 for two different days during summer, specifically a clear and cloudy day. During the clear day, a smooth diurnal curve is observed as expected. Conversely for a cloudy day an extremely erratic diurnal signal is observed, consistent with time dependent broken cloud passing overhead throughout the day resulting in a large increase in scattering processes. Though the degree of cloud cover cannot be derived from this profile, it verifies the ability of the sensor to detect such atmospheric conditions.

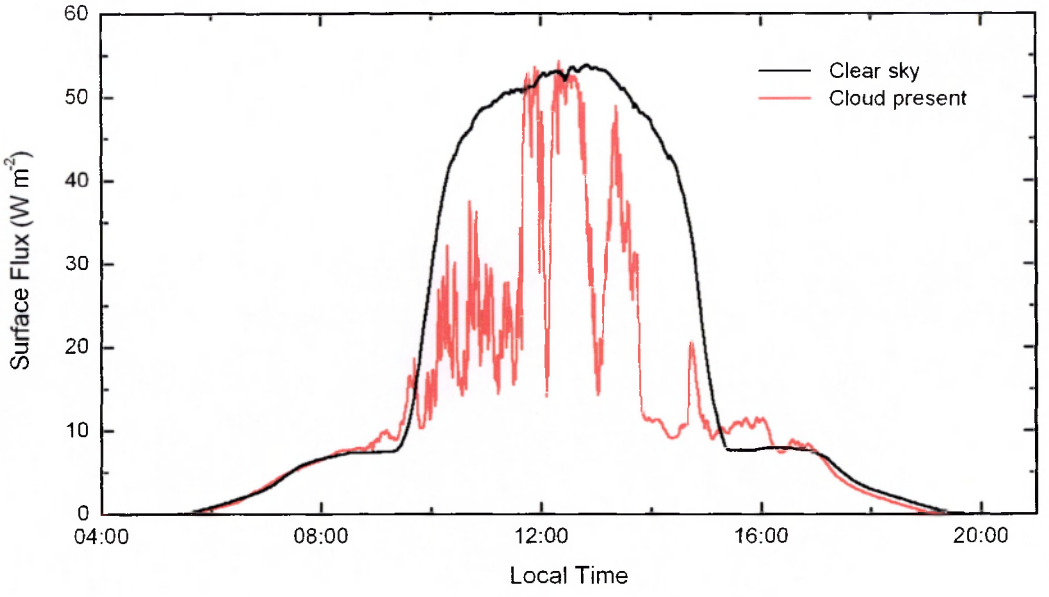

Figure 6-17: Terrestrial clear and cloudy day diurnal profile.

An important physical limitation of the sensor is also highlighted here, observed in all profiles. As the Sun traverses the sky throughout the day, the line of sight can at times be outside the FOV. For these data the sensor was near horizontal, so the approximate position of the Sun in the sky relative to the FOV of the sensor can be inferred. For the case of a horizontal platform, the FOV of the UV sensor extends to a local SZA of 30° (and 27° for the open channel). At times near sunrise/sunset, SZA will be large and the Sun will be out of the FOV of the sensor. Thus at these times the sensor will be viewing a region of sky which contains diffuse flux alone and thus be observing a far lower irradiance, since the direct component will be out of view. As the day progresses towards local noon, *SZA* decreases until the Sun is within the FOV. At this time, the flux observed by the sensor should increase sharply, since the majority of the total flux consists of the direct component. This effect is confirmed in Figure 6-17 near 09:30 and 15:30 local time. During winter, this effect was not observed since *SZA* is also a function of season. At such times the minimum *SZA* is greater, and the Sun can remain out of the FOV throughout the entire day.

This effect will also be observed on Mars, though in this case the situation is far more complex. The Beagle 2 landing position is not guaranteed to be horizontal, since the lander may land on scattered rocks or a localised slope. The range of possible scenarios is far too great to be covered here. The worst case (operable) scenario would be if the normal from the plane of the lander base was orientated at an angle greater than 30° from zenith, away from the path of the Sun – in such a case the line of sight of the Sun would never enter the FOV of the sensor. At the beginning of the Beagle 2 mission, it will be late northern winter at the landing site, and the minimum *SZA* will be 26.5° at local noon – thus assuming a horizontal landing, the solar line of sight will enter the FOV of the sensor for a brief period only near local noon. SZA was calculated as a function of time for each sol, and the time when the Sun will enter and leave the FOV is shown in Figure 6-18 for each sol of the mission.

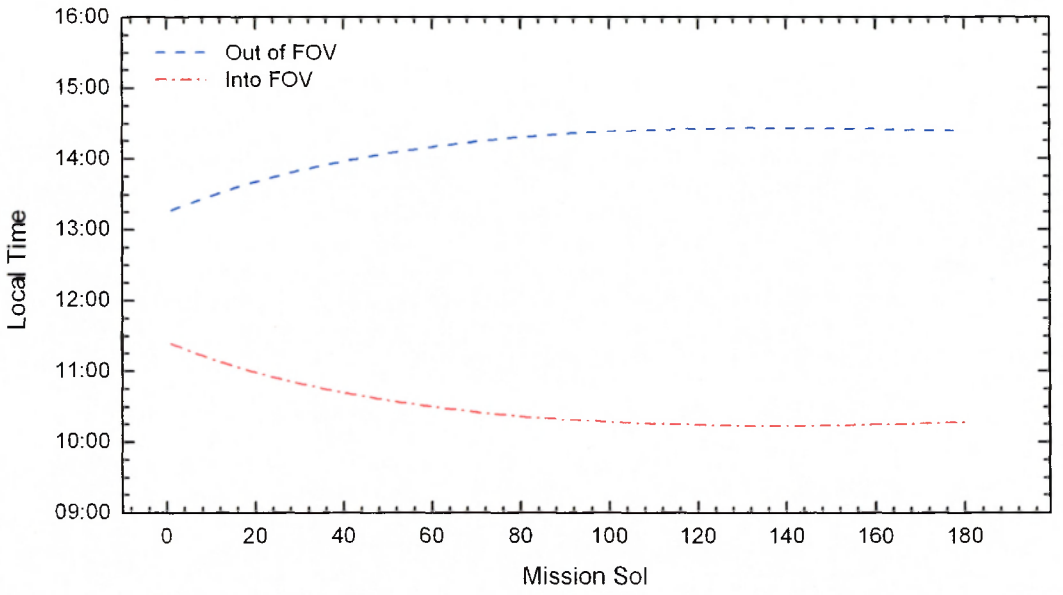

Figure 6-18: Times when the solar disc will be within the UV sensor field of view on Mars.

The region between the two lines in Figure 6-18 depicts the period each sol when the Sun is within the sensor FOV. As the mission progresses, the daylight period each sol will increase and minimum *SZA* will decrease. The Sun will therefore enter the FOV at progressively earlier times. The characteristic sudden increase in signal observed in

Figure 6-17 will thus be observed on Mars also, with the time between entering/leaving the FOV gradually increasing in width as the mission progresses.

6.7.3 Shadowing Events

It will be possible on Beagle 2 to monitor the diffuse component of UV flux separately, with no contribution from the direct flux. Though the sensor passively monitors the total incoming solar UV (*i.e.* direct + diffuse), measurements of the diffuse flux alone will give a better understanding of the scattering nature of the martian aerosols. In such a case the flux observed would be solely that due to UV which has been scattered by the aerosol laden atmosphere, out of the direct line of sight of the Sun. This will be possible using the Beagle 2 robot arm, which carries the majority of the geochemical investigation instruments. The instruments are located on the end of a 1 m elbow jointed arm and grouped together in a semi-circular arrangement on the PAW, with the connection to the arm located at the radial centre of the instrument arrangement. This non-uniform semi-circular PAW arrangement reaches a maximum of 20 cm in radius, attaining a maximum apparent angular diameter at full arm vertical extension of 23° from the position of the UV sensor. This diameter far exceeds the apparent solar diameter from the surface of Mars (~21 arcmins).

Thus if the arm is deployed in a suitable configuration directly above the UV sensor, it will be possible to block completely the direct irradiance from the solar disc, by ensuring that the sensor is within the shadow of the PAW. In this (shadowed) configuration, only the diffuse flux will be observable by the sensor, giving an accurate hitherto unmeasured value of the diffuse UV irradiance alone at the martian surface. These events will of course occur throughout the day, as the robot arm is moved during operations, and manifest in the diurnal data by sudden decreases in flux levels coinciding with arm movement. In addition to this, planned shadowing events will be scheduled at specific times allowing the full profile to be observed as the sensor enters and emerges from the shadowed region, shown in Figure 6-19.

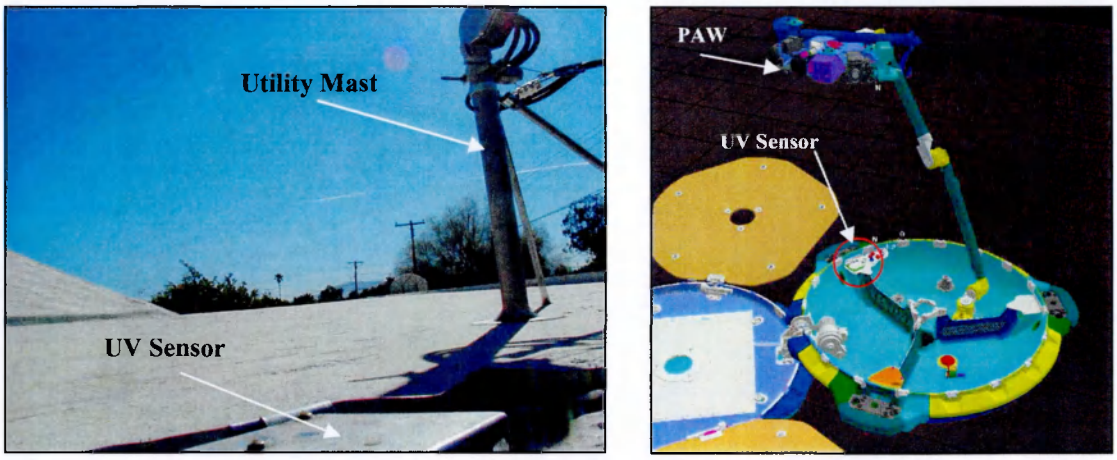

Figure 6-19: Arizona UV sensor showing the shadowing utility pole (left), and a simulation of UV sensor shadowing using the PAW on Beagle 2 (right, image courtesy of the Space Robotics Group, Dept. of Computer Sciences, University of Wales, Aberystwyth).

Such events were also experienced in Arizona deployment, and offer valuable insights into the procedures required for similar occurrences on Mars. A small utility pole (60 cm tall, 7.5 cm wide and 120 cm from the sensor) was close to the instrument, and at certain times of the year cast a shadow over the sensor at particular times of the day, shown in Figure 6-19.

The progression of the apparent path of the Sun through the sky to higher altitudes meant that at some points in the year the shadow fell upon the sensor. The response of the UV sensor to a typical shadowing event[1] is shown in Figure 6-20, where the event occurs in the late-morning, lasting for nearly 9 minutes. Such mid-morning 'dips' in the diurnal profile were seen on clear days, when cloud effects did not mask the shadowing.

[1] Sensor output voltage values (proportional to flux) are plotted to allow both channels to be displayed on a single plot for comparison.

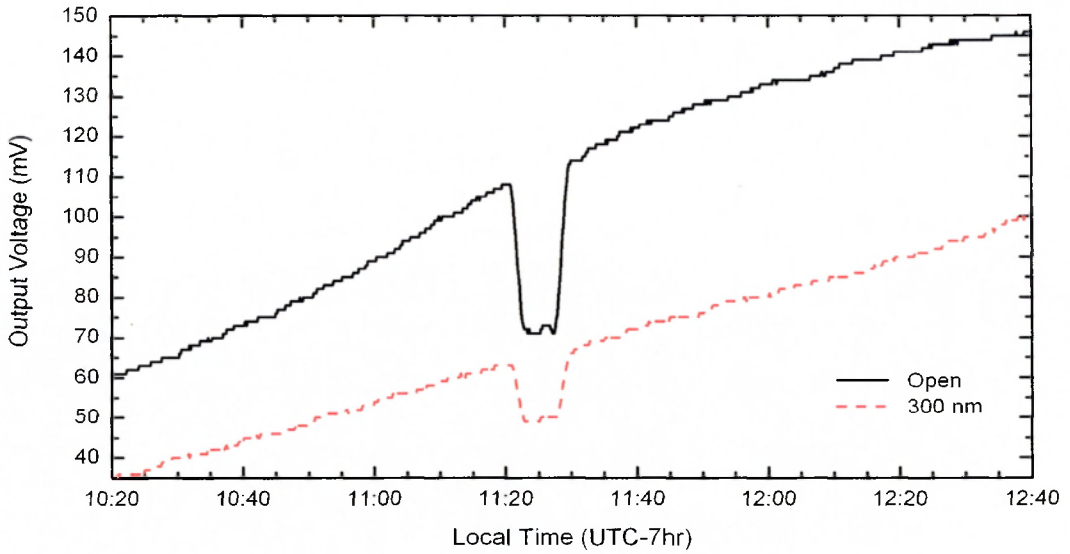

Figure 6-20: Shadowing profile created by a utility pole.

6.7.4 Partial Solar Eclipse

An interesting event of relevance to the Beagle 2 mission was the partial solar eclipse which was observable during the fieldwork site in Arizona. The event occurred on 10th June 2002 and the shadow track passed over the Arizona region with an eclipse magnitude of 0.743 (fraction of solar *diameter* eclipsed) and an eclipse obscuration of 0.673 (fraction of solar *area* eclipsed). The timing of the event as officially recorded is given in Table 6-7.

Eclipse Event	Time (UTC-7hr)	Altitude	Azimuth
Partial Begins	17:20:45	25°	283°
Maximum	18:24:45	12°	290°
Partial Ends	19:22:16	1°	297°

Table 6-7: Partial solar eclipse parameters for 10th June 2002, Arizona U.S.A. (Gupta 2001).

A terrestrial partial solar eclipse is analogous to the predicted partial solar eclipses on Mars by Phobos in terms of solar disc obscuration, and the sensor was used here to demonstrate directly the ability of the sensor to monitor this type of event. Though the specifics of the event are not the same (*i.e.* different obscuration profiles, passage times etc) the overall eclipse obscuration levels (*i.e.* light level reductions) are the same as in the Phobos case.

The measured UV reduction in the open channel during the event is shown in Figure 6-21. In order to derive a percentage reduction, the previous day (9th June) was used for comparison of flux levels at the event time. Pre-event light levels could not be used (as in section 6.5) since the event lasted nearly 2 hrs, over which time the flux levels varied substantially. 9th and 10th June had identical smooth diurnal UV profiles devoid of any cloud features, allowing the difference in the two spectra at the time of event on each day to be used to determine the percentage reduction in UV flux.

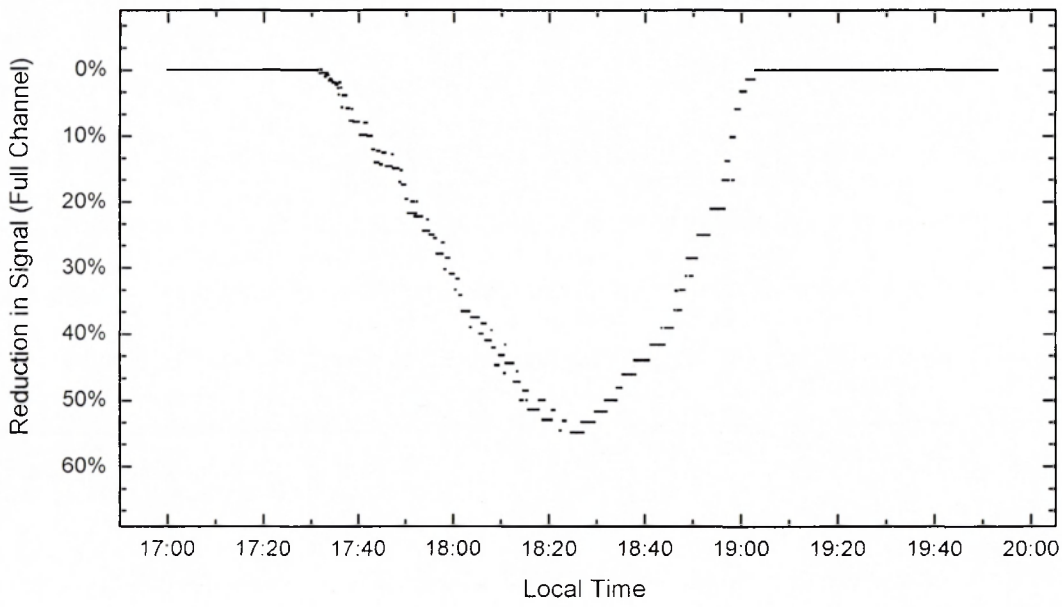

Figure 6-21: Measured % reduction in signal during a terrestrial partial solar eclipse.

The maximum % reduction in signal is observed at around 55%, in rough agreement with official measurements. Maximum eclipse was also measured at 18:24:30 (UTC-7 hrs), agreeing extremely well with official values. In terms of viewing geometry, at the time of the event the Sun would have been outside the FOV of the sensor. At the onset of eclipse the *SZA* was 65°, and at maximum obscuration the *SZA* was 78°. The half angle FOV of the open channel sensor is 27° and consequently the observed flux variation at that time would have been due to scattered UV only. It is thus demonstrated here that the sensor is fully capable of partial eclipse investigations when the Sun is outside of the FOV of the sensor, through measurements of the variation of diffuse flux levels. On Mars, the relative contribution from diffuse UV is even higher than on Earth, and thus such events should in theory be easier to detect.

Chapter Seven

Discussion and Further Work

This thesis has been centred around the role of UV at the surface of Mars, its effects in a range of areas, design of an instrument for *in situ* measurement, and a variety of simulations using a theoretical model. Accurate measurements of this region of the electromagnetic spectrum will reveal great insights into the nature of the martian radiation environment, and the unique situations which can modify the nominal surface spectrum.

7.1 Radiative Transfer Modelling

A radiative transfer model has been developed to simulate the transfer of solar UV through the martian atmosphere to the surface, for almost any martian situation. The atmosphere was represented by 10 separate homogenous layers, each accounting for all major species of atmospheric gases and aerosols in a representative vertical distribution. The most up to date low-temperature absorption cross-sections for these atmospheric gases were used, offering a more accurate representation of the effects of gaseous absorption of UV than previous work. Using the delta-Eddington approximation combined with optical properties from the work of Ockert-Bell *et al.* (1997), the effects of multiple scattering were modelled, especially relevant in the aerosol-laden martian atmosphere.

The ubiquitous diffuse flux created through atmospheric scattering is highly dependent upon the assumed optical properties of the atmospheric dust. This dependence of the diffuse spectrum was demonstrated through comparison with an alternate set of published values (Zurek 1978), and through individual and combined systematic variation of ω_{bd} and g_{bd}. Use of the values derived by Zurek (1978) yields an underestimation between 190 and 250 nm, equality between 250 and 270 nm and an overestimation above 270 nm when compared to use of the values of Ockert-Bell *et al.* (1997). Systematic reduction of ω_{bd} shows a corresponding decrease in the magnitude of the diffuse spectrum, as more UV is absorbed per scattering event. An increase in ω_{bd} leads to the opposite effect. Conversely, diffuse levels increase as g_{bd} is reduced, since the light is scattered more isotropically. Combined variation shows an interesting effect – if *both* parameters are reduced, no difference between a 10% variation and a 30% variation is observed in the diffuse spectrum. A combined enlargement of both ω_{bd} and g_{bd} however leads to a significant reduction in diffuse UV.

For the case of Mars, these factors are an important point since no agreement has yet been reached regarding the UV optical properties of martian atmospheric dust. More work, both observational and theoretical, regarding the interaction of suspended dust with UV is required to constrain more accurately the diffuse flux created at the surface. High-resolution *in situ* spectrometry from the surface is required over a range of conditions to measure accurately the effect of dust on the diffuse spectrum, and also monitor its variability over time and changing conditions. Ideally this would lead to a complete description of the dust optical properties at 1 nm resolution between 190 and 400 nm, through the iterative fitting of optical parameters in the model to re-create the observed spectrum. Furthermore, the development of an atmospheric model at higher vertical resolution (preferably 1 km) would yield a more accurate model representation of the martian atmosphere, allowing variability of different species-altitude distributions over time. Such a development could also utilise a more accurate radiative transfer code such as the discrete-ordinate method (Stamnes and Conklin

1984), allowing both cross-comparison with this model and more rigorous high resolution computation of the martian surface UV environment.

7.2 *In Situ* UV Instrumentation

The development, production and flight of the Beagle 2 UV sensor formed the basis of this study. These results will offer for the first time *in situ* measurements of the UV flux at the martian surface, which previously had only been inferred using orbital and telescopic observations, coupled with simple atmospheric modelling. The use of the model to define the spectral characteristics of the sensor has been demonstrated, given the stringent mass, volume and power constraints imposed from the beginning. A 6 channel SiC photodiode array incorporating bandpass filters will monitor the 190-400 nm region, yielding a 5-point averaged spectrum of martian surface UV. The plateau-like region in the UV-A is monitored by two broad-band channels at CWL = 320 and 350 nm, with the varying UV-C region covered by narrow-band channels at CWL = 210, 235 and 250 nm. The gain settings of the sensor were defined through the use of a maximum case flux scenario from the UV model, to ensure that signal levels will be measurable. The sensor will provide data on the direct and diffuse flux components encountered at the martian surface. Analysis of the diffuse data coupled with optical depth data from the Beagle 2 camera will allow the derivation of low resolution values for ω_{bd} and g_{bd} in the UV range, through iterative fitting of the model optical properties to match the observed data. The completed sensor successfully passed a range of space qualification tests, including thermal-vacuum cycling and vibration. Absolute calibration of the sensor was performed before and after each stage of testing, and showed no susceptibility to any of the conditions imposed upon it.

Remaining testing which will occur on a separate representative unit will include simulated ageing of the sensor assembly to assess the long term functionality over the mission

lifetime. These data will provide vital information on how the performance of the sensor will change with time, as high UV and ionising radiation doses and extended thermal cycling effects degrade the sensor performance. In the case of future missions to Mars, a move to the use of spectrometers for surface landers will provide the vital data on the optical properties of suspended dust. This technique will require higher mass, power and volume, but is still feasible in a miniaturised context. Further work involves the development of a commercially available miniature spectrometer to space qualified standards, which could offer coverage of UV-VIS-IR wavelengths between 200 and 1100 nm at 1-2 nm resolution, requiring a mass allocation of only ~100 g. This work is currently in the initial concept stage, and with further development will form part of a payload proposal for the next ESA mission to Mars.

7.3 General Martian UV Conditions

The radiative transfer UV model was then applied to a range of situations encountered both over the martian surface, and throughout the year. General flux levels in the UV-A are higher on Earth, attributable to the greater mean orbital distance of Mars compared to the Earth, and the fact that only molecular and aerosol scattering occurs in this wavelength region both on Earth and Mars. As wavelength decreases, the relative martian flux levels increase, and near 290 nm, no UV-C is encountered at the terrestrial surface due to O_3 absorption. On Mars, the UV surface spectrum penetrates to wavelengths as low as 190 nm where the characteristic CO_2 cut-off is encountered. Biological weighting of martian spectra using a DNA action spectrum shows the UV environment to be almost three orders of magnitude higher on Mars than on Earth from the viewpoint of DNA, indicating that any putative organisms or organics (with a DNA-like biological response to UV) would quickly be killed.

Large-scale dust storms, such as occasionally encountered towards southern summer, are found to affect substantially the surface UV spectrum. High dust loadings ($\tau_{back} = 4.0$) reduce

the total UV dose by 75%, and also alter the component contributions to the total flux. Direct flux is attenuated rapidly, leaving diffuse flux forming the majority of the total surface flux and providing a more ubiquitous illumination. The dependence of the direct component upon increasing dust loading shows an exponential decrease. The diffuse flux however, shows a weak increase with increased dust loading, until a value of around $\tau_{back} = 2.0$ at which point it begins to decrease. Unlike the direct component however, it does not tend to zero, but instead persists through multiple scattering to extremely high optical depths. The dependence of UV flux on pressure was found to be minimal, with an order of magnitude decrease in pressure resulting in an increase of surface flux of only 3%. Variation of surface UV across the martian surface due to topography and over the martian year due to CO_2 condensation and sublimation is therefore minimal.

Over the year, an increase in daylight length of 3 hrs as demonstrated in Figure 5-13 results in an increase of total daily UV dose of nearly 30%. The variation of the local noon flux over L_s at latitudes between north and south pole reveals a maximum formed in the southern hemisphere at perihelion, due to planetary obliquity and orbital eccentricity. The location of this noon maximum is highly dependent upon the annual dust loading for the year in question. Polar night regions are apparent, where the Sun never rises above the horizon for long periods of time at winter at high latitudes. High dust activity towards perihelion has the effect of spreading the maximum temporally and spatially, with more presence in the equatorial region and beginning earlier in the year. Towards high latitude/polar regions, extended daytime lengths lead to a substantially increased total daily dose during summer. Due to the polar day effect, high UV doses are experienced at each pole during summer comparable to mid-latitude values, followed by continual zero irradiance periods during polar winter. For total daily doses, two maxima have been found, occurring at aphelion and perihelion at mid-northern and southern latitudes respectively. Nominal dust loadings result in a more intense maximum in the southern region, but high dust loadings result in a more

even distribution between the two. The variation in distribution of UV with dust scenarios shows that the levels of dust activity during the year under study is of extreme importance.

The modelling of UV flux distribution over latitude and L_s would benefit from the addition of certain seasonally dependent aerosols, including O_3, cloud formation and the polar hood phenomenon. These factors were not included in the annual simulations, due to their complex variability in the martian atmosphere. Further studies should include the detailed occurrence and distribution of these phenomena over the martian year, and latitudes. More detailed long-term observations of each of these phenomena are also required, to understand better the trend in behaviour of these phenomena.

The presence of O_3 has been observed previously, and the effects upon the UV spectrum are important. The O_3 absorption spectrum is co-incident with the DNA action spectrum, offering vital terrestrial protection from UV-B and UV-C. The presence of O_3 on Mars offers some partial protection from short wavelength UV. Absorption by O_3 occurs at high latitudes towards northern winter centred around 250 nm, when H_2O abundance is at its lowest. This protection is not complete though, as O_3 abundances are not high enough to prevent wavelengths below 230 nm from reaching the surface, thus still producing a degree of damage. Using the present-day martian atmosphere, an increase in O_3 abundance of nearly two orders of magnitude was required to offer similar protection as found on Earth.

The total annual UV dose as a function of latitude was investigated to ascertain which latitude experienced the highest cumulative UV dose over the entire martian year, and confirmed again that the magnitude of UV flux reaching the surface is heavily dependent upon dust activity throughout the year. Under all conditions, peak flux is received at the equator, however during years of nominal and high dust loading, the northern hemisphere is found to receive a higher annual total UV dose when compared to the south. Consistent cumulative irradiation of relatively high levels overrides the maximum daily dose effect since lower dust loadings are encountered at northern summer, leading to a longer, more sustained

irradiation when compared to the southern equivalent. In terms of the suitability of hemispheres for the persistence of organisms and organics, the southern hemisphere offers a relatively less hostile UV environment.

7.4 UV Signatures of Atmospheric Phenomena

Through analysis of expected diurnal variations in each of the Beagle 2 UV sensor channels, the effect of Rayleigh scattering is demonstrated. In the shortest wavelength band, higher contribution is observed from the diffuse component. In the longest wavelength channel under the same conditions, the diffuse flux contributes only slightly to the overall flux, since the wavelength dependent effects of Rayleigh scattering are less at longer wavelengths.

The simulated passage of a dust devil directly over the lander reveals a characteristic double minimum/maximum profile. The minima in total and direct fluxes are caused by the sudden introduction of high dust loading above the lander. For small dust devils (and subsequently low dust loadings) the diffuse flux shows a double maximum profile, since the increase in dust optical depth is still below the threshold where diffuse flux increases with increasing dust loading (τ_{back} = 1.5). Variation in the optical properties with particle size is minimal given such large particle sizes, but differences are found relating to optical depth. Assuming a specific dust loading density, the use of smaller particle sizes results in greater optical depths, due to the greater number of particles occupying an equivalent volume. Smaller particle sizes thus lead to deeper minima in the UV profile. An increase in dust loading was found to have a similar effect, though to a greater degree. Increasing the height of the dust devil between 1 and 10 km increased the dust loading, creating the deeper minima. These double minima/maxima profiles are characteristic of a dust devil encounter.

The detection of cloud formation above the landing site can be achieved through measurements of the diffuse/direct ratio. Elevated diffuse/direct ratios during times of low dust activity will indicate the presence of condensate clouds. With increasing opacity, the diffuse/direct ratio is also found to increase. A small departure from the diffuse/direct ratio curve is observed for extremely small cloud particles, showing oscillatory effects in the spectrum due to the oscillation in the asymmetry parameter of the cloud aerosols. Such a signature is characteristic of the presence of condensate clouds above the landing site.

Comparison of morning profiles will also reveal the presence of near-surface morning fogs. The presence of such fogs creates a characteristic 'dip' in the ratio of total UV flux of a foggy morning to that of a clear morning, the magnitude of which is dependent upon the opacity of the fog. At sunrise, the effect of fog reduces the total UV flux, creating the dip in the ratio profile. As the Sun rises further, the water-ice mantle sublimates, and the effect of the fog lessens with the fog/fog-free ratio returning to unity. Day-to-day comparisons of morning profiles will reveal this signature.

A number of partial eclipses of the Sun by Phobos will be encountered over the mission, with the greatest reduction of nearly 60% seen in the shortest channel. A characteristic lightcurve signature, dropping to a minimum then returning to pre-event levels over a period of around 60 s at pre-determined times will indicate positive detection of these events. The relatively high aerosol loading of the martian atmosphere also allows the detection of "near miss" eclipse events, which will be noticeable by a sudden decrease in diffuse flux, accompanied by a constant direct flux. These characteristic signatures will also be detectable even when certain events occur simultaneously, with the exception of morning fog concurrent with cloud formation. The presence of clouds keeps the fog/fog-free UV ratio below unity for most of the morning, and though the presence of cloud formation can be inferred, the presence of fog cannot. Other combinations are mutually exclusive, such as the formation of condensate aerosols during times of high dust activity. Combinations of high dust loadings

with partial eclipse events or dust devil encounters however are not, but can still be detected within the capabilities of the UV sensor.

Fieldwork involving the use of a terrestrial version of the UV sensor has proven the ability of the sensor to detect such phenomena. The diurnal profiles of clear and cloudy days show a distinct difference, being smooth and jagged respectively. Times when the Sun will enter the field of view of the Beagle 2 sensor throughout the mission have also been calculated, gradually occurring earlier in the day throughout the mission. A characteristic sudden increase in signal will be observed as was seen in the fieldwork results, when the direct flux impinges on the detecting area. Shadowing events will also be possible, where the diffuse flux alone will be monitored. A partial solar eclipse offered a terrestrial equivalent to a partial solar eclipse on Mars by Phobos, demonstrating that the sensor can monitor such events to a high degree of accuracy, even when the Sun is outside the field of view of the sensor.

7.5 Concluding Remarks

The development of a radiative transfer model to aid both in the design of an instrument to measure martian UV *in situ*, and to investigate the martian UV environment has been presented in this study. The primary achievement has been the successful investigation of martian UV environments which were previously unexplored. Important points regarding the magnitude, variation and distribution of UV over geographic location and time have been presented, and detection signatures corresponding to specific atmospheric states have been identified. These theoretical signatures now remain to be detected by future *in situ* instrumentation, and will be within the capabilities of detection by the UV sensor on Beagle 2 currently *en route* to Mars.

Appendix A

IDL Radiative Transfer Code

```
;*****************************************
; 01_Main_Prog.pro
; Calculation of martian surface UV spectrum
; 180-400nm for total, direct and diffuse flux
; Manish Patel
; PSSRI - The Open University
;*****************************************

in=obj_new('datafile',1,'Inputs_01_Main_Prog.txt')
;read in input parameters
p=in->number()
ls=in->number()
localtime=in->number()
lat=in->number()
taudlower=in->number()
taudd=in->number()
tauhighcloud=in->number()
taulowcloud=in->number()
ozone=in->number()
water=in->number()
a=in->number()
co2=in->number()
n2=in->number()
ar=in->number()
o2=in->number()
co=in->number()
;read in basic constants
[illegible],g,m,ecc,d,j,bq670,lq670,dq670,l,co2x,co2r,n2x,$
        n2r,arx,arr,o2x,o2r,cox,cor,h2ox,h2or,o3x,o3r,flux1_52,n
;read in dust optical parameters
dusttype=0
[illegible],n,dbackw,dbackqext,dbackgchighw,chighg,dlowerw,dlowerqext,$
        dlowerg,$cloww,clowg, ddw,ddqext,ddg,dusttype
t=(36d0*localtime)-44387d0
;define solar zenith angle
secz=1d0/((sin(lat*!dtor)*sin(j*!dtor)*sin(ls*!dtor))+((cos(lat*!dtor)*cos(2d0*!dpi*t/d))*$
        (sqrt(1d0-(((sin(j*!dtor)^2)*((sin(ls*!dtor)^2))))))))
mu=1/secz
theta=acos(mu)/!dpi*180d0
;Apply airmass correction
if (theta gt 60) and (theta lt 90) then secz=1.07174- 0.0495*theta+0.00739*(theta^2)-4.09694E-4*(theta^3)$
        +1.0742E-5*(theta^4)-1.31137E-7*(theta^5)+6.12067E-10*(theta^6)
;sun-mars distance
 smd=(1d0-ecc^2)/(1d0+(ecc*cos((ls-250d0)*!dtor)))
;Gaseous column abundances
caco2=(p*100d0)/(g*(m*1.66054d-27))*1d-4*co2
can2=(p*100d0)/(g*(m*1.66054d-27))*1d-4*n2
caar=(p*100d0)/(g*(m*1.66054d-27))*1d-4*ar
```

```
cao2=(p*100d0)/(g*(m*1.66054d-27))*1d-4*o2
caco=(p*100d0)/(g*(m*1.66054d-27))*1d-4*co
;mars initial flux (top of atmosphere)
 mif=flux1_52/(secz*(smd^2))
 if (secz lt 0) then mif=mif*0
;Now define a time dependent tau value for a particular L_s - there are 3 choices: MGS(nominal),
;Viking(High) and Low dust case (taken from Mars Climate Database - http://huchard.lmd.jussieu.fr)
 ;VIKING DUST (Peak removed high dust case)
  ;taudbackg=0.7d0+(0.3d0*cos((ls+80d0)*!dtor))
 ;MGS DUST (nominal case)
  tauequator=0.2d0+(0.5d0-0.2d0)*(cos(((ls-250d0)/2)*!dtor))^14
  tausouth=0.1d0+(0.5d0-0.1d0)*(cos(((ls-250d0)/2)*!dtor))^14
  taunorth=0.1d0
  if (lat ge 0) then taudbackg=taunorth+((tauequator-taunorth)*0.5d0)*(1+tanh(((45-lat)/10)*!dtor)) else $
        taudbackg=tausouth+((tauequator-tausouth)*0.5d0)*(1+tanh(((45+lat)/10)*!dtor))
 ;LOW Dust case
     ;taudbackg=0.1
     ,ozone,caco2,can2,caar,cao2,caco,co2x,co2r,n2r,arr,o2x,o2r,cor,h2or,o3x,o3r,$
 taudbackg,taudlower,lq670,dq670,dbackqext,dlowerqext,bq670,dbackw,dbackg,dlowerw,$
 taudd,ddqext,ddw,ddg,dlowerg,taulowcloud,tauhighcloud,chighw,chighqext,chighg,cloww,$
 clowqext,clowg,pkstrct,mif,mu,alphastrct,betastrct,tautotextstrct,tottaustrct
;Tau, w and g values now defined for each layer, along with constants.
;Extract p_ and k_ values from the condensed structure "pkstrct"
p_1=pkstrct.p1
p_2=pkstrct.p2
p_3=pkstrct.p3
p_4=pkstrct.p4
p_5=pkstrct.p5
p_6=pkstrct.p6
p_7=pkstrct.p7
p_8=pkstrct.p8
p_9=pkstrct.p9
p_10=pkstrct.p10
k_1=pkstrct.k1
k_2=pkstrct.k2
k_3=pkstrct.k3
k_4=pkstrct.k4
k_5=pkstrct.k5
k_6=pkstrct.k6
k_7=pkstrct.k7
k_8=pkstrct.k8
k_9=pkstrct.k9
k_10=pkstrct.k10
;Extract alpha_ values from the condensed structure "alphastrct"
alpha_1=alphastrct.al1
alpha_2=alphastrct.al2
alpha_3=alphastrct.al3
alpha_4=alphastrct.al4
alpha_5=alphastrct.al5
alpha_6=alphastrct.al6
alpha_7=alphastrct.al7
alpha_8=alphastrct.al8
alpha_9=alphastrct.al9
alpha_10=alphastrct.al10
;Extract beta_ values from the condensed structure "betastrct"
beta_1=betastrct.be1
beta_2=betastrct.be2
beta_3=betastrct.be3
beta_4=betastrct.be4
beta_5=betastrct.be5
beta_6=betastrct.be6
beta_7=betastrct.be7
beta_8=betastrct.be8
beta_9=betastrct.be9
beta_10=betastrct.be10
;Extract tautotext_ values from the condensed structure "tautotextstrct"
tautotext_1=tautotextstrct.taut1
tautotext_2=tautotextstrct.taut2
tautotext_3=tautotextstrct.taut3
tautotext_4=tautotextstrct.taut4
tautotext_5=tautotextstrct.taut5
tautotext_6=tautotextstrct.taut6
tautotext_7=tautotextstrct.taut7
tautotext_8=tautotextstrct.taut8
```

```
tautotext_9=tautotextstrct.taut9
tautotext_10=tautotextstrct.taut10
;Extract tautotext_ values from the condensed structure "tautotextstrct"
tottau_1=tottaustrct.tott1
tottau_2=tottaustrct.tott2
tottau_3=tottaustrct.tott3
tottau_4=tottaustrct.tott4
tottau_5=tottaustrct.tott5
tottau_6=tottaustrct.tott6
tottau_7=tottaustrct.tott7
tottau_8=tottaustrct.tott8
tottau_9=tottaustrct.tott9
tottau_10=tottaustrct.tott10
;Define the coefficients for each layer using matrix inversion
[illegible],pkstrct,tautotext_1,tautotext_2,tautotext_3,tautotext_4, tautotext_5,tautotext_6,$
 tautotext_7, tautotext_8,tautotext_9,tautotext_10,a,alpha_1,alpha_2,alpha_3,alpha_4,alpha_5,$
 alpha_6,alpha_7,alpha_8, alpha_9,alpha_10,beta_1,beta_2,beta_3,beta_4,beta_5,beta_6,$
 beta_7,beta_8,beta_9,beta_10,mu,mif,c1,c2,c3, c4,c5,c6,c7,c8,c9,c10,d1,d2,d3,d4,d5,d6,d7,d8,d9,d10
;Define total atmospheric optical depth for all layers:
;delta-edd taus:
taudiff_1=tautotext_1
taudiff_2=tautotext_1+tautotext_2
taudiff_3=tautotext_1+tautotext_2+tautotext_3
taudiff_4=tautotext_1+tautotext_2+tautotext_3+tautotext_4
taudiff_5=tautotext_1+tautotext_2+tautotext_3+tautotext_4+tautotext_5
taudiff_6=tautotext_1+tautotext_2+tautotext_3+tautotext_4+tautotext_5+tautotext_6
taudiff_7=tautotext_1+tautotext_2+tautotext_3+tautotext_4+tautotext_5+tautotext_6+tautotext_7
taudiff_8=tautotext_1+tautotext_2+tautotext_3+tautotext_4+tautotext_5+tautotext_6+tautotext_7+tautotext_8
taudiff_9=tautotext_1+tautotext_2+tautotext_3+tautotext_4+tautotext_5+tautotext_6+tautotext_7+tautotext_8+$
        tautotext_9
taudiff_10=tautotext_1+tautotext_2+tautotext_3+tautotext_4+tautotext_5+tautotext_6+tautotext_7 +$
        tautotext_8+tautotext_9+tautotext_10
;Direct flux taus:
taudir_1=tottau_1
taudir_2=tottau_1+tottau_2
taudir_3=tottau_1+tottau_2+tottau_3
taudir_4=tottau_1+tottau_2+tottau_3+tottau_4
taudir_5=tottau_1+tottau_2+tottau_3+tottau_4+tottau_5
taudir_6=tottau_1+tottau_2+tottau_3+tottau_4+tottau_5+tottau_6
taudir_7=tottau_1+tottau_2+tottau_3+tottau_4+tottau_5+tottau_6+tottau_7
taudir_8=tottau_1+tottau_2+tottau_3+tottau_4+tottau_5+tottau_6+tottau_7+tottau_8
taudir_9=tottau_1+tottau_2+tottau_3+tottau_4+tottau_5+tottau_6+tottau_7+tottau_8+tottau_9
taudir_10=tottau_1+tottau_2+tottau_3+tottau_4+tottau_5+tottau_6+tottau_7+tottau_8+tottau_9+tottau_10
;Calculate I solutions for bottom layer boundary (layer 10) using total tau:
;I_alpha=I_0, and I_beta=I_1 in reference
I_alpha10=(c10*exp(-k_10*taudiff_10))+(d10*exp(k_10*taudiff_10))-(alpha_10*exp(-taudiff_10/mu))
I_beta10=p_10*((c10*exp(-k_10*taudiff_10))-(d10*exp(k_10*taudiff_10)))-(beta_10*exp(-taudiff_10/mu))
;Compute diffuse component at bottom layer:
Fdiffuse_10=!dpi*(I_alpha10+((2d0*I_beta10)/3d0))
  for i=0,220 do begin
        if (Fdiffuse_10(i) lt 0) then Fdiffuse_10(i)=Fdiffuse_10(i)*0
        if (Fdiffuse_10(i) gt 1) then Fdiffuse_10(i)=Fdiffuse_10(i)*0
  endfor
;Compute the direct component using Beer's law and direct(non transformed) tau:
Fdirect_10=mif*(exp(-(taudir_10)/mu))
;The total flux is the sum
Ftotal_10=Fdiffuse_10+Fdirect_10
;Plot the output spectrum. TOA flux and print the total UV flux
plot_io,l,Ftotal_10,yrange=[1d-6,1d0],xrange=[180,400],xtitle='Wavelength [nm]',$
 ytitle='Flux [Wm!E2!Nnm!E-1!N]',title='UV transmission through the Martian Atmosphere'
oplot,l,mif
oplot,l,Fdirect_10, linestyle=1
oplot,l,Fdiffuse_10, linestyle=2
plots, [0.75,0.86],[0.25,0.25], linestyle=0,/normal;,thick=2
 plots, [0.75,0.86],[0.2,0.2], linestyle=1,/normal;,thick=2
 plots, [0.75,0.86],[0.15,0.15], linestyle=2,/normal;,thick=2
 xyouts, 0.87,0.25, 'Total', /normal
 xyouts, 0.87,0.2, 'Direct', /normal
 xyouts, 0.87,0.15, 'Diffuse', /normal
print,'Total Flux='
print,total(Ftotal_10,/nan)
print,''
obj_destroy,in
end
```

```
; Subroutines:

[illegible],g,m,ecc,d,j,bq670,lq670,dq670,l,co2x,co2r,n2x,n2r,arx,arr,o2x,o2r,cox,cor,$
            h2ox,h2or,o3x,o3r,flux1_52,n,T7,uracil,bsubtilis,dna
 in=obj_new('datafile',21,'.\constants\constants_Basicconst.txt')
            g=in->number()
            m=in->number()
            ecc=in->number()
            d=in->number()
            j=in->number()
            bq670=in->number()
            lq670=in->number()
            dq670=in->number()
            l0=in->number()
            dl=in->number()
 obj_destroy,in
 in=obj_new('datafile',21,'.\constants\constants_Gasdata.txt')
            n=in->number()
            l=l0+dl*dindgen(n)
            co2x=dblarr(n)
            co2r=dblarr(n)
            n2x=dblarr(n)
            n2r=dblarr(n)
            arx=dblarr(n)
            arr=dblarr(n)
            o2x=dblarr(n)
            o2r=dblarr(n)
            cox=dblarr(n)
            cor=dblarr(n)
            h2ox=dblarr(n)
            h2or=dblarr(n)
            o3x=dblarr(n)
            o3r=dblarr(n)
  for i=0,n-1 do begin
   co2x(i)=in->number()
   co2r(i)=in->number()
   n2x(i)=in->number()
   n2r(i)=in->number()
   arx(i)=in->number()
   arr(i)=in->number()
   o2x(i)=in->number()
   o2r(i)=in->number()
   cox(i)=in->number()
   cor(i)=in->number()
   h2ox(i)=in->number()
   h2or(i)=in->number()
   o3x(i)=in->number()
   o3r(i)=in->number()
  endfor
 obj_destroy,in
 in=obj_new('datafile',21,'.\constants\constants_Flux1_52.txt')
            n=in->number()
            flux1_52=dblarr(n)
  for i=0,n-1 do begin
   flux1_52(i)=in->number()
  endfor
 obj_destroy,in
 in=obj_new('datafile',21,'.\constants\constants_Action_spectra.txt')
            n=in->number()
            T7=dblarr(n)
            uracil=dblarr(n)
            bsubtilis=dblarr(n)
            dna=dblarr(n)
  for i=0,n-1 do begin
   T7(i)=in->number()
   uracil(i)=in->number()
   bsubtilis(i)=in->number()
   dna(i)=in->number()
  endfor
 obj_destroy,in
 end

                        ,ngas,dbackw,dbackqext,dbackg,chighw,chighg,dlowerw,dlowerqext, $
            dlowerg,cloww,clowg,ddw,ddqext,ddg,dusttype
```

```
 if (dusttype eq 1) then filenm='constants_Aerosols_SURFACE_FOG.txt' else filenm='constants_aerosols.txt'
 in=obj_new('datafile',21,filenm)
            n=in->number()
  if (n ne ngas) then begin
    stop,'wrong number of rows'
  endif
            dbackw=dblarr(n)
            dbackqext=dblarr(n)
            dbackg=dblarr(n)
            chighw=dblarr(n)
            chighg=dblarr(n)
            dlowerw=dblarr(n)
            dlowerqext=dblarr(n)
            dlowerg=dblarr(n)
            cloww=dblarr(n)
            clowg=dblarr(n)
            ddw=dblarr(n)
            ddqext=dblarr(n)
            ddg=dblarr(n)
  for i=0,n-1 do begin
    dbackw(i)=in->number()
    dbackqext(i)=in->number()
    dbackg(i)=in->number()
    chighw(i)=in->number()
    chighg(i)=in->number()
    dlowerw(i)=in->number()
    dlowerqext(i)=in->number()
    dlowerg(i)=in->number()
    cloww(i)=in->number()
    clowg(i)=in->number()
    ddw(i)=in->number()
    ddqext(i)=in->number()
    ddg(i)=in->number()
  endfor
end

[illegible],ozone,caco2,can2,caar,cao2,caco,co2x,co2r,n2r,arr,o2x,o2r,cor,h2or,o3x,o3r,taudbackg, $
            taudlower,lq670,dq670,dbackqext,dlowerqext,bq670,dbackw,dbackg,dlowerw,taudd,ddqext,ddw,ddg, $
            dlowerg,taulowcloud,tauhighcloud,chighw,chighqext,chighg,cloww,clowqext,clowg,pkstrct,mif,mu, $
            alphastrct,betastrct,tautotextstrct,tottaustrct
;LAYER 1 (top):
;gas species
 n_1=0.0044d0
 cao3_1=0.0025d0*ozone
 cah2o_1=0d0
 taugs_1=(n_1*((co2r*caco2)+(n2r*can2)+(arr*caar)+(o2r*cao2)+(cor*caco)))+(h2or*cah2o_1)+(o3r*cao3_1)
 tauga_1=(n_1*((co2x*caco2)+(o2x*cao2)))+(o3x*cao3_1)
;dust aerosol tau abs and scat
 taud_1=0.00001d0
 taudtot_1=(dbackqext*taud_1)/bq670
 taudscat_1=dbackw*taudtot_1
 taudabs_1=taudtot_1-taudscat_1
;cloud aerosol tau abs and scat
 tauc_1=dblarr(221)
 tauc_1=tauc_1+0.000001d0
 taucscat_1=chighw*tauc_1
 taucabs_1=tauc_1-taucscat_1
;total tau scat and abs
 tautotscat_1=taugs_1+taudscat_1+taucscat_1
 tautotabs_1=tauga_1+taudabs_1+taucabs_1
 tottau_1=tautotscat_1+tautotabs_1
;composite optical properties
 weff_1=tautotscat_1/tottau_1
 geff_1=((taudtot_1*dbackg)+(tauc_1*chighg))/(taugs_1+tauga_1+taudtot_1+tauc_1)
;transformation of optical properties to Delta-Edd
 w_1=((1d0-(geff_1^2))*weff_1)/((1d0-(weff_1*(geff_1^2))))
 g_1=geff_1/(1d0+geff_1)
 tautotext_1=(1d0-(weff_1*(geff_1^2)))*tottau_1
;constants for calculation of c_X and d_X coefficients
 k_1=sqrt((3d0*(1d0-w_1)*(1d0-(w_1*g_1))))
 p_1=sqrt((3d0*(1d0-w_1)/(1d0-(w_1*g_1))))
 alpha_1=(3d0*w_1*(mif)*mu^2*(1d0+(g_1*(1d0-w_1))))/(4d0*(1d0-((k_1^2)*(mu^2))))
 beta_1=(3d0*w_1*(mif)*mu*(1d0+(3d0*g_1*(1d0-w_1)*mu^2)))/(4d0*(1d0-((k_1^2)*(mu^2))))
;LAYER 2:
```

```
;gas species
 n_2=0.0005d0
 cao3_2=0.0008d0*ozone
 cah2o_2=0d0
 taugs_2=(n_2*((co2r*caco2)+(n2r*can2)+(arr*caar)+(o2r*cao2)+(cor*caco)))+(h2or*cah2o_2)+(o3r*cao3_2)
 tauga_2=(n_2*((co2x*caco2)+(o2x*cao2)))+(o3x*cao3_2)
;dust aerosol tau abs and scat
 taud_2=0.0001d0
 taudtot_2=(dbackqext*taud_2)/bq670
 taudscat_2=dbackw*taudtot_2
 taudabs_2=taudtot_2-taudscat_2
;cloud aerosol tau abs and scat
 tauc_2=dblarr(221)
 tauc_2=tauc_2+tauhighcloud
 taucscat_2=chighw*tauc_2
 taucabs_2=tauc_2-taucscat_2
;total tau scat and abs
 tautotscat_2=taugs_2+taudscat_2+taucscat_2
 tautotabs_2=tauga_2+taudabs_2+taucabs_2
 tottau_2=tautotscat_2+tautotabs_2
;composite optical properties
 weff_2=tautotscat_2/tottau_2
 geff_2=((taudtot_2*dbackg)+(tauc_2*chighg))/(taugs_2+tauga_2+taudtot_2+tauc_2)
;transformation of optical properties to Delta-Edd
 w_2=((1d0-(geff_2^2))*weff_2)/((1d0-(weff_2*(geff_2^2))))
 g_2=geff_2/(1d0+geff_2)
 tautotext_2=(1d0-(weff_2*(geff_2^2)))*tottau_2
;constants for calculation of c_X and d_X coefficients
 k_2=sqrt((3d0*(1d0-w_2)*(1d0-(w_2*g_2))))
 p_2=sqrt((3d0*(1d0-w_2)/(1d0-(w_2*g_2))))
 alpha_2=(3d0*w_2*(mif)*mu^2*(1d0+(g_2*(1d0-w_2))))/(4d0*(1d0-((k_2^2)*(mu^2))))
 beta_2=(3d0*w_2*(mif)*mu*(1d0+(3d0*g_2*(1d0-w_2)*mu^2)))/(4d0*(1d0-((k_2^2)*(mu^2))))
;LAYER 3:
;gas species
 n_3=0.0217d0
 cao3_3=0.1520*ozone
 cah2o_3=0.0550d0
 taugs_3=(n_3*((co2r*caco2)+(n2r*can2)+(arr*caar)+(o2r*cao2)+(cor*caco)))+(h2or*cah2o_3)+(o3r*cao3_3)
 tauga_3=(n_3*((co2x*caco2)+(o2x*cao2)))+(o3x*cao3_3)
;dust aerosol tau abs and scat
 taud_3=0d0*taudbackg
 taudtot_3=(dbackqext*taud_3)/bq670
 taudscat_3=dbackw*taudtot_3
 taudabs_3=taudtot_3-taudscat_3
;cloud aerosol tau abs and scat
 tauc_3=dblarr(221)
 tauc_3=tauc_3+0.000001d0
 taucscat_3=cloww*tauc_3
 taucabs_3=tauc_3-taucscat_3
;total tau scat and abs
 tautotscat_3=taugs_3+taudscat_3+taucscat_3
 tautotabs_3=tauga_3+taudabs_3+taucabs_3
 tottau_3=tautotscat_3+tautotabs_3
;composite optical properties
 weff_3=tautotscat_3/tottau_3
 geff_3=((taudtot_3*dbackg)+(tauc_3*clowg))/(taugs_3+tauga_3+taudtot_3+tauc_3)
;transformation of optical properties to Delta-Edd
 w_3=((1d0-(geff_3^2))*weff_3)/((1d0-(weff_3*(geff_3^2))))
 g_3=geff_3/(1d0+geff_3)
 tautotext_3=(1d0-(weff_3*(geff_3^2)))*tottau_3
;constants for calculation of c_X and d_X coefficients
 k_3=sqrt((3d0*(1d0-w_3)*(1d0-(w_3*g_3))))
 p_3=sqrt((3d0*(1d0-w_3)/(1d0-(w_3*g_3))))
 alpha_3=(3d0*w_3*(mif)*mu^2*(1d0+(g_3*(1d0-w_3))))/(4d0*(1d0-((k_3^2)*(mu^2))))
 beta_3=(3d0*w_3*(mif)*mu*(1d0+(3d0*g_3*(1d0-w_3)*mu^2)))/(4d0*(1d0-((k_3^2)*(mu^2))))
;LAYER 4:
;gas species
 n_4=0.0900d0
 cao3_4=0.0970d0*ozone
 cah2o_4=0d0
 taugs_4=(n_4*((co2r*caco2)+(n2r*can2)+(arr*caar)+(o2r*cao2)+(cor*caco)))+(h2or*cah2o_4)+(o3r*cao3_4)
 tauga_4=(n_4*((co2x*caco2)+(o2x*cao2)))+(o3x*cao3_4)
;dust aerosol tau abs and scat
 taud_4=0.00001d0*taudbackg
```

```
 taudtot_4=(dbackqext*taud_4)/bq670
 taudscat_4=dbackw*taudtot_4
 taudabs_4=taudtot_4-taudscat_4
;cloud aerosol tau abs and scat
 tauc_4=dblarr(221)
 tauc_4=tauc_4+0.000001d0
 taucscat_4=cloww*tauc_4
 taucabs_4=tauc_4-taucscat_4
;total tau scat and abs
 tautotscat_4=taugs_4+taudscat_4+taucscat_4
 tautotabs_4=tauga_4+taudabs_4+taucabs_4
 tottau_4=tautotscat_4+tautotabs_4
;composite optical properties
 weff_4=tautotscat_4/tottau_4
 geff_4=((taudtot_4*dbackg)+(tauc_4*clowg))/(taugs_4+tauga_4+taudtot_4+tauc_4)
;transformation of optical properties to Delta-Edd
 w_4=((1d0-(geff_4^2))*weff_4)/((1d0-(weff_4*(geff_4^2))))
 g_4=geff_4/(1d0+geff_4)
 tautotext_4=(1d0-(weff_4*(geff_4^2)))*tottau_4
;constants for calculation of c_X and d_X coefficients
 k_4=sqrt((3d0*(1d0-w_4)*(1d0-(w_4*g_4))))
 p_4=sqrt((3d0*(1d0-w_4)/(1d0-(w_4*g_4))))
 alpha_4=(3d0*w_4*(mif)*mu^2*(1d0+(g_4*(1d0-w_4))))/(4d0*(1d0-((k_4^2)*(mu^2))))
 beta_4=(3d0*w_4*(mif)*mu*(1d0+(3d0*g_4*(1d0-w_4)*mu^2)))/(4d0*(1d0-((k_4^2)*(mu^2))))
;LAYER 5:
;gas species
 n_5=0.0126d0
 cao3_5=0.0148*ozone
 cah2o_5=0d0
 taugs_5=(n_5*((co2r*caco2)+(n2r*can2)+(arr*caar)+(o2r*cao2)+(cor*caco)))+(h2or*cah2o_5)+(o3r*cao3_5)
 tauga_5=(n_5*((co2x*caco2)+(o2x*cao2)))+(o3x*cao3_5)
;dust aerosol tau abs and scat
 taud_5=0.000001d0*taudbackg
 taudtot_5=(dbackqext*taud_5)/bq670
 taudscat_5=dbackw*taudtot_5
 taudabs_5=taudtot_5-taudscat_5
;cloud aerosol tau abs and scat
 tauc_5=dblarr(221)
 tauc_5=tauc_5+taulowcloud
 taucscat_5=cloww*tauc_5
 taucabs_5=tauc_5-taucscat_5
;total tau scat and abs
 tautotscat_5=taugs_5+taudscat_5+taucscat_5
 tautotabs_5=tauga_5+taudabs_5+taucabs_5
 tottau_5=tautotscat_5+tautotabs_5
;composite optical properties
 weff_5=tautotscat_5/tottau_5
 geff_5=((taudtot_5*dbackg)+(tauc_5*clowg))/(taugs_5+tauga_5+taudtot_5+tauc_5)
;transformation of optical properties to Delta-Edd
 w_5=((1d0-(geff_5^2))*weff_5)/((1d0-(weff_5*(geff_5^2))))
 g_5=geff_5/(1d0+geff_5)
 tautotext_5=(1d0-(weff_5*(geff_5^2)))*tottau_5
;constants for calculation of c_X and d_X coefficients
 k_5=sqrt((3d0*(1d0-w_5)*(1d0-(w_5*g_5))))
 p_5=sqrt((3d0*(1d0-w_5)/(1d0-(w_5*g_5))))
 alpha_5=(3d0*w_5*(mif)*mu^2*(1d0+(g_5*(1d0-w_5))))/(4d0*(1d0-((k_5^2)*(mu^2))))
 beta_5=(3d0*w_5*(mif)*mu*(1d0+(3d0*g_5*(1d0-w_5)*mu^2)))/(4d0*(1d0-((k_5^2)*(mu^2))))
;LAYER 6:
;gas species
 n_6=0.08d0
 cao3_6=0.1005d0*ozone
 cah2o_6=0d0
 taugs_6=(n_6*((co2r*caco2)+(n2r*can2)+(arr*caar)+(o2r*cao2)+(cor*caco)))+(h2or*cah2o_6)+(o3r*cao3_6)
 tauga_6=(n_6*((co2x*caco2)+(o2x*cao2)))+(o3x*cao3_6)
;background dust aerosol tau abs and scat
 taud_6=0.0953d0*taudbackg
 taudtot_6=(dbackqext*taud_6)/bq670
 taudscat_6=dbackw*taudtot_6
 taudabs_6=taudtot_6-taudscat_6
;large (storm) dust
 taudlarge_6=0.0953d0*taudlower
 taudlargetot_6=(dlowerqext*taudlarge_6)/lq670
 taudlargescat_6=dlowerw*taudlargetot_6
 taudlargeabs_6=taudlargetot_6-taudlargescat_6
```

```
;cloud aerosol tau abs and scat
  tauc_6=dblarr(221)
  tauc_6=tauc_6+0.0000001d0
  taucscat_6=cloww*tauc_6
  taucabs_6=tauc_6-taucscat_6
;total tau scat and abs
  tautotscat_6=taugs_6+taudscat_6+taucscat_6+taudlargescat_6
  tautotabs_6=tauga_6+taudabs_6+taucabs_6+taudlargeabs_6
  tottau_6=tautotscat_6+tautotabs_6
;composite optical properties
  weff_6=tautotscat_6/tottau_6
  geff_6=((taudtot_6*dbackg)+(taudlargetot_6*dlowerg)+(tauc_6*clowg))/(taugs_6+tauga_6+taudtot_6+$
          taudlargetot_6+tauc_6)
;transformation of optical properties to Delta-Edd
  w_6=((1d0-(geff_6^2))*weff_6)/((1d0-(weff_6*(geff_6^2))))
  g_6=geff_6/(1d0+geff_6)
  tautotext_6=(1d0-(weff_6*(geff_6^2)))*tottau_6
;constants for calculation of c_X and d_X coefficients
  k_6=sqrt((3d0*(1d0-w_6)*(1d0-(w_6*g_6))))
  p_6=sqrt((3d0*(1d0-w_6)/(1d0-(w_6*g_6))))
  alpha_6=(3d0*w_6*(mif)*mu^2*(1d0+(g_6*(1d0-w_6))))/(4d0*(1d0-((k_6^2)*(mu^2))))
  beta_6=(3d0*w_6*(mif)*mu*(1d0+(3d0*g_6*(1d0-w_6)*mu^2)))/(4d0*(1d0-((k_6^2)*(mu^2))))
;LAYER 7:
;gas species
  n_7=0.1398d0
  cao3_7=0.1566d0*ozone
  cah2o_7=0d0
  taugs_7=(n_7*((co2r*caco2)+(n2r*can2)+(arr*caar)+(o2r*cao2)+(cor*caco)))+(h2or*cah2o_7)+(o3r*cao3_7)
  tauga_7=(n_7*((co2x*caco2)+(o2x*cao2)))+(o3x*cao3_7)
;background dust aerosol tau abs and scat
  taud_7=0.1605d0*taudbackg
  taudtot_7=(dbackqext*taud_7)/bq670
  taudscat_7=dbackw*taudtot_7
  taudabs_7=taudtot_7-taudscat_7
;large (storm) dust
  taudlarge_7=0.1605d0*taudlower
  taudlargetot_7=(dlowerqext*taudlarge_7)/lq670
  taudlargescat_7=dlowerw*taudlargetot_7
  taudlargeabs_7=taudlargetot_7-taudlargescat_7
;cloud aerosol tau abs and scat
  tauc_7=dblarr(221)
  tauc_7=tauc_7+0.0000001d0
  taucscat_7=cloww*tauc_7
  taucabs_7=tauc_7-taucscat_7
;total tau scat and abs
  tautotscat_7=taugs_7+taudscat_7+taucscat_7+taudlargescat_7
  tautotabs_7=tauga_7+taudabs_7+taucabs_7+taudlargeabs_7
  tottau_7=tautotscat_7+tautotabs_7
;composite optical properties
  weff_7=tautotscat_7/tottau_7
  geff_7=((taudtot_7*dbackg)+(taudlargetot_7*dlowerg)+(tauc_7*clowg))/(taugs_7+tauga_7+taudtot_7+$
          taudlargetot_7+tauc_7)
;transformation of optical properties to Delta-Edd
  w_7=((1d0-(geff_7^2))*weff_7)/((1d0-(weff_7*(geff_7^2))))
  g_7=geff_7/(1d0+geff_7)
  tautotext_7=(1d0-(weff_7*(geff_7^2)))*tottau_7
;constants for calculation of c_X and d_X coefficients
  k_7=sqrt((3d0*(1d0-w_7)*(1d0-(w_7*g_7))))
  p_7=sqrt((3d0*(1d0-w_7)/(1d0-(w_7*g_7))))
  alpha_7=(3d0*w_7*(mif)*mu^2*(1d0+(g_7*(1d0-w_7))))/(4d0*(1d0-((k_7^2)*(mu^2))))
  beta_7=(3d0*w_7*(mif)*mu*(1d0+(3d0*g_7*(1d0-w_7)*mu^2)))/(4d0*(1d0-((k_7^2)*(mu^2))))
;LAYER 8:
;gas species
  n_8=0.2413d0
  cao3_8=0.2336d0*ozone
  cah2o_8=0d0
  taugs_8=(n_8*((co2r*caco2)+(n2r*can2)+(arr*caar)+(o2r*cao2)+(cor*caco)))+(h2or*cah2o_8)+(o3r*cao3_8)
  tauga_8=(n_8*((co2x*caco2)+(o2x*cao2)))+(o3x*cao3_8)
;background dust aerosol tau abs and scat
  taud_8=0.2771d0*taudbackg
  taudtot_8=(dbackqext*taud_8)/bq670
  taudscat_8=dbackw*taudtot_8
  taudabs_8=taudtot_8-taudscat_8
;large (storm) dust
```

```
  taudlarge_8=0.2771d0*taudlower
  taudlargetot_8=(dlowerqext*taudlarge_8)/lq670
  taudlargescat_8=dlowerw*taudlargetot_8
  taudlargeabs_8=taudlargetot_8-taudlargescat_8
;cloud aerosol tau abs and scat
  tauc_8=dblarr(221)
  tauc_8=tauc_8+0.0000001d0
  taucscat_8=cloww*tauc_8
  taucabs_8=tauc_8-taucscat_8
;total tau scat and abs
  tautotscat_8=taugs_8+taudscat_8+taucscat_8+taudlargescat_8
  tautotabs_8=tauga_8+taudabs_8+taucabs_8+taudlargeabs_8
  tottau_8=tautotscat_8+tautotabs_8
;composite optical properties
  weff_8=tautotscat_8/tottau_8
  geff_8=((taudtot_8*dbackg)+(taudlargetot_8*dlowerg)+(tauc_8*clowg))/(taugs_8+tauga_8+taudtot_8+$
          taudlargetot_8+tauc_8)
;transformation of optical properties to Delta-Edd
  w_8=((1d0-(geff_8^2))*weff_8)/((1d0-(weff_8*(geff_8^2))))
  g_8=geff_8/(1d0+geff_8)
  tautotext_8=(1d0-(weff_8*(geff_8^2)))*tottau_8
;constants for calculation of c_X and d_X coefficients
  k_8=sqrt((3d0*(1d0-w_8)*(1d0-(w_8*g_8))))
  p_8=sqrt((3d0*(1d0-w_8)/(1d0-(w_8*g_8))))
  alpha_8=(3d0*w_8*(mif)*mu^2*(1d0+(g_8*(1d0-w_8))))/(4d0*(1d0-((k_8^2)*(mu^2))))
  beta_8=(3d0*w_8*(mif)*mu*(1d0+(3d0*g_8*(1d0-w_8)*mu^2)))/(4d0*(1d0-((k_8^2)*(mu^2))))
;LAYER 9:
;gas species
  n_9=0.3076d0
  cao3_9=0.2613d0*ozone
  cah2o_9=0d0
  taugs_9=(n_9*((co2r*caco2)+(n2r*can2)+(arr*caar)+(o2r*cao2)+(cor*caco)))+(h2or*cah2o_9)+(o3r*cao3_9)
  tauga_9=(n_9*((co2x*caco2)+(o2x*cao2)))+(o3x*cao3_9)
;background dust aerosol tau abs and scat
  taud_9=0.3532d0*taudbackg
  taudtot_9=(dbackqext*taud_9)/bq670
  taudscat_9=dbackw*taudtot_9
  taudabs_9=taudtot_9-taudscat_9
;large (storm) dust
  taudlarge_9=0.3532d0*taudlower
  taudlargetot_9=(dlowerqext*taudlarge_9)/lq670
  taudlargescat_9=dlowerw*taudlargetot_9
  taudlargeabs_9=taudlargetot_9-taudlargescat_9
;cloud aerosol tau abs and scat
  tauc_9=dblarr(221)
  tauc_9=tauc_9+0.0000001d0
  taucscat_9=cloww*tauc_9
  taucabs_9=tauc_9-taucscat_9
;total tau scat and abs
  tautotscat_9=taugs_9+taudscat_9+taucscat_9+taudlargescat_9
  tautotabs_9=tauga_9+taudabs_9+taucabs_9+taudlargeabs_9
  tottau_9=tautotscat_9+tautotabs_9
;composite optical properties
  weff_9=tautotscat_9/tottau_9
  geff_9=((taudtot_9*dbackg)+(taudlargetot_9*dlowerg)+(tauc_9*clowg))/(taugs_9+tauga_9+taudtot_9+$
          taudlargetot_9+tauc_9)
;transformation of optical properties to Delta-Edd
  w_9=((1d0-(geff_9^2))*weff_9)/((1d0-(weff_9*(geff_9^2))))
  g_9=geff_9/(1d0+geff_9)
  tautotext_9=(1d0-(weff_9*(geff_9^2)))*tottau_9
;constants for calculation of c_X and d_X coefficients
  k_9=sqrt((3d0*(1d0-w_9)*(1d0-(w_9*g_9))))
  p_9=sqrt((3d0*(1d0-w_9)/(1d0-(w_9*g_9))))
  alpha_9=(3d0*w_9*(mif)*mu^2*(1d0+(g_9*(1d0-w_9))))/(4d0*(1d0-((k_9^2)*(mu^2))))
  beta_9=(3d0*w_9*(mif)*mu*(1d0+(3d0*g_9*(1d0-w_9)*mu^2)))/(4d0*(1d0-((k_9^2)*(mu^2))))
;LAYER 10:
;gas species
  n_10=0.0991d0
  cao3_10=0.0778d0*ozone
  cah2o_10=0d0
  taugs_10=(n_10*((co2r*caco2)+(n2r*can2)+(arr*caar)+(o2r*cao2)+(cor*caco)))+(h2or*cah2o_10)+$
          (o3r*cao3_10)
  tauga_10=(n_10*((co2x*caco2)+(o2x*cao2)))+(o3x*cao3_10)
;Two dust calculations are now required, one for the background dust and
```

```
;one for the lower (storm) dust.  They are then combined in the weff_10 stage
;background dust aerosol tau abs and scat
 taud_10=0.1139d0*taudbackg
 taudtot_10=(dbackqext*taud_10)/bq670
 taudscat_10=dbackw*taudtot_10
 taudabs_10=taudtot_10-taudscat_10
;large (storm) dust
 taudlarge_10=0.1139d0*taudlower
 taudlargetot_10=(dlowerqext*taudlarge_10)/lq670
 taudlargescat_10=dlowerw*taudlargetot_10
 taudlargeabs_10=taudlargetot_10-taudlargescat_10
;dust devil dust
 taudd_10=taudd
 tauddtot_10=(ddqext*taudd_10)/dq670
 tauddscat_10=ddw*tauddtot_10
 tauddabs_10=tauddtot_10-tauddscat_10
;cloud aerosol tau abs and scat
 tauc_10=dblarr(221)
 tauc_10=tauc_10+0.0000001d0
 taucscat_10=cloww*tauc_10
 taucabs_10=tauc_10-taucscat_10
;total tau scat and abs
 tautotscat_10=taugs_10+taudscat_10+taucscat_10+taudlargescat_10+tauddscat_10
 tautotabs_10=tauga_10+taudabs_10+taucabs_10+taudlargeabs_10+tauddabs_10
 tottau_10=tautotscat_10+tautotabs_10
;composite optical properties
 weff_10=tautotscat_10/tottau_10
 geff_10=((taudtot_10*dbackg)+(taudlargetot_10*dlowerg)+(tauddtot_10*ddg)+(tauc_10*clowg))/ $
          (taugs_10+tauga_10+taudtot_10+taudlargetot_10+tauddtot_10+tauc_10)
;transformation of optical properties to Delta-Edd
 w_10=((1d0-(geff_10^2))*weff_10)/((1d0-(weff_10*(geff_10^2))))
 g_10=geff_10/(1d0+geff_10)
 tautotext_10=(1d0-(weff_10*(geff_10^2)))*tottau_10
;constants for calculation of c_X and d_X coefficients
 k_10=sqrt((3d0*(1d0-w_10)*(1d0-(w_10*g_10))))
 p_10=sqrt((3d0*(1d0-w_10)/(1d0-(w_10*g_10))))
 alpha_10=(3d0*w_10*(mif)*mu^2*(1d0+(g_10*(1d0-w_10))))/(4d0*(1d0-((k_10^2)*(mu^2))))
 beta_10=(3d0*w_10*(mif)*mu*(1d0+(3d0*g_10*(1d0-w_10)*mu^2)))/(4d0*(1d0-((k_10^2)*(mu^2))))
pkstrct={p1:p_1,p2:p_2,p3:p_3,p4:p_4,p5:p_5,p6:p_6,p7:p_7,p8:p_8,p9:p_9,p10:p_10,$
          k1:k_1,k2:k_2,k3:k_3,k4:k_4,k5:k_5,k6:k_6,k7:k_7,k8:k_8,k9:k_9,k10:k_10}
alphastrct={al1:alpha_1,al2:alpha_2,al3:alpha_3,al4:alpha_4,al5:alpha_5,$
          al6:alpha_6,al7:alpha_7,al8:alpha_8,al9:alpha_9,al10:alpha_10}
betastrct={be1:beta_1,be2:beta_2,be3:beta_3,be4:beta_4,be5:beta_5,$
          be6:beta_6,be7:beta_7,be8:beta_8,be9:beta_9,be10:beta_10}
tautotextstrct={taut1:tautotext_1,taut2:tautotext_2,taut3:tautotext_3,taut4:tautotext_4,taut5:tautotext_5,$
          taut6:tautotext_6,taut7:tautotext_7,taut8:tautotext_8,taut9:tautotext_9,taut10:tautotext_10}

tottaustrct={tott1:tottau_1,tott2:tottau_2,tott3:tottau_3,tott4:tottau_4,tott5:tottau_5,$
          tott6:tottau_6,tott7:tottau_7,tott8:tottau_8,tott9:tottau_9,tott10:tottau_10}
end

[illegible],pkstrct,tautotext_1,tautotext_2,tautotext_3,tautotext_4,tautotext_5,tautotext_6,tautotext_7, $
          tautotext_8,tautotext_9,tautotext_10,a,alpha_1,alpha_2,alpha_3,alpha_4,alpha_5,alpha_6, $
          alpha_7,alpha_8,alpha_9,alpha_10,beta_1,beta_2,beta_3,beta_4,beta_5,beta_6,beta_7,beta_8,beta_9, $
          beta_10,mu,mif,c1,c2,c3,c4,c5,c6,c7,c8,c9,c10,d1,d2,d3,d4,d5,d6,d7,d8,d9,d10
;Extract p_ and k_ values from the condensed structure "pkstrct"
p_1=pkstrct.p1
p_2=pkstrct.p2
p_3=pkstrct.p3
p_4=pkstrct.p4
p_5=pkstrct.p5
p_6=pkstrct.p6
p_7=pkstrct.p7
p_8=pkstrct.p8
p_9=pkstrct.p9
p_10=pkstrct.p10
k_1=pkstrct.k1
k_2=pkstrct.k2
k_3=pkstrct.k3
k_4=pkstrct.k4
k_5=pkstrct.k5
k_6=pkstrct.k6
k_7=pkstrct.k7
k_8=pkstrct.k8
```

```
k_9=pkstrct.k9
k_10=pkstrct.k10
;Define matrices to satisfy derived layer equation
n=221
;Define elements in LHS array:
r1c1=(1d0+(2d0*p_1)/3d0)
r1c11=(1d0-(2d0*p_1)/3d0)
r2c1=(exp(-k_1*tautotext_1))
r2c2=(-exp(-k_2*tautotext_1))
r2c11=(exp(k_1*tautotext_1))
r2c12=(-exp(k_2*tautotext_1))
r3c2=(exp(-k_2*(tautotext_2+tautotext_1)))
r3c3=(-exp(-k_3*(tautotext_2+tautotext_1)))
r3c12=(exp(k_2*(tautotext_2+tautotext_1)))
r3c13=(-exp(k_3*(tautotext_2+tautotext_1)))
r4c3=(exp(-k_3*(tautotext_3+tautotext_2+tautotext_1)))
r4c4=(-exp(-k_4*(tautotext_3+tautotext_2+tautotext_1)))
r4c13=(exp(k_3*(tautotext_3+tautotext_2+tautotext_1)))
r4c14=(-exp(k_4*(tautotext_3+tautotext_2+tautotext_1)))
r5c4=(exp(-k_4*(tautotext_4+tautotext_3+tautotext_2+tautotext_1)))
r5c5=(-exp(-k_5*(tautotext_4+tautotext_3+tautotext_2+tautotext_1)))
r5c14=(exp(k_4*(tautotext_4+tautotext_3+tautotext_2+tautotext_1)))
r5c15=(-exp(k_5*(tautotext_4+tautotext_3+tautotext_2+tautotext_1)))
r6c5=(exp(-k_5*(tautotext_5+tautotext_4+tautotext_3+tautotext_2+tautotext_1)))
r6c6=(-exp(-k_6*(tautotext_5+tautotext_4+tautotext_3+tautotext_2+tautotext_1)))
r6c15=(exp(k_5*(tautotext_5+tautotext_4+tautotext_3+tautotext_2+tautotext_1)))
r6c16=(-exp(k_6*(tautotext_5+tautotext_4+tautotext_3+tautotext_2+tautotext_1)))
r7c6=(exp(-k_6*(tautotext_6+tautotext_5+tautotext_4+tautotext_3+tautotext_2+tautotext_1)))
r7c7=(-exp(-k_7*(tautotext_6+tautotext_5+tautotext_4+tautotext_3+tautotext_2+tautotext_1)))
r7c16=(exp(k_6*(tautotext_6+tautotext_5+tautotext_4+tautotext_3+tautotext_2+tautotext_1)))
r7c17=(-exp(k_7*(tautotext_6+tautotext_5+tautotext_4+tautotext_3+tautotext_2+tautotext_1)))
r8c7=(exp(-k_7*(tautotext_7+tautotext_6+tautotext_5+tautotext_4+tautotext_3+tautotext_2+tautotext_1)))
r8c8=(-exp(-k_8*(tautotext_7+tautotext_6+tautotext_5+tautotext_4+tautotext_3+tautotext_2+tautotext_1)))
r8c17=(exp(k_7*(tautotext_7+tautotext_6+tautotext_5+tautotext_4+tautotext_3+tautotext_2+tautotext_1)))
r8c18=(-exp(k_8*(tautotext_7+tautotext_6+tautotext_5+tautotext_4+tautotext_3+tautotext_2+tautotext_1)))
r9c8=(exp(-k_8*(tautotext_8+tautotext_7+tautotext_6+tautotext_5+tautotext_4+tautotext_3+tautotext_2+$
        tautotext_1)))
r9c9=(-exp(-k_9*(tautotext_8+tautotext_7+tautotext_6+tautotext_5+tautotext_4+tautotext_3+tautotext_2+$
        tautotext_1)))
r9c18=(exp(k_8*(tautotext_8+tautotext_7+tautotext_6+tautotext_5+tautotext_4+tautotext_3+$
        tautotext_2+tautotext_1)))
r9c19=(-exp(k_9*(tautotext_8+tautotext_7+tautotext_6+tautotext_5+tautotext_4+tautotext_3+$
        tautotext_2+tautotext_1)))
r10c9=(exp(-k_9*(tautotext_9+tautotext_8+tautotext_7+tautotext_6+tautotext_5+tautotext_4+$
        tautotext_3+tautotext_2+tautotext_1)))
r10c10=(-exp(-k_10*(tautotext_9+tautotext_8+tautotext_7+tautotext_6+tautotext_5+tautotext_4+$
        tautotext_3+tautotext_2+tautotext_1)))
r10c19=(exp(k_9*(tautotext_9+tautotext_8+tautotext_7+tautotext_6+tautotext_5+tautotext_4+$
        tautotext_3+tautotext_2+tautotext_1)))
r10c20=(-exp(k_10*(tautotext_9+tautotext_8+tautotext_7+tautotext_6+tautotext_5+tautotext_4+$
        tautotext_3+tautotext_2+tautotext_1)))
r11c1=(p_1*exp(-k_1*tautotext_1))
r11c2=(-p_2*exp(-k_2*tautotext_1))
r11c11=(-p_1*exp(k_1*tautotext_1))
r11c12=(p_2*exp(k_2*tautotext_1))
r12c2=(p_2*exp(-k_2*(tautotext_2+tautotext_1)))
r12c3=(-p_3*exp(-k_3*(tautotext_2+tautotext_1)))
r12c12=(-p_2*exp(k_2*(tautotext_2+tautotext_1)))
r12c13=(p_3*exp(k_3*(tautotext_2+tautotext_1)))
r13c3=(p_3*exp(-k_3*(tautotext_3+tautotext_2+tautotext_1)))
r13c4=(-p_4*exp(-k_4*(tautotext_3+tautotext_2+tautotext_1)))
r13c13=(-p_3*exp(k_3*(tautotext_3+tautotext_2+tautotext_1)))
r13c14=(p_4*exp(k_4*(tautotext_3+tautotext_2+tautotext_1)))
r14c4=(p_4*exp(-k_4*(tautotext_4+tautotext_3+tautotext_2+tautotext_1)))
r14c5=(-p_5*exp(-k_5*(tautotext_4+tautotext_3+tautotext_2+tautotext_1)))
r14c14=(-p_4*exp(k_4*(tautotext_4+tautotext_3+tautotext_2+tautotext_1)))
r14c15=(p_5*exp(k_5*(tautotext_4+tautotext_3+tautotext_2+tautotext_1)))
r15c5=(p_5*exp(-k_5*(tautotext_5+tautotext_4+tautotext_3+tautotext_2+tautotext_1)))
r15c6=(-p_6*exp(-k_6*(tautotext_5+tautotext_4+tautotext_3+tautotext_2+tautotext_1)))
r15c15=(-p_5*exp(k_5*(tautotext_5+tautotext_4+tautotext_3+tautotext_2+tautotext_1)))
r15c16=(p_6*exp(k_6*(tautotext_5+tautotext_4+tautotext_3+tautotext_2+tautotext_1)))
r16c6=(p_6*exp(-k_6*(tautotext_6+tautotext_5+tautotext_4+tautotext_3+tautotext_2+tautotext_1)))
r16c7=(-p_7*exp(-k_7*(tautotext_6+tautotext_5+tautotext_4+tautotext_3+tautotext_2+tautotext_1)))
r16c16=(-p_6*exp(k_6*(tautotext_6+tautotext_5+tautotext_4+tautotext_3+tautotext_2+tautotext_1)))
```

```
r16c17=(p_7*exp(k_7*(tautotext_6+tautotext_5+tautotext_4+tautotext_3+tautotext_2+tautotext_1)))
r17c7=(p_7*exp(-k_7*(tautotext_7+tautotext_6+tautotext_5+tautotext_4+tautotext_3+tautotext_2+tautotext_1)))
r17c8=(-p_8*exp(-k_8*(tautotext_7+tautotext_6+tautotext_5+tautotext_4+tautotext_3+tautotext_2+tautotext_1)))
r17c17=(-p_7*exp(k_7*(tautotext_7+tautotext_6+tautotext_5+tautotext_4+tautotext_3+tautotext_2+tautotext_1)))
r17c18=(p_8*exp(k_8*(tautotext_7+tautotext_6+tautotext_5+tautotext_4+tautotext_3+tautotext_2+tautotext_1)))
r18c8=(p_8*exp(-k_8*(tautotext_8+tautotext_7+tautotext_6+tautotext_5+tautotext_4+tautotext_3+$
        tautotext_2+tautotext_1)))
r18c9=(-p_9*exp(-k_9*(tautotext_8+tautotext_7+tautotext_6+tautotext_5+tautotext_4+tautotext_3+$
        tautotext_2+tautotext_1)))
r18c18=(-p_8*exp(k_8*(tautotext_8+tautotext_7+tautotext_6+tautotext_5+tautotext_4+$
        tautotext_3+tautotext_2+tautotext_1)))
r18c19=(p_9*exp(k_9*(tautotext_8+tautotext_7+tautotext_6+tautotext_5+tautotext_4+$
        tautotext_3+tautotext_2+tautotext_1)))
r19c9=(p_9*exp(-k_9*(tautotext_9+tautotext_8+tautotext_7+tautotext_6+tautotext_5+tautotext_4+$
        tautotext_3+tautotext_2+tautotext_1)))
r19c10=(-p_10*exp(-
k_10*(tautotext_9+tautotext_8+tautotext_7+tautotext_6+tautotext_5+tautotext_4+tautotext_3+tautotext_2+tautotext_1)))
r19c19=(-p_9*exp(k_9*(tautotext_9+tautotext_8+tautotext_7+tautotext_6+tautotext_5+$
        tautotext_4+tautotext_3+tautotext_2+tautotext_1)))
r19c20=(p_10*exp(k_10*(tautotext_9+tautotext_8+tautotext_7+tautotext_6+$
        tautotext_5+tautotext_4+tautotext_3+tautotext_2+tautotext_1)))
r20c10=(1d0-a-((2d0*(1d0+a)*p_10)/3d0))*exp(-k_10*(tautotext_10+tautotext_9+tautotext_8+tautotext_7+tautotext_6+$
        tautotext_5+tautotext_4+tautotext_3+tautotext_2+tautotext_1))
r20c20=((1d0-a+((2d0*(1d0+a)*p_10)/3d0))*exp(k_10*(tautotext_10+tautotext_9+$
        tautotext_8+tautotext_7+tautotext_6+tautotext_5+tautotext_4+tautotext_3+tautotext_2+tautotext_1)))
;Define elements for RHS array:
right1=(alpha_1+((2d0*beta_1)/3d0))
right2=((alpha_1-alpha_2)*exp(-tautotext_1/mu))
right3=((alpha_2-alpha_3)*exp(-(tautotext_2+tautotext_1)/mu))
right4=((alpha_3-alpha_4)*exp(-(tautotext_3+tautotext_2+tautotext_1)/mu))
right5=((alpha_4-alpha_5)*exp(-(tautotext_4+tautotext_3+tautotext_2+tautotext_1)/mu))
right6=((alpha_5-alpha_6)*exp(-(tautotext_5+tautotext_4+tautotext_3+tautotext_2+tautotext_1)/mu))
right7=((alpha_6-alpha_7)*exp(-(tautotext_6+tautotext_5+tautotext_4+tautotext_3+tautotext_2+tautotext_1)/mu))
right8=((alpha_7-alpha_8)*exp(-(tautotext_7+tautotext_6+tautotext_5+tautotext_4+tautotext_3+$
        tautotext_2+tautotext_1)/mu))
right9=((alpha_8-alpha_9)*exp(-(tautotext_8+tautotext_7+tautotext_6+tautotext_5+tautotext_4+tautotext_3+$
        tautotext_2+tautotext_1)/mu))
right10=((alpha_9-alpha_10)*exp(-(tautotext_9+tautotext_8+tautotext_7+tautotext_6+tautotext_5+tautotext_4+$
        tautotext_3+tautotext_2+tautotext_1)/mu))
right11=((beta_1-beta_2)*exp(-tautotext_1/mu))
right12=((beta_2-beta_3)*exp(-(tautotext_2+tautotext_1)/mu))
right13=((beta_3-beta_4)*exp(-(tautotext_3+tautotext_2+tautotext_1)/mu))
right14=((beta_4-beta_5)*exp(-(tautotext_4+tautotext_3+tautotext_2+tautotext_1)/mu))
right15=((beta_5-beta_6)*exp(-(tautotext_5+tautotext_4+tautotext_3+tautotext_2+tautotext_1)/mu))
right16=((beta_6-beta_7)*exp(-(tautotext_6+tautotext_5+tautotext_4+tautotext_3+tautotext_2+tautotext_1)/mu))
right17=((beta_7-beta_8)*exp(-(tautotext_7+tautotext_6+tautotext_5+tautotext_4+tautotext_3+$
        tautotext_2+tautotext_1)/mu))
right18=((beta_8-beta_9)*exp(-(tautotext_8+tautotext_7+tautotext_6+tautotext_5+tautotext_4+$
        tautotext_3+tautotext_2+tautotext_1)/mu))
right19=((beta_9-beta_10)*exp(-(tautotext_9+tautotext_8+tautotext_7+tautotext_6+tautotext_5+$
        tautotext_4+tautotext_3+tautotext_2+tautotext_1)/mu))
right20=(((1d0-a)*alpha_10-(((2d0*(1d0+a))/3d0)*beta_10)+((a*mu*mif)))*exp(-(tautotext_10+tautotext_9+$
      tautotext_8+tautotext_7+tautotext_6+tautotext_5+tautotext_4+tautotext_3+tautotext_2+tautotext_1)/mu))
LHS=dblarr(20,20,221)
RHS=dblarr(221,20)
result=dblarr(221,20)
; assign array places in matrices
; note the matrix element reference (x,y,z) is defined as x=column, y=row, z=wavelength dependence 180-400nm.
lhs(0,0,*)=r1c1
lhs(10,0,*)=r1c11
lhs(0,1,*)=r2c1
lhs(1,1,*)=r2c2
lhs(10,1,*)=r2c11
lhs(11,1,*)=r2c12
lhs(1,2,*)=r3c2
lhs(2,2,*)=r3c3
lhs(11,2,*)=r3c12
lhs(12,2,*)=r3c13
lhs(2,3,*)=r4c3
lhs(3,3,*)=r4c4
lhs(12,3,*)=r4c13
lhs(13,3,*)=r4c14
lhs(3,4,*)=r5c4
lhs(4,4,*)=r5c5
```

```
lhs(13,4,*)=r5c14
lhs(14,4,*)=r5c15
lhs(4,5,*)=r6c5
lhs(5,5,*)=r6c6
lhs(14,5,*)=r6c15
lhs(15,5,*)=r6c16
lhs(5,6,*)=r7c6
lhs(6,6,*)=r7c7
lhs(15,6,*)=r7c16
lhs(16,6,*)=r7c17
lhs(6,7,*)=r8c7
lhs(7,7,*)=r8c8
lhs(16,7,*)=r8c17
lhs(17,7,*)=r8c18
lhs(7,8,*)=r9c8
lhs(8,8,*)=r9c9
lhs(17,8,*)=r9c18
lhs(18,8,*)=r9c19
lhs(8,9,*)=r10c9
lhs(9,9,*)=r10c10
lhs(18,9,*)=r10c19
lhs(19,9,*)=r10c20
lhs(0,10,*)=r11c1
lhs(1,10,*)=r11c2
lhs(10,10,*)=r11c11
lhs(11,10,*)=r11c12
lhs(1,11,*)=r12c2
lhs(2,11,*)=r12c3
lhs(11,11,*)=r12c12
lhs(12,11,*)=r12c13
lhs(2,12,*)=r13c3
lhs(3,12,*)=r13c4
lhs(12,12,*)=r13c13
lhs(13,12,*)=r13c14
lhs(3,13,*)=r14c4
lhs(4,13,*)=r14c5
lhs(13,13,*)=r14c14
lhs(14,13,*)=r14c15
lhs(4,14,*)=r15c5
lhs(5,14,*)=r15c6
lhs(14,14,*)=r15c15
lhs(15,14,*)=r15c16
lhs(5,15,*)=r16c6
lhs(6,15,*)=r16c7
lhs(15,15,*)=r16c16
lhs(16,15,*)=r16c17
lhs(6,16,*)=r17c7
lhs(7,16,*)=r17c8
lhs(16,16,*)=r17c17
lhs(17,16,*)=r17c18
lhs(7,17,*)=r18c8
lhs(8,17,*)=r18c9
lhs(17,17,*)=r18c18
lhs(18,17,*)=r18c19
lhs(8,18,*)=r19c9
lhs(9,18,*)=r19c10
lhs(18,18,*)=r19c19
lhs(19,18,*)=r19c20
lhs(9,19,*)=r20c10
lhs(19,19,*)=r20c20
rhs(*,0)=right1
rhs(*,1)=right2
rhs(*,2)=right3
rhs(*,3)=right4
rhs(*,4)=right5
rhs(*,5)=right6
rhs(*,6)=right7
rhs(*,7)=right8
rhs(*,8)=right9
rhs(*,9)=right10
rhs(*,10)=right11
rhs(*,11)=right12
rhs(*,12)=right13
rhs(*,13)=right14
```

```
rhs(*,14)=right15
rhs(*,15)=right16
rhs(*,16)=right17
rhs(*,17)=right18
rhs(*,18)=right19
rhs(*,19)=right20
;Now the two matrices are defined, invert to solve the equation
 for i=0,n-1 do begin
            result[i,*]=INVERT(LHS[*,*,i])##RHS[i,*]
 endfor
;Test whether the result is true by seeing if it returns rhs
test=dblarr(221,20)
 for i=0,n-1 do begin
            test[i,*]=LHS[*,*,i]##result[i,*]
endfor
;express array elements as single variables:
 c1=dblarr(221)
 c2=dblarr(221)
 c3=dblarr(221)
 c4=dblarr(221)
 c5=dblarr(221)
 c6=dblarr(221)
 c7=dblarr(221)
 c8=dblarr(221)
 c9=dblarr(221)
 c10=dblarr(221)
 d1=dblarr(221)
 d2=dblarr(221)
 d3=dblarr(221)
 d4=dblarr(221)
 d5=dblarr(221)
 d6=dblarr(221)
 d7=dblarr(221)
 d8=dblarr(221)
 d9=dblarr(221)
 d10=dblarr(221)
 c1(*)=result(*,0)                ; ie c1=first element in array 'result'
 c2(*)=result(*,1)
 c3(*)=result(*,2)
 c4(*)=result(*,3)
 c5(*)=result(*,4)
 c6(*)=result(*,5)
 c7(*)=result(*,6)
 c8(*)=result(*,7)
 c9(*)=result(*,8)
 c10(*)=result(*,9)
 d1(*)=result(*,10)
 d2(*)=result(*,11)
 d3(*)=result(*,12)
 d4(*)=result(*,13)
 d5(*)=result(*,14)
 d6(*)=result(*,15)               ; ie d6=12th element in array 'result'
 d7(*)=result(*,16)
 d8(*)=result(*,17)
 d9(*)=result(*,18)
 d10(*)=result(*,19)
end
```

Appendix B

UV Sensor Circuit Diagrams

This appendix contains circuit diagrams for each channel of the UV sensor, and the interface block.

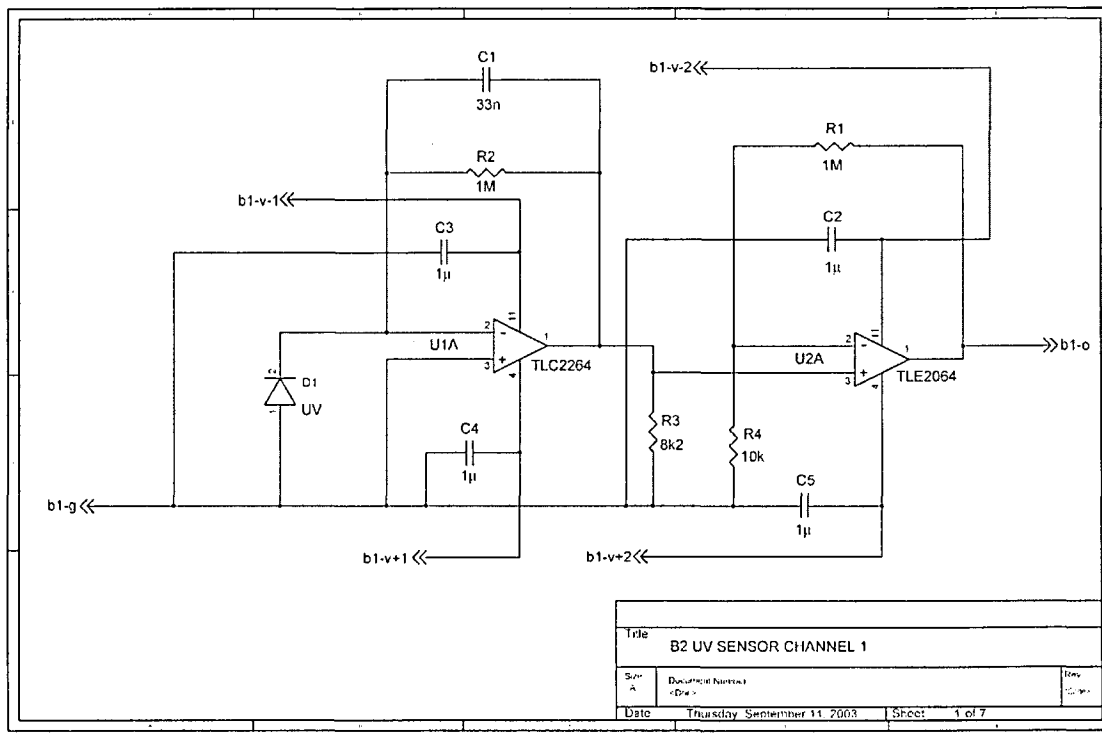

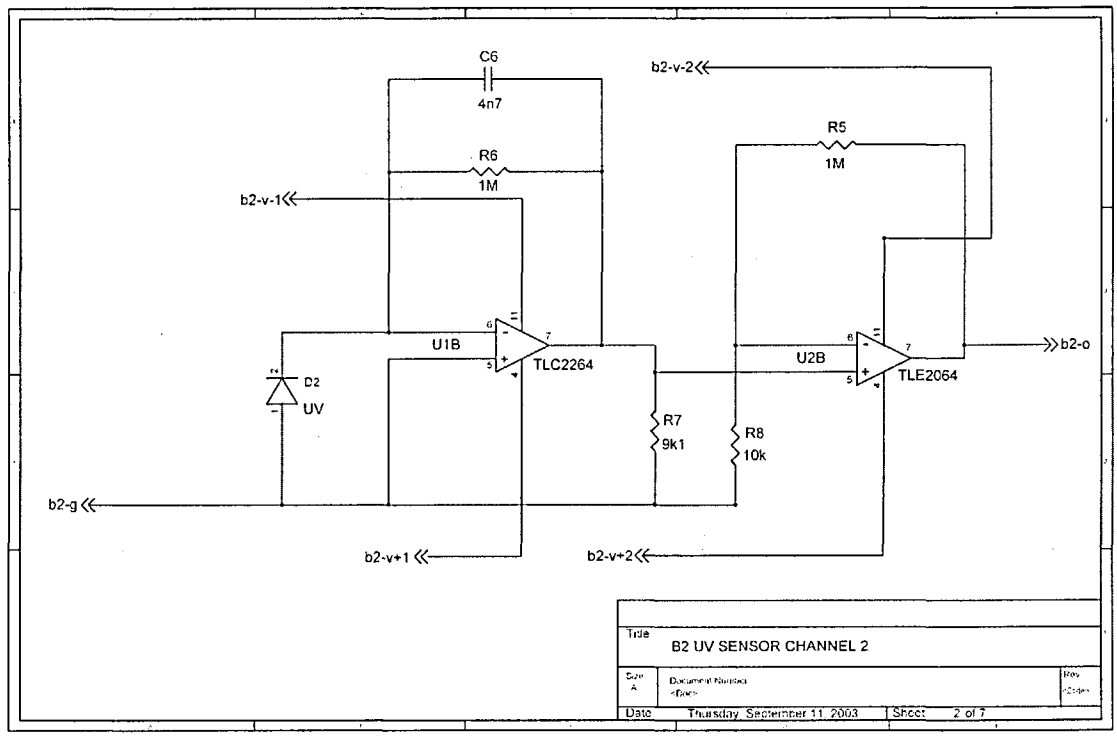
C6
4n7
b2-v-2
R5
1M
R6
1M
b2-v-1
U1B
TLC2264
U2B
TLE2064
b2-o
D2
UV
R7
9k1
R8
10k
b2-g
b2-v+1
b2-v+2
Title
B2 UV SENSOR CHANNEL 2
Size
A
Date: Thursday, September 11, 2003
Sheet 2 of 7

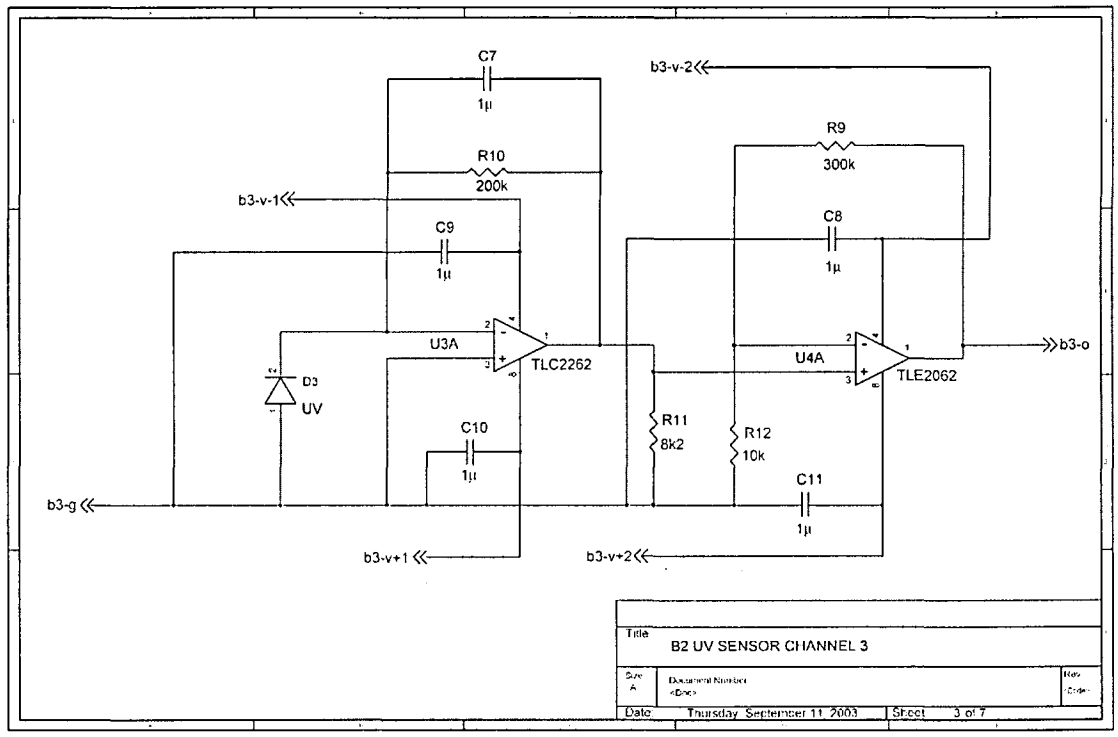
C7
1µ
b3-v-2
R9
300k
R10
200k
b3-v-1
C9
1µ
C8
1µ
U3A
TLC2262
U4A
TLE2062
b3-o
D3
UV
C10
1µ
R11
8k2
R12
10k
C11
1µ
b3-g
b3-v+1
b3-v+2
Title
B2 UV SENSOR CHANNEL 3
Size
A
Date: Thursday, September 11, 2003
Sheet 3 of 7

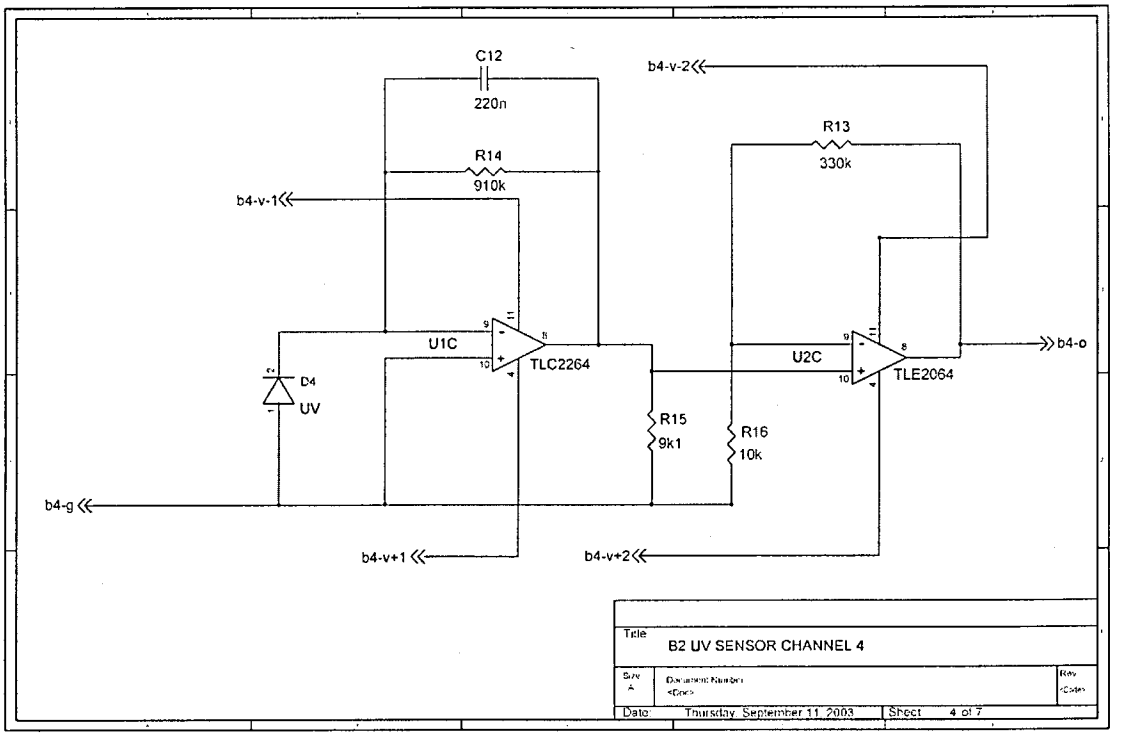
C12
220n
R14
910k
b4-v-1
b4-v-2
R13
330k
U1C
TLC2264
U2C
TLE2064
b4-o
D4
UV
R15
9k1
R16
10k
b4-g
b4-v+1
b4-v+2
Title
B2 UV SENSOR CHANNEL 4
Size
A
Document Number
<Doc>
Rev
<Code>
Date: Thursday, September 11, 2003
Sheet 4 of 7

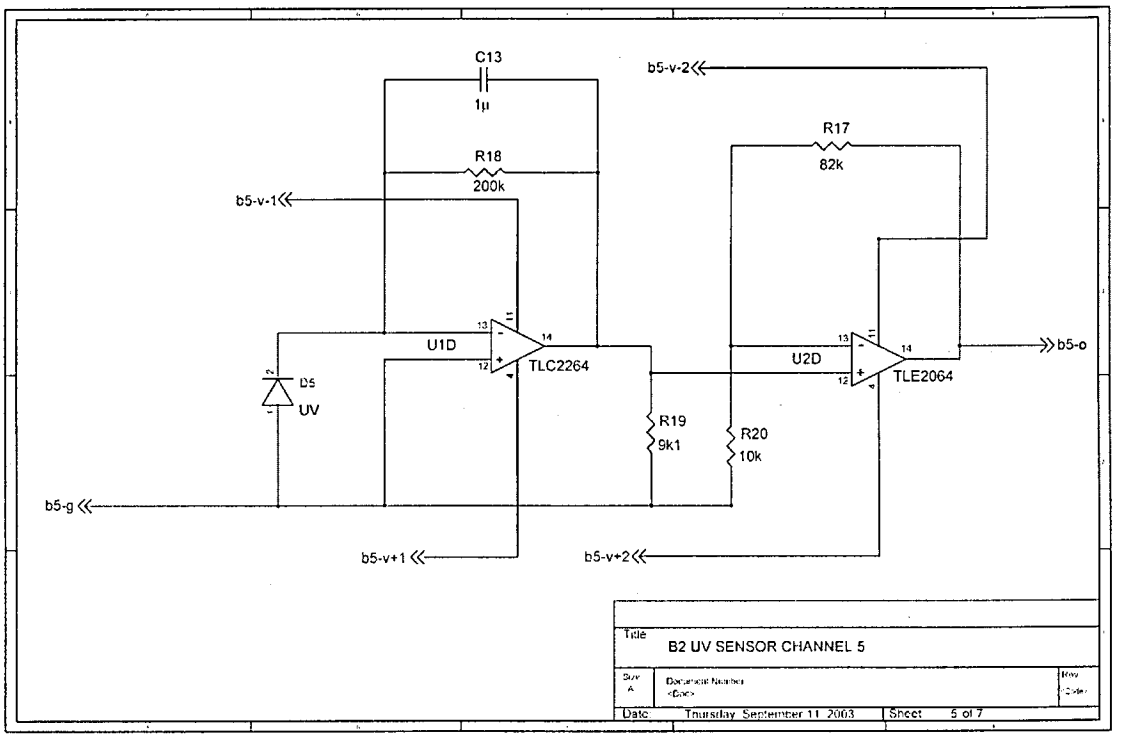
C13
1µ
R18
200k
b5-v-1
b5-v-2
R17
82k
U1D
TLC2264
U2D
TLE2064
b5-o
D5
UV
R19
9k1
R20
10k
b5-g
b5-v+1
b5-v+2
Title
B2 UV SENSOR CHANNEL 5
Size
A
Document Number
<Doc>
Rev
<Code>
Date: Thursday, September 11, 2003
Sheet 5 of 7

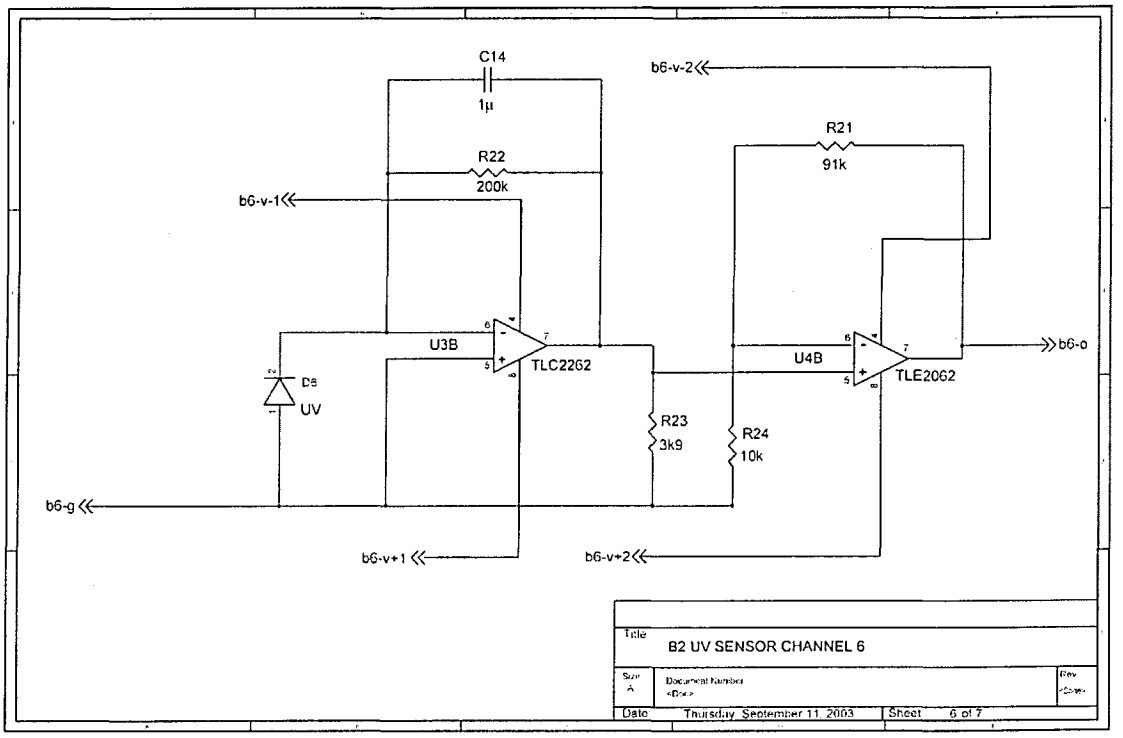
C14
1µ
R22
200k
b6-v-1
b6-v-2
R21
91k
U3B
TLC2262
U4B
TLE2062
b6-o
D8
UV
R23
3k9
R24
10k
b6-g
b6-v+1
b6-v+2
Title
B2 UV SENSOR CHANNEL 6
Size
A
Document Number
Rev
Date
Thursday, September 11, 2003
Sheet
6 of 7

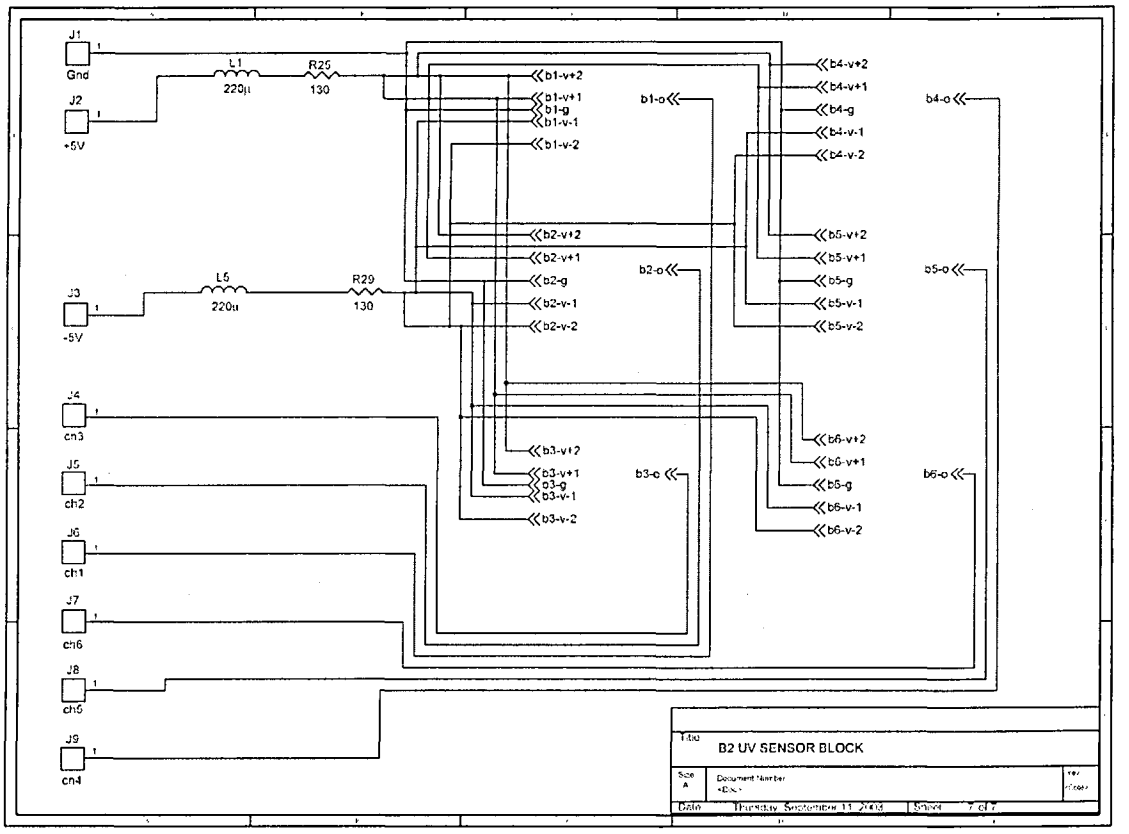
J1
Gnd
J2
+5V
L1
220µ
R25
130
b1-v+2
b1-v+1
b1-g
b1-v-1
b1-v-2
b1-o
b4-v+2
b4-v+1
b4-g
b4-v-1
b4-v-2
b4-o
J3
-5V
L5
220µ
R29
130
b2-v+2
b2-v+1
b2-g
b2-v-1
b2-v-2
b2-o
b5-v+2
b5-v+1
b5-g
b5-v-1
b5-v-2
b5-o
J4
ch3
J5
ch2
J6
ch1
J7
ch6
J8
ch5
J9
ch4
b3-v+2
b3-v+1
b3-g
b3-v-1
b3-v-2
b3-o
b6-v+2
b6-v+1
b6-g
b6-v-1
b6-v-2
b6-o
Title
B2 UV SENSOR BLOCK
Size
A
Document Number
Rev
Date
Thursday, September 11, 2003
Sheet
7 of 7

References

Akabane, T., K. Iwasaki, Y. Saito and Y. Narumi, 1993. *Astron. Astrophys.*, **277**, 302-308.

Akabane, T., Y. Saito, K. Iwasaki and L.J. Martin, 1995. *Astron. Astrophys.*, **304**, 595-601.

Akabane, T., T. Nakakushi, K. Iwasaki and S.M. Larson, 2002. *Astron. Astrophys.*, **384**, 678-688.

Amoruso, A., L. Crescentini, M. Silvia Cola and G. Fiocco, 1996. *J. Quant. Spec. Rad. Trans.*, **56** (1), 145-152.

Atreya, S.K. and Z.G. Gu, 1995. *Adv. Space Res.*, **16** (6), 57-68.

Bandfield, J.L., P.R. Christensen and M.D. Smith, 2000. *J. Geophys. Res.*, **105** (E4), 9573-9587.

Barth, C.A. and C.W. Hord, 1971. *Science*, **173**, 197-201.

Barth, C.A. and M.L. Dick, 1974. *Icarus*, **22**, 205-211.

Bell III, J.F., H.Y. McSween Jr, J.A. Crisp, R.V. Morris, S.L. Murchie et al., 2000. *J. Geophys. Res.*, **105** (E1), 1721-1755.

Bertaux, J.-L., D. Fonteyn, O.I. Korablev, E. Chassefiere, E. Dimarellis et al., 2000. *Planet. Space Sci.*, **48**, 1303-1320.

Boggess, A. and L. Dunkelman, 1959. *Ap. J.*, **129**, 236-237.

Bohren, C.F. and D.R. Huffman 1983. *Absorption and scattering of light by small particles.* Wiley, New York.

Boynton, W., W.C. Feldman, S.W. Squyres, T.H. Prettyman, J. Bruckner et al., 2002. *Science*, **297**, 81-85.

Briegleb, B.P., 1992. *J. Geophys. Res.*, **97** (D7), 7603-7612.

Brown, D.M., E.T. Downey, M. Ghezzo, J.W. Kretchmer, R.J. Saia et al., 1993. *IEEE Trans. Electron Dev.*, **40** (2), 325-333.

Cabeza, I. 2003. *ESS Ultraviolet Sensor Calibration Report.* (EADS-BGL-TRP-004), CASA-EADS Technical Report.

Caldwell, J.J. 1971. Ultraviolet observations of Mars made by the Orbiting Astronomical Observatory. *Ph.D.* Thesis, University of Wisconsin

Cantor, B.A., P.B. James, M. Caplinger and M.J. Wolff, 2001. *J. Geophys. Res.*, **106** (E10), 23653-23687.

Carlson, T.N. and R.S. Caverly, 1977. *J. Geophys. Res.*, **82**, 3141-3152.

Catling, D.C., C.S. Cockell and C.P. McKay, 1999. Ultraviolet radiation on the surface of Mars. *The Fifth International Conference on Mars*, Pasadena, California, abstract no 6128. http://mars.jpl.nasa.gov/mgs/sci/fifthconf99/author.html

Cebula, R.P., G.O. Thuillier, M.E. Vanhoosier, E. Hilsenrath, M. Herse, G.E. Brueckner and P.C. Simon, 1996. *Geophys. Res. Letters*, **23** (17), 2289.

Chamberlain, J.W. 1978. *Theory of planetary atmospheres: An introduction to their physics and chemistry.* Academic Press, New York.

Che, M. and A.J. Tench, 1982. *Advances in Catalysis*, **31**, 77-133.

Che, M. and A.J. Tench, 1983. *Advances in Catalysis*, **32**, 1-148.

Christou, A.A., 2002. *Planet. Space Sci.*, **50**, 781-788.

Chylek, P. and G.W. Grams, 1978. *Icarus*, **36**, 198-203.

CIE 1987. *International Lighting Vocabulary - Publication CIE 17.4.* CIE.

Clancy, R.T., A.W. Grossman, M.J. Wolff, P.B. James, D.J. Rudy, Y.N. Billawala, B.J. Sandor , S.W. Lee and D.O. Muhleman, 1996. *Icarus*, **122**, 36-62.

Clancy, R.T., M.J. Wolff, P.B. James, E. Smith, Y.N. Billawala, S.W. Lee and M. Callan, 1996. *J. Geophys. Res.*, **101** (E5), 12,777-12,783.

Clancy, R.T. and B.J. Sandor 1998. *Geophys. Res. Letters*, **25** (4), 489-492.

Clancy, R.T., M.J. Wolff and P.B. James, 1999. *Icarus*, **138**, 49-63.

Cockell, C.S. and J. Knowland, 1999. *Biol. Rev. Cambridge Phil. Soc.*, **74**, 311-345.

Cockell, C.S., D.C. Catling, W.L. Davis, K. Snook, R.L. Kepner, P. Lee and C.P. McKay, 2000. *Icarus*, **146**, 343-359.

Cockell, C.S., 2001. *Acta Astro.*, **49** (11), 631-640.

Colburn, D.S., J.B. Pollack and R.M. Haberle, 1989. *Icarus*, **79**, 159-189.

Curran, R.J., B.J. Conrath, R.A. Hanel, V.G. Kunde and J.C. Pearl, 1973. *Science*, **183**, 381-383.

Dementyeva, N.N., V.G. Kurt, A.S. Smirnov, L.G. Titarchuk and S.D. Chuvahin, 1972. *Icarus*, **17**, 475-483.

Dose, K. and A. Klein, 1996. *Origin. Life Evol. Biosph.*, **26**, 47-59.

Engelsen, O. and A. Kylling, 2001. Fast simulations of downward UV doses, indices and irradiances at the Earth's surface. *NDSC 2001 Symposium*, Arcachon, France, 24th-27th September 2001. http://zardoz.nilu.no/~olaeng/fastrt/fastrt.html

Evans, D.C., 1965. *Science*, **149**, 969-972.

Feldman, W.C., W.V. Boynton, R.L. Tokar, T.H. Prettyman, O. Gasnault et al., 2002. *Science*, **297**, 75-78.

Floyd, L.E., D.K. Prinz, P.C. Crane, L.C. Herring and G.E. Brueckner, 1999. *Adv. Space Res.*, **24** (2), 225-228. http://wwwsolar.nrl.navy.mil/susim_atlas_data.html

Floyd, L.E., W. Kent Tobiska and R.P. Cebula, 2002. *Adv. Space Res.*, **29** (10), 1427-1440.

Fukunishi, H., S. Watanabe, M. Taguchi, S. Okano and Y. Takahashi, 1999. *Adv. Space Res.*, **23** (11), 1903-1906.

Gierasch, P.J. and R.M. Goody, 1972. *J. Atmos. Sci.*, **29**, 400-420.

Golombeck, M.P., 1997. *J. Geophys. Res.*, **102** (E2), 3953-3966.

Greeley, R. and J.D. Iverson 1985. *Wind as a geological process on Earth, Mars, Venus, and Titan*. Cambridge University Press, Cambridge.

Greeley, R., M.R. Balme, J.D. Iverson, S.M. Metzger, R. Mickelson, J. Phoreman and B. White, 2003. *J. Geophys. Res.*, **108** (E5), 5041.

Gupta, R. 2001. *Observer's Handbook 2002*. Royal Astronomical Society of Canada, Toronto, Ontario.

Haberle, R.M., C.P. McKay, J.B. Pollack, O.E. Gwynne, D.H. Atkinson, J. Appelbaum, G.A. Landis, R.W. Zurek and D.J. Flood 1993. Atmospheric effects on the utility of solar power on Mars. In *Resources of Near-Earth Space* (J. S. Lewis, M. S. Matthews and M. L. Guerrieri, Eds.), pp. 845-885, University of Arizona Press, Tuscon.

Haberle, R.M., D. Tyler, C.P. McKay and W.L. Davis, 1994. *Icarus*, **109**, 102-120.

Hansen, J.E. and L.D. Travis, 1974. *Space Sci. Rev.*, **16**, 527-610.

Harri, A.M., B. Fagerstrom, A. Lehto, G.W. Leppelmeier, T. Makinen, R. Pirjola, T. Siikonen and T. Siili, 1998. *Planet. Space Sci.*, **46** (9/10), 1383-1392.

Heddle, D.W.O., 1962. *J. Quant. Spec. Rad. Trans.*, **2**, 349-357.

Herr, K.C. and G.C. Pimental, 1970. *Science*, **167**, 47-49.

Hess, S.L., R.M. Henry, C.B. Leovy, J.A. Ryan and J.E. Tillman, 1977. *J. Geophys. Res.*, **82** (28), 4559-4574.

Hess, S.L., R.M. Henry and J.E. Tillman, 1979. *J. Geophys. Res.*, **1979**, 2923-2927.

Hess, S.L., J.A. Ryan, J.E. Tillman, R.M. Henry and C.B. Leovy, 1980. *Geophys. Res. Letters*, **7** (3), 197-200.

Hiscox, J.A. and B.L. Lindner, 1997. *J. Brit. Interplan. Soc.*, **50**, 109-114.

Hord, C.W., C.A. Barth and J.B. Pearce, 1970. *Icarus*, **12**, 63-77.

Hord, C.W., 1972. *Icarus*, **16**, 253-280.

Horneck, G., 1993. *Origin. Life Evol. Biosph.*, **23**, 37-52.

Hsu, C.T. and B. Fattahi, 1976. *The Physics of Fluids*, **19** (12), 1853-1857.

Inada, A., A.M. Nakamura and T. Mukai, 2002. *Adv. Space Res.*, **29** (2), 209-214.

Jacobson, M.Z. 1999. *Fundamentals of atmospheric modelling*. Cambridge University Press, Cambridge.

James, P.B., M. Pierce and L.J. Martin, 1987. *Icarus*, **71**, 306-312.

James, P.B., H.H. Kieffer and D.A. Paige 1992. The seasonal cycle of carbon dioxide on Mars. In *Mars* (H. H. Keiffer, Jakosky, B.M., Snyder, C.W. and Matthews, M.S., Eds.), pp. 934-968, University of Arizona Press, Tuscon.

James, P.B., R.T. Clancy, s.W. Lee, L.J. Martin, R.B. Singer, E. Smith, R.A. Kahn and R.W. Zurek, 1994. *Icarus*, **109**, 79-101.

Johnson, J.R., W.M. Grundy and M.T. Lemmon, 2003. *Icarus*, **163** (2), 330-346.

Joseph, J.H., W.A. Wiscombe and J.A. Weinman, 1976. *J. Atmos. Sci.*, **33**, 2452-2459.

Kahn, R.A., T.Z. Martin and R.W. Zureck 1992. The Martian Dust Cycle. In *Mars* (H. H. Kieffer, B. M. Jakosky, C. W. Snyder and M. S. Matthews, Eds.), pp. 1017-1053, University of Arizona Press, Tucson.

Kasten, F., 1966. *Arch. Meteorol. Geophys. Bioklimatol. Ser. B*, **14** (206), 206-223.

Kent Tobiska, W., T. Woods, F. Eparvier, R. Viereck, L.E. Floyd, D. Bouwer, G. Rottman and O.R. White, 2000. *J. Atmos. Solar. Terr. Phys.*, **62**, 1233-1250.

Kish, L.B., R. Vajtai and P.M. Ajayan, 2001. *Chaos*, **11** (3), 674-677.

Klein, H.P., N.H. Horowitz and K. Biemann 1992. The search for extant life on Mars. In *Mars* (H. H. Kieffer, B. M. Jakosky, C. W. Snyder and M. S. Matthews, Eds.), pp. 1221-1233, University of Arizona Press, Tuscon.

Klein, H.P., 1999. *Origin. Life Evol. Biosph.*, **29** (6), 625-631.

Korablev, O.I., V.V. Krasnopolsky, A.V. Rodin and E. Chassefiere, 1993. *Icarus*, **102**, 76-87.

Krasnopol'skii, V.A., A.A. Krys'ko and V.N. Rogachev, 1975. *Cosmic Res.*, **13** (1), 31-34.

Krasnopol'skii, V.A., A.A. Krys'ko and V.N. Rogachev, 1977. *Cosmic Res.*, **15** (2), 214-218.

Kuhn, W.R. and S.K. Atreya, 1979. *J. Mol. Evol.*, **14**, 57-64.

Kurt, V.G., A.S. Smirnov, L.G. Titarchuk and S.D. Chuvahin, 1974. *Icarus*, **21**, 35-41.

Lewis, B.R. and J.H. Carver, 1983. *J. Quant. Spec. Rad. Trans.*, **30** (4), 297-309.

Lewis, S.R., M. Collins, P.L. Read, F. Forget, F. Hourdin, R. Fournier, C. Hourdin, O. Talagrand and J.-P. Huot, 1999. *J. Geophys. Res.*, **104** (E10), 24177-24194. http://www-mars.lmd.jussieu.fr/mars/live_access.html

Lunsford, J.H., 1973. *Catal. Rev.*, **8** (1), 135-157.

Magalhaes, J.A., J.T. Schofield and A. Seiff, 1999. *J. Geophys. Res.*, **104** (E4), 8943-8955.

Malicet, J., D. Daumont, J. Charbonnier, C. Parisse, A. Chakir and J. Brion, 1995. *J. Atmos. Chem.*, **21**, 263-273.

Martin, L.J., 1974. *Icarus*, **23**, 108-115.

Martin, L.J. and W.M. McKinney, 1974. *Icarus*, **23**, 380-387.

Martin, L.J., P.B. James, A. Dollfus, K. Iwasaki and J.D. Beish 1992. Telescopic observations: Visual, photographic, polarmetric. In *Mars* (H. H. Kieffer, B. M. Jakosky, C. W. Snyder and M. S. Matthews, Eds.), pp. 34-70, University of Arizona Press, Tucson.

Martin, T.J., B.G. Gardiner and G. Seckmeyer, 2000. *J. Geophys. Res.*, **105** (D22), 27005-27011.

McKinley, A.F. and B.L. Diffey, 1987. *C.I.E Journal*, **6** (1), 17-22.

Metzger, S.M. 1999. Dust Devils as Aeolian Transport Mechanisms in Southern Nevada and the Mars Pathfinder Landing Site. *Ph.D.* Thesis, University of Nevada

Metzger, S.M., J.A. Carr, J.R. Johnson, T.J. Parker and M.T. Lemmon, 1999. *Geophys. Res. Letters*, **26** (18), 2781-2784.

Miller, T.M. 1991. Atomic and Molecular Polarizabilities. In *CRC Handbook of Chemistry and Physics* (D. R. Lide, Eds.), pp. 10/194-10/210, CRC Press, Boston.

Mishchenko, M.I., W.J. Wiscombe, J.W. Hovenier and L.D. Travis 2000. Overview of scattering by non-spherical particles. In *Light scattering by nonspherical particles* (M. I. Mishchenko, J. W. Hovenier and L. D. Travis, Eds.), pp. 29-60, Academic Press, San Diego.

Mitrofanov, I., D. Anfimov, A. Kozyrev, M. Litvak, A. Sanin et al., 2002. *Science*, **297**, 78-81.

Moroz, V.I., E.V. Petrova and L.V. Ksanfomality, 1993. *Planet. Space Sci.*, **41** (8), 569-585.

Moroz, V.I., Y.M. Getkin, M.K. Naraeva, A.S. Selivanov and D.V. Titov, 1994. *Planet. Space Sci.*, **42** (10), 831-845.

Muller, C., D. Moreau, D. Fonteyn, J.-L. Bertaux and O.I. Korablev, 2001. *Planet. Space Sci.*, **49**, 165-171.

Munakata, N., M. Saito and K. Hieda, 1991. *Photochem. and Photobiol.*, **54**, 761-768.

Nakakushi, T., T. Akabane, K. Iwasaki and S.M. Larson, 2001. *J. Geophys. Res.*, **106** (E3), 5043-5056.

Neudeck, P.G. 2001. Silicon Carbide Electronic Devices. In *Encyclopedia of Materials: Science and Technology* (K. H. J. Buschow, R. W. Cahn, M. C. Flemings et al, Eds.), **9**, pp. 8508-8519, Elsevier, Oxford.

Ockert-Bell, M.E., J.F. Bell III, J.B. Pollack, C.P. McKay and F. Forget, 1997. *J. Geophys. Res.*, **102** (E4), 9039-9050.

Owen, T. and C. Sagan, 1972. *Icarus*, **16**, 557-568.

Owen, T. 1992. The Composition and Early History of the Atmosphere of Mars. In *Mars* (B. M. J. H.H. Kieffer, C.W. Snyder and M.S. Matthews, Eds.), pp. 818-834, University of Arizona Press, Tucson.

Pang, K. and C.W. Hord, 1973. *Icarus*, **18**, 481.

Pang, K., J.M. Ajello, C.W. Hord and W.G. Egan, 1976. *Icarus*, **27**, 55-67.

Pang, K. and J.M. Ajello, 1977. *Icarus*, **30**, 63-74.

Patel, M.R., J.C. Zarnecki and D.C. Catling, 2002. *Planet. Space Sci.*, **50** (9), 915-927.

Patel, M.R., A. Berces, C. Kolb, H. Lammer, P. Rettberg, J.C. Zarnecki and F. Selsis, 2003a. *Int. J. Astrobiology*, **2** (1), 21-34.

Patel, M.R., A.A. Christou, C.S. Cockell, T.J. Ringrose and J.C. Zarnecki, 2003b. *Icarus*, (in press).

Pearce, J.B., K.A. Gause, E.F. Mackey, K.K. Kelly, W.G. Fastie and C.A. Barth, 1971. *App. Opt.*, **10** (4), 805-812.

Pearl, J.C., M.D. Smith, B.J. Conrath, J.L. Bandfield and P.R. Christensen, 2001. *J. Geophys. Res.*, **106** (E6), 12325-12338.

Peeters, P., J.-F. Muller, P.C. Simon, D. Gillotay, E.A. Celarier and J.R. Herman, 2000. *Adv. Space Res.*, **26** (12), 1941-1947.

Peskett, S. 2001. *Phase C TMM: First design and analysis campaign report issue1.1.* (BGL2-RAL-TN-0022), Beagle 2 Internal Document.

Petrova, E., H.U. Keller, W.J. Markiewicz, N. Thomas and M.W. Wuttke, 1996. *Planet. Space Sci.*, **44** (10), 1163-1176.

Petrova, E.V. and W.J. Markiewicz, 1998. *Sol. Sys. Res.*, **32** (6), 469-479.

Pillinger, J.M., J.A. Spry and C.T. Pillinger, 2002. Planetary protection plan for the Beagle 2 lander. *COSPAR 2002*, Houston, Texas U.S.A., abstract no. A-02628.

Pollack, J.B., D. Colburn, R. Kahn, J. Hunter, W. Van Camp, C.E. Carlston and M.R. Wolf, 1977. *J. Geophys. Res.*, **82** (28), 4479-4496.

Pollack, J.B., D.S. Colburn, F. Michael Flaser, R. Kahn, C.E. Carlston and D. Pidek, 1979. *J. Geophys. Res.*, **84** (B6), 2929-2945.

Pollack, J.B., M.E. Ockert-Bell and M.K. Shepard, 1995. *J. Geophys. Res.*, **100** (E3), 5235-5250.

Rea, D.G., 1966. The atmosphere and surface of Mars - A selective review. *Caltech-JPL Lunar and Planetary Conference*, Pasadena, CA, 13-18 September 1965. California Institute of Technology, pp. 209.

Ringrose, T.J., M.C. Towner and J.C. Zarnecki, 2003. *Icarus*, **162**, 78-87.

Rodin, A.V., O.I. Korablev and V.I. Moroz, 1997. *Icarus*, **125**, 212-229.

Rodrigo, R., E. Garcia-Alvarez, M.J. Lopez-Gonzalez and J. Lopez-Moreno, 1990. *J. Geophys. Res.*, **95**, 14795-14810.

Rottman, G., T. Woods, M. Snow and G. DeToma, 2001. *Adv. Space Res.*, **27** (12), 1927-1932.

Ryan, J.A. and J.J. Carroll, 1970. *J. Geophys. Res.*, **75** (3), 531-541.

Ryan, J.A. and R.D. Sharman, 1981. *J. Geophys. Res.*, **86** (C4), 3247-3254.

Ryan, J.A. and R.D. Lucich, 1983. *J. Geophys. Res.*, **88** (C15), 11005-11011.

Schmidt, R., J.D. Credland, A. Chicarro and P. Moulinier, 1999. *ESA Bulletin*, **98**, 56-66.

Schmidt, R., 2003. *Acta Astro.*, **52** (2-6), 197-202.

Scourfield, M.W.J. and G.E. Bodeker, 2000. *Phys. Chem. Earth (B)*, **25** (5-6), 521-523.

Seiff, A., J.E. Tillman, J.R. Murphy, J.T. Schofield, D. Crisp et al., 1997. *J. Geophys. Res.*, **102** (E2), 4045-4056.

Setlow, R. and B. Doyle, 1954. *Biochim. et Biophys. Acta*, **15**, 117-125.

Shao, Y. and H. Lu, 2000. *J. Geophys. Res.*, **105** (D17), 22437-22443.

Shaw, P.S., K.R. Lykke, R. Gupta, T.R. O'Brian, U. Arp, H.H. White, T.B. Lucatorto, J.H. Dehmer and A.C. Parr, 1999. *App. Opt.*, **38** (1), 18-28.

Shettle, E.P. and J.A. Weinman, 1970. *J. Atmos. Sci.*, **27**, 1048-1055.

Simonsen, L.C., J.E. Nealy, L.W. Townsend and J.W. Wilson, 1990. *J. Space. Rockets*, **27** (4), 353-354.

Sinclair, P. 1966. A quantitative analysis of the dust devil. *Ph.D.* Thesis, Arizona State University

Smith, M.D., J.L. Bandfield and P.R. Christensen, 2000. *J. Geophys. Res.*, **105** (E4), 9589-9608.

Smith, M.D., J.C. Pearl, B.J. Conrath and P.R. Christensen, 2001. *Geophysical Research Letters*, **28** (22), 4263-4266.

Smith, M.D., J.C. Pearl, B.J. Conrath and P.R. Christensen, 2001. *J. Geophys. Res.*, **106** (E10), 23929-23945.

Smith, M.D., B.J. Conrath, J.C. Pearl and P.R. Christensen, 2002. *Icarus*, **157** (1), 259-263.

Smith, P.H. and M. Lemmon, 1999. *J. Geophys. Res.*, **104** (E4), 8975-8985.

Spry, J.A. 2001. *Planetary protection implementation plan for Beagle 2.* (BGL2-OU-PL-007), Beagle 2 Internal Document.

Stamnes, K. and P. Conklin, 1984. *J. Quant. Spec. Rad. Trans.*, **31** (3), 273-282.

Stephens, G.L., P.M. Gabriel and P.T. Partain, 2001. *J. Atmos. Sci.*, **58**, 3391-3409.

Stiegman, A.E. and R.H. Liang 1993. Ultraviolet and vacuum-ultraviolet radiation effects on spacecraft thermal control materials. In *The behaviour of systems in the space environment* (R. N. DeWitt, D. Duston and A. K. Hyder, Eds.), pp. 259-265, Kluwer Academic Publishers, Dordrecht.

Sykes, J. 2002. *Beagle 2 ESS Vibration and Thermal Test Levels issue 2.* (BGL-LUX-SP-207), Beagle 2 Internal Document.

Toon, O.B., J.B. Pollack and C. Sagan, 1977. *Icarus*, **30**, 663-696.

Towner, M.C., M.R. Patel, T.J. Ringrose, J.C. Zarnecki, D. Pullan et al., 2003. *Planet. Space Sci.*, (submitted).

Wallace, L., J.J. Caldwell and B.D. Savage, 1972. *Ap. J.*, **172**, 755-769.

Warren, S.G., 1984. *App. Opt.*, **23** (8), 1206-1223.

Wolff, M.J., S.W. Lee, R.T. Clancy, L.J. Martin, J.F. Bell III and P.B. James, 1997. *J. Geophys. Res.*, **102** (E1), 1679-1692.

Wolff, M.J., J.F. Bell III, P.B. James, R.T. Clancy and S.W. Lee, 1999. *J. Geophys. Res.*, **104** (E4), 9027-9041.

Wright, I.P., M.R. Sims and C.T. Pillinger, 2003. *Acta Astro.*, **52**, 219-225.

Wuttke, M.W., H.U. Keller, W.J. Markiewicz, E.V. Petrova, K. Richter and N. Thomas, 1997. *Planet. Space Sci.*, **45** (3), 281-288.

Yen, A.S., S.S. Kim, M.H. Hecht, M.S. Frant and B. Murray, 2000. *Science*, **289**, 1909-1912.

Zurek, R.W., 1978. *Icarus*, **35**, 196-208.

Zurek, R.W. 1992. Comparative aspects of the climate of Mars: An introduction to the current atmosphere. In *Mars* (H. H. Kieffer, B. M. Jakosky, C. W. Snyder and M. S. Matthews, Eds.), pp. 799-817, University of Arizona Press, Tucson.

Zurek, R.W., J.R. Barnes, R.M. Haberle, J.B. Pollack, J.E. Tillman and C.B. Leovy 1992. Dynamics of the atmosphere of Mars. In *Mars* (H. H. Kieffer, B. M. Jakosky, C. W. Snyder and M. S. Matthews, Eds.), pp. 835-933, University of Arizona Press, Tucson.